Flow Vaporization of CO_2 in Microchannel Tubes

by

Jostein Pettersen

A Thesis Submitted for the Degree of

Doctor Technicae

Norwegian University of Science and Technology
Faculty of Engineering and Technology
Department of Refrigeration and Air Conditioning

February 2002

URN:NBN:no-2319

URN:NBN:no-2319

Foreword

This thesis is based on studies carried out at the Norwegian University of Science and Technology (NTNU), Department of Refrigeration and Air Conditioning, in the years 1999-2001. The close and integrated relationship between this NTNU Department and the sister Department of the contract research institute SINTEF Energy Research has been an indispensable factor in terms of infrastructure, test rig funding, and supporting personnel.

External funding or resources for projects leading up to this work has been available from

- U.S. Army European Research Office, London, and the CECOM Research, Development, and Engineering Center of the U.S. Army at Ft. Belvoir, Virginia (Contract N-68171-99-M5674, 1999-2000)
- Norsk Hydro, through Hydro Aluminium, Hydro Pronova, and Hydro Alunova
- IEA Annex 27: Selected Issues on CO_2 as Working Fluid in Compression Systems.

A number of great people contributed in various ways to the foundation for this work. I would like to thank some of them, in alphabetical order:

- *Kåre Aflekt*, for building, instrumenting, troubleshooting and operating the flow pattern test rig, processing test data, programming and plotting flow regime maps, and helping getting things finished.
- *Arne M. Bredesen*, for offering inspiration, direction and good humour.
- *Armin Hafner*, for helping to get things working in the laboratory
- *Andreas Leister*, for his pioneering work on the heat transfer test rig and the data processing software.
- *Svend Tollak Munkejord*, for laying the foundation for this work, and establishing the heat transfer test rig and the testing principles.
- *René Rieberer*, for spending long hours in the lab and the office with results, organizing and analysing these, and completing all tasks on time.
- *Geir Skaugen*, for helping out with tricky spreadsheet problems, for keeping literature organized, and for generously making programs and functions available on short notice.
- *Ingvald Strømmen*, for releasing me from other duties at the Department, so I could concentrate.
- *Katrine Vestbøstad*, for conducting heat transfer experiments.
- *Eugen Uthaug*, for helping when healthy computers were needed.

My family gave me endless amounts of tolerance and understanding while I was working on this report. For this I would like to thank you, dear Signe, Astrid, Marit and Peder. I hope you can forgive me for all the time I spent inside small tubes instead of being with you.

I have realized that an undertaking like this should be completed while you are still young and not too tied into all sorts of other projects and responsibilities that distract the focus. Concentration and time is essential but increasingly hard to find as the years go by.

If you ask me, is there someone you do not want to thank, the answer is yes. I do not want to thank a certain software company for the often strange, annoying and highly frustrating behaviour of their word processing and spreadsheet products, as well as their operating system. But, in the name of standardization and low price you have to swallow a lot.

Trondheim, 14 February 2002

Jostein Pettersen

Summary and Conclusion

Background and introduction

Carbon dioxide (CO_2) is receiving renewed interest as an efficient and environmentally safe refrigerant in a number of applications, including mobile air conditioning and heat pump systems, and hot water heat pumps. Compact heat exchangers for CO_2 systems are designed with small-diameter tubing. Geometries using flat extruded microchannel[a] tubes with flow through a number of parallel channels give compact and lightweight heat exchangers even with a high-pressure fluid like CO_2.

Studies on two-phase flow and heat transfer in microchannel geometries have mostly been focused on low-pressure refrigerants, and air/water systems at atmospheric pressure. Even for conventional fluids, the knowledge on microchannel flow and heat transfer is limited, and very few data have been published on CO_2. The purpose of this study is therefore to provide a better basis for understanding and predicting heat transfer and pressure drop during flow vaporization[b] of CO_2 in microchannels

The "unusual" properties of carbon dioxide give heat transfer and two-phase flow characteristics that are very different from those of conventional refrigerants. Examples of these differences are the much higher pressure, the resulting high vapour density, a very low surface tension, and a low liquid viscosity. High pressure and low surface tension has a major effect on nucleate boiling characteristics, and earlier test data have shown a clear dominance of nucleate boiling even at very high mass flux.

Theoretical framework

Several authors have observed "confinement effects" for boiling in small channels, and nucleate flow boiling characteristics may be affected by channel size when the diameter is comparable to the bubble departure size. Gravity is believed to be of reduced importance in small-channel flow, and the flow pattern will mainly be influenced by shear forces, surface tension, and liquid/surface interactions.

Entrainment is likely to play an important role in CO_2 two-phase flow in evaporators. Estimated vapour flow velocity of onset of entrainment range from 0.5 to 1.5 ms^{-1}, which is considerably lower than for a fluid like HFC-

[a] A microchannel is assumed to have a hydraulic diameter of less than 2 mm
[b] Vaporization is a general term for (nucleate) boiling and (convective) evaporation

134a at the same temperatures. Entrainment caused by heat flux is also known to increase at high pressure.

Dryout is a critical heat flux (CHF) phenomenon that occurs when the liquid film on the tube wall is discontinued due to entrainment and evaporation. Earlier tests have demonstrated that dryout may occur at moderate vapour fractions in CO_2 flow, particularly at high mass flux and high temperature conditions. The onset of dryout can be predicted using detailed two-phase flow models with integration of mass continuity along the tube, or empirical correlations can be used. Since dryout data on CO_2 are generally not available, the empirical method relies on data for water which are converted by fluid-to-fluid scaling laws, e.g. by the method of Ahmad (1973).

Generalized flow pattern maps show transition lines between different two-phase flow patterns, usually for adiabatic flow. Most existing maps were developed based on flow in larger-diameter tubes, and several investigations on small-diameter tubes have shown that the predicted flow pattern transitions do not match the observations. Stratified flow is generally not observed in microchannel tubes (diameter in the order of 1 mm), where forces induced by surface tension become important.

Numerous flow vaporization correlations have been developed over the years. Many of these are based on experimental data regression and lack the necessary mechanistic foundation. The model of Kattan et al. (1998b) attempts to avoid the deficiencies of earlier correlations, using two-phase flow pattern data and detailed models for heat transfer in various flow patterns. Nucleate boiling can be predicted by correlations that account for boiling pressure (reduced pressure), as well as heat flux and surface roughness. Convective evaporation can be predicted using single-phase liquid film flow models. Heat transfer coefficient for "wetted" surface can then be found by combining the convective and nucleate contributions using an asymptotic model. Heat transfer in the post-dryout mist or droplet flow regime can be predicted using assuming models that assume equilibrium (unlimited heat transfer between vapour or droplets), or models that account for departure from equilibrium, for instance the correlation by Shah and Siddiqui (2000).

Test methods

Heat transfer tests were conducted in a rig using a flat, extruded aluminium microchannel tube of 540 mm length with 25 channels of 0.81 mm diameter. The horizontal test tube was heated by a water jacket in order to get representative boundary conditions for air-to-refrigerant heat transfer ("fluid heating"). Constant heat flux conditions do not simulate these boundary conditions well, and may give unrealistic behaviour especially in relation to

dryout and post-dryout heat transfer. Systematic tests at constant heat flux with single-phase CO_2 flow on the inside generated data that were used in the derivation of a model for water-side heat transfer coefficient. A regression based on these data gave a calibrated equation for water-side heat transfer on the form $Nu=Nu(Re,Pr)$. This equation was then used in later experiments to subtract water-side thermal resistance from the measured overall resistance ($1/UA$), thereby finding the internal heat transfer coefficient. A data reduction scheme was developed to find the mean vaporization heat transfer coefficient h as well as the mean vapour fraction x in each test. Measured pressure drop between the inlet and outlet manifolds of the test section was corrected to find the net frictional pressure drop in the heated part of the tube.

Uncertainties in measured parameters are summarized in the following Table

Parameter	Uncertainty
Evaporating temperature, T	±(0.08-0.13) K
Refrigerant mass flux, G	±(2.6-2.8) %
Heat flux, q	±(1.8-8.5) %
Mean vapour fraction, x	±(0.028-0.137)
Overall heat transfer coefficient, U	±(2.5-10) %

A special rig was built in order to observe two-phase flow patterns. A horizontal quartz glass tube with ID 0.98 mm was coated by transparent resistive coating of indium tin oxide (ITO), and connected to an open fluid circuit where liquid CO_2 was taken from a heated storage cylinder, its pressure reduced and mass flow adjusted by valves before a preheater section that gave the desired x into the observation tube. Heat flux was obtained by applying DC power to the ITO film, and flow patterns were recorded at 4000-8000 frames per second by a digital video camera. Compared to "standard" test arrangements, this enabled recordings in the heated zone, and not in an adiabatic observation tube installed after or between heated tubes. In heat transfer dominated by nucleate boiling this makes quite a difference.

Test results and observations

Vaporization heat transfer and pressure drop data were recorded over a wide range of conditions, including temperatures from 0 to 25°C, heat flux from 5 to 20 kWm^{-2}, mass flux from 190 to 570 $kgm^{-2}s^{-1}$, and vapour fraction between 0.2 and 0.8. The test section design did not enable measurement of local h and x inside the tube, and the results are therefore mean values. Relative uncertainty of the measured heat transfer coefficient ($\delta h/h$) increased with h, from about ±10% at h=5 $kWm^{-2}K^{-1}$, to about ±40% at h=20 $kWm^{-2}K^{-1}$. The influence of uncertainty in water-side resistance

becomes greater as refrigerant-side resistance drops (when h increases) for a given overall resistance.

Test results showed that the nucleate boiling mechanism dominated at low/moderate vapour fractions, where h increased with heat flux and temperature, but was less affected by varying mass flux and vapour fraction. Heat transfer coefficients ranging from about 10 to 20 $kWm^{-2}K^{-1}$ were measured in this region. Dryout effects became very important at higher mass flux and temperature, where h dropped rapidly at increasing x.

Two-phase flow patterns were recorded mainly at a temperature of 20°C, and for mass flux ranging from 100 to 580 $kgm^{-2}s^{-1}$. The observations showed a dominance of intermittent (slug) flow at low x, and wavy annular flow with entrainment of droplets at higher x. At high mass flux, the annular/entrained flow pattern could be described as dispersed. The aggravated dryout problem at higher mass flux could be explained by increased entrainment. Stratified flow was not observed in the tests with heat load. Bubble formation and growth could be observed in the liquid film, and the presence of bubbles gave differences in flow pattern compared to adiabatic flow.

Analysis and discussion

Heat transfer data at low x and widely varying mass flux at a given temperature could be correlated by curves in heat flux/wall superheat coordinates, thus confirming the nucleate boiling domination. Test data published by others gave values that were generally within ±30-40% of the present low-x data, mostly at lower values than in the present tests. The nucleate (pool) boiling correlation of Cooper (1984) predicted 20-30% lower heat transfer coefficient, while the best fit was obtained with the correlation of Gorenflo (1993) which gave values 8% above the present test data on average (using a reference coefficient of 4170 $Wm^{-2}K^{-1}$). The special small-tube correlation of Tran et al. (1997) failed to reproduce the level and trend of the data.

Dryout was predicted using the water dryout data of Kon'kov (1965) scaled to CO_2 by the method of Ahmad (1973). The predicted onset of dryout corresponded reasonably well with observations from present tests, although at somewhat higher x than observed. The lack of truly local data made this comparison difficult, however. Compared to the local (constant q) CO_2 dryout data of Hihara and Tanaka (2000) in a 1 mm tube, predicted dryout was generally at too low x. Present test data gave significantly lower x at dryout than in the experiments of Hihara and Tanaka (2000), even though their larger tube diameter would be expected to give the opposite situation. Flow oscillations are known to reduce CHF, and oscillations in the parallel

channels of the present test tube may explain this difference. Generalized CHF prediction methods did not reproduce the dryout observations.

Post-dryout heat transfer coefficients may approach equilibrium values at very high mass flux and/or high vapour flow velocity, but significant non-equilibrium effects can be observed in test data at moderate/realistic mass flux. Non-equilibrium effects occur when vapour becomes superheated due to poor heat transfer to the liquid droplets. The correlation of Shah and Siddiqui (2000) seems to reproduce the test data well, while the much quoted model of Groeneveld and Delorme (1976) gave larger deviation.

The flow pattern observations on CO_2 did not fit any of the generalized maps or transition lines, including the map proposed by Kattan et al. (1998a). Only the intermittent-annular transition prediction of Weisman et al. (1979) was close to the observed behaviour. Compared to small-diameter observations with air/water at low pressure, the transition into annular flow occurred at much lower superficial vapour velocity (superficial velocity of approximately 0.5 ms^{-1}). The observed inception of entrainment at 0.5-0.6 ms^{-1} superficial vapour flow velocity was close to the predicted onset at 0.4 ms^{-1}.

Frictional pressure drop was correlated with a mean/average deviation of 22.3/-17.4% using the Friedel (1979) correlation. The underprediction was significant at low pressure drop (low mass flux), and at low temperature. The "CESNEF-2" correlation by Lombardi and Carsana (1992) gave much better accuracy, with a mean/average deviation of 16.4/-1.1%. The small-tube correlations of Tran et al. (1999) and Zhang and Webb (2001) gave poor correspondence, with mean/average deviation of 80.4/74.5% and 40.5/-40.5%, respectively.

Correlation of heat transfer data

Heat transfer coefficients were calculated using combinations of the above models for nucleate boiling, convective evaporation, dryout inception, and post-dryout heat transfer, and compared to the experimental data from this study. The best fit was found using the Cooper (1984) nucleate boiling correlation and the Kattan et al. (1998b) convective evaporation correlation in an asymptotic model with n=3 for the pre-dryout regime. Dryout was predicted using the water data of Kon'kov (1965) scaled from H_2O to CO_2 using the Ahmad (1973) scaling factor based on *Barnett* number. Post-dryout heat transfer was modelled using the correlation of Shah and Siddiqui (2000). This combined correlation reproduced the 140 test data points with an average deviation of 7.7% and a mean deviation of 35.1%.

Conclusions

A number of conclusions can be drawn from the present investigations on heat transfer, pressure drop and flow patterns in microchannel vaporization of CO_2. The most important points are emphasized in the following text:

- The understanding of characteristics and mechanisms of CO_2 flow-vaporization in horizontal microchannels has been improved. Nucleate boiling is the dominant heat transfer mechanism, and the convective contribution is quite small. Dryout may occur at moderate vapour fraction if the mass flux is large and/or the temperature is high. Flow instabilities in parallel channels may give noticeable reduction in critical vapour fraction. Non-equilibrium effects may influence post-dryout heat transfer significantly, giving local heat transfer coefficients well below single-phase vapour flow values.

- An important consequence of the above results is that efficient compact CO_2 evaporators for mobile or unitary applications can be designed with low mass flux. Increased G does not improve heat transfer while the added pressure drop acts negatively by reducing the temperature difference. Another reason for selecting low mass flux is the increased critical vapour fraction. Thus, dryout can be avoided by reducing G. It follows from this that the evaporator preferably should be fed with liquid only or with a low vapour fraction, and if possible, the outlet condition should be kept in the wet region. This will make sure that efficient nucleate boiling dominates, and dryout problems will be avoided or reduced, and the negative effects of poor post-dryout heat transfer will be avoided. A secondary advantage is that flow distribution between parallel channels can be improved with liquid inlet, especially at low mass flux.

- Heat transfer can be predicted with reasonable accuracy, using known models for nucleate boiling, convective evaporation, onset of dryout, and post-dryout heat transfer. The resulting correlation procedure is quite complicated though, and simplifications may be needed in order to have a model that can be used in practical evaporator design and modelling.

- Pressure drop data can be predicted with good accuracy using existing correlations, even though the underprediction may become significant at low temperature and/or low mass flux. If the above evaporator design guidelines are followed, however, the pressure drop will be of minor importance.

- Two-phase flow regimes in horizontal microchannel CO_2 vaporization flow could not be predicted using existing models and generalized flow charts. Since the observed patterns (prior to dryout) were dominated by intermittent and annular flow with good wetting of the tube wall, and since stratified flow was not observed, the flow pattern may be of secondary importance.

- A comprehensive analysis of the experimental uncertainties has demonstrated the accuracy of measured heat transfer coefficients using a heat exchanger regression ("Wilson plot") method. The accuracy of this method has been widely discussed, and very little systematic work has been done on documenting the uncertainties involved. Results from the present study show that the uncertainty of measured heat transfer coefficients is comparable to what can be obtained by direct measurement of tube wall temperature, provided that the water-side heat transfer coefficient is high enough.

- Further studies in this area should extend the range of test conditions and flow observations, e.g. to lower temperature and lower mass flux, and to other tube diameters. The effects of lubricant on heat transfer and pressure drop also needs to be investigated. Lubricant may have considerable influence on nucleate boiling heat transfer.

- Further developments in modelling and prediction should consider the potential of using a detailed two-phase flow model with entrainment and deposition as a basis, not just for dryout prediction but also as a basis for heat transfer modelling. As shown by some published studies on water/steam systems, this type of model can give good accuracy in prediction of critical vapour fraction, and can also aid the modelling of pre- and post-dryout heat transfer.

Contents

URN:NBN:no-2319

1. Introduction

1.1 The CO_2 revival

With increasing focus on the environmental consequences of refrigerants and refrigerant systems, carbon dioxide has become an essential candidate fluid in many air conditioning, heat pump and refrigeration applications. CO_2 was widely used as a refrigerant before the Second World War, especially in marine systems, but the introduction of CFC and HCFC fluids led to a decline and eventually a discontinuation of its use. The reasons for this were many, the most important probably being that low-pressure CFC/HFC systems were easier to handle from a practical standpoint, especially at high ambient temperature conditions.

Since then, the vapour compression systems, their components and the underlying materials and production technology have developed significantly, and higher pressures can now be handled more easily. In many cases, a higher pressure may even be an advantage, owing to the more compact piping and components. Concepts have been developed that allow efficient and simple operation of a transcritical system (Lorentzen, Pettersen and Bang, 1993). In the search for environmentally safe technology, the natural refrigerant CO_2 thus received more interest, being a non-toxic and non-flammable fluid as well.

Lorentzen and Pettersen (1992) initiated work in the late eighties and published the first "modern" experimental results on a prototype transcritical CO_2 system for mobile air conditioning. This and other studies led to considerable interest and development activities in the automotive industry, and pilot vehicles have now been on the road for several years with such systems. Recently, system designs have been developed that may also provide heating of the passenger compartment in cold weather. Such reversible air conditioning and heat pump systems can give improved passenger and driver comfort and safety in vehicles with limited or no

engine waste heat, and the first commercial system will be introduced in fuel cell vehicles in 2003.

Another very promising area of CO_2 technology is hot water heat pumps. The transcritical cycle is well adapted to heating water at gliding temperature, and high water outlet temperature can be achieved with very good coefficient of performance. After several years of development, including testing of a laboratory prototype system, an industrial pilot system was installed in a food processing facility in Larvik, Norway in late 1999 (Zakeri, Nekså et al., 2000). Domestic hot water heat pumps based on CO_2 were introduced on the Japanese market in spring 2001. Other application areas that are being investigated include commercial refrigeration systems, transport refrigeration units, residential heat pumps and air conditioning systems, and clothes and food product drying systems.

Over the last decade, carbon dioxide has therefore had something of a revival as refrigerant, at least in terms of a massive research and development effort. This renewed interest is clearly shown by the number and share of published papers on CO_2 at the biennial IIR Gustav Lorentzen Conference on Natural Working Fluids, Figure 1.1

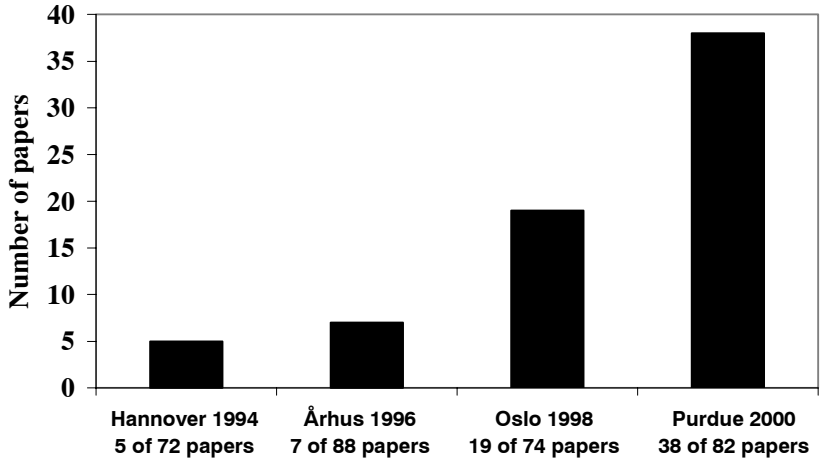

Figure 1.1 *Number of papers on CO_2 as primary refrigerant at the IIR Gustav Lorentzen Conference on Natural Working Fluids*

In the further development of systems adapted to CO_2 as a refrigerant, the design of heat exchangers is one of the key issues. Especially in transport air conditioning or refrigeration applications, an efficient, compact and lightweight design is needed (Pettersen et al., 1998). Owing to the higher pressures, optimum compact heat exchanger designs for CO_2 generally tend to use small-diameter flowchannels, in many cases based on extruded "multi-port" tubing with parallel flow of refrigerant in several tubes and

flowchannels. In this type of heat exchanger the heat transfer tubes extend between two manifolds, Figure 1.2. A special "double barrel" compact manifold design for high pressure is shown in the Figure.

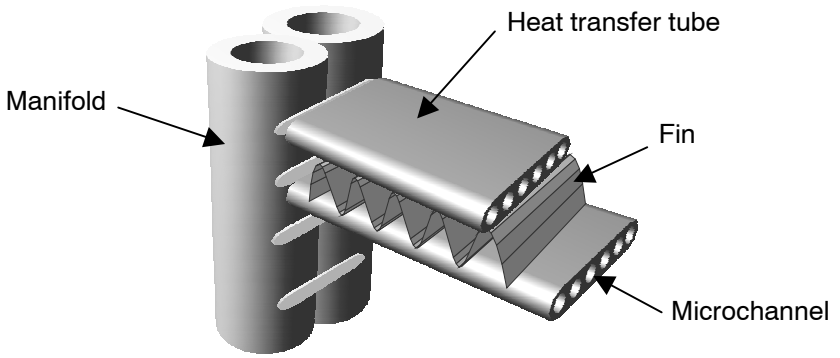

Figure 1.2 *Principles of CO_2 heat exchanger geometry using "multi-port" extruded tubes with microchannels, folded fins, and a compact "double barrel" manifold. The heat exchanger is assembled by brazing in a furnace.*

The manifolds may have vertical or horizontal orientation, and the heat transfer tubes are partially inserted into the slots in the manifolds before brazing.

In some cases it may be more economical to use small-diameter round tubes and a mechanically expanded heat exchanger. Also in this case, the internal diameter will most likely be smaller than for conventional refrigerants, and generally below the range of diameters where experimental data exist or where heat transfer or pressure drop correlations are valid. Pettersen et al. (1998) showed some compact heat exchanger concepts for CO_2 air conditioning systems having internal tube diameter of 2 mm.

In order to design and optimise heat exchangers, local heat transfer and pressure drop data both on the air and refrigerant side are needed, and the fundamental mechanisms need to be understood. Since air-side conditions and geometry are not very different from those of heat exchangers for conventional refrigerants, the major issue facing designers of CO_2 heat exchangers is the lack of data and correlations adapted to CO_2 and microchannel[c] flow. The current study aims at providing some of this information.

[c] In this context, a microchannel is assumed to have a hydraulic diameter less than 2 mm

1.2 Focus of research

In a study on heat transfer and pressure drop characteristics of CO_2 in relation to heat exchangers for vapour compression systems, there are three distinct factors that stand out as important:

- Thermodynamic and transport properties of CO_2 are quite different from those of conventional refrigerants. This is important both for the heat rejection and for the heat absorption process. In heat absorption, the high evaporation pressure gives high vapour density, and thus the difference or ratio between liquid and vapour density is quite small for CO_2. This will affect the flow pattern and two-phase flow characteristics. The surface tension of liquid CO_2 is quite low, at least for medium- and high-temperature evaporator conditions. The special properties of CO_2 in relation to evaporation are discussed in more detail in Chapter 2.

- Transcritical CO_2 systems reject heat at supercritical high-side pressure, i.e. with single-phase refrigerant flow. The single-phase situation makes the picture less complicated than for two-phase flow, but again the thermodynamic and transport properties and their variation may affect heat transfer and pressure drop in ways that are different from in conventional single-phase flow. Large gradients in density, specific heat capacity and conductivity near the critical point and near pseudocritical[d] states may affect local heat transfer significantly.

- Compact heat exchangers for CO_2 mobile and unitary equipment will most likely be designed with small-diameter or microchannel tubing. Even though some work on two-phase heat transfer with conventional refrigerants in such tube geometries has been reported, there is generally a need for a better understanding of mechanisms and characteristics of two-phase flow and heat transfer in microchannels. For CO_2 only a few experimental data on microchannel heat transfer have been published so far.

Earlier research (Pettersen et al., 2000) addressed some aspects of these issues, especially regarding heat transfer and pressure drop at supercritical pressure. The results indicated that in microchannel tubes and for mass flux and heat flux conditions in air-cooled heat exchangers, single-phase heat transfer and pressure drop data were reproduced in a satisfactory way by standard correlations, even close to pseudocritical conditions. The reason

[d] Location where isobaric specific heat capacity has a maximum

may be that the small-diameter tube geometry and the moderate heat flux did not give significant property variation between film and bulk fluid conditions in the tube. Thus, the need for further studies into single-phase heat transfer and pressure drop in microchannels was not regarded as pressing.

Results on microchannel vaporization reported by Pettersen et al. (2000) as well as other authors gave a quite different picture, however. In this case, the experimental data were not correlated well by any of the tested heat transfer and pressure drop models from literature. Also, the occurrence of what appeared to be dryout at moderate/high vapour fractions was discovered, with dramatic reductions in the heat transfer coefficient for vapour fraction beyond a certain critical level. These phenomena primarily occurred at high mass flux conditions and high evaporating temperatures. Two-phase flow patterns were not observed, however, and the theory that dryout was caused by a transition from annular flow to dispersed flow could not be confirmed. In order to improve the understanding of heat transfer mechanisms in evaporating CO_2 flow in general, and dryout phenomena in particular, some information on flow patterns was needed.

There was and still is a dispute on accuracy and relevance of the various experimental methods that are applied in the study of vaporization heat transfer. Key issues here are the relevance of constant heat flux conditions especially when studying dryout and post-dryout phenomena, experimental uncertainty of internal surface temperature measurement/calculation, and uncertainty of regression-based methods (e.g. Wilson-plot methods) for determining the heat transfer coefficient. The experimental methods need to be thoroughly evaluated both in terms of uncertainty and realism in relation to the conditions in actual air-cooling or water-cooling evaporators.

On this background it was clear that the present work had to address several issues, and the research question for the study was defined as:

"Provide a basis for understanding and predicting heat transfer and pressure-drop behaviour of evaporating CO_2 flow in microchannel tubes at realistic conditions, including the influence of dryout and two-phase flow regimes".

The term "realistic conditions" was used in order to emphasize a number of important factors: Tube material and tube geometry had to be relevant for compact air coolers, test section heating should be done by a secondary fluid instead of electric resistance heating, and a realistic range of operating conditions (temperature, mass flux, heat flux, vapour fraction) had to be applied. In addition to experiments at these conditions, heat transfer tests and flow patterns were observed at high evaporating temperature (20°C), where dryout mechanisms could be studied in more detail.

Specific objectives of the work were to:

- measure heat transfer coefficient and pressure drop of evaporating CO_2 flow in microchannel tubes at a range of realistic conditions,
- evaluate the applied regression-based data reduction method with respect to uncertainty of the measured heat transfer coefficient,
- observe two-phase flow patterns in evaporating CO_2 microchannel flow at varying conditions,
- analyse results, observations and findings in relation to other published data, and in comparison to heat transfer and pressure drop models, and,
- provide recommendations on engineering design models for microchannel CO_2 evaporators.

1.3 Structure of report

In Chapter 2 the thermophysical properties of CO_2 in relation to vaporization heat transfer are discussed, and the conceptual framework for two-phase flow and pressure drop is outlined, including a discussion on flow vaporization principles, typical two-phase flow patterns, mathematical models for in-tube heat transfer and pressure drop, and a brief review on small-channel flow evaporation and high pressure evaporation based on published literature.

A more specific focus on CO_2 heat transfer and pressure drop data and results is presented in Chapter 3. Available literature, data and models for CO_2 flow vaporization are reviewed, emphasizing results and experience on microchannel and small-channel flow.

Heat transfer and pressure drop data in the present report were taken in a test rig using a microchannel test tube heated by a water jacket. The test section and the complete test rig, and all instrumentation and experimental uncertainty data are documented in Chapter 4. This Chapter also outlines the data reduction scheme for overall heat transfer coefficient and pressure drop in the test section, as well as a description of a separate rig that was used in the study on two-phase flow patterns of CO_2 in a microchannel.

The CO_2 heat transfer coefficient was derived based on the measured overall heat transfer coefficient for the test section, and a calibrated equation for water-side heat transfer. Chapter 5 explains the principles of the calibration/regression scheme to find an equation for water-side heat transfer, shows how this expression was determined, and explains the subsequent use of the equation in the determination of CO_2-side heat

transfer. Rigorous calculations were needed in order to find the propagation of uncertainty through this scheme. The principles of these calculations are explained, and resulting uncertainty in water-side heat transfer coefficient is shown.

The uncertainty propagation analysis is continued in Chapter 6, arriving at uncertainty data for the CO_2 vaporization heat transfer coefficient in Section 6.3. The experimental program is outlined, and all experimental data on heat transfer and pressure drop are shown and commented. Chapter 6 also presents and comments the observations on flow regimes and flow phenomena.

Chapter 7 provides analysis and discussion of the data and observations, and compares the data and findings to models and published results on heat transfer, pressure drop, and dryout inception. The various mechanisms of heat transfer are discussed separately, including nucleate boiling, convective evaporation, dryout, post-dryout heat transfer, and frictional pressure drop. Accuracy of predictions is commented, and recommendations are made for selection of models.

In the eight and final Chapter, the basis for development of a heat transfer correlation is outlined, and three different combinations of models are compared to the heat transfer test data. One of these models is then proposed as a design tool for predicting heat transfer in microchannel flow vaporization of pure CO_2.

URN:NBN:no-2319

2. Theoretical framework

2.1 Chapter overview

Since some readers may be unfamiliar with the properties and characteristics of refrigerant CO_2, the initial part of the Chapter outlines some of these data. The remaining parts of the Chapter contains basic information on heat transfer and pressure drop for in-tube vaporization that some readers may find elementary, but for the sake of completeness and to provide a well-defined background for the later discussion, this material was included.

2.2 Properties of CO_2

Compared to conventional refrigerants, the properties and characteristics of carbon dioxide (R-744) are quite peculiar. Critical parameters are 31.1°C and 7.4 MPa, and the system pressure for a given temperature is therefore higher than with all conventional refrigerants. Figure 2.1 shows the saturation pressure curve between the triple point (-56.6°C, 0.52 MPa) and the critical point. Thermodynamic property data in the present report were based on the program library *co2lib* at NTNU/SINTEF, using equations of state by Angus et al. (1976) and Pitzer and Schreiber (1988), in addition to transport property data equations of Vesovic et al. (1990). As may be observed from Figure 2.1, the saturation pressure at 0°C is about 3.5 MPa, which is about ten times higher than the pressure level with normal fluorocarbon or hydrocarbon refrigerants.

Owing to the low critical temperature of CO_2, evaporator conditions will be much closer to the critical point than with conventional fluids. Table 2.1, shows reduced temperature and pressure for CO_2 and HFC-134a at 0°C and

illustrates this fact. The difference in p_r stands out as the most significant difference.

Table 2.1 *Reduced temperature and pressure of refrigerants at 0°C*

CO_2 (R-744) T_c = 304.2 K p_c = 7.38 MPa			CF_3CH_2F (HFC-134a) T_c = 374.3 K p_c = 4.07 MPa		
p_{sat}(0°C) MPa	T/T_c	p/p_c	p_{sat}(0°C) MPa	T/T_c	p/p_c
3.48	0.90	0.47	0.29	0.73	0.07

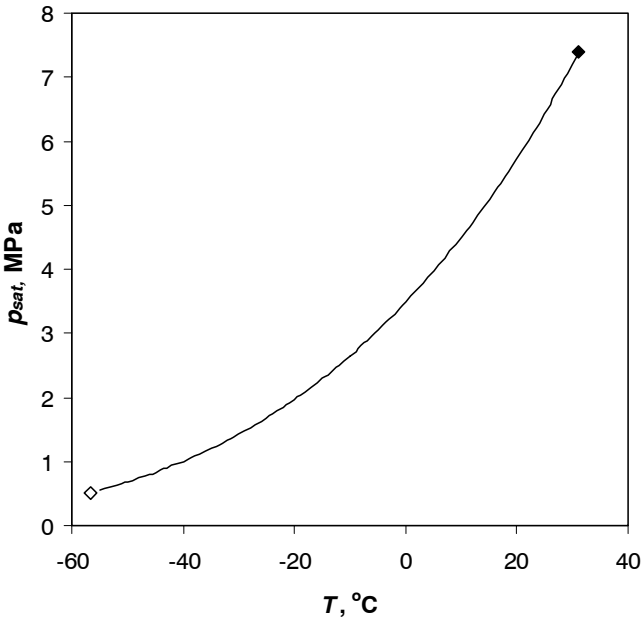

Figure 2.1 *Saturation pressure curve for CO_2, between triple point and critical point*

In terms of evaporator design and performance, one important consequence of near-critical operation is a steeper saturation pressure curve. Higher steepness gives a smaller temperature change for a given pressure change, and the temperature loss associated with pressure drop in the evaporator tubes thus becomes smaller (less steep saturation *temperature* curve).

Figure 2.2 shows the slope of the CO_2 saturation temperature curve for temperatures ranging from –10 to +30°C. At 0°C for instance, the temperature drop for 1 kPa pressure drop is about 0.01 K. With HFC-134a, the same pressure drop gives a temperature change of 0.09 K, i.e. almost ten times higher.

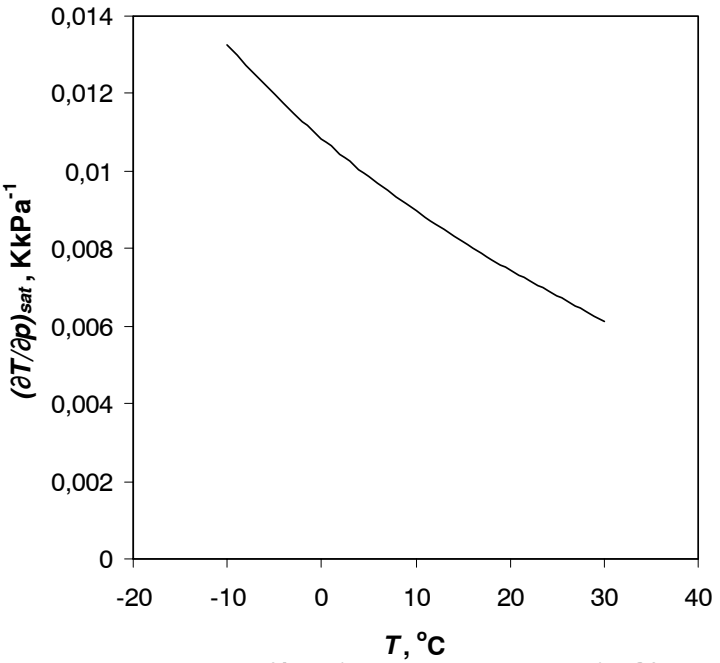

Figure 2.2 *Slope of saturation pressure curve for CO_2*

High saturation pressure and proximity to the critical point give vapour and liquid density characteristics that are quite different from those of conventional refrigerants. The vapour density is high, a fact that may have significant effects on two-phase flow patterns where differences in phase density determine phase separation characteristics, and vapour density influences the flow momentum of the vapour phase and the shear force between vapour and liquid phase. Saturated liquid and vapour densities of CO_2 at varying temperature is shown in Figure 2.3, and the ratio of vapour to liquid density are shown in Figure 2.4. At 0°C, the saturated liquid and vapour density of CO_2 are 931 and 98 kgm^{-3}, respectively, i.e. a density ratio of 0.10. The corresponding densities for HFC-134a are 1294 and 14 kgm^{-3}, respectively; giving a density ratio that is a factor of 10 lower and a vapour density that is only 14% of the CO_2 vapour density.

Nucleate boiling and two-phase flow characteristics are influenced by surface tension of the liquid. A small surface tension reduces the superheat required for nucleation and growth of vapour bubbles, which may positively affect heat transfer. Wetting characteristics of the liquid is affected by surface tension, thus influencing evaporation heat transfer. Reduced liquid surface stability with small surface tension may affect heat transfer negatively due to increased droplet formation and entrainment. Figure 2.5 shows surface tension of saturated CO_2 liquid at varying temperature. At the critical point, σ becomes zero. The surface tension of HFC-134a at 0°C is

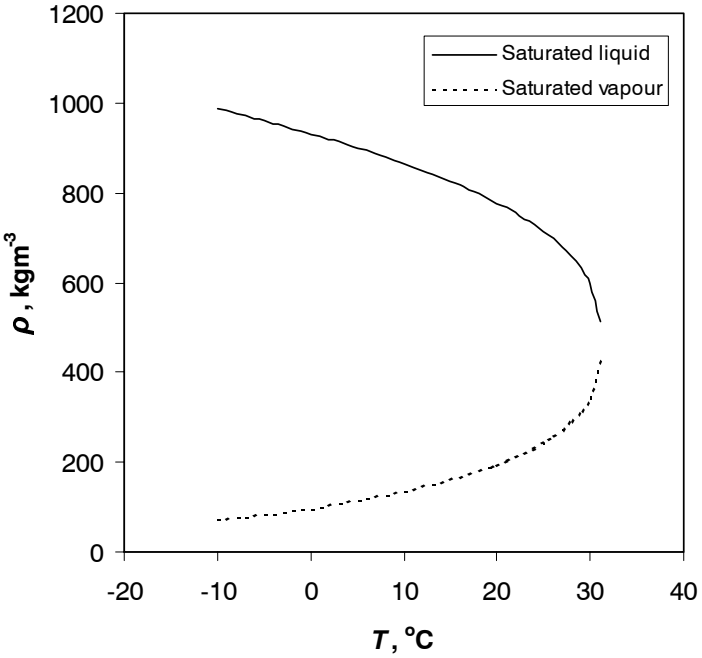

Figure 2.3 *Saturated liquid and vapour density for CO_2*

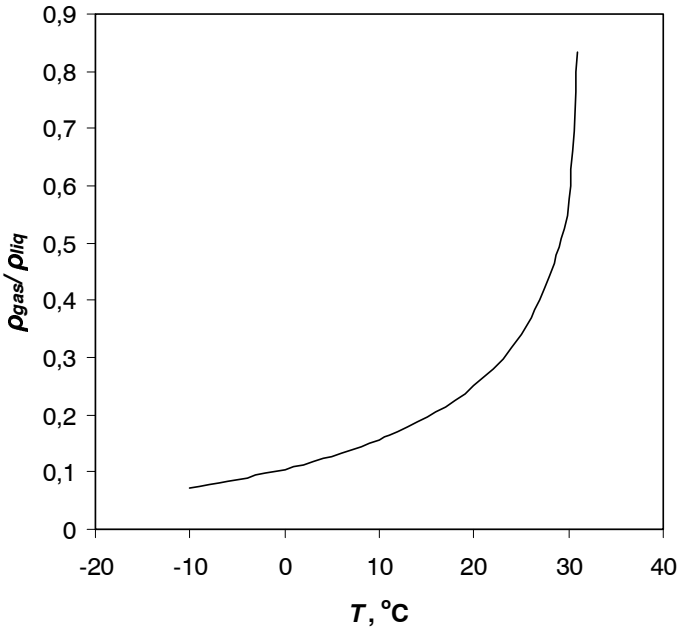

Figure 2.4 *Ratio of saturated vapour and liquid density for CO_2*

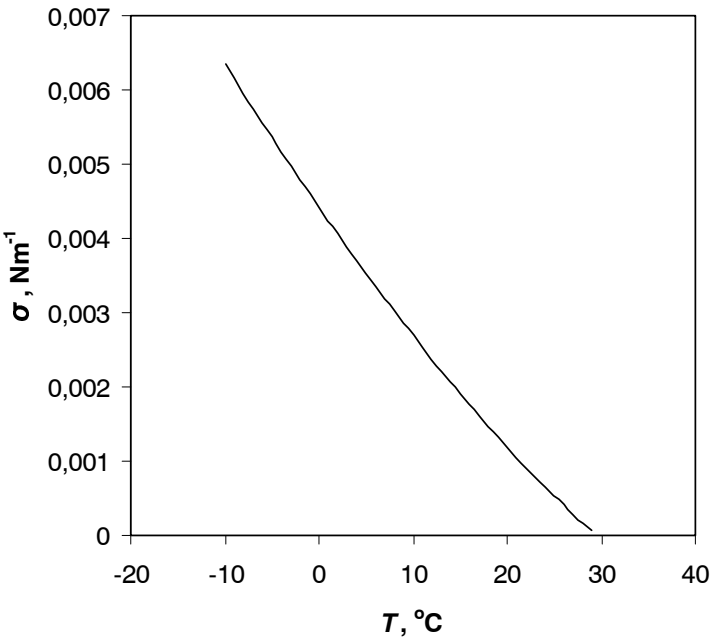

Figure 2.5 *Surface tension of saturated CO_2 liquid*

0.0112 Nm^{-1}, which is about 2.5 times the value for CO_2 for the same temperature.

Viscosity, particularly of the liquid phase, and the ratio of liquid to vapour viscosity, are important parameters for the fluid flow characteristics, convection behaviour and two-phase heat transfer/pressure drop. Figure 2.6 shows saturated vapour and liquid viscosity of CO_2 at varying temperature. At 0°C, the viscosity of saturated CO_2 liquid is only 40% of HFC-134a liquid viscosity, while the vapour viscosities of the two refrigerants are comparable.

A final parameter that plays an important role in heat transfer processes is the thermal conductivity of the liquid and vapour phase. A high thermal conductivity is essential for heat transfer effectiveness both in single-phase and two-phase flow. Figure 2.7 shows the thermal conductivity characteristics of CO_2 at varying temperature. Compared to the baseline refrigerant HFC-134a, the conductivity at 0°C of CO_2 is 20% higher in the saturated liquid phase, and 60% higher in the saturated vapour phase.

In summary, the thermodynamic and transport properties of CO_2 seem favourable in terms of heat transfer and pressure drop, compared to a typical fluorocarbon refrigerant like HFC-134a.

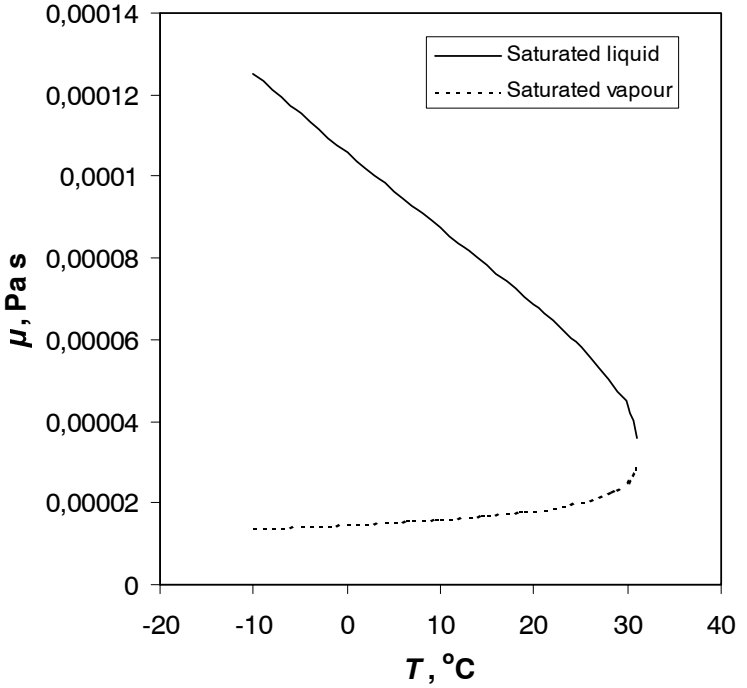

Figure 2.6 *Dynamic viscosity of saturated CO_2 liquid and vapour*

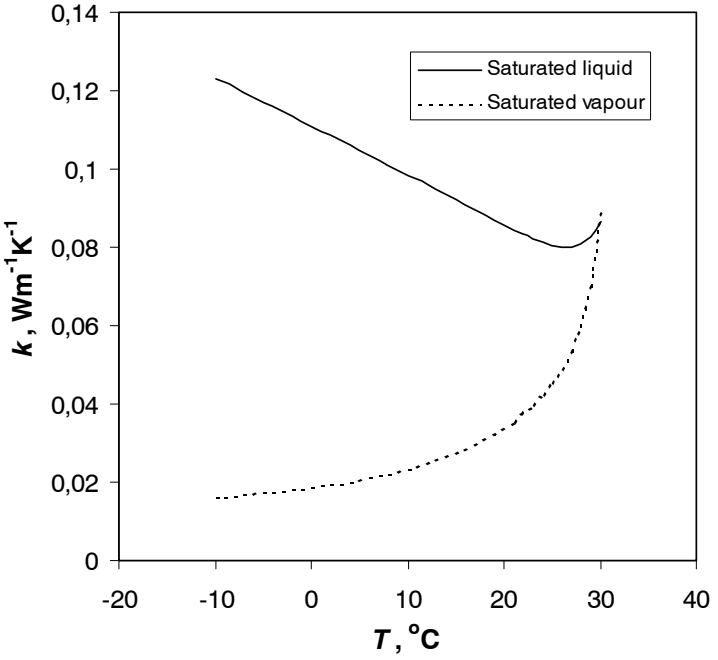

Figure 2.7 *Thermal conductivity of saturated CO_2 liquid and vapour*

2.3 Heat transfer and pressure drop for in-tube vaporization

2.3.1 General

The local heat transfer coefficient h for in-tube vaporization is defined as

$$h = \frac{q}{T_w - T_{sat}} \quad \text{Wm}^{-2}\text{K}^{-1} \tag{2.1}$$

where q (Wm^{-2}) is the heat flux, defined as heat transfer rate divided by heat transfer area, T_w is the local tube wall temperature and T_{sat} is the local fluid temperature. For a pure fluid T_{sat} is usually defined as the saturation temperature for the local pressure.

In-tube vaporization or flow boiling is characterized by

- the two-phase flow pattern, and
- the dominant mechanism of heat transfer.

As vaporization proceeds along the tube, the vapour content of the flow increases, and the difference in velocity between the two phases increases. The development in relative velocity and flow rate of the two phases, plus the influence of gravity, result in changes in the flow pattern. Two-phase flow patterns are discussed in some detail in Section 2.3.3. The two different heat transfer mechanisms in flow vaporization are *nucleate boiling* and *convective evaporation* - with one mechanism being superimposed on the other to a varying degree.

- *Nucleate boiling* is characterized by the mechanism of nucleation and vapour bubble formation on the heated wall, and bubble growth and movement in the liquid phase. In fully developed nucleate boiling, the flow-boiling heat transfer coefficient is virtually independent of mass flux and vapour fraction, both being measures of the effective flow velocity. Thus, nucleate boiling heat transfer is mainly a function of heat flux and/or wall superheat.

- *Convective evaporation* is characterised by convective heat transfer in the liquid film, without any bubble formation, and evaporation from the liquid-vapour interface. For heat flux or wall superheat below the onset of nucleate boiling, only convective vaporization is present and the heat transfer coefficient is largely independent

of heat flux. Convective evaporation heat transfer is mainly a function of flow velocity, characterized for instance by mass flux or vapour fraction.

Very often, the dominant mechanism at low vapour fraction is nucleate boiling (provided that the wall superheat is high enough), and as more vapour is generated and the void fraction increases, evaporation from the liquid-vapour interface becomes more important, i.e. convective flow evaporation becomes dominant.

Figure 2.8 shows a schematic model of flow vaporization processes as the fluid moves through a tube, reproduced from Steiner and Taborek (1992). Even though this scheme was developed for vertical tube flow, the general principles are valid also for horizontal flow, especially in small-diameter tubes and high mass flux situations where flow is shear-dominated and gravity plays a minor role. Gravity will be less important for two-phase flow of fluids having a small difference between liquid and vapour density, such as CO_2 at the boiling temperatures studied in the present work. The diagram is based on constant mass flux.

From a region of single-phase convective heat transfer to subcooled liquid, and approaching point A in Figure 2.8, the flow enters a regime of subcooled nucleate boiling provided that the heat flux or wall superheat is high enough to give nucleation. At point B the saturation temperature is reached (x=0), and a regime of nucleate boiling and bubbly flow is entered provided that conditions satisfy the requirement for onset of nucleate boiling (ONB – see next Section for definition).

The horizontal dashed lines in Figure 2.8 represent pure nucleate boiling heat transfer, which is insensitive to x. Full lines represent the combination of nucleate and convective components. This region may be characterized by plug flow or slug flow regimes in horizontal tubes. Churn flow is not usually present in horizontal tubes. In some cases, the heat flux may be too low for ONB at point B, and vapour generation instead takes place by a convective mechanism at liquid-vapour interfaces of vapour nuclei and small bubbles. This latter case is shown by the "pure convective boiling" curve in Figure 2.8. As the flow continues beyond point D, the flow pattern may become annular with a gradually thinner liquid film on the tube wall, and with liquid droplets or mist entrained in the vapour core flow. Depending on the heat flux level, two different situations may occur as the film thickness reduces. At heat flux levels above ONB, the liquid film is likely to dry out partly or fully as the film is sheared off the tube wall. This will give a dramatic drop in heat transfer coefficient and a corresponding rise in tube wall temperature, as shown in the diagram. Beyond the onset and completion of *dryout* (Region F-G), the *post-dryout* heat transfer coef-

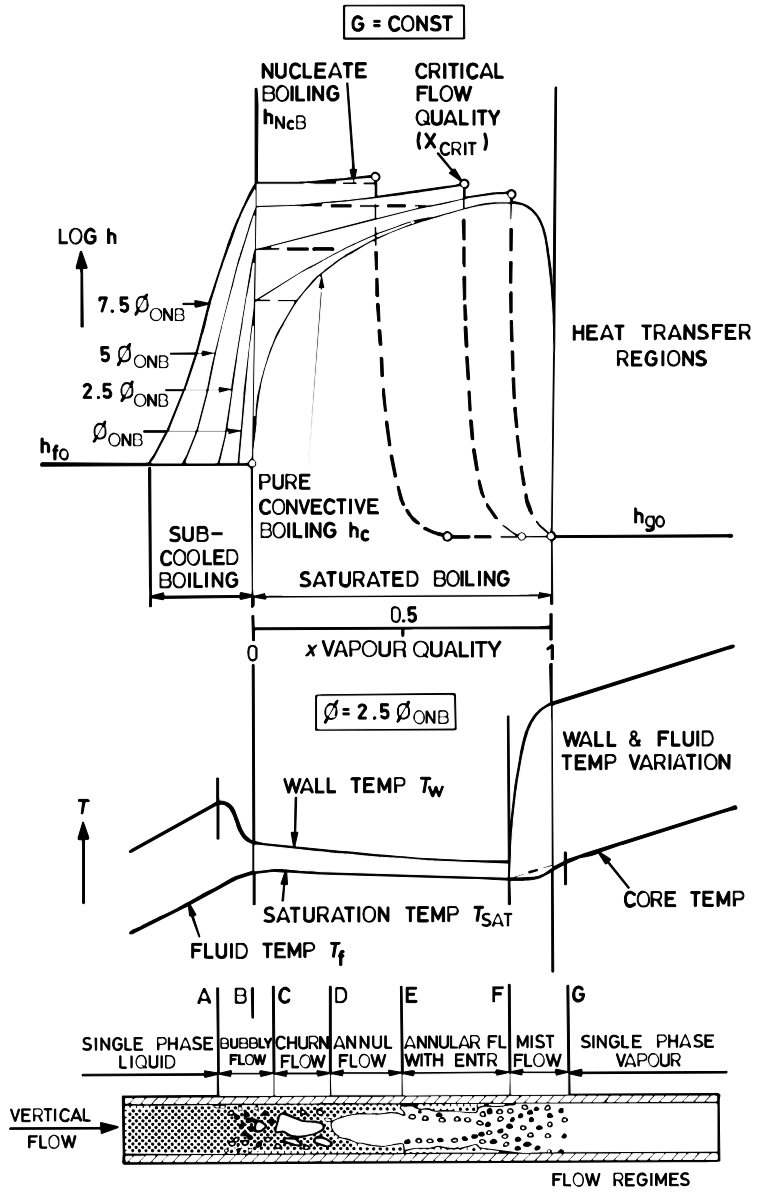

Figure 2.8 *Schematic representation of flow boiling process in vertical tubes, based on Steiner and Taborek (1992), as reproduced by Collier and Thome (1996). The mass flux G is constant. Symbol Ø is used for heat flux*

ficient will be close to the single-phase vapour coefficient, and a slight increase may occur beyond the dryout completion point due to the increase in flow velocity as the remaining liquid droplets evaporate. Post-dryout heat

transfer may also suffer from *non-equilibrium* effects, if the vapour becomes superheated due to poor heat transfer to the entrained droplets

When heat flux is below ONB, only convective boiling will be present, and dryout will not occur before x is very close to 1.0. This case is illustrated by the "pure convective boiling" curve. Depending on the fluid properties and the heat and mass flux conditions, the relative magnitude of nucleate and convective boiling heat transfer coefficients may vary.

2.3.2 Definitions

Several terms used throughout the report are ambiguously defined in the literature, and the following paragraphs explain how these terms are interpreted in the present report.

Onset of Nucleate Boiling (ONB) is the location and conditions where wall superheat (wall temperature minus fluid saturation temperature) and heat flux conditions become sufficient to cause vapour nucleation on the heating surface.

Critical Heat Flux (CHF) in pool boiling occurs because of a hydrodynamic flow pattern transition close to the heating surface. The mechanism is one in which insufficient amount of liquid is able to reach the heating surface due to the rate at which vapour is leaving the surface (Collier and Thome, 1996). The term *boiling crisis* may also be used to characterise this transition. In forced flow boiling, CHF is used as a generic term that covers three processes: Departure from Nucleate Boiling DNB (subcooled), DNB (saturated), and dryout, all of which cause an abrupt wall temperature rise in a heat-flux controlled situation (Collier and Thome, 1996). Details of these mechanisms are explained below. In general, DNB occurs at low x and high heat flux conditions, while dryout occurs at moderate to high x, and low heat flux.

Departure from Nucleate Boiling (DNB) characterizes a change in boiling mechanism from nucleate boiling to film boiling, usually as x is increased for a given heat flux. The flow may initially be in the subcooled nucleate boiling region where the local bulk liquid temperature has not yet reached the saturation temperature, or the initial conditions can be in the saturated nucleate boiling regime. In both cases the transition that occurs at DNB is to a film boiling mechanism, where an insulating vapour film covers the heating surface. In some situations at higher x, the transition may occur to a "liquid-deficient" region instead.

Dryout characterizes the transition that occurs when the flow changes from a mechanism dominated by forced-convection evaporation to a "liquid-deficient" regime, usually through dryout of the liquid film on the tube wall in annular flow. The film dryout typically changes the flow pattern from annular flow to mist flow or droplet flow, in which the remaining liquid exists as entrained droplets. A flow boiling crisis is thus termed dryout if the initial conditions were in the convective evaporation regime and/or if a liquid film was present on the tube wall. If conditions initially were in the subcooled or saturated nucleate boiling regime, typically at low x and bubbly flow or vapour plug flow, the boiling crisis is termed DNB.

Critical Vapour Fraction (x_{cr}) or critical flow quality is the vapour fraction at which dryout starts, i.e. onset of dryout. Typically, this is the vapour fraction where a significant part of the liquid film disappears due to vaporization and/or entrainment. In some cases with stratified or "crescent" flow, a different x_{cr} may be defined for the top and bottom of the tube since the top tends to dry out earlier.

2.3.3 Two-phase flow patterns

The flow patterns or regimes that may be observed in horizontal co-current two-phase flow are indicated in Figure 2.9. These patterns may be characterized as follows, in typical order of increasing vapour fraction:

- *Bubbly flow* – with discrete bubbles of vapour dispersed in a continuous liquid phase. The mean size of the bubbles is generally small compared to the diameter of the tube. Because of buoyancy, the bubbles may tend to flow in the upper part of the tube. Bubbly flow is a form of *dispersed* flow.
- *Plug flow* – or *elongated bubble* flow may develop when bubbles coalesce into larger, elongated plug-type bubbles, generally flowing in the upper part of the tube. Plug flow is a form of *intermittent* flow
- *Slug flow* – where liquid slugs span the entire cross-section of the tube. The liquid slugs may contain a dispersion of smaller bubbles. Slug flow is a form of *intermittent* flow
- *Stratified flow* – is characterized by the liquid flowing in the lower part of the tube and the vapour in the upper, with a relatively smooth interface in between. Stratified flow is a form of *separated* flow
- *Wavy flow* – with increasing flow rate and/or vapour fraction, the interface may become unstable and wavy. The waves are caused by vapour shear on the liquid, and the formation and breaking of waves

on the surface may lead to entrainment of liquid droplets in the vapour flow. Wavy flow is a form of *separated* flow.

- *Annular flow* – occurs when the liquid flows in a continuous annulus along the tube wall, and the vapour flows in the core of the tube. The vapour may contain entrained droplets or mist. Buoyancy effects may tend to thin the liquid film at the top of the tube and make the film thicker at the bottom ("*crescent*" flow). Gravitational forces are small compared to shear forces.
- *Mist flow* or *droplet flow* - occurs if the liquid film dries up, and the vapour flow still contains entrained droplets or mist.

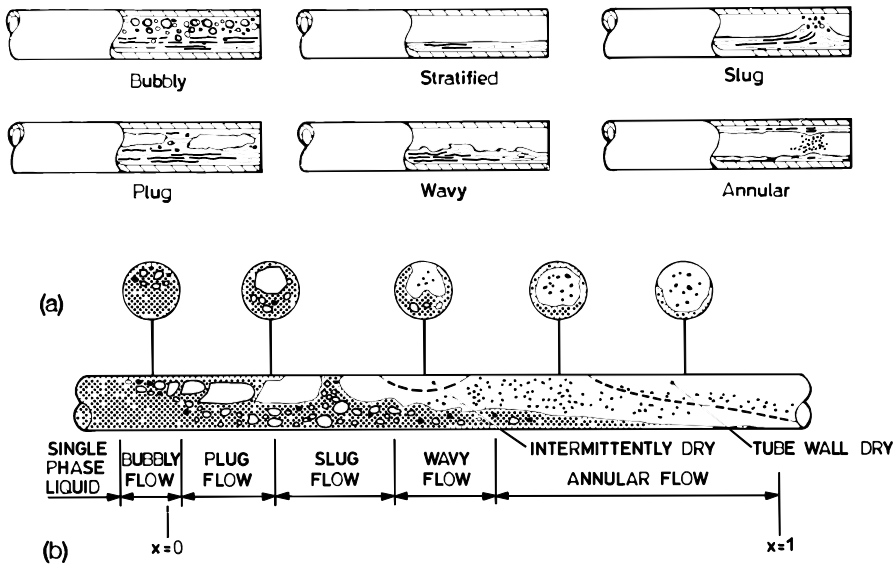

Figure 2.9 *Flow patterns in horizontal two-phase flow (top), and typical flow pattern development in evaporator tube (bottom). Reproduced from Collier and Thome (1996)*

Plug flow and slug flow are sometimes grouped together as *intermittent flow*, for instance in relation to the Taitel and Dukler (1976) two-phase flow regime map, as explained in Section 2.4.

The flow regime at varying gas- and liquid phase flow velocities depends on shear forces between the phases, gravity, and surface tension. In smaller tube diameters, capillary effects may become important, giving flow-patterns that may deviate from those described above (Carey, 1992). Flow regime maps may be used in predicting or analysing two-phase flow patterns and transitions between these. Such maps are discussed in Section 2.4.

2.3.4 Vaporization flow in small tubes

Wambsganss et al. (1997) reviewed the subject of vaporization in compact heat exchanger geometries. Based on the few available studies of evaporation in small-diameter channels, they observed that reduced hydraulic diameter reduced the value of critical wall superheat required for transition to fully developed nucleate boiling. Experimental data shown by Steiner (1993) show improved nucleate boiling heat transfer in smaller tubes. The changes in the nucleate boiling heat transfer coefficient in horizontal tubes at varying diameter D were correlated by $D^{-0.5}$, all other parameters being constant.

Studies of low-velocity flow boiling in confined spaces have demonstrated that channel dimensions can have a critical role in determining the heat transfer mechanism and the potential for enhancement. The heat transfer enhancement observed in microchannels is mainly caused by

i) in isolated, confined or slug flow, by the formation of a thin liquid film between the heated wall and the vapour, and

ii) in annular flow, by the reduction of the liquid film thickness.

Wambsganss et al. (1997) concluded that these two mechanisms are typical of the smaller channel dimensions and lose their effect in larger ducts. Therefore, most of the heat transfer correlations developed for traditional geometries and large tubes, are not suitable to microchannels.

Gravity is believed to be of reduced importance in small-channel flow, because surface tension and flow shear forces will dominate. Thus, there should be a reduced tendency of flow stratification in small-channel two-phase flow. Even though surface tension effects may be of large importance in small-channel two-phase flow in general, the low surface tension of CO_2 at high temperature may give reduced importance for this particular fluid, especially since the vapour density and resulting shear force are high.

Studies on nucleate flow boiling in small channels by Tran et al. (1997) showed a very abrupt transition from forced convection (single phase liquid) heat transfer to nucleate boiling, with the transition occurring at a unusually low wall superheat. In the nucleate-boiling regime, the measured local heat transfer coefficient of CFC and HFC refrigerants was independent of x in the range x=0.2 to x=0.8.

Owing to the larger relative influence of vapour bubbles in small tubes than in larger tubes, the bubble size, growth and dynamics are likely to be more

important in small-channel boiling. Kew and Cornwell (1994) used the concept of *confined bubble flow* and a *Confinement Number*,

$$N_{conf} = \frac{\left[\dfrac{\sigma}{g(\rho_l - \rho_v)}\right]^{0.5}}{D} \tag{2.2}$$

for boiling in small channels. N_{conf}, which is the inverse of the *Bond* number, represents the ratio of characteristic bubble departure size, based on the 1935 correlation of *Fritz* (Carey, 1992), to hydraulic diameter (D) of the flow channel. The numerator of Eq. (2.2) represents the *Laplace* constant, i.e. ratio of surface tension force to buoyancy force. Kew and Cornwell (1994) observed flow patterns and studied literature on small-channel flow, and were able to identify three distinct flow regimes: isolated bubbles, confined bubbles, and annular-slug flow. The effect of the confined space is to provide additional heat transfer in the confined bubble region where the bubbles lead to thin liquid films on the surfaces. By including the influence of confinement in their model, they could account for the added heat transfer due to space restriction over that already included as the physical dimension in the Reynolds number. The critical value of N_{conf} for these effects to become significant was defined as 0.5.

According to a theoretical study by Monde (1998), the enhanced heat transfer mechanism in the confined (coalesced) bubble region can be attributed to evaporation of the liquid film as the bubble passes over the heated surface. The sensible heat transport caused by substitution of the superheated liquid swept away by the bubble, with liquid at bulk temperature after the bubble transit, plays an important role in this mechanism.

In flow visualization tests with water in a 2.5 by 6.0 mm channel, Kasza et al. (1997) observed these flow phenomena at high heat flux (110 kWm^{-2}) and low mass flux (21 $kgm^{-2}s^{-1}$). The channel cross-section was chosen to be of the same nominal size as the individual bubbles nucleating at discrete wall sites, with water as the fluid. Bubble size and nucleation rate was observed, and the authors found that both of these were larger at nucleation sites under vapour plugs, where a thin liquid film existed, than at sites where there was no vapour plug present. In small channels, where individual vapour bubbles can grow to the same size as the channel cross section, only a few bubbles would be needed for coalescence to form a vapour plug. When this plug flows down the channel, it would create situations of nucleation in the thin liquid layer. This sweeping action would occur more readily in small channels, and could explain why small channels exhibit

higher heat transfer coefficients, and why nucleate boiling occurs over a wider range of conditions in small channels.

Another phenomenon discussed by Kasza et al. (1997) was the flattening and trapping of vapour bubbles in the film remaining under vapour slugs, which was believed to create a liquid microlayer between the bubble and the wall that was favourable for heat transfer. Even at low heat flux, the dynamics of bubble nucleation, growth and coalescence were observed to have an intensity that created periodic flow reversal and intense mixing of the flow. Such interface movements and mixing was believed to have much more influence on heat transfer in small channels than the effect of nucleating bubbles along the walls of larger channel sizes.

2.3.5 Boiling and evaporation at high pressure

In nucleate pool boiling, the liquid surrounding a growing bubble nucleus must be overheated to create an excess pressure inside the bubble. The excess pressure needed for bubble growth is proportional to surface tension, and inversely proportional to bubble radius. i.e.

$$\Delta T\left(\frac{\partial p}{\partial T}\right)_{sat} = \Delta p = \frac{2\sigma}{r} \tag{2.3}$$

where ΔT is the liquid superheat at the heated surface, Δp is the excess pressure created inside the bubble. The bubble radius r may be understood as the radius of curvature of the smallest active cavities in the heated material surface. At high saturation pressure, for instance in a CO_2 evaporator, the surface tension σ is low, and the slope of the saturation pressure curve (Figure 2.1) is steep. Thus, at high pressure, the required superheat for ONB is lower, or more nucleation sites become active for a given superheat. In both cases, this gives higher nucleate boiling heat transfer at higher pressure, and experimental data show that the heat transfer coefficient rises exponentially as the critical pressure is approached. A possible negative aspect of boiling at high pressure is the reduction in critical heat flux giving film boiling conditions. The critical heat flux, i.e. the maximum heat flux for nucleate boiling, approaches zero as the reduced pressure approaches 1 (Cichelli and Bonilla, 1945). This can be seen from the critical heat flux model developed by Kutateladze (1948) and Zuber (1959):

$$q_{cr} = C \cdot h_{lv}\left[\sigma\rho_v^2(\rho_l - \rho_v)g\right]^{0.25} \tag{2.4}$$

where C is a constant depending on the geometry. As $p_r \rightarrow 1$, the evaporation enthalpy (h_{lv}), surface tension (σ), and density difference ($\rho_l - \rho_v$) all approach zero, thus making the critical heat flux approach zero as well. Actual heat flux and critical heat flux conditions in CO_2 experiments at high boiling pressure therefore need to be checked for possible boiling crisis occurrence.

Experimental data by Wambsganss et al. (1997) showed that in the nucleate boiling regime of in-tube vaporization, pressure was indeed an important parameter, and an increase in system pressure caused the boiling curve to shift to the left in the $\Delta T/q$-diagram, i.e. fully developed nucleate boiling was achieved at a lower ΔT.

A literature review made as part of a paper by Kandlikar and Alves (1999) led to the conclusion that a reduction in surface tension led to a higher nucleation site density, larger number of small bubbles on the surface, and generally a higher heat transfer coefficient. Two effects were believed to account for improved heat transfer; the range of active nucleation sites increased, and the bubbles did not coalesce readily, causing a large number of bubbles to exist on the surface. Departure bubble diameter was also reduced. Even though reduced surface tension could be expected to have a negative effect because of liquid entering surface cavities more easily, experimental evidence shows that the positive effect of lowering the necessary surface superheat more than offset any such effects.

Regarding the isolated effect of low surface tension on nucleate boiling, Wu et al. (1998) offered a more critical point of view. They claimed that some of the complicated phenomena involved in the physics of nucleate boiling were not well understood, and if surface tension would had any effect on boiling, this would be the dynamic surface tension and not the equilibrium one. Their experimental data on water showed significant improvement in nucleate boiling heat transfer with the addition of surfactants, but the heat transfer coefficient improvement did not correlate well with the surface tension data, thus indicating that other effects than surface tension were more important. They observed that the heat transfer coefficient enhancement correlated reasonably well with the area occupied by vapour bubbles near the heating surface, however. This rather surprising result was explained by a micro-wedge model, considering evaporation at the interface of the bubble base and the mass flow between the interface and the heated wall due to capillary forces. Wu et al. (1998) also collected experimental data on superheat necessary for boiling incipience (ONB) with varying surfactant concentration. The data showed that there was no clear correlation between reduced surface tension and reduced superheat at boiling incipience.

A study on nucleate boiling in narrow spaces reported by Ishibashi and Nishikawa (1969) showed that surface tension had an effect on heat transfer

coefficient in the isolated bubble region, and heat transfer increased exponentially with pressure by $p^{0.4}$. In the coalesced-bubble region, however, no surface-tension effects were observed, and the heat transfer coefficient decreased with pressure as $p^{-0.353}$. These results may indicate that the reduced vapour volume at higher pressure reduces the enhancement in coalescent-bubble flow. This is in accordance with the results discussed above, where a reduction in Confinement number for instance by reduced vapour bubble size, gives less heat transfer enhancement. In summary, increased pressure is favourable for single-bubble boiling due to the higher number of active nucleation sites and the reduced wall-superheat requirements, but the reduced vapour volume at higher pressure reduces the coalescent-bubble effects discussed in Section 2.3.4.

The two-phase flow mechanisms and flow pattern regimes for in-tube evaporation are also affected by pressure level, mainly due to the effects of increasing pressure on fluid density, viscosity, and surface tension. A smaller difference between liquid and vapour density will reduce the void fraction and the tendency of the phases to separate. Thus, flow stratification should be less pronounced in two-phase flow at high pressure. The balance of entrainment and deposition may also be affected by changes in pressure, due to reduction in surface tension and reduced density difference between the phases. Ruder et al. (1987) reported that an increase in pressure moved the transition from annular to dispersed flow to lower vapour fraction.

2.3.6 Entrainment in evaporating flow

Droplet entrainment into the vapour flow field starts when the retaining force of surface tension is exceeded by the interfacial shear force by vapour flow. An entrainment inception criterion for turbulent liquid film (film Reynolds number above 1635) is given by the critical superficial vapour flow velocity j_{vc} (Utsuno and Kaminaga, 1998):

$$\frac{\mu_l j_{vc}}{\sigma}\left(\frac{\rho_v}{\rho_l}\right)^{1/2} = N_\mu^{0.8} \qquad \text{for } N_\mu < 1/15 \tag{2.5}$$

$$\frac{\mu_l j_{vc}}{\sigma}\left(\frac{\rho_v}{\rho_l}\right)^{1/2} = 0.1146 \quad \text{for } N_\mu > 1/15 \tag{2.6}$$

where N_μ is the viscosity number given by

$$N_\mu = \frac{\mu_l}{\left(\rho_l \sigma \sqrt{\frac{\sigma}{g(\rho_l - \rho_v)}}\right)^{1/2}} \tag{2.7}$$

For CO_2 and HFC-134a in the current range of temperatures, the viscosity Number is lower than 1/15, and Eq. (2.5) applies. The above model for critical vapour flow velocity shows the importance of liquid surface tension, viscosity and liquid/vapour density in entrainment inception. Figure 2.10 shows calculated critical superficial velocities for onset of entrainment at varying temperature for CO_2 and HFC-134a. Entrainment is predicted to occur at a quite low superficial vapour flow velocity for CO_2, especially at high evaporating temperature, while the inception velocities for HFC-134a are 3 to 20 times higher in the temperature range shown.

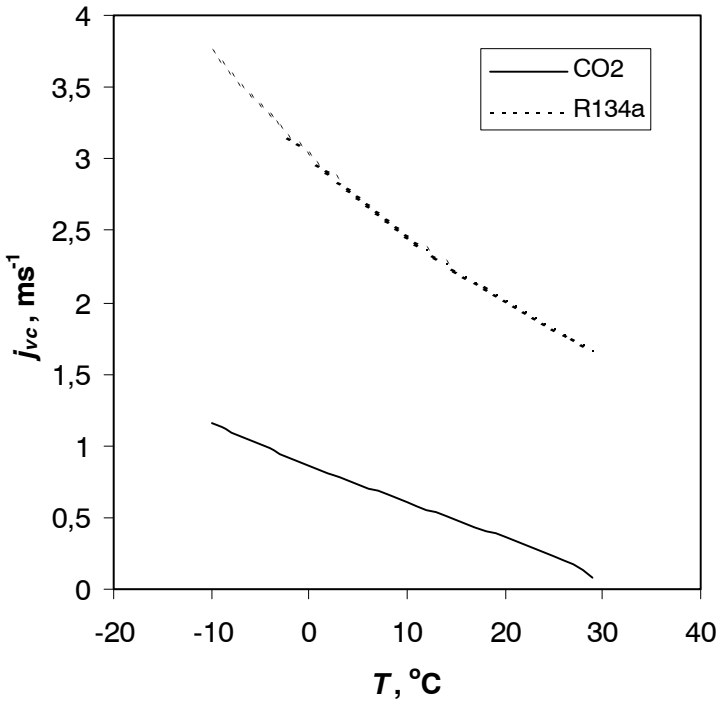

Figure 2.10 *Predicted critical superficial vapour flow velocity for onset of entrainment from a fully turbulent liquid film in vertical annular flow (Based on Eq. 2.5).*

Ishii and Mishima (1981) and Kataoka et al. (2000) developed correlations for entrainment rate and entrainment fraction (the fraction of the liquid phase flowing as droplets) in vertical adiabatic annular two-phase flow. The basis was a mechanistic model of shearing-off of a roll wave crest by a streaming gas. They found that equilibrium entrainment fraction as well as

the entrainment rate, could be correlated by the superficial liquid Reynolds number

$$Re = \frac{\rho_l j_l D}{\mu_l} \tag{2.8}$$

and a Weber number defined as

$$We = \frac{\rho_v j_v^2 D}{\sigma}\left(\frac{\rho_l - \rho_v}{\rho_v}\right)^{1/3} \tag{2.9}$$

Figure 2.11 shows how these two dimensionless numbers depend on vapour fraction for flow of CO_2 and HFC-134a in 1 mm ID tubes at 0°C, for a mass flux of 500 $kgm^{-2}s^{-1}$.

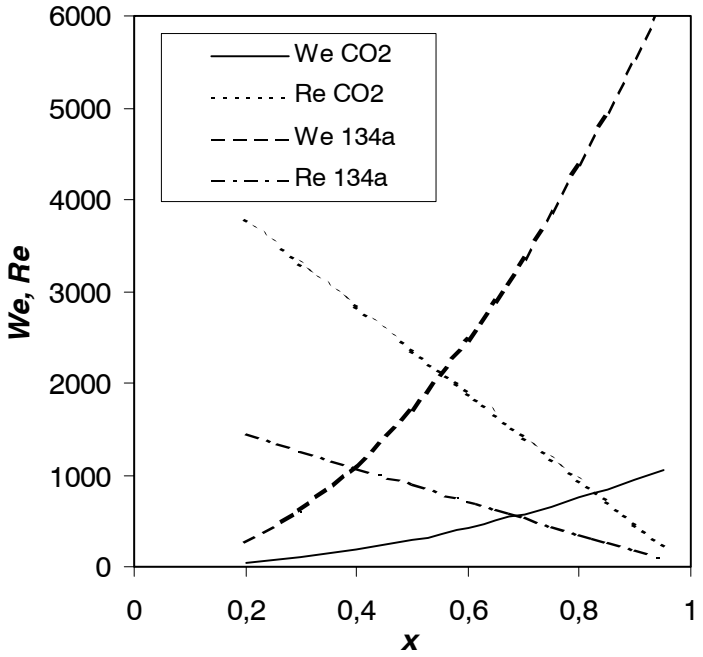

Figure 2.11 *Weber number (Eq. 2.9) and liquid Reynolds number (Eq. 2.8) for annular two-phase flow of CO_2 and HFC-134a. Conditions: Temperature 0°C, mass flux 500 $kgm^{-2}s^{-1}$, and tube diameter 1 mm*

Even though these two dimensionless numbers cannot be expected to fully reflect the situation in horizontal evaporator tubes at high pressure, some interesting tendencies are shown. The vapour superficial velocity is much higher for HFC-134a than for CO_2, and the Weber number is therefore

much higher with HFC-134a, even though the surface tension of CO_2 is low and the vapour density is high. As may be expected, the liquid Reynolds number of the CO_2 flow is higher due to the lower viscosity and higher liquid superficial velocity (due to lower liquid density). The difference in magnitude of the *We*-numbers is likely to dominate, thus giving a larger hydrodynamic flow-induced entrainment in the HFC-134a system than with CO_2, but this is somewhat speculative considering the change in conditions when flow is horizontal instead of vertical.

A similar comparison of entrainment rates and fractions based on vertical annular- flow entrainment and deposition models of Govan et al. (1988) and Hewitt and Govan (1990) gives comparable results, i.e. a higher predicted flow-induced entrainment fraction for HFC-134a than for CO_2.

Regarding entrainment caused by heat flux, the situation may be different. This entrainment is caused by the boiling process due to release of bubbles from the liquid film, and the dominance of nucleate boiling for CO_2 may give increased entrainment caused by boiling. In addition, deposition will be suppressed due to the vapour flux from the interface. Vaporization of HFC-134a is likely to be dominated by convective evaporation that does not give boiling-induced entrainment.

Milashenko et al. (1989) studied entrainment due to heat flux in water steam systems, and found that net entrainment rate could be correlated by heat flux and density ratio:

$$E_q \sim \left(q \frac{\rho_v}{\rho_l} \right)^{1.3} \tag{2.10}$$

At 0°C and a heat flux of 20 kWm^{-2} this will give a *q*-induced entrainment rate that is almost 20 times higher with CO_2 than with HFC-134a. Even though this comparison does not pretend to give accurate answers, it shows the important trend that this mechanism of entrainment becomes significant at higher pressure.

In summary, the onset of entrainment is likely to start at low superficial vapour velocity with CO_2, but the magnitude of the entrainment rate and entrainment fraction is not clear.

2.3.7 Dryout in flow vaporization

Dryout is characterized by discontinuation of the liquid film on the tube wall, usually in annular flow. This category of boiling crisis typically occurs at moderate heat flux conditions, and the mechanisms in medium or high-x flow may be (Tong and Tang, 1997):

- Dryout in low/medium-x flow due to disruption of the liquid layer caused by surface wave instability.
- Dryout in high-x annular flow caused by dryup of the liquid layer on the heating wall due to entrainment and vaporization.

Auracher et al. (1993) also describes a third mechanism in low heat flux systems, where the number of entrained droplets that are redeposited on the heated surface increases. In this case, the boiling crisis is referred to as *deposition-controlled burnout* since the onset of dryout is determined by the deposition rate.

When evaluating CHF data or modelling the behaviour, a separation need to be done between dryout, as listed above, and DNB, which instead resembles film boiling. In a situation dominated by DNB, increased mass flux gives higher turbulence, improved bubble transport and thus higher CHF, while in a dryout situation, increased mass flux gives more entrainment and reduced CHF. According to Hewitt (1992), the criterion of Katto (1981) can determine the critical mass flux beyond which CHF dominates:

$$G_{cr} = 1.42\left(\frac{z}{D}\right)^{0.85}\left(\frac{\sigma\rho_l}{D}\right)^{0.5} \tag{2.11}$$

At given tube diameter (D) and heated length (z) the critical mass flux drops as the temperature rises. For CO_2 at temperatures below 25°C, G_{cr} is always above 800 $kgm^{-2}s^{-1}$ as long as $D < 3$ mm and $z/D > 100$. The above criterion was proposed based on data for larger tube diameters, and the application to microchannel flow is questionable. Nevertheless, the parameter indicates that dryout is likely to be the dominant mechanism in the present tests.

Published data on dryout in flow boiling of water show how the critical vapour fraction (onset of dryout) is reduced for increased mass flux and increased pressure. Both these parameters give increased entrainment. The dryout x is also expected to depend on heat flux, especially at high mass flux and low heat flux levels (Carey, 1992).

The literature contains numerous data and correlations for CHF in water/steam systems, but studies on other fluids are of a more limited nature. Some general CHF correlations have been published, including the models of Katto and Ohno (1984), and Shah (1987), but these correlations are focused on boiling crisis at high heat and mass flux giving DNB instead of dryout. In absence of reliable general correlations for dryout at higher x, two other approaches have been presented in the literature:

- Fluid-to-fluid scaling laws that relate empirical dryout data for water to the value for the non-aqueous fluid, and,
- phenomenological dryout models involving numerical modelling of the annular two-phase flow with entrainment, deposition and vaporization.

The first method relies on the extensive amount of data that exist on CHF/dryout data for water, in particular at conditions for boilers in nuclear reactors.

The latter method uses a three-field model for the liquid film, vapour and droplet field. Based on given inlet conditions, e.g inception of entrainment, given evaporation rate, and analytical correlations for local entrainment and deposition rates, the change of liquid film flow rate along the heated tube is found by integration of the continuity equation. Dryout is then identified at the location where liquid film flow rate becomes zero. Methods and results for dryout prediction using such methods have been presented by several authors, including Govan, Hewitt et al. (1998), Hoyer (1998) and Utsuno and Kaminaga (1998). Use of these methods in microchannel flow has not been reported, and the validity of the empirically-based entrainment and deposition correlations is doubtful for microchannel geometries especially with the "unusual" fluid properties of CO_2.

Using the first approach above, Ahmad (1973) developed a fluid-to-fluid scaling model based on dimensional analysis, finding a mass flux scaling/modelling parameter ψ, based on the Weber number and liquid/vapour superficial Reynolds numbers. Parameters for the fluid concerned (in this case CO_2) must be converted into equivalent values for water, using the modelling parameter ψ that should have the same value for both fluids:

$$\psi = \left[\frac{GD}{\mu_l}\right]\left[\frac{\mu_l^2}{\sigma D \rho_l}\right]^{2/3}\left[\frac{\mu_l}{\mu_v}\right]^{-1/5} \tag{2.12}$$

The second dimensionless group in the above expression may be termed a *Weber-Reynolds number*. Hydraulic diameter (D) is the same for both fluids. If

surface tension data are unavailable or inaccurate, it has been suggested to replace the Weber-Reynolds group and convert the expression to

$$\psi = \left[\frac{GD}{\mu_l}\right]\left[\frac{\gamma^{0.5}\mu_l}{D\rho_l^{0.5}}\right]^{2/3}\left[\frac{\mu_l}{\mu_v}\right]^{1/8} \tag{2.13}$$

$$\gamma = \left|\frac{\partial(\rho_l/\rho_v)_{sat}}{\partial p}\right| \tag{2.14}$$

where the second dimensionless group in Eq. (2.13) is called *Barnett number* (Ahmad, 1973). Property data for water should be evaluated at a saturation pressure giving the same density ratio as for the fluid concerned, in this case CO_2. Finally, the heat flux need to be scaled so that the Boiling number

$$Bo = \frac{q}{Gh_{lv}} \tag{2.15}$$

is the same for both fluids. Conditions for similarity in the Ahmad method for round tubes are listed in Table 2.2 (Auracher et al., 1993).

Table 2.2 *Conditions for similarity when using the method of Ahmad (1973) (Auracher et al., 1993)*

Parameter	Dimensionless number	Range of validity
System pressure, as defined by liquid-to-vapour density ratio	$(\rho_l/\rho_v)_{sat}$	7 - 980
Mass flux	ψ	5 to 100
Vapour fraction at boiling crisis	x_{crit}	-0.35 to 0.9
Vapour fraction at channel inlet	x_{in}	-0.04 to –0.8
Ratio of heated length to hydraulic diameter	l/D	60 to 310

The limits given in Table 2.2 restrict the use of this method to temperatures below 8°C for CO_2, and to tube lengths below 250 mm for ID 0.81 mm tubes. In addition, the inlet state has to be subcooled (negative x).

For estimation of dryout parameters of water, Auracher et al. (1993) recommends empirical equations from Kon'kov (1965). These equations give the following data for critical vapour fraction of water (only the relevant equation for equivalent water/steam saturation pressure above 9.8 MPa is shown here):

$$x_{cr} = 32.302 q^{-0.125} G^{-0.333} D^{-0.07} e^{-0.00795 p} \tag{2.16}$$

with q in kWm^{-2}, G in kgm^{-2}s^{-1}, D in mm, and p in bar. The range of parameters (for water) covered by this relation is:

9.8 MPa < p < 19.6 MPa
200 kgm^{-2}s^{-1} < G < 5000 kgm^{-2}s^{-1}
$4 \cdot 10^{-3}$ m < D < $32 \cdot 10^{-3}$ m

The use of Eq. (2.16) for small-diameter tubes (less than 4 mm ID) is very questionable, since this geometry is well below the stated range of the model. The above correlation was developed for vertical tubes, and phase separation (stratification) in horizontal tubes may give earlier dryout at the crest of the tube while the bottom part dries out later. Auracher et al (1993), referring to studies by Kefer (1989) and Wallis (1969), provides a basis for estimating the effect of tube inclination. The stratification tendency of the two-phase flow can be correlated by a modified Froude number

$$Fr = \frac{\dfrac{x_{cr,vertical} G}{\rho_v^{1/2}}}{\left[gD(\rho_l - \rho_v)\cos\varphi \right]^{1/2}} \tag{2.17}$$

which relates inertia force to buoyancy force. Here, φ is the inclination angle from the horizontal, i.e. cosφ=1 for horizontal flow. Test data show that if Fr > 10, there is little or no flow stratification at horizontal flow, while stratification effects are very pronounced at Fr < 3. As a consequence, it is recommended to account for stratification effects if Fr < 10, using the following relation:

$$\Delta x_{cr} = x_{cr,bottom} - x_{cr,crest} = \frac{16}{(2 + Fr)^2} \tag{2.18}$$

Thus, the critical vapour fraction from Equation (2.16) can be regarded as a mean value, and the corresponding values for the crest and bottom of the tube can be estimated as:

$$x_{cr,1} = x_{cr} - \frac{\Delta x_{cr}}{2} \tag{2.19}$$

$$x_{cr,2} = x_{cr} + \frac{\Delta x_{cr}}{2} \tag{2.20}$$

If $x_{cr,2}$ is higher than 1.0, its value should be taken as 1.0. The above procedure enables an estimation of onset and completion of dryout with CO_2, based on empirical data for H_2O and a scaling model.

Levitan and Lantsman (1975) recommended another empirical correlation for predicting dryout vapour fraction in upflow of water in a uniformly heated 8 mm tube:

$$x_{cr} = \left[0.39 + 1.57\left(\frac{p}{98}\right) - 2.04\left(\frac{p}{98}\right)^2 + 0.68\left(\frac{p}{98}\right)^3 \right] \left(\frac{G}{1000}\right)^{-0.5} \qquad (2.21)$$

where p is pressure in bar and G is mass flux in $kgm^{-2}s^{-1}$. This equation was stated to predict x_{cr} for water within ± 0.05 for $9.8 < p < 166.6$ bar and $750 < G < 3000$ $kgm^{-2}s^{-1}$. In contrast to the correlation by Kon'kov (1965), this model assumes that heat flux variation does not influence the critical vapour fraction in dryout. For tube diameters other than 8 mm, Carey (1992) recommends scaling x_{cr} in Eq. (2.21) by the factor $(8/D)^{0.15}$, where D is in mm.

2.4 Two-phase flow pattern maps

2.4.1 Generalized transition lines in flow charts

Various flow pattern maps showing transitions between two-phase flow regimes have been developed for both vertical and horizontal flow, and for adiabatic and diabatic (with heat load) conditions. Coordinates and transition regimes/lines in such maps may have a basis in the mechanisms of two-phase flow. Baker (1954) developed a chart for horizontal adiabatic flow using superficial gas (vapour) and liquid velocities (See Notation and Definitions), together with scaling parameters for fluid properties as coordinates. This map was purely empirical and based on observations, not considering the physics in transition mechanisms.

Taitel and Dukler (1976) analysed flow regime transitions and developed a generalized chart for adiabatic horizontal flow, using the *Lockhart-Martinelli parameter* (two-phase multiplier)

$$X = \left[\frac{(dp/dz)_{fric,lo}}{(dp/dz)_{fric,vo}} \right]^{1/2} \qquad (2.22)$$

as abscissa. When both phases are turbulent, this expression may be approximated by

$$X_{tt} = \left(\frac{\rho_v}{\rho_l}\right)^{0.5} \left(\frac{\mu_l}{\mu_v}\right)^{0.125} \left(\frac{1-x}{x}\right)^{0.875} \tag{2.23}$$

Three different parameters *F*, *T* and *K* were used as ordinates, depending on the type of flow regime transition considered. These parameters were non-dimensional functions of liquid and gas superficial velocities, and fluid properties. The use of this flowchart is rather complicated due to the use of three different factors, and since a specific procedure has to be followed when determining the flow pattern.

The application of adiabatic flow pattern maps to diabatic flow is generally not recommended (Tong and Tang, 1997). Dukler and Taitel (1991) showed that introduction of (a large) heat flux shifted the transition boundaries, and introduced a dimensionless heat transfer parameter in order to extend their flow pattern map to diabatic flows. At low heat flux, however, the influence may be expected to be smaller. In any case, flow pattern observations are hardly ever done in the heated zone of the tube, even in studies on diabatic flow patterns. The term *pseudo-diabatic* was proposed by Sun and Groll (2001) to characterise this situation

Steiner (1993) modified the flow chart of Taitel and Dukler (1976), and Kattan et al. (1998) suggested even further changes, including conversion of the coordinates and modifications of some of the transition boundaries based on improved models and their extensive flow pattern data for pseudo-diabatic refrigerant flow. Coordinates in the Kattan et al (1998) flow chart are x (abscissa) and *G* (ordinate). The transition between annular flow and annular flow with partial dryout was revised since their heat transfer test data showed onset of partial dryout (due to stratification) at lower x than predicted by the Steiner (1993) map. In the original Steiner (1993) map, the ratio between liquid Weber and Froude numbers decided the location of transition from annular to stratified-wavy flow. By replacing the *We*/*Fr* ratio by an expression containing *We*, *Fr*, x and *q*, Kattan et al (1998) adapted the transition curve to their test data. The annular-to-mist flow transition curve was also modified, since the original Steiner (1993) map gave a transition from mist flow and back into annular or stratified-wavy flow at increasing x that did not seem plausible. An example of the final flow pattern map by Kattan et al. (1998a) is shown in Figure 2.12 for adiabatic flow of refrigerant HFC-134a at 10.3°C in a horizontal 12 mm ID tube.

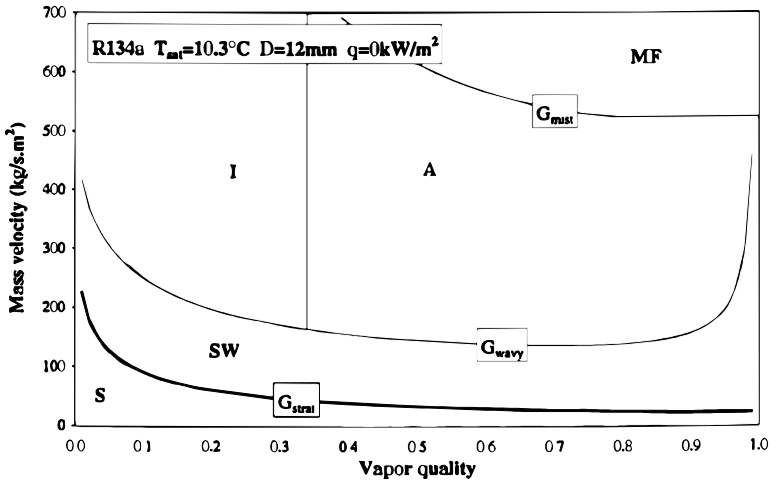

Figure 2.12 *Example of horizontal flow pattern map for HFC-134a (q=0, D=12 mm, T=10.3°C), from Kattan et al. (1998a). Symbols are S: Stratified, SW: Stratified-Wavy, I: Intermittent, A: Annular, MF: Mist*

The Kattan et al. (1998a) flow map predicts a transition from intermittent to annular flow at a Martinelli parameter (Eq. 2.23) of X_{tt} =0.34, giving the following expression for the constant-x transition line:

$$x = \frac{1}{0.34^{1/0.875}\left(\frac{\rho_v}{\rho_l}\right)^{-1/1.75}\left(\frac{\mu_l}{\mu_v}\right)^{-1/7} + 1} \tag{2.24}$$

The transition lines to stratified and stratified-wavy flow are of less interest in relation to microchannel flow, where stratification is generally not observed.

Weisman et al. (1979) compiled extensive data; proposed property and diameter corrections to an overall flow map, and found that superficial velocities were the primary factors in determining the flow pattern. They also presented several correlations for transitions between flow patterns, including the following model for transition from intermittent to annular flow:

$$1.9\left(\frac{j_v}{j_l}\right)^{1/8} = \left(\frac{j_v \rho_v^{1/2}}{\left[g(\rho_l - \rho_v)\sigma\right]^{1/4}}\right)^{0.2}\left(\frac{j_v^2}{gD}\right)^{0.18} \tag{2.25}$$

2.4.2 Flow charts for small tubes

Barnea et al. (1983) studied adiabatic two-phase flow patterns of air and water at atmospheric pressure in horizontal small-diameter tubes, with diameters down to 4 mm. They found that a large part of the stratified smooth regime predicted by Taitel and Dukler (1976) instead had intermittent flow. The smaller the pipe diameter the larger was the deviation from the Taitel and Dukler model. It was claimed that for small tube diameters, the surface tension that pulls the liquid upward becomes the mechanism for stratified to non-stratified transition. This mechanism is not accounted for in the Taitel and Dukler model, which uses Kelvin-Helmholz instability criteria in the stratified-intermittent transition. Brauner and Moalem-Maron (1992) conducted a linear stability analysis of stratified flow, postulating that neutral stability should consider a disturbance wavelength of the order of the channel diameter. On this basis, they developed the following criterion for the dominance of surface tension

$$\frac{(2\pi)^2 \sigma}{(\rho_l - \rho_v) D^2 g} > 1 \tag{2.26}$$

For CO_2 flow in a 1 mm channel, the left hand side of the above expression range from 8.2 at 20°C to 34.5 at –20°C, thus indicating surface tension domination. Even though the low surface tension of CO_2 could be expected to reduce this dominance, the small density difference and tube diameter offset this.

Damianides and Westwater (1988) determined flow patterns of air-water mixtures at adiabatic conditions in offset strip fin geometries and small-diameter horizontal glass tubes. In their observations in a 1 mm ID tube, separated flow was never detected. Again, surface tension was believed to play an important role in governing the flow pattern. The onset of annular flow for the 1 mm ID tube was caused by the generation of roll waves that crept up the tube wall. The Taitel and Dukler (1976) flow regime transition predictions were poor for all boundaries. Figure 2.13 shows the regime boundaries for the 1 mm ID tube (with regime names in CAPITALS) based on their test data, compared to the (dashed) boundaries for the Taitel and Dukler flow chart (with regime names in *ITALICS*). Coordinates are vapour and liquid superficial velocity.

Stratified flow was not observed in the 1 mm tube, and transition to annular flow occurred at much higher velocity than predicted by the Taitel and Dukler boundary.

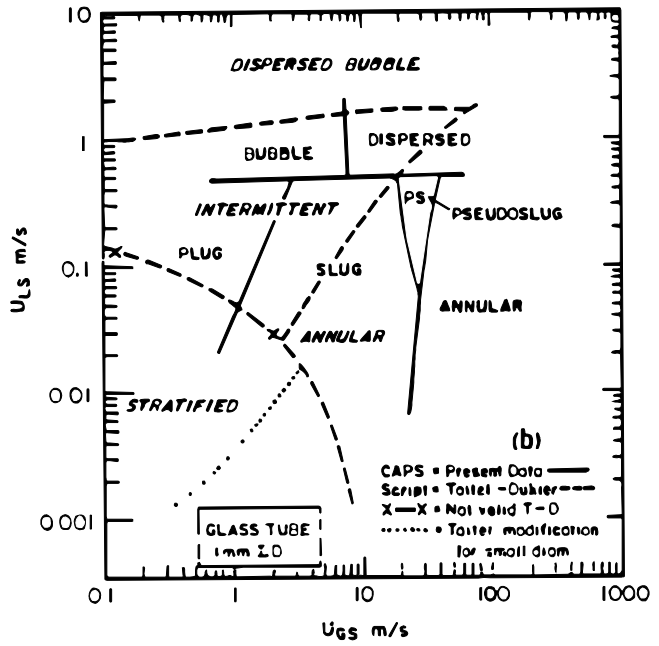

Figure 2.13 *Flow chart of Damianides and Westwater (1988) for adiabatic air-water flow in 1 mm ID horizontal glass tube, including boundaries (dashed – with regime names in ITALICS) based on the model of Taitel and Dukler (1976). Coordinates are superficial gas and liquid velocity.*

Coleman and Garimella (1999) observed flow patterns for air/water flow in horizontal small-diameter tubes, with diameter ranging from ID 1.3 to 5.5 mm. Stratified smooth flow was not observed in any test, and stratified-wavy flow was not observed in the tubes with ID less than 5.5 mm. Flow pattern observations for the ID 1.3 mm tube is shown in Figure 2.14.

Although the general tendencies are in agreement, some differences may be observed compared to the chart of Damianides and Westwater (1988), Figure 2.13. The transition from intermittent (plug/slug) flow to annular flow occurs at a lower superficial gas velocity (6 ms^{-1} instead of 20-30 ms^{-1} in the earlier study), and transition from intermittent to bubble flow occurs at higher liquid superficial velocity (5-6 ms^{-1} vs 0.5 ms^{-1}). Large deviations from the transition criteria of Taitel and Dukler (1976) were found also by Coleman and Garimella (1999), and the authors concluded that the inherent assumptions in this analysis might not be valid for small diameter tubes. Even though somewhat better correspondence was found with the transition correlations of Weisman et al. (1979), especially for the intermittent-annular transition, but authors also regarded these correlations as inapplicable for small-diameter tubes.

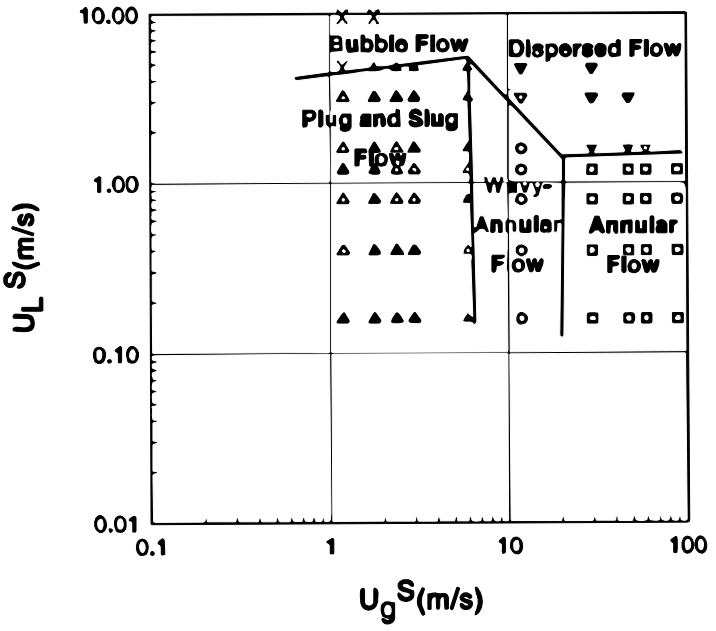

Figure 2.14 *Flow chart of Coleman and Garimella (1999) for adiabatic air-water flow in 1.3 mm ID horizontal glass tube. Coordinates are superficial gas and liquid velocity.*

Triplett et al. (1999) studied two-phase flow patterns for air-water flow in horizontal tubes, including circular microchannels of 1.1 and 1.45 mm diameter. Observations compared well with earlier studies, and confirmed that semi-analytical flow regime transition models developed for larger tubes do not fit the microchannel flow pattern observations.

The air-water flow patterns in the above studies were all observed at atmospheric pressure, with fluid properties that are very different from those of high-pressure CO_2 flow. Parameters like liquid and vapour density, surface tension, and viscosities all differ from those of CO_2 two-phase flow, as shown in Table 2.3.

Table 2.3 *Properties of water/air at atmospheric conditions, and CO_2 liquid/vapour at 10°C*

Water/air at 20°C and 1 atm				CO_2 at 0°C			
$\rho_l - \rho_v$ kgm^{-3}	ρ_l/ρ_v	σ Nm^{-1}	μ_l Pa·s	$\rho_l - \rho_v$ kgm^{-3}	ρ_l/ρ_v	σ Nm^{-1}	μ_l Pa·s
997	846	0.072	$1.0 \cdot 10^{-3}$	729	6.4	0.0027	$8.7 \cdot 10^{-5}$

Even though the density difference is comparable in the two systems, the very high vapour density of CO_2 gives a much smaller density ratio. In

addition, the dramatic reduction in surface tension and liquid viscosity gives a completely different situation in the CO_2 two-phase flow.

Besides, all the above recordings and flow pattern studies were made in adiabatic tubes with results that may not be relevant for flow patterns in heated tubes.

2.5 Heat transfer models for flow vaporization

2.5.1 General models for in-tube convective vaporization

In their review paper on correlations for convective vaporization, Webb and Gupte (1992) differentiated between

- *vaporization*, which is any process with heat addition converting liquid to vapour,
- *evaporation* (convective evaporation), which occurs when the liquid is superheated at the wall and vaporization takes place at the liquid-vapour interface within the flowing fluid, and
- *boiling* (nucleate boiling), which occurs when vapour bubbles are formed at the heated wall.

Thus, vaporization is the general term, and the total heat flux in convective vaporization is assumed to have two components: a convective evaporation component, and a nucleate boiling component.

Correlations for in-tube flow vaporization generally fall into two categories - vertical (upward) flow, and horizontal flow correlations. The direction of gravity influences the phase separation characteristics in two-phase flow, and thereby also the heat transfer and pressure drop behaviour. Many of the general correlations that are discussed in the following were developed for vertical flow situations, and should primarily be used in such geometries. The model may still be valid for horizontal non-separated flow, however, especially in microchannels where stratified flow situations are less likely to occur.

Webb and Gupte (1992) divided the correlations for convective vaporization into three models, where a *model* describes the concept used to combine the nucleate boiling and convective evaporation contributions:

- The s*uperposition* model assumes that the total heat flux is the sum of nucleate boiling and convective evaporation components:

$$h = h_{nb} + h_{ce} \tag{2.27}$$

A well-known correlation based on this model was developed by Chen (1966) for water, where the nucleate boiling contribution was derived from the pool boiling heat transfer coefficient (h_{nbp}), using a Reynolds number-dependent suppression factor S to account for the expected suppression of boiling in forced convection. The convective evaporation contribution was derived from the liquid-only heat transfer coefficient using a two-phase convection multiplier F that depended on the Lockhart-Martinelli parameter (Eq. 2.23). Superposition models are sometimes called *additive* models (Steiner and Taborek, 1992). This model may also be categorized as asymptotic (see below) with n=1. Bennet and Chen (1980) modified the original Chen correlation by introducing a Prandtl-number factor, in an attempt to generalize the correlation for other fluids than water. Steiner and Taborek (1992) criticized the suppression factor theory and pointed out that experimental data do not support this theory.

- The *asymptotic* model uses a "power-type" addition of the two contributions

$$h = \left[(h_{nb})^n + (h_{ce})^n \right]^{1/n} \tag{2.28}$$

There is no theoretical basis for selection of the exponent n. Kutateladze (1961) introduced an asymptotic correlation using n=2 for subcooled water in plain tubes. Later on, Gungor and Winterton (1986) and Liu and Winterton (1988) used this model for convective vaporization in tubes. More recently, Steiner and Taborek (1992) used an asymptotic model with n=3 for vertical upflow in tubes, using an "enhancement" model for the convective evaporation term with a "liquid-only" coefficient where the entire mass flux is assumed to be in the liquid phase. They also used newer correlations for the nucleate boiling term, based on generalized reduced-pressure models (see Section 2.5.4).

- The *enhancement* model, which was introduced by Shah (1976) for flow in tubes, is based on an enhancement factor E which is multiplied with the "liquid-only" heat transfer coefficient

$$h = Eh_{lo} \tag{2.29}$$

E is a function of the Boiling number Bo (Eq. 2.15) and a Convection number or Convective number (Co)

$$Co = \left(\frac{1-x}{x}\right)^{0.8}\left(\frac{\rho_v}{\rho_l}\right)^{0.5} \tag{2.30}$$

The Convection number is a modified Lockhart-Martinelli two-phase multiplier that accounts for the convective evaporation part, and the Boiling number accounts for the nucleate boiling part of the heat transfer. The latter assumption seriously limits the application of the model, since a number of effects on nucleate boiling (e.g. pressure) are not accounted for. The correlation of Shah (1976) uses a graphical chart or a set of equations to select between the two vaporization components, and the method is therefore sometimes called "greater of the two". For application to horizontal tubes, E also depends on the Froude number if this is less than 0.04, with the purpose of accounting for stratification. The correlations of Kandlikar (1983, 1990) and Gungor and Winterton (1987) are also of the "enhancement" type, using various correction factors to fit their models to experimental data. The Gungor and Winterton (1987) correlation is similar in structure to the Schrock and Grossmann (1959) correlation.

Webb and Gupte (1992) concluded their review paper by recommending the Steiner and Taborek (1992) correlation for vertical flow. The asymptotic features as well as the mechanistic foundation made this correlation superior to correlations mostly based on regression of test data. Although the Liu and Winterton (1988) correlation predicted the test data of Webb and Gupte (1992) well, the model is flawed due to an incorrect calculation of the multiplier F, and its use was not recommended by Webb and Gupte (1992). All the correlations mentioned above have been presented numerous times in papers, publications and books, and there is no need to show the details here.

Kattan et al. (1998b) pointed out that most flow boiling correlations were vertical tube models with some correction that tried to account for flow stratification effects. Besides, experimental data used in the development of these correlations was mostly taken at vapour fractions below dryout. A number of deficiencies with existing flow vaporization correlations were identified by Thome (1995):

- Predicted variation and peak in local heat transfer coefficient at varying x are not matched by experimental data.
- The drop in h at high x is not predicted well.
- The liquid convection heat transfer coefficient is not consistently used, since tubular flow velocity is used instead of film velocity in annular flow. Besides, the Reynolds number in the two-phase convection multiplier should be based on the effective liquid velocity.
- Most correlations do not approach the single-phase vapour heat transfer coefficient as $x \rightarrow 1$.
- Effects of flow stratification are based on criteria using the liquid Froude number, which has proven ineffective for predicting onset of stratification.
- Existing correlations have no mist flow or partial dryout criteria.

2.5.2 The model of Kattan, Thome and Favrat (1998b)

Kattan et al. (1998b) developed a heat transfer correlation attempting to avoid the above deficiencies, using the methods shown by Steiner (1993) as a basis. The new correlation scheme includes the effects of flow pattern, partial tube wall wetting in stratified flow, and partial dryout in annular flow. Four models were developed to predict local heat transfer coefficients: an annular flow model, a stratified flow model, a stratified-wavy flow model, and a stratified-wavy flow model for annular flow with partial dryout. The calculation scheme involves a stepwise procedure, starting with estimation of flow pattern as outlined in Section 2.4.1 (Kattan et al., 1998a), continuing with estimation of dry and wet fraction of tube perimeter (defined as dry and wet angles θ_{dry} and θ_{wet}), and mean liquid film thickness. Heat transfer coefficients for the wet (h_{wet}) and dry/vapour (h_v) parts of the tube are then calculated and combined into a "weighted average" two-phase heat transfer coefficient (h_{tp}) using the wet and dry perimeter segments:

$$h_{tp} = \frac{\theta_{dry} h_v + (2\pi - \theta_{dry}) h_{wet}}{2\pi} \tag{2.31}$$

The wet coefficient is estimated using an asymptotic model (Eq. 2.28) combining convective (h_{ce}) and nucleate (h_{nb}) contributions with n=3:

$$h_{wet} = \left[(h_{nb})^3 + (h_{ce})^3 \right]^{1/3} \tag{2.32}$$

The dry and wet fractions of the tube perimeter in stratified and stratified-wavy-flow are found based on local void fraction α and geometry considerations using tube, liquid and vapour cross sections. In stratified-wavy flow, the estimation of θ_{dry} also uses information from the flow chart on maximum and minimum G giving stratified-wavy flow at the given x.

Kattan et al. (1998a) recommended the correlation of Rouhani and Axelsson (1970) for void fraction calculation:

$$\alpha = \frac{x}{\rho_v}\left[(1+0.12(1-x))\left(\frac{x}{\rho_v}+\frac{1-x}{\rho_l}\right)+\frac{1.18(1-x)\left[g\sigma(\rho_l-\rho_v)\right]^{0.25}}{G\rho_l^{0.5}}\right]^{-1} \tag{2.33}$$

A film thickness δ is found based on local void fraction and flow regime, either as the equivalent film thickness for stratified/stratified-wavy flow, and for annular flow with partial dryout, or as the actual film thickness in annular flow. Entrainment is not considered.

Convective evaporation heat transfer to turbulent liquid film (h_{ch}) is calculated using a Dittus-Boelter type single-phase correlation, with film thickness δ as the characteristic length. Based on regression using experimental data for CFC and HFC refrigerants, the following expression was found:

$$h_{ce} = 0.0133\,Re_l^{0.69}\,Pr_l^{0.4}\,\frac{k_l}{\delta} \tag{2.34}$$

where the liquid Reynolds number is based on liquid film thickness, and "actual" liquid flow velocity (not superficial), i.e. using a hydraulic diameter of $4\cdot\delta$, and the calculated void fraction to estimate velocity:

$$Re_l = \frac{4G(1-x)\delta}{(1-\alpha)\mu_l} \tag{2.35}$$

The arguments for using estimated film thickness and liquid flow velocity instead of tube diameter and superficial velocity are that the above model is more consistent with the "Dittus-Boelter" type of single-phase correlation, and that the use of empirical "enhancement factors" to scale the superficial velocity is avoided.

Nucleate boiling heat transfer (h_{nb}) is calculated using the Cooper (1984) correlation (Eq. 2.46), and the dry/vapour heat transfer coeffient is calculated using

$$h_v = 0.023\, Re_v^{0.8} Pr_v^{0.4} \frac{k_v}{D} \tag{2.36}$$

with Reynolds number based on tube diameter and estimated vapour flow velocity, i.e.

$$Re_v = \frac{GxD}{\alpha \mu_v} \tag{2.37}$$

The correlation of Kattan et al. (1998b) outlined above is presently the most carefully conceived model available for in-tube vaporization, and the comparison made by the authors for various refrigerants show improved prediction accuracy compared to all other correlations.

An important feature of the Kattan et al. (1998b) correlation is the prediction of stratification, and the effects on heat transfer by partial wetting in stratified or stratified-wavy flow. Regarding dryout in annular flow, however, the model of Kattan et al. (1998b) seem to have a weaker foundation, not the least since entrainment is not accounted for. The authors also admit that the transition into mist flow is not well covered in their experimental data and models.

2.5.3 Onset of nucleate boiling

Onset of nucleate boiling heat transfer depends on local conditions with sufficient wall superheat and heat flux. Several methods have been developed to predict the onset conditions, including the analytical model of Sato and Matsumura (1964) and Davis and Anderson (1966), adapted to liquids other than water by Frost and Dzakowic (1967):

$$q_{ONB} = \frac{k_l h_{lv} \rho_v}{8 \sigma T_{sat}} \left[\left(T_w - T_{sat} \right)_{ONB} \right]^2 Pr_l^2 \tag{2.38}$$

Here, h_{lv} is the enthalpy of evaporation. This correlation defines the threshold conditions at which nucleation is initiated, and it was found to agree well with data for a variety of fluids (Carey, 1992). For a given wall superheat, the correlation predicts the maximum heat flux that allows

nucleate boiling, and for a given heat flux, the correlation predicts the minimum wall superheat needed to initiate nucleate boiling. The ability of Eq (2.38) to predict onset of nucleate boiling depends on the existence of a sufficient range of potential nucleation sites on the wall surface.

2.5.4 Nucleate pool boiling heat transfer

Owing to the high saturation pressure of CO_2, nucleate boiling plays an important role in flow vaporization heat transfer. A number of correlations and models have been developed for pool boiling, and some of these will be outlined here. Borishanski (1969) used thermodynamic similitude (law of corresponding states) as a basis, and developed a correlation that can be written as

$$h = A^* q^{0.7} F(p) \tag{2.39}$$

where $F(p)$ is a function of reduced pressure, and A^* is a fluid-dependent constant. Mostinski (1963) found the following relations for these parameters:

$$A^* = 0.1011 p_{cr}^{0.69} \tag{2.40}$$

$$F(p) = 1.8 p_r^{0.17} + 4 p_r^{1.2} + 10 p_r^{10} \tag{2.41}$$

Bier et al. (1976) developed an alternative pressure function $F(p)$ adapted to refrigerants, based on experimental data on boiling heat transfer with various fluorocarbon refrigerants, including data at reduced pressures approaching 1.0:

$$F(p) = 0.7 + 2 p_r \left(4 + \frac{1}{1 + p_r} \right) \tag{2.42}$$

As shown by Figure 2.15, the reduced-pressure function of Bier et al. (1976) gives considerably higher values than the Mostinski (1963) function (Eq. 2.41).

A more refined reduced-pressure correlation was proposed by Gorenflo (1993), using a reference heat transfer coefficient h_o at a reduced pressure of p_r=0.1, a reference heat flux of q_o=20 kWm^{-2}, and a reference surface roughness of R_{p0}=0.4μm:

$$h = h_0 F_{PF} \left(\frac{q}{q_o} \right)^{nf} \left(\frac{R_p}{R_{po}} \right)^{0.133} \tag{2.43}$$

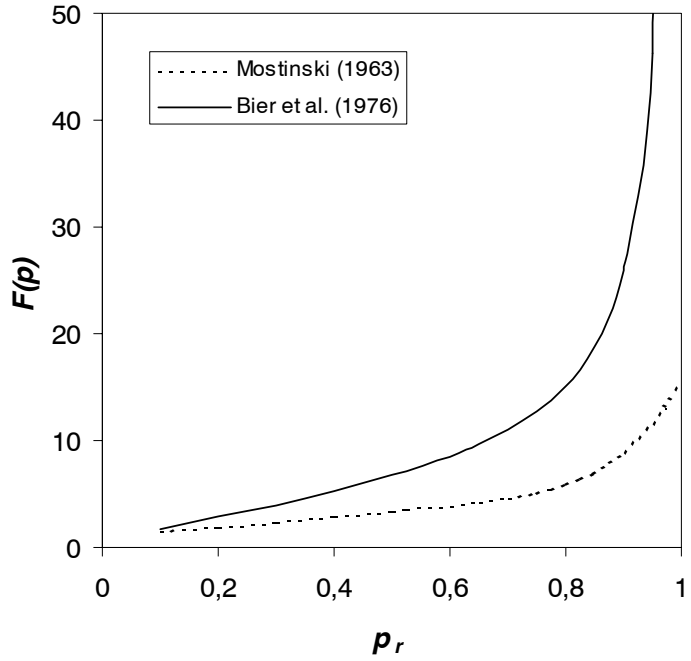

Figure 2.15 *Function F(p) in Eq. (2.39) at varying reduced pressure p_r as proposed by Mostinski (1963) and Bier et al. (1974).*

The following general relations were derived for the pressure function F_{PF} and the exponent *nf* based on extensive experimental data on various non-aqueous fluids:

$$F_{PF} = 1.2 p_r^{0.27} + \left(2.5 + \frac{1}{1 - p_r} \right) p_r \tag{2.44}$$

$$nf = 0.9 - 0.3 p_r^{0.3} \tag{2.45}$$

For CO_2, Gorenflo (1993) lists a reference pool boiling heat transfer coefficient of h_o = 5100 $Wm^{-2}K^{-1}$ based on experimental data, and a coefficient of 4170 $Wm^{-2}K^{-1}$ (i.e. 18% lower) based on a recommended correlation by Stephan and Preusser (1979).

Finally, a simple and widely used correlations for nucleate boiling heat transfer is the reduced-pressure model by Cooper (1984):

$$h = 55 p_r^{0.12-0.4343\ln(R_p)} (-0.4343 \ln p_r)^{-0.55} M^{-0.5} q^{0.67} \quad (2.46)$$

R_p is a surface roughness parameter, with dimension μm, which is set equal to 1.0 for an unspecified surface, and M is the molecular mass of the fluid.

2.5.5 Mist flow evaporation

Several authors have developed models for heat transfer in the mist (droplet) flow regime, i.e. post-dryout heat transfer. This regime is also called liquid-deficient region, with a flow pattern of dispersed flow.

A number of heat transfer mechanisms can be identified in this regime, including (Carey, 1992):

- convective heat transfer from tube wall to vapour,
- convective heat transfer from vapour to droplets,
- evaporation from droplets that collide with the wall and wet the surface,
- evaporation of droplets that come close to the wall but do not wet the surface,
- radiation from wall to droplets, and
- radiation from wall to vapour.

The two first mechanisms act in series to transfer heat from the wall to the droplets. Convective heat transfer from the vapour to the droplets relies on some superheat in the vapour flow. The interactions between liquid droplets, wall surface and vapour flow are quite complex, and the flow is generally in a non-equilibrium state with superheated vapour and saturated liquid droplets. There are two limiting conditions for mist flow heat transfer:

- *Thermodynamic equilibrium*, where the vapour temperature is assumed to be constant and at the saturation temperature. This corresponds to a situation with extremely good heat transfer between the vapour and the liquid droplets.
- *Complete departure from equilibrium*. In the extreme case with complete non-equilibrium, there is zero heat transfer between vapour and droplets, and between wall and droplets. Thus, the vapour absorbs all the heat, and the vapour temperature rises linearly if the heat flux is constant.

Real systems have some departure from equilibrium and operate between these two extremes. At high mass flux levels, and/or if the convective

transport between the phases is good (high turbulence level), the situation may approach thermodynamic equilibrium. Increased pressure also gives conditions closer to thermodynamic equilibrium.

Models for mist-flow heat transfer fall into two categories: equilibrium conditions models, and models where departure from equilibrium is accounted for. Equilibrium correlations generally use a homogeneous model for the dispersed flow, and equivalent fluid properties for the vapour/liquid mixture. The form of such empirical correlations may be of a single-phase vapour heat transfer model, e.g. based on a Dittus-Boelter type expression, and a correction factor that depends on x and liquid/vapour fluid properties. One such equilibrium dispersed-flow correlation was proposed by Groeneveld (1973). In case of tube flow, the model is:

$$Nu_v = \frac{hD}{k_v} = 0.00109\left[\left(\frac{GD}{\mu_v}\right)\left(x + \frac{\rho_v}{\rho_l}(1-x)\right)\right]^{0.989} Pr_{v,w}^{1.41} Y^{-1.15} \tag{2.47}$$

where

$$Y = 1 - 0.1\left(\frac{\rho_l}{\rho v} - 1\right)^{0.4} (1-x)^{0.4} \tag{2.48}$$

The vapour Prandtl number $Pr_{v,w}$ is evaluated at the wall temperature, and an iterative solution is needed where the wall temperature is found depending on heat transfer coefficient and heat flux. The other properties are evaluated at saturation conditions. Dougall and Rohsenow (1963) proposed a slightly different correlation, assuming equilibrium conditions:

$$Nu_v = \frac{hD}{k_v} = 0.023\left[\left(\frac{GD}{\mu_v}\right)\left(x + \frac{\rho_v}{\rho_l}(1-x)\right)\right]^{0.8} Pr^{0.4} \tag{2.49}$$

This correlation is simpler to use and it also has the advantage of being reduced to the standard Dittus-Boelter equation for heated turbulent pipe flow when $x = 1$. The modified Reynolds number in the above equation can also be used in other single-phase correlations, e.g. the Gnielinski (1976) correlation, to account for mist-flow conditions.

Models that account for departure from equilibrium distinguish between the "normal" equilibrium vapour fraction (thermodynamic vapour fraction) x (often with symbol x_E in mist-flow calculations), and the actual vapour fraction x_A. Numerically, the equilibrium vapour fraction x_E can reach values higher than 1.0 when the vapour phase is superheated. Equilibrium vapour fraction is defined as

$$x_E = \frac{h - h_{l,sat}}{h_{lv}} \tag{2.50}$$

where h is the equilibrium specific enthalpy of the flow, including liquid and vapour phases, and $h_{l,sat}$ is the specific enthalpy of saturated liquid. Actual vapour fraction is defined as

$$x_A = \frac{x_E h_{lv}}{h_v - h_{l,sat}} \tag{2.51}$$

where h_v is the specific enthalpy of vapour at the actual temperature.

The correlation of Groeneveld and Delorme (1976) is one of the most quoted methods that account for non-equilibrium effects in post-dryout heat transfer. Its basis is post-dryout test data on water, mainly at high heat flux and mass flux. Comparisons made for instance by Shah and Siddiqui (2000) and Nishikawa et al. (1986) show large deviations between measured wall temperatures and predictions using the correlation of Groeneveld and Delorme (1976) at low mass flux and heat flux, and with other fluids than water.

Shah and Siddiqui (2000) proposed a general correlation based on data for a wide range of conditions and fluids. Its procedure for evaluating the heat transfer coefficient is based on finding the actual vapour fraction x_A and then calculating void fraction and resulting Reynolds number, before finding the wall-to-vapour heat transfer coefficient based on Re. The heat flux removed from the wall is

$$q = F_{dc} h (T_w - T_v) \tag{2.52}$$

where T_v is the vapour temperature, h is the wall-to-vapour heat transfer coefficient, and the factor $F_{dc} = 1.0$ unless the reduced pressure is higher than 0.8. In this case

$$F_{dc} = 2.64 p_r - 1.11 \quad \text{for } p_r > 0.8 \tag{2.53}$$

The heat transfer coefficient is calculated using standard correlations, and Shah and Siddiqui (2000) recommend

$$Nu = 0.023 Re^{0.8} Pr_v^{0.4} \quad \text{for } Re > 10^4 \tag{2.54}$$

$$Nu = 0.00834 Re^{0.8774} Pr_v^{0.6112} \quad \text{for } Re < 10^4 \tag{2.55}$$

where the last expression is due to Hadaller and Banerjee (1969). The Nusselt number is based on tube diameter and vapour thermal conductivity, and the Reynolds number is calculated from estimated vapour flow velocity

$$Re = \frac{GDx_A}{\mu_v \alpha} \tag{2.56}$$

where the void fraction is calculated using a homogeneous model

$$\alpha = \frac{x_A \rho_l}{(1 - x_A)\rho_v + x_A \rho_l} \tag{2.57}$$

The procedure for finding x_A is based on a quite complex algorithm involving the Boiling number (Eq. 2.15) and the liquid Froude number:

$$Fr_l = \frac{G^2}{\rho_l^2 gD} \tag{2.58}$$

First, the intersection between the correlating curve for x_A and the equilibrium vapour fraction x_E is found. For $Fr_l \geq 100$, the intersection is found at the point ($x_{E,INT} = x_{A,INT}$) satisfying the relation

$$x_A = (A_1 + A_2 x_E + A_3 x_E^2 + A_4 x_E^3) Fr_l^{0.064} \tag{2.59}$$

where the constants are

$A_1 = -0.0347$
$A_2 = 0.9335$
$A_3 = -0.2875$
$A_4 = 0.035$

If $x_A > x_E$ in (2.59) then $x_A = x_E$, and if $x_A > 1$ then $x_A = 1$.

For $Fr_l < 100$, the intersection point is found at

$$x_{A,INT} = x_{E,INT} = 0.19 Fr_l^{0.16} \tag{2.60}$$

Depending on the vapour fraction at dryout (x_{CR}), two different models are used. For $x_{CR} \leq x_{E,INT}$, the actual vapour fraction is set equal to the equilibrium vapour fraction up to the intersection point, and from there and upwards, x_A is calculated from x_E using Eq. (2.59-2.60). For $x_{CR} > x_{E,INT}$, a tangent point need to be found, at the intersection of Eq. (2.59) and the following equation:

$$x_A = x_{CR} + (x_E - x_{CR})(A_2 + 2A_3 x_E + 3A_4 x_E^2) Fr_l^{0.064} \tag{2.61}$$

The tangent point ($x_{E,TAN}$, $x_{A,TAN}$) is found by simultaneous solution of Eq. (2.59) and (2.61). For $x_E > x_{E,TAN}$, x_A is found from Eq. (2.59). For $x_E < x_{E,TAN}$, x_A is found from the following expression:

$$x_A = \frac{x_{A,TAN} - x_{CR}}{x_{E,TAN} - x_{CR}} x_E + \frac{x_{E,TAN} - x_{A,TAN}}{x_{E,TAN} - x_{CR}} x_{CR} \tag{2.62}$$

A final correction of x_A is needed if Bo is greater than $5 \cdot 10^{-4}$. Setting the actual vapour fraction from the above scheme to $x_{A,o}$, the corrected value is

$$x_A = x_E - (x_E - x_{A,o}) \frac{Bo}{5 \cdot 10^{-4}} \quad \text{if } Bo > 5 \cdot 10^{-4} \tag{2.63}$$

With the difference between wall and vapour temperature known from Eq. (2.52) the vapour temperature can be found based on the vapour enthalpy h_v in the following expression derived from Eq. (2.51):

$$h_v = h_{v,sat} + \frac{x_E - x_A}{x_A} h_{lv} \tag{2.64}$$

Now the wall temperature can be calculated, and the equivalent heat transfer coefficient referring to the difference between wall and saturation temperature can be found.

Shah and Siddiqui (2000) reproduced measured post-dryout heat transfer coefficients in 546 data points with a mean deviation of 15.2% using the above correlation. The range of data for water, helium, hydrocarbons, nitrogen and fluorocarbons included pressures from 0.1 to 21.5 MPa, reduced pressure from 0.0046 to 0.97, mass flux from 4 to 5176 $kgm^{-2}s^{-1}$, tube diameters from 1.1 to 24.3 mm, and equilibrium vapour fraction from 0.1 to 2.4.

Even though the authors claimed that the above equations could be easily programmed for computerized calculations, the algorithm is quite complicated, and careful checking is necessary in order to arrive at the desired result.

2.5.6 Special heat transfer correlations for small-channel vaporization

Tran et al. (1997) developed a special correlation for nucleate flow boiling in small channels. The authors had noted the importance of the transition from forced-convection boiling to nucleate boiling in small-diameter flow, and that this transition occurred at lower tube wall superheat than with larger tube diameters. Some authors had even showed that for very small channels with hydraulic diameter in the range 0.30-0.65 mm, fully developed nucleate boiling took place immediately without any transition (Peng et al., 1996). A correlation for the heat transfer coefficient h_{nb} in nucleate-flow boiling was developed based on Rohsenow's nucleate-boiling model, and the confinement number concept by Kew and Cornwell (1994), Eq. (2.2). The form of the Tran et al. (1997) correlation is:

$$Nu = \frac{hD}{k_l} = c_1 \left(Bo \cdot Re_l \cdot N_{conf} \right)^{c_2} \left(\frac{\rho_g}{\rho_l} \right)^{c_3} \tag{2.65}$$

Using experimental data and regression to find the coefficients c_1, c_2 and c_3, the correlation predicted a majority of 438 experimental data points for nucleate flow-boiling of refrigerants R113, R-12 and R-134a in 2.4-2.9 mm hydraulic diameter tubes within ±15%.

2.6 Pressure drop in flow vaporization

2.6.1 Pressure drop in evaporator tubes

Local pressure drop or pressure gradient of two-phase flow in tubes can be divided into three components; wall friction loss, momentum change, and elevation pressure drop due to gravity. Thus,

$$\left(\frac{dp}{dz} \right) = \left(\frac{dp}{dz} \right)_f + \left(\frac{dp}{dz} \right)_m + \left(\frac{dp}{dz} \right)_g \tag{2.66}$$

For horizontal tubes, as in the present study, the last term is zero. Using general relations for two-phase flow (Collier and Thome, 1994), the following expression for momentum change (acceleration) pressure drop can be found:

$$\left(\frac{dp}{dz}\right)_m = G^2 \frac{d}{dz}\left[\frac{x^2}{\rho_v \alpha} + \frac{(1-x)^2}{\rho_l (1-\alpha)}\right] \tag{2.67}$$

With knowledge of local vapour fraction and void fraction, this expression can be applied in the estimation of acceleration pressure drop.

The two-phase frictional pressure gradient is often expressed in terms of the single-phase gradient assuming that the total flow is in liquid phase, using a two-phase frictional multiplier Φ_{lo}:

$$\left(\frac{dp}{dz}\right)_f = \left(\frac{dp}{dz}\right)_{f,lo} \phi_{lo}^2 \tag{2.68}$$

Here, the frictional pressure drop gradient for the entire flow as liquid can be evaluated from

$$\left(\frac{dp}{dz}\right)_{f,lo} = \frac{f_{lo} G^2}{2\rho_l D} \tag{2.69}$$

where f_{lo} is the *Darcy friction factor* for turbulent single-phase (liquid) flow (See Notation and definitions). The literature contains numerous models for the single-phase friction factor, and correlations for the two-phase frictional multiplier, enabling estimation of pressure drop due to flow friction.

2.6.2 Two-phase pressure drop correlations

The correlation of Friedel (1979) was developed using a database of 25,000 experimental points, and is regarded as the most accurate general correlation for two-phase frictional pressure drop in tube flow. For horizontal flow, the database included tube diameters down to 4 mm. The following expression was derived by Friedel for the two-phase frictional multiplier in horizontal flow:

$$\phi_{lo}^2 = A + \frac{3.24 B_1}{Fr_{tp}^{\,0.0454} We_{tp}^{\,0.035}} \tag{2.70}$$

where

$$A = (1-x)^2 + x^2\left(\frac{\rho_l}{\rho_v}\right)\left(\frac{f_{vo}}{f_{lo}}\right) \tag{2.71}$$

$$B_1 = x^{0.78}(1-x)^{0.224}\left(\frac{\rho_l}{\rho_v}\right)^{0.91}\left(\frac{\mu_v}{\mu_l}\right)^{0.19}\left(1-\frac{\mu_v}{\mu_l}\right)^{0.7} \tag{2.72}$$

$$Fr_{tp} = \frac{G^2}{gD\rho_{tp}} \tag{2.73}$$

$$We_{tp} = \frac{G^2 D}{\rho_{tp}\sigma} \tag{2.74}$$

$$\rho_{tp} = \left(\frac{x}{\rho_v} + \frac{1-x}{\rho_l}\right)^{-1} \tag{2.75}$$

The friction factor f_{vo} is for the total mass flow in vapour phase, and the density ρ_{tp} is calculated assuming homogeneous flow using Eq. (2.75).

For circular tubes, Friedel (1979) recommended the following expressions for the Darcy friction factors for single-phase flow in circular tubes:

$$f = 64/Re, \quad Re \leq 1055 \ \text{(Blasius)} \tag{2.76}$$

$$f = \left[0.86859 \ln\left(\frac{Re}{1.964 \ln Re - 3.8215}\right)\right]^{-2}, \quad Re > 1055 \tag{2.77}$$

Friedel (1979) also proposed another version of the above correlation, using Froude and Weber numbers based on liquid properties only, i.e. replacing "*tp*" by "*l*" in Equations (2.73) and (2.74). Equations (2.70) and (2.72) are then replaced by:

$$\phi_{lo}^2 = A + \frac{3.43 B_2}{Fr_l^{0.047} We_l^{0.0334}} \tag{2.78}$$

$$B_2 = x^{0.685}(1-x)^{0.24}\left(\frac{\rho_l}{\rho_v}\right)^{0.8}\left(\frac{\mu_v}{\mu_l}\right)^{0.22}\left(1-\frac{\mu_v}{\mu_l}\right)^{0.89} \tag{2.79}$$

In some cases, for instance in Carey (1992), and Zhang and Webb (2001), the exponent 0.224 in Eq.(2.72) is replaced with 0.24, which is incorrect in combination with the two-phase *We-*/*Fr*-definitions and the exponents of Eq. (2.70) and (2.72). This exponent belongs in the second "liquid-property" version of the Friedel model, but then with several other exponents and constants changed as well, as shown above.

Collier and Thome (1994), citing Whalley (1980), recommends the Friedel (1979) correlation if the liquid/vapour dynamic viscosity ratio is less than 1000. For CO_2, this ratio is much lower than 1000, with a value of 7.2 at 0°C increasing to approximately 24 at the triple point.

Lombardi and Carsana (1992) developed the following expression for two-phase frictional pressure drop in vertical and inclined (including horizontal) tubes, in a model termed "CESNEF-2":

$$\left(\frac{dp}{dz}\right)_f = \frac{2G^2}{\rho_m D}\left[c_{fv}\cdot b_v + c_{fl}\cdot b_l + c_{fm}\cdot b_m\right]. \tag{2.80}$$

where the *Fanning* friction coefficients (c_f) and weight functions (b) are for vapour (v), liquid (l), and two-phase (m) homogeneous mixture, respectively. Density ρ_m is also based on a homogeneous model, calculated as shown in Eq. (2.75).

The liquid and vapour *Fanning* friction factors are evaluated using the following modified Colebrook-White expression from Selander (1978):

$$c_f = \frac{0.25}{\left[1 - 9\log_{10}\left(\frac{10}{Re} + 0.2\frac{r}{D}\right)\right]^2} \tag{2.81}$$

for turbulent flow in tube with roughness r, and the Blasius formula

$$c_f = \frac{16}{Re} \tag{2.82}$$

for laminar flow (Re < 2400). The two-phase friction coefficient was correlated empirically using a dimensionless group Lo:

$$Lo = \frac{G^2 D}{\rho_m \sigma}\left(\frac{\mu_v}{\mu_l}\right)^{0.5} \tag{2.83}$$

where ρ_m is the two-phase mixture density. Another dimensionless group, the *Ce* number, represented the ratio of liquid column height to surface tension, corrected by the two-phase viscosity ratio, for tube diameter $D >$ 0.001 m:

$$Ce = \rho_l g \frac{(D - 0.001)^2}{\sigma}\left(\frac{\mu_v}{\mu_v}\right) \tag{2.84}$$

For $D \leq 0.001$ m, *Ce* was set to zero. The two-phase friction factor could then be calculated as follows:

$$c_{fm} = 0.046 \cdot Lo^{-0.25} \qquad Lo \geq 30 \cdot Ce \tag{2.85}$$

$$c_{fm} = 1.38 \cdot Ce \cdot Lo^{-1.25} \quad Lo < 30 \cdot Ce \tag{2.86}$$

Finally, the dimensionless weight functions were defined as:

$$b_v = x^{600\frac{\rho_v}{\rho_l}}, \quad b_l = (1-x)^{2\frac{\rho_l}{\rho_v}}, \quad b_m = 1 - b_v - b_l \tag{2.87}$$

The frictional pressure drop correlation of Lombardi and Carsana (1992) was developed for flow in vertical or inclined tubes, with adiabatic and diabatic conditions. A comparison to more than 10000 experimental data points, mainly for water/gas flow, was reported to correlate 80.5% of the data to within ±20%. Validity range for the correlation is:

$$20 < G < 4000 \text{ kgm}^{-2}\text{s}^{-1}$$
$$0.0005 < D < 0.446 \text{ m}$$
$$1 < p < 97 \text{ bar}$$

2.6.3 Special correlations for small-diameter flow

Tran et al. (1999) conducted measurements on flow evaporation pressure drop of CFC and HFC refrigerants in tubes of 2.4 to 2.9 mm hydraulic diameter. Existing correlations[e] for two-phase frictional pressure drop in large tubes failed to reproduce the test data, mainly by predicting too small pressure drops. A new correlation was developed based on Chisholm's B-coefficient method (Chisholm, 1983). A scaling factor was introduced in the model to represent the difference in pressure gradient between small tubes and large tubes. Furthermore, the B-factor in the original model was replaced by the confinement number (N_{conf} in Eq. 2.2), thus bringing in a parameter that accounted for surface tension and bubble confinement effects on pressure drop. The resulting correlation was written as

$$\Delta p_f = \Delta p_{f,lo}\left\{1+\left(4.3X^2-1\right)-\left[N_{conf}\cdot x^{0.875}(1-x)^{0.875}+x^{1.75}\right]\right\} \qquad (2.88)$$

where the factor 4.3 was based on regression using the test data of Tran et al. (1999), and the parameter X is the Lockhart-Martinelli parameter (Eq. 2.23).

Zhang and Webb (2001) modified the Friedel (1979) correlation in an attempt to fit experimental data for small diameter tubes. The viscosity and density ratios in the original Friedel model were replaced by reduced pressure (p_r), which was believed to provide better correlation. Also, since the We and Fr dependencies in the Friedel model were weak, these terms were omitted. On this basis, and by regression analysis, the authors found the following expression for the two-phase frictional multiplier:

$$\phi_{lo}^2 = (1-x)^2 + 2.87x^2\frac{1}{p_r} + 1.68x^{0.8}(1-x)^{0.25}p_r^{-1.64} \qquad (2.89)$$

This correlation was able to correlate 119 data points for refrigerant (mainly HFC-134a) two-phase frictional pressure drop in small-diameter tubes with a mean deviation of 11.5%, and 85% of the calculated data were within 20% of the experimental data.

[e]Correlations by Friedel (1979), Chisholm (1983) (B- and C-coefficient), Jung and Radermacher (1989), and Souza and Pimenta (1995).

URN:NBN:no-2319

3. Earlier studies on CO_2 evaporation heat transfer and pressure drop

3.1 Heat transfer and pressure drop in large-diameter flow

3.1.1 Experimental results on heat transfer

Some results have been published from studies on CO_2 evaporation heat transfer coefficients in larger tubes, either in dedicated test rigs or as part of system studies. Bredesen et al. (1997) measured heat transfer and pressure drop of pure CO_2 in a horizontal 7 mm ID aluminium test tube, at mass flux between 200 and 400 $kgm^{-2}s^{-1}$, heat flux between 3 and 9 kWm^{-2}, and evaporating temperature from –25 to 5°C. The test section was heated by electrical resistance wires that were wound on the OD 10 mm test tube and embedded in a thermally conductive epoxy. Tube wall temperatures were measured by thermocouples located in 0.5 mm deep grooves on the outside tube wall, and local pressures were measured with pressure taps. Local temperatures were taken as saturation temperature at the measured pressure. Initially, the authors experienced significant scattering of wall temperatures and test data due to the difficulties of measuring wall temperature accurately. The rig was then calibrated by circulating water through the test section at varying the heat flux to obtain correction data for each thermocouple. This reduced the scattering significantly, but still the authors stated that they were on the edge of what could be handled by this experimental method. The heat transfer test data indicated regimes of convective boiling at high mass flux and low evaporating temperature, and nucleate boiling regimes at lower mass flux and higher temperatures. Typical heat transfer coefficients were in the range of 6000 to 10000 $Wm^{-2}K^{-1}$ at

T=–10°C and q=6 kWm^{-2}, increasing to about 12000 at a heat flux of q=9 kWm^{-2}. At most conditions, the local heat transfer coefficient increased up to a vapour fraction of around 0.9, but at the highest evaporating temperature, the behaviour was quite different, with a decreasing heat transfer coefficient at increasing x. In the latter case (G= 200 kgm^{-2}s^{-1}, T=5°C, q=6 kWm^{-2}), the heat transfer coefficient dropped from about 14000 Wm^{-2}K^{-1} at x=0.2 to about 8000 Wm^{-2}K^{-1} at x=0.9. This was explained by the authors by referring to the high pressure and low liquid/vapour density near the critical point. A comparison to a few common heat transfer correlations gave poor correspondence for all test data, the experimental coefficients being about twice as high as predicted.

Høgaard Knudsen and Jensen (1997) measured boiling heat transfer of pure CO_2 in a horizontal 10/30 mm ID/OD seamless steel tube, at mass flux ranging from 85 to 175 kgm^{-2}s^{-1}, heat flux 7 and 13 kWm^{-2}, and evaporating temperature T=–10 and –28°C. The test tube was heated by condensing R-22, and instrumented with 12 thermocouples (3 locations along the tube with 4 thermocouples each). The thermocouples were located inside stainless steel capillary tubes that were embedded in grooves in the test tube wall. These grooves were filled with tin. Average temperature for all thermocouples was used as tube wall temperature. With condensing vapour heating, as in this case, the conditions would be close to constant wall temperature conditions. The experimental data at –28°C and 80 kgm^{-2}s^{-1} show a heat transfer coefficient of about 4000 Wm^{-2}K^{-1} at 8 kWm^{-2} heat flux and about 5000 Wm^{-2}K^{-1} at 13 kWm^{-2} heat flux. In both cases, the heat transfer coefficient dropped slightly with increasing vapour fraction, indicating a dominance of nucleate boiling. The authors were able to correlate the experimental data (87 tests) within 14% (RMS) by applying the model of Shah (1982) and multiplying the result by a constant factor of 1.9.

As part of his PhD study on CO_2-based heat pumps, Rieberer (1998) measured overall heat transfer coefficients in the system evaporator and compared the data to models. The measurements were carried out on coaxial tube-in-tube heat exchangers with CO_2 in two horizontal 5.7 m long serial-connected 12 mm ID inner tubes, which were heated by brine flowing in the annulus. Type K thermocouples were embedded in the top and bottom of the tube wall at eight locations along the tubes. The evaporator was connected to a circuit having a compressor, and some lubricant (at unknown concentration) was therefore present in the CO_2 flow. The oil was a Reniso CO_2 150E by Fuchs, with a kinematic viscosity of 130·10^{-6} m^{2}s^{-1} at 40°C. Since an oil separator was installed, the oil concentration was believed to be below 1%. The measured local heat transfer coefficients at –10°C evaporating temperature ranged from about 2000 Wm^{-2}K^{-1} at a mass flux of 358 kgm^{-2}s^{-1} to about 4000 Wm^{-2}K^{-1} at 681 kgm^{-2}s^{-1}. The heat flux ranged from 20 to 35 kWm^{-2}. The measurements indicated a slight decrease in h

with increasing *x*. The level and the behaviour was thus quite different from the measurements of Bredesen et al. (1997), where the level was 8000-12000 $Wm^{-2}K^{-1}$ even at lower heat and mass flux, and where the coefficient increased with *x*. Additional measurements by Rieberer (1998) on a 10 mm ID horizontal evaporator tube gave similar results as for the 12 mm tube. Common heat transfer correlations gave considerably higher predicted heat transfer coefficients than the experimental data. Models that gave best fit to the data of Bredesen et al. (1997) overpredicted the experimental data of Rieberer (1998) by a factor of 3 to 4. The correlation of Shah (1982) overpredicted the data by 50-100%, in clear contrast to the findings of Høgaard Knudsen and Jensen (1997). These large differences were believed to be caused by the presence of lubricant in the system of Rieberer (1998), and the data gives some indication a possible serious impact of lubricant on nucleate boiling heat transfer. Test data on the 10 mm tube shows that the heat transfer coefficient is almost unaffected by a doubling of the heat flux, and that the coefficient increases with mass flux. Both these observations indicate that nucleate boiling is not a dominant mechanism of heat transfer, or that this mechanism is suppressed by a lubricant concentration.

In the data of Rieberer (1998), there was a noticeable difference in temperature between the top and bottom thermocouples in the 12 mm tube, especially at higher vapour fraction, where the difference was more than 3 K at a mass flux of 600 $kgm^{-2}s^{-1}$. This was explained by a separation of the two phases and a stratified flow pattern.

Sun and Groll (2001) conducted experiments on a horizontal 4.6 mm ID stainless steel tube. The test apparatus had eight tube-in-tube sections in series where the CO_2 flow in the inner tube was heated by water flowing in the annulus. A Wilson-plot method was used to fit a Gnielinski-type heat transfer equation to the water side. Test data were recorded at CO_2 mass flux between 500 and 1670 $kgm^{-2}s^{-1}$, heat flux 10-50 kWm^{-2} and vapour fraction 0-0.95. Evaporating temperatures were maintained between –2 and +10°C. Some test data at varying vapour fraction are shown in Figure 3.1, with test conditions as shown above the diagram. For both heat flux levels, the heat transfer coefficient dropped at increasing *x*. A more or less abrupt drop in heat transfer above a vapour fraction of 0.4-0.6 was observed in most tests, and was explained by dryout of the liquid film. The heat transfer was not influenced much by varying mass flux at low vapour fractions, while heat flux variation had significant influence. This was taken as evidence of nucleate boiling as the dominant heat transfer mechanism at lower *x*. The heat transfer after dryout was influenced by mass flux, indicating a convection-dominated heat transfer.

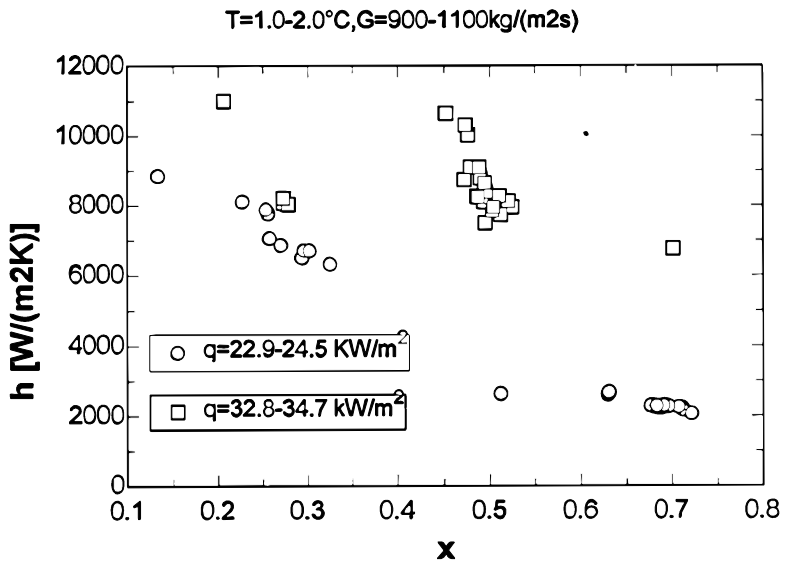

Figure 3.1 *Measured heat transfer coefficient during flow boiling of CO_2 in a 4.6 mm ID tube, at conditions shown above the figure. Reproduced from Sun and Groll (2001)*

Yun et al. (2001) conducted measurements on a horizontal DC-power heated stainless steel tube with ID 6.0 mm and length 1600 mm. Local heat transfer coefficients along the tube were measured by wall thermocouples. Tests were conducted at 5 and 10°C evaporating temperature, with mass flux varying from 170 to 320 $kgm^{-2}s^{-1}$, and heat flux from 10 to 20 kWm^{-2}. The authors noted the peculiar behaviour of CO_2 in that local heat transfer coefficients dropped with increasing vapour fraction, due to efficient nucleate boiling at low x and effects of dryout at higher x. Entrainment was believed to be more important with CO_2 than with conventional fluorocarbon refrigerants. In tubes with larger diameter the film thickness would be higher, the authors noted, and this would give more entrainment and earlier dryout than in microchannel tubes. Yun et al. compared their test data to several common heat transfer correlations, but none of these could predict the local coefficients that were measured. Reasons for this were believed to be that the correlations were developed for flow conditions where annular mist flow dominated and nucleate boiling was suppressed at moderate x, and especially at low mass flux CO_2 behaves differently from this.

3.1.2 Correlations for CO_2 vaporization in larger-diameter tubes

As mentioned above, Høgaard Knudsen and Jensen correlated their data by using the model of Shah (1982) and multiplying the result by a constant factor of 1.9.

Hwang et al. (1997) correlated the data of Bredesen et al. (1997) by a modified Bennett-Chen correlation, achieving a mean deviation of 14%. The other correlations that were examined included the models of Chen, Bennett-Chen (original), Shah, Gungor-Winterton, Schrock-Grossmann, and Liu-Winterton, which all gave poor correspondence.

Rieberer (1998) compared the experimental data of Bredesen et al. (1997), who used pure CO_2 and constant heat flux in a 7mm ID tube, to a number of correlations from literature. The qualitative variation in measured heat transfer coefficient was correlated best by the model of Wattelet et al. (1994), although the predicted data were generally too low. Rieberer (1998) also modified the nucleate boiling model of Steiner (1993) by using a multiplier C_f=1.5 instead of 1.11 as given by Steiner. The modified Steiner model correlated the data of Bredesen et al. (1997) with a deviation of about ±30%.

Sun and Groll (2001) developed a CO_2 flow boiling heat transfer prediction method based on three regimes: pre-dryout, dryout, and post-dryout. Initially, the location of onset and completion of dryout is estimated, based on the method of Ahmad (1973), and adapted to horizontal tubes by Wallis (1969). In the pre-dryout region, a Chen (1966) heat transfer correlation is used if the tube diameter is above the microchannel range (limit not given, but probably around 1-2 mm). For microchannel tubes, the Chen correlation is replaced by the Cooper (1984) nucleate boiling heat transfer correlation if the heat flux is larger than 10 kWm^{-2}. The Dougall and Rohsenow (1963) correlation (Eq. 2.49) is used in the post-dryout regime, and a linear drop between the two correlations is assumed in the dryout region. Compared to the test data of Sun and Groll (2001), the model gave an average deviation of 6.3% and a mean deviation of 29.7%. (Mean and average deviation is defined in the Notation and Definitions Chapter). Compared to the microchannel test data of Pettersen et al. (2000), the model gave an average deviation of –1.3% and a mean deviation of 26.3%. In their analysis of the new model, Sun and Groll (2001) believed that their approach was a starting point in the effort to include dry-out effects, which are of great importance in CO_2 flow boiling and generally not taken into account in existing correlations. Further refinements were needed though, since the Ahmad model had an upper limit of x=0.9 for onset of dryout,

and since the Chen correlation did not properly reflect the influence of varying heat flux.

3.1.3 Pressure drop data

In the pressure drop measurements on a 7 mm ID tube of Bredesen et al. (1997), there was little or no influence of varying heat flux at –10°C and 400 $kgm^{-2}s^{-1}$, with a maximum pressure gradient of about 4000 $Pa \cdot m^{-1}$ at a vapour fraction of 0.8. The pressure drop was influenced significantly by varying evaporating temperature, however. Pressure drop data were correlated well by the model of Fuchs (1975).

Rieberer (1998) evaluated pressure-drop correlations in relation to the experimental data of Bredesen et al. (1997), and his own measurements. The friction pressure drop correlation of Friedel (1979) was found to reproduce the pressure drop data of Bredesen et al. (1997) quite well. A homogeneous model was shown to predict too small pressure drop, especially at higher vapour fraction. The correlation of Chawla (1993) was shown to give unrealistic jumps in pressure drop gradient due to change of model from the "homogeneous" regime to the "separated" regime, depending on a Froude-number parameter. The acceleration pressure drop was shown to have only a minor influence compared to the friction pressure loss. Rieberer (1998) also showed excellent correspondence between pressure drop measurements in heat exchangers and predictions using the Friedel (1979) correlation. These data were taken on components in an experimental rig where a small concentration of compressor lubricant was present. Only at the highest evaporating temperature (10°C) and for mass flux below 1000 $kgm^{-2}s^{-1}$ did the Friedel model overpredict the experimental pressure drop data.

3.2 Heat transfer and pressure drop in microchannel flow

3.2.1 Heat transfer data

Results from a few studies on CO_2 heat transfer and pressure drop in microchannel tubes have been reported in the literature. Hihara and Tanaka (2000) conducted measurements on a horizontal stainless steel test tube with 1 mm internal diameter. The tube was heated by direct DC power. Inside tube wall temperatures were found by measuring the outside wall temperatures by T-type thermocouples and then calculating the radial

temperature profile for the given heat flux. The thermocouples were electrically insulated from the tube by a PTFE film. Experiments at varying vapour fraction were conducted at 15°C evaporating temperature, with mass flux and heat flux ranging from 360 to 1440 $kgm^{-2}s^{-1}$ and 9 to 36 kWm^{-2}, respectively. The authors measured very high heat transfer coefficients (10-20 $kWm^{-2}K^{-1}$) in the nucleate boiling regime at low vapour fractions. At the onset of dryout the coefficients dropped abruptly to only a small fraction of the nucleate boiling level. Onset of dryout occurred at a vapour fraction of around 0.8 at a mass flux of 360 $kgm^{-2}s^{-1}$, decreasing to 0.4 at a mass flux of 1440 $kgm^{-2}s^{-1}$. Experimental data from Hihara and Tanaka (2000) are shown in Figure 3.2. The authors believed that the earlier onset of dryout for higher mass flux was unique for carbon dioxide. They further concluded that forced convection did not contribute to the heat transfer since the measured coefficients were independent from mass flux and vapour fraction.

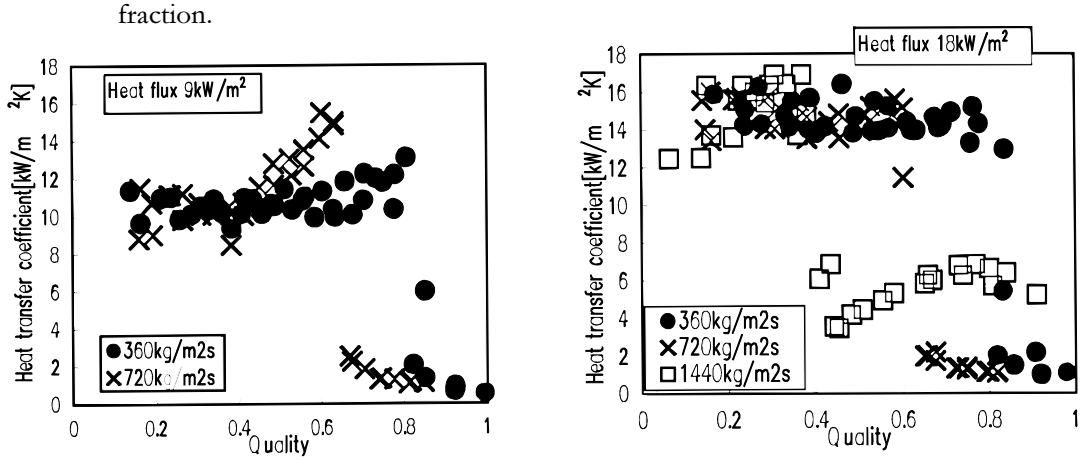

Figure 3.2 *Experimental results on CO_2 heat transfer in microchannel with 1mm diameter at 15°C. Reproduced from Hihara (2000).*

Zhao et al. (2000) conducted experiments on a direct-DC power heated horizontal tube with several parallel microchannels, and T-type thermocouples that measured wall temperatures. The tube width was 28 mm, but the channel dimensions were not reported. Preliminary results were reported for an evaporating temperature of 10°C, an inlet vapour fraction to the test section of 0.05, and in most cases an outlet vapour fraction of 0.30. Mass flux ranged from 250 to 700 $kgm^{-2}s^{-1}$, and heat flux from 8 to 25 kWm^{-2}. Measured heat transfer coefficients were generally around 10 $kWm^{-2}K^{-1}$, and the effects of varying mass flux and heat flux on heat transfer coefficient were negligible. The authors concluded that nucleate boiling dominated over forced convection for CO_2 flow boiling in microchannels. Dryout phenomena were not observed, probably because of the low vapour fraction at the test section outlet.

In a presentation of results from further experiments on the same rig as above, Ohadi, Molki and Zhao (2000) showed CO_2 heat transfer and pressure drop data on microchannel tubes with rectangular and triangular cross sections, with hydraulic diameter of 0.7 and 0.86 mm, respectively. The authors reported problems of achieving uniform distribution of two-phase flow in the inlet of the test tube, and showed how these problems were solved by careful design of the inlet manifold, including a redesigned narrow inlet port normal to the tube axis. Experimental data in rectangular tubes for mass flux 300 $kgm^{-2}s^{-1}$ and heat flux 8.5 kWm^{-2} at 10°C show a heat transfer coefficient of about 12 $kWm^{-2}K^{-1}$ at vapour fractions of 0.2 to 0.5. The coefficient drop to around 7 $kWm^{-2}K^{-1}$ at a vapour fraction of 0.8. Data for triangular tubes show 10-20% lower heat transfer coefficients for low and moderate vapour fractions, and similar level from $x = 0.5$.

Koyama et al. (2001) measured CO_2 heat transfer coefficients in a 1.79 mm ID horizontal stainless steel tube of 771 mm length, using direct DC heating and wall thermocouples. Local fluid pressures/temperatures were not measured, and a calculation scheme was developed to find local refrigerant temperature along the tube. Only a few test data were published, at mass flux 100-260 $kgm^{-2}s^{-1}$, heat flux 4-37 kWm^{-2} and evaporating temperatures 0 and 10°C. The authors tried to correlate their data with a heat transfer model by Yu et al. (1999), but the model generally underpredicted their data, especially at low mass flux. The reason may be that the tested correlation did not account for the dominance of nucleate boiling heat transfer with CO_2.

3.2.2 Correlations for flow vaporization heat transfer of CO_2 in small-diameter tubes

Ohadi, Molki and Zhao (2000) recommended the Liu and Winterton (1991) correlation as a basis for modelling CO_2 microchannel heat transfer in evaporators, and they also proposed a modified flow-boiling correlation on this basis. The modification consisted in adjusting the two-phase convection multiplier by using a different exponent, and multiplying the total heat transfer coefficient from an asymptotic model by a factor of 1.23. Ohadi Molki and Zhao (2000) also found that the model of Kandlikar (1990) could predict their heat transfer measurements reasonably well, and that their pressure drop recordings at low/moderate x could be reproduced by the correlation of Tran et al. (1999).

Hihara and Tanaka (2000) found that a Schrock and Grossmann (1962) model with adapted constants reproduced their experimental data quite

good in the nucleate boiling region, but failed to predict the measured data during dryout and in the post-dryout region.

As already discussed in Section 3.1.2, Sun and Groll (2001) proposed a method of predicting boiling CO_2 heat transfer in microchannel flow, using separate schemes for the pre-dryout, dryout and post-dryout regimes. Their method reproduced the experimental data of Pettersen et al. (2000) and Hihara and Tanaka (2000) reasonably well.

URN:NBN:no-2319

4. Experimental methods

4.1 Chapter overview

The present Chapter starts by discussing some general principles for measurement of heat transfer in tube flow vaporization. Design details of the present heat transfer and pressure drop test rig are shown, and details of the test section and the rig are discussed. Principles for data reduction are shown both for heat transfer and pressure drop measurements. A large part of the Chapter is focused on instrumentation and uncertainty of measurements, and uncertainty data for all test results are found. Finally, the test system for flow pattern observation and visualization is explained, and the principles for capturing images are shown.

4.2 Methods of measuring in-tube evaporation heat transfer

4.2.1 Overview

Principles for measuring in-tube heat transfer for evaporating flow can be categorized based on the method of providing heat load on the test tube. In practice, three different methods can be used:

- *Electric resistance heating*, either by applying a heating foil or a heating wire to the outside of the test tube, or by applying DC or AC power directly to the test tube. In case of a thin-wall tube a constant heat flux boundary condition will result, and the local equilibrium enthalpy and vapour fraction of the fluid in the test tube can be calculated from a simple heat balance. Tubes with

large wall thickness and high material conductivity may approach constant-temperature boundary conditions.

- *Heating by a secondary single-phase fluid*, e.g. water or brine. This will give a varying heat flux and wall temperature along the test tube, and the local vapour fraction along the test section cannot be accurately determined. By installing local wall and fluid temperature sensors along the tube and in the secondary fluid channel, local coefficients can be estimated, although with limited accuracy due to the varying heat flux.

- *Heating by a condensing fluid*. In this case the boundary conditions will be similar to a constant wall temperature situation. Again, the local vapour fraction along the test tube cannot be accurately estimated.

When deciding on method of heat supply, the dilemma is that electric resistance heating can give local measurements along the test tube, but the constant heat flux boundary condition is not quite relevant for evaporators that are heated by a fluid, as in air coolers or water chillers. With constant heat flux conditions, the local tube wall temperature can become quite high in regions of poor heat transfer, a situation that is physically impossible in fluid-heated heat exchangers. In reality, most evaporators in refrigerating, heat pump and air conditioning applications will have a local heat flux that is determined by local heat transfer coefficient and local temperature difference between cooled fluid and refrigerant. The local heat flux conditions are of particular importance when studying boiling crisis phenomena and post-dryout heat transfer, where constant heat flux may give wall temperature excursions that cannot occur with fluid heating. Thome (1998) strongly advised against using electrical heating at high x with partial dryout of annular flow, and instead recommended a combination of fluid heating and local thermocouples to measure local wall temperature and hot fluid temperature.

With electric resistance heating, the inside tube wall temperature must be determined in order to find the local temperature difference in Eq. (2.1). With fluid heating, there is a choice between measuring local tube wall temperature, or using a calculation scheme to separate the measured overall heat transfer coefficient into a refrigerant-side coefficient and a heating-fluid side coefficient (including wall resistance and fouling).

The discussion of test rig principles thus becomes a matter of choosing the heating method, and deciding between using local tube wall surface temperature measurement or a scheme to find refrigerant-side heat transfer from overall heat transfer.

4.2.2 Discussion and choice of test rig principles

In the present study, the circular cross-section of the test tube and its internal diameter of approximately 0.8 mm were regarded as given parameters, based on extruded tubing that had been produced for prototype CO_2 heat exchangers (Pettersen et al., 1998). Even though smaller tube diameters could have been manufactured, this size seemed to be a reasonable compromise between high heat transfer efficiency, reduced heat exchanger size and mass on the one side, and practical concerns in real systems such as clogging (in operation or during production/brazing), cost of production, and tolerance requirements on the other side. There was a choice between using one single test tube, and using a multi-channel extruded tube, however. A single tube would have required extreme care in the heat balance, since the heat load would have been quite small. Also, the material and surface properties may not have been representative to the conditions in an extruded aluminium tube that would be used in real heat exchangers. It was therefore decided to use a multi-channel extruded aluminium test tube, of the same type as in prototype heat exchangers.

With this type of test tube geometry, it would be quite difficult to obtain accurate and representative measurements of tube wall temperatures. Owing to the geometry of the multi-channel tube, the temperature profile in the tube wall would be rather complex. One possibility would be to apply inverse methods to calculate the two-dimensional temperature field in the tube wall, but this would still rely on very accurate and very accurately located temperature sensors. Owing to the small dimensions of the test tube, this was not regarded as a practical possibility.

The following example may give an idea about the numbers involved: A heat flux of 10 kWm^{-2} and a heat transfer coefficient of 20,000 $Wm^{-2}K^{-1}$ would give a temperature difference between tube wall and refrigerant of 0.5 K. With a total uncertainty in tube surface temperature of ± 0.2 K [f], this would give an interval for the heat transfer coefficient ranging from 14,300 $Wm^{-2}K^{-1}$ (-29%) to 33,300 $Wm^{-2}K^{-1}$ (+67%). On average, this gives an uncertainty of $\pm 47.5\%$. Earlier experiments (Bredesen et al., 1997) had shown that even with a simple round tube geometry and larger dimensions (7 mm ID) the accurate measurement of wall temperature was very difficult.

Based on the desire for relevant heat flux conditions, relevant tube geometry, relevant tube surface properties, and acceptable measurement accuracy, it was thus concluded that the present tests had to rely on

[f] Including the whole measurement chain, as well as uncertainties in estimation of inner surface temperature based on an externally measured temperature.

measuring the overall heat transfer coefficient for the test tube, and then using test rig calibration and a calculation scheme to find the refrigerant-side coefficient. These calibration and regression principles, often called "Wilson Plot Methods" are discussed in Chapter 5.

4.3 Heat transfer and pressure drop test rig

This Section gives an overview of the laboratory test rig for measuring vaporization heat transfer and pressure drop data of CO_2 in the microchannel tube.

4.3.1 Overview

The test rig consisted of three main parts:

- Refrigerant (CO_2) circuit,
- test section, and
- heating fluid (water) circuit.

Figure 4.1 shows a flow chart of the complete test rig, including a list of components and their positions.

Refrigerant circulation was maintained by a pump (1) that was fed from a receiver (7) through a heat exchanger (8). The purpose of the heat exchanger (8) was to maintain subcooled liquid state (approximately 3-5 K) at the pump inlet, thus avoiding flashing and/or cavitation in the pump. A separate cooling circuit was connected at position "c/d" in order to absorb heat from the liquid refrigerant. Pressurized liquid from the pump flowed through a filter (2) and a refrigerant mass flow meter (3), before reaching a preheater (4). In the preheater, the desired inlet vapour fraction or inlet enthalpy to the test section (9) was adjusted by regulating the amount of electric power supplied. The refrigerant leaving the test section (9) entered a condenser (6) where the vapour was condensed. A separate cooling system was connected at position "e/f" to remove heat from the condenser. Liquid from the condenser was then led back to the receiver, thus completing the circuit. The refrigerant charge had to be chosen in such a way that during the tests, a liquid level could be maintained in the receiver, i.e. the refrigerant left the condenser in a saturated liquid state. Refrigerant was charged through connection "a".

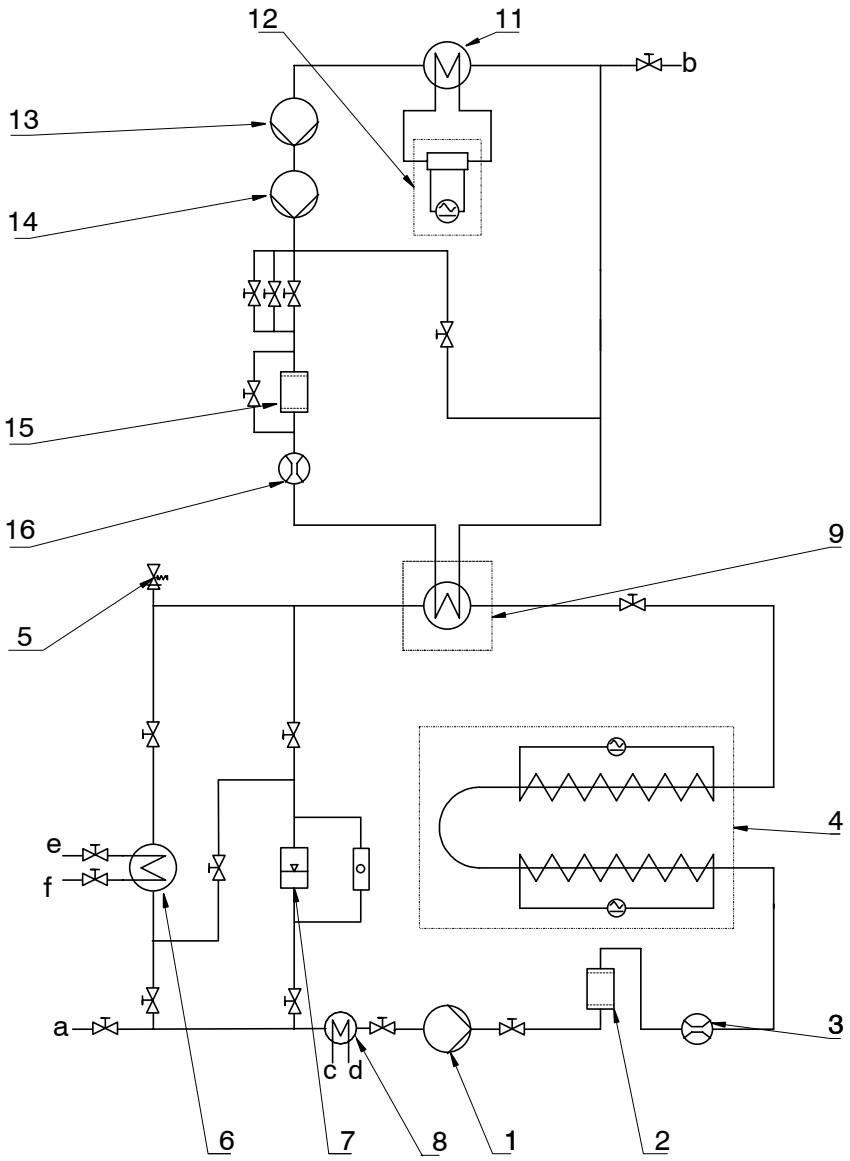

Refrigerant circuit:
1 Refrigerant pump
2 Refrigerant filter
3 Refrigerant mass flow meter
4 Pre-heater
5 Safety valve (102 bar)
6 Refrigerant cooler
7 Refrigerant receiver with sight glass
8 'Sub-cooler'

Test section:
9 Test section

Water circuit:
11 Water tank with heat exchanger
12 Water heater (Type HAAKE)
13 Main water pump
14 Booster water pump
15 Water filter
16 Water mass flow meter

Supply lines:
a Refrigerant charge
b Water charge
c City water inlet
d City water outlet

Figure 4.1
Flow circuit and components list of the heat transfer and pressure drop test rig

Figure 4.2 shows the measurement points of the refrigerant (CO_2) circuit, which included a Coriolis-type mass flow meter (M_{CO2}), pressure and temperature measurements at the preheater inlet (p_1, T_1), temperature and pressure at the test section inlet (T_3, p_2), temperature at the test section outlet (T_4), and pressure drop across the test section (Δp). In addition to these data, which were sampled by a logger, observations were made of the temperature between the two preheater sections, as well as the secondary coolant temperatures (at c/d and e/f).

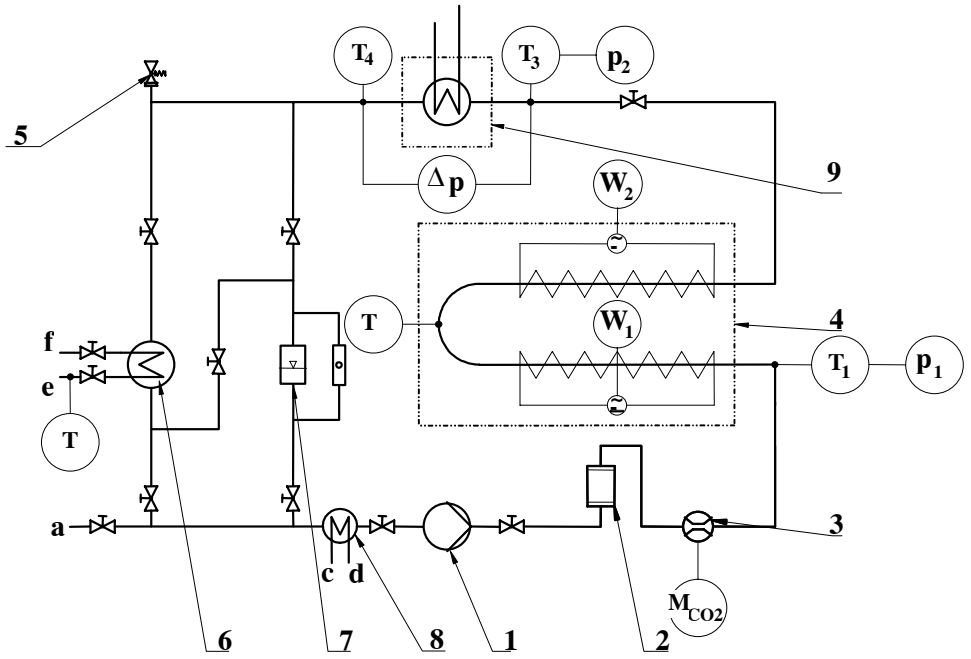

Figure 4.2 *Refrigerant (CO_2) circuit with instrumentation locations*

The heating fluid (water) circuit with the measurement points is shown in Figure 4.3. After exiting the test section (9) the cooled water flowed to a tank (11) containing a heat exchanger that was connected to a water heater of the type Haake (12). Water supply temperature to the test section was adjusted by regulating the heat transfer in the tank (11). Two centrifugal pumps (13 and 14) circulated the water through the circuit. The water flow rate could be regulated by varying the opening of the bypasses.

The mass flow rate of water (M_{H2O}) was measured with a Coriolis-type mass flow meter (16) that was installed after the pumps (13,14), and after a filter (15). Temperatures at the test section inlet (T_6, T_9) and outlet (T_8, T_{10}) were logged, and pressures at the test section inlet and outlet were observed.

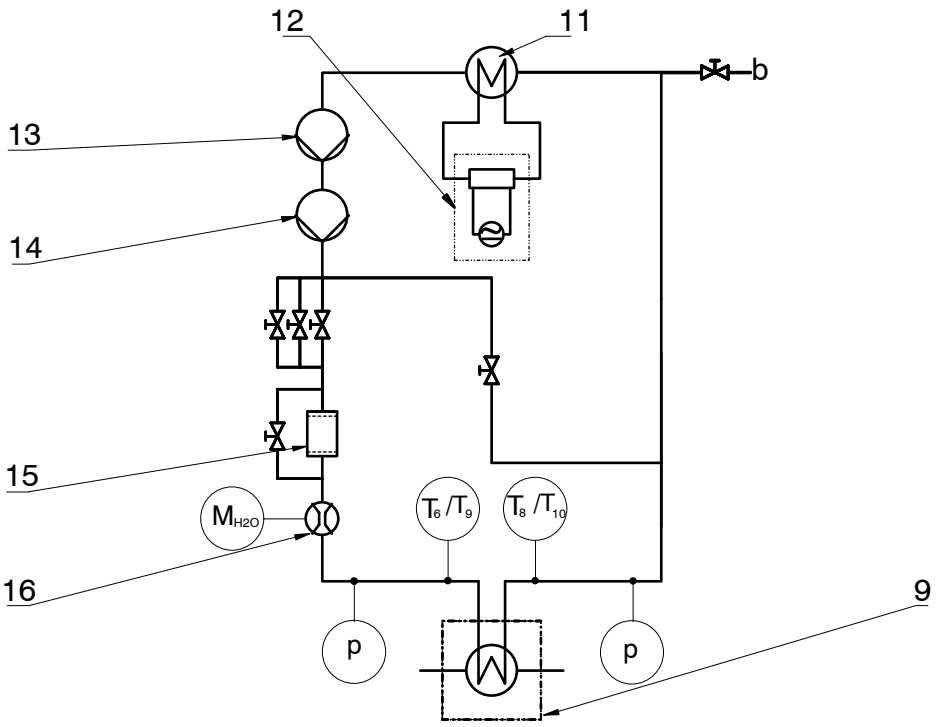

Figure 4.3 *Heating fluid (water) circuit with measurement points*

4.4 Test Rig Components

4.4.1 Test Section

The microchannel tube had a length of 540 mm and was brazed into manifolds on both ends. The cross-section of the tube can be seen in Figure 4.4. The tube was an externally zinc-coated aluminium "multiport" tube having 25 round ports with an average diameter of 0.81 mm (manufactured by Hydro Aluminum Adrian). Some additional data on the test tube are shown in Table 4.1

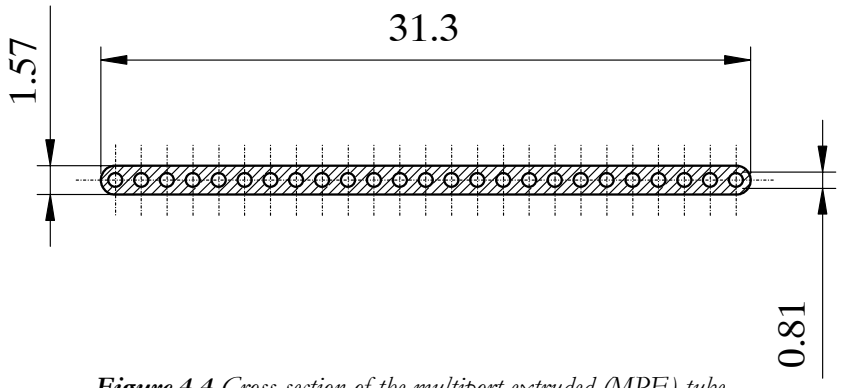

Figure 4.4 *Cross-section of the multiport extruded (MPE) tube*

Table 4.1 *Test section data*

CO_2 flowchannel diameter	0.81 ±0.03	mm
CO_2 flowchannel roughness (assumed)	10^{-6}	m
Internal heat transfer area (25 ports)	$0.03202 \pm 3.96 \cdot 10^{-4}$	m^2
CO_2 flow cross-section (25 ports)	$1.2882 \cdot 10^{-5} \pm 3.18 \cdot 10^{-7}$	m^2
Length of extruded tube	540 ±0.5	mm
Length of heated part of tube	503.4	mm
Internal diameter of CO_2 manifold	7	mm

The nominal diameter of the microchannels was 0.79 mm, based on tube production drawings. The actual diameter was determined from measurements on enlarged photos of tube cross-sections. Measurements on a total of eight channels from random positions across the width of the tube gave an average diameter of 0.81 mm, with a variation of ±0.03 mm (several measurements were made of each port, in different directions). A typical view of the actual microchannel geometry is shown in Figure 4.5. As may be observed from the photo, there was quite some variation in diameter and roundness of the channels. The scale in the lower right corner is 1 mm.

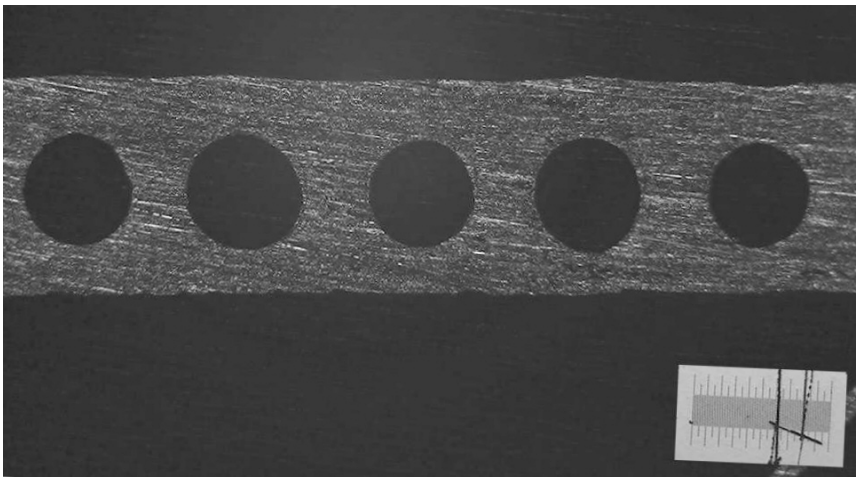

Figure 4.5 *Enlarged photo of tube cross-section (1mm scale in lower right corner of photo)*

Even though there was variation between the individual channels, the average diameter is considered as representative of the tube geometry. The present tests are based on results for flow in all channels simultaneously, and it does not make sense to consider the effects of individual variation in diameter between the channels. In the uncertainty analysis in Section 4.7, the channel diameter is thus regarded as defined within the uncertainty of measurement for one individual channel, estimated at ± 0.01 mm.

The test tube was placed inside a jacket that had flow-channels for the water. These channels, each having a semicircular cross-section, led the water in a "spiral" flow around the test tube, at a pitch of 16.5°. A photograph of the tube placed in the (opened) jacket is shown in Figure 4.6, and Figure 4.7 shows the pattern of the water channels. The jacket was manufactured from PTFE (Teflon), and its outside was insulated with 25 mm polystyrene (Styrofoam).

When deciding on the length of the test section, there were some conflicting requirements due to need for accuracy of measurement (Munkejord, 1997). A long test section was desired in order to increase heat load and water-side temperature change between inlet and outlet. A larger temperature difference here would give a more accurate heat load measurement[g]. On the other hand, a too long test section with large surface area would give less sensitivity in temperatures to changes in overall heat transfer coefficient *U*. Also, the vapour fraction would change significantly in the section, thereby making the test data less "local". Finally, the test section length should not be too far from the tube length in actual heat exchangers. Munkejord (1997) concluded that the test section should not be longer than 0.7 m.

[g] This restriction can be removed by measuring the load elsewhere, either as electric power supply, or in a separate heat exchanger as pointed out by Garimella and Bandhauer (2001)

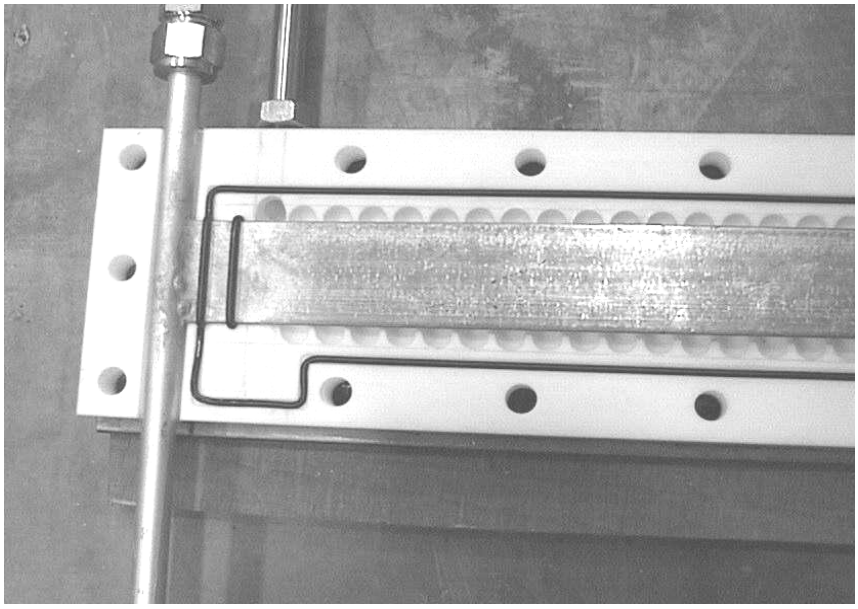

Figure 4.6 *The microchannel test tube with manifold (left), positioned in the lower part of the jacket. Water inlet is at the upper left, and water channels are milled in the jacket at a pitch of 16.5°*

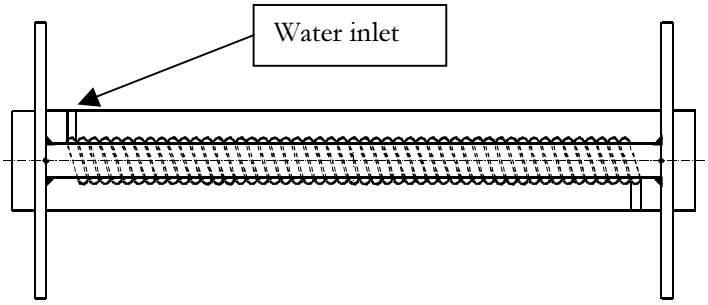

Figure 4.7 *Principle of water channel around test tube*

Another concern in the test section design was the water channel dimensions and layout. Again, there were conflicting requirements because high water flow velocity and large channel diameter were needed to have turbulent Reynolds numbers; while the accurate measurement of transferred heat relied on large temperature change, which meant smaller water flow rate. The resulting design of the water jacket had small flow-channels that led the water in a helical orientation around the test tube, with the water flow split on two parallel channels. Figure 4.8 shows the design of the water

channel cross-section, with one water channel above and one below the test tube, shown by the hatched area. The dimensions and geometry parameters are listed in Table 4.2. Temperature sensors were located in the water inlets and water outlets to/from the jacket.

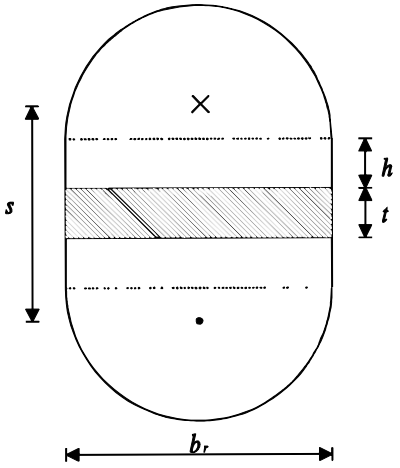

Figure 4.8 *Cross-section of water channels. Hatched area with height* ***t*** *represents the test tube.*

Table 4.2 *Water channel geometry data*

h	Height of rectangular part	0.75 ±0.05	mm
b_r	Diameter of circular part	8.0 ±0.1	mm
A_f	Flow area in one channel[(a)]	$3.11 \cdot 10^{-5}$ $\pm 1.6 \cdot 10^{-6}$	m^2
D	Hydraulic diameter	5.64 ±0.1	mm

(a): Water flows in two channels in parallel

4.4.2 Preheater

The preheater (4) consisted of two stainless-steel tube-in-tube sections connected in series, where CO_2 flowed inside the 22 mm OD inner tube, and a bifilar heating wire was wrapped on the outside. The heating wires were then jacketed by a 38 mm OD outer tube, and the preheater unit was wrapped in thermal insulation.

4.4.3 Refrigerant condenser

The refrigerant condenser (6) was a coaxial tube-in-tube heat exchanger with an ID/OD 7/10 mm inner tube and a ID/OD 16/20 mm outer tube. A 2 mm wire was spun with 100 mm pitch on the inner tube in order to

maintain a spacing in the annulus. The total length of the heat exchanger was about 40 m, which was coiled into a unit with diameter 450 mm.

4.4.4 Refrigerant Pump

The refrigerant pump (1) was a gear pump of the type MICROPUMP 219. By controlling the voltage (0 to 24 V DC) it was possible to vary the number of revolutions between 0 and 3,000 rpm. The maximum capacity of the pump was 2.5 liter per minute, and the maximum pressure differential was 0.4 MPa.

4.4.5 Water Pumps

The main pump (13)) was a centrifugal pump of the type GRUNDFOS CHI 4-60 with a capacity of 10 liter per minute at 0.6 MPa pressure differential. It was driven by a 220 V AC motor.

During the test section calibration and some experiments it was necessary to vary the coolant (water) flow rate in a wide range. In the high end of the range a large pressure drop had to be overcome. Therefore a 'booster' pump was needed (14). This pump was a centrifugal pump of the type GRUNDFOS CH 2-50 with a capacity of 10 liter per minute at 0.4 MPa pressure differential. It was connected in series to the main pump. This pump was only used when high water flow rates were required.

4.5 Instrumentation

This Section describes the instrumentation and measurement equipment in the heat transfer and pressure drop test rig. During the tests it was necessary to measure temperatures, pressures, mass flow rates, and electrical power input. All these data were logged and processed. Table 4.3 gives an overview of the instruments used and their uncertainty, with reference to the locations shown in Figures 4.2 and 4.3. Instrument uncertainties are based on calibration data or manufacturer data, and include uncertainty of the sensor, logger and reference (e.g. ice point for thermocouple and atmospheric pressure for gauge pressure sensors).

Table 4.3 *Heat transfer and pressure drop test rig instrumentation summary*

Location	Spreadsheet name	Fig 4.2 and 4.3	Type of instrument	Uncertainty (2σ)
Electric power, lower preheat section,	P_el,l:	W_1	Watt transducer, LWT-24-A1-H	±20 W
Electric power, upper preheat section,	P_el,u:	W_2	Watt transducer, LWT-24-A1-H	±20 W
CO_2 temperature, preheat section inlet,	T_CO2,ips:	T_1	Thermocouple type T, 0.07 mm	±0.015 K
CO_2 temperature, test section inlet,	T_CO2,its:	T_3	Pt100, H&B Sensors Ltd.	±0.064 K
CO_2 temperature, test section outlet	T_CO2,ots:	T_4	Pt100, H&B Sensors Ltd.	±0.064
CO_2 pressure, preheat section inlet	p_CO2,ips:	p_1	Gauge pressure transmitter, Honeywell	± 12.4 kPa
CO_2 pressure, test section inlet	p_CO2,its:	p_2	Gauge pressure transmitter, Honeywell	± 12.4 kPa
CO_2 pressure drop across test section,	dp_CO2,ts:	Δp	Differential pressure transducer, Honeywell	±1.0 kPa
Water temp., lower test section inlet	T_H2O,il:	T_6	Pt100, H&B Sensors Ltd.	±0.064 K
Water temp., lower test section outlet	T_H2O,ol:	T_8	Pt100, H&B Sensors Ltd.	±0.064 K
Water temp., upper test section inlet	T_H2O,iu:	T_9	Pt100, H&B Sensors Ltd.	±0.064 K
Water temp.. upper test section outlet	T_H2O,ou:	T_{10}	Pt100, H&B Sensors Ltd.	±0.064 K
Mass flow of CO_2	M_CO2:	M_1	Coriolis type, Danfoss	±0.00003 kg/s
Water mass flow	M_H2O:	M_2	Coriolis type, Rheonik	±0.2% of reading

Even though the directly measured test data were calculated as averages of 20-30 samplings, the result was regarded as single-sample. According to ASHRAE (1986), a repeated reading with the same procedure and equipment does not provide a multi-sample result. The uncertainties in Table 4.3 represent $\pm 2\sigma$, i.e. with a confidence level of 95%. Combined uncertainties are calculated based on the individual uncertainties using root-sum-square addition (Moffat, 1988).

4.5.1 Temperature

Two different methods were used to measure temperature. The preheater section inlet temperature was measured with a thermocouple, and the temperatures in the test section were measured with calibrated platinum resistance (Pt100) sensors from H&B Sensors Ltd. The thermocouple was of the type T, i.e. Copper (Cu) / Constantan (CuNi). The reference

temperature was given by crushed ice. Measurement uncertainties for the Pt100 sensors in Table 4.3 include the sensor, measurement bridge, and thermometer. The temperature sensors on the CO_2 inlet and outlet of the test section were mainly used during calibration tests (See Chapter 5), since CO_2 temperature was determined by pressure in the evaporation tests.

4.5.2 Pressure

The test section CO_2 inlet and outlet pressures were measured with pressure transducers of the type Honeywell STA3000 (gauge = pressure over atmospheric pressure). The atmospheric pressure in the laboratory was added to obtain absolute pressure. The refrigerant pressure difference between test section inlet and outlet was measured with a Honeywell STD924 differential pressure transducer. All pressure transducers were calibrated to the accuracy shown in Table 4.3 (including uncertainty in reference and logger uncertainties). Manometers were connected to the water inlet and outlet to determine the pressure on the water-side along the test section.

4.5.3 Mass Flow

Refrigerant mass flow rate was measured with a Coriolis-type Danfoss MASS 2100 sensor connected to a Danfoss MASS 3000 signal converter. The manufacturer specified the uncertainty to ±0.15% of full scale.

Water mass flow rate was also measured with a Coriolis-type mass flow meter, but in this case the sensor was a Rheonik RHM 04 GNT connected to a Rheonik RHE 08 signal converter. The manufacturer specified the accuracy for a measurement range of 1:20 to ±0.2 % of reading.

4.5.4 Electric Power

The electrical power supply to the pre-heat section was regulated by two variable resistances (Variacs) and displayed on two Elcontrol VIPD watt transducers. Two L-Unit LWT-24-A1-H watt transducers provided the logged signals.

4.5.5 Data Logging and Processing

Data from thermocouple, pressure transducers, mass flow meters and watt transducers were processed and logged by a KEITHLEY 7001 Switch System and a KEITHLEY 2010 Multimeter. The switcher changed between the different input channels, while the multimeter measured the voltage, digitised it, and transferred the result to a PC.

The KEITHLEY data logger was not capable of measuring with Pt100-elements. Therefore an Automatic System Laboratories (ASL) F250 MK II Precision Thermometer was used combined with a ASL SB250 Multichannel switch box.

The PC processed the data by a computer program that converted the data to values with physical units. The data could also be shown as graphs on the computer screen. At the same time the program wrote data to a file that could be processed by other programs.

After the measurement, these data files could be analysed in spreadsheets. The thermodynamic and transport properties of carbon dioxide and water were supplied by the libraries *xlco2lib.dll* and *h2oprop_p.xls*, respectively. The library *xlco2lib.dll* is an implementation of the IUPAC thermodynamic equations of state for CO_2 (Angus et al., 1986), with improvements by Pitzer and Schreiber (1988). The transport properties were taken from Vesovic et al. (1990).

4.6 Data reduction

4.6.1 Heat transfer measurements

The data from each experiment at a given nominal refrigerant mass flux, heat flux, evaporating temperature, and mean vapour fraction were processed in a PC spreadsheet as explained above. In addition to actual measured data for the nominal test parameters, the following main results were the basis for the data reduction in the spreadsheet:

- Net heat supply from water to CO_2 in the test section
- Water inlet and outlet temperatures and pressures
- Water mass flow rate
- CO_2 inlet and outlet pressure in test section

- CO_2 inlet enthalpy to the test section
- CO_2 mass flow rate

A key result that was desired from each experiment was the mean overall heat transfer coefficient (U) for the test section. The refrigerant-side heat transfer coefficient (h_i) was determined based on this value, using the techniques described in Chapter 5.

In principle U could have been calculated based on the logarithmic mean temperature difference between water and refrigerant in the test section, but this would have required constant evaporating temperature and constant water properties. In reality, the evaporating temperature changed through the test section due to pressure drop, and the water properties were not constant due to temperature and pressure change. Earlier tests had shown that pressure changes on the water side were in fact large enough to influence the water enthalpy significantly. The determination of U was therefore based on a procedure where the test section numerically was divided into N=60 elements having equal heat load, i.e. unequal length. Each cell was regarded as small enough to have approximately constant CO_2 temperature and constant water properties. The choice of 60 cells was based on convergence studies made by Tang (1998), who showed that U was almost constant for $N > 60$.

The following approach was then used. Local refrigerant pressure was assumed to drop linearly with exchanged heat along the test section, from the inlet of the heated part of the section to the outlet of the heated part. These pressures were found based on measured inlet and outlet pressures in the test section manifolds, as outlined in Section 4.6.2. Based on the pressure profile, a corresponding saturation temperature profile inside the test section could be found. A similar approach was used on the water side, thereby obtaining local water pressures. On this basis, the local CO_2 and water temperatures at the inlet and outlet of each cell could be estimated based on a heat balance on the cell. Thus, the logarithmic mean temperature difference $\Delta T_{lm,n}$ could be calculated for each cell. From the heat balance of cell n it is known that

$$\frac{\dot{Q}_n}{\Delta T_{lm,n}} = U_n A_{i,n} \tag{4.1}$$

where $\dot{Q}_n$ is the heat load and U_n is the overall heat transfer coefficient in cell n, and $A_{i,n}$ is the refrigerant-side heat transfer area in cell n. The heat load $\dot{Q}_n$ could be calculated as the total exchanged heat divided by the

number of cells. Now, with $\dot{Q}_n$ and $\Delta T_{lm,n}$ known for each cell, the overall heat transfer coefficient U for the entire test section could be calculated as

$$U = \frac{1}{A_i}\sum_{n=1}^{N} U_n A_{i,n} = \frac{1}{A_i}\sum_{n=1}^{N} \frac{\dot{Q}_n}{\Delta T_{lm,n}} \tag{4.2}$$

where N was the total number of cells. It was inherent in the design of the experiment that the overall heat transfer coefficient U was assumed to be constant, and equal in all cells. Apart from experiments with very large difference in x from inlet to outlet, and tests with dryout inside the test section, this assumption holds reasonably well. In the absence of local data inside the test section, the above method is in fact the only viable solution in order to account for temperature- and pressure variation along the test section. The alternative would be to ignore these effects and use an overall logarithmic temperature difference (Olson, 2000), but this would introduce considerably larger errors in the measurement of "local" heat transfer coefficient.

With U known, the CO_2-side area $\Delta A_{i,n}$ and length ΔL_n of each cell could be calculated as

$$\Delta A_{i,n} = \frac{\dot{Q}_n}{U_n \cdot \Delta T_{lm,n}} \quad \text{and} \tag{4.3}$$

$$\Delta L_n = \frac{\Delta A_{i,n}}{\pi \cdot D \cdot Z} \tag{4.4}$$

where D is the diameter of a flowchannel (0.81 mm) and Z is the number of parallel flowchannels (25).

On this basis, the mean refrigerant temperature $\overline{T_i}$ (evaporating temperature) and the mean vapour fraction $\bar{x}$ could be calculated as

$$\overline{T_i} = \frac{1}{L}\sum_{n=1}^{N} T_{i,n}(p_n) \cdot \Delta L_n \quad \text{and} \tag{4.5}$$

$$\bar{x} = \frac{1}{L}\sum_{n=1}^{N} x_n \cdot \Delta L_n \tag{4.6}$$

where $T_{i,n}(p_n)$ is the saturation temperature at the local pressure in cell n. The local vapour fraction in cell n, x_n is calculated as a function of local refrigerant enthalpy and temperature in the cell. Local enthalpy is a linear function of the cell number, since every cell has the same heat load. Also the pressure is a linear function from the inlet to the outlet.

For the sake of simplicity, the symbols T and x are used in the report to represent the results from Equations (4.5) and (4.6). Furthermore, the heat flux q is taken as the total heat transfer rate divided by the internal (refrigerant-side) heat transfer area.

4.6.2 Pressure-drop measurements

The test section design allowed only the measurement of the total pressure drop between the inlet and outlet manifold, and a few corrections thus had to be made in order to find the pressure drop along the part of the tube being heated. Figure 4.9 shows how the heated part (where there are water channels) does not cover the entire length of the tube. The Figure also illustrates the principles of the pressure drop measurement and the necessary corrections.

While flowing from the manifold into the MPE tube – consisting of 25 parallel ports - a sudden flow-area contraction occurs to the refrigerant. This leads to a pressure drop at the inlet. At the outlet of the MPE tube the opposite effect occurs where the expansion leads to a pressure rise. Calculation models for sudden enlargements and contractions in two-phase flow are given by Collier and Thome (1994).

The pressure drop due to a sudden contraction in separated flow was modelled as

$$\Delta p_{i,c} = \left(\frac{G}{C_c}\right)^2 \cdot (1 - C_c) \cdot \left\{ \frac{(1 + C_c) \cdot \left(\frac{x^3 \cdot v_v^{\,2}}{\alpha^2} + \frac{(1-x)^3 \cdot v_l^{\,2}}{(1-\alpha)^2} \right)}{2 \cdot [x \cdot v_v + (1-x) \cdot v_l]} - C_c \cdot \left(\frac{x^2 \cdot v_v}{\alpha} + \frac{(1-x)^2 \cdot v_l}{(1-\alpha)} \right) \right\} \tag{4.7}$$

and the pressure rise due to a sudden enlargement (assuming constant void fraction) as

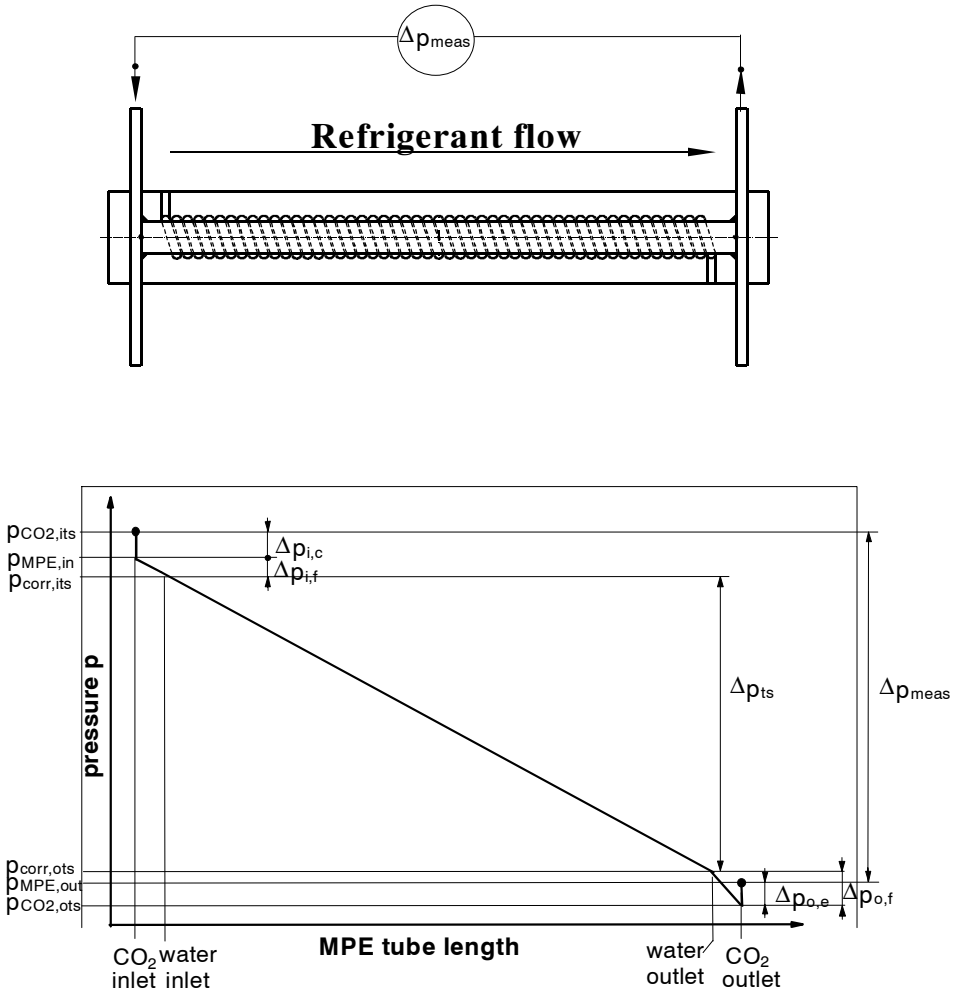

Figure 4.9 *Sketch of the test tube (with water channels) and refrigerant pressure along the tube (simplified)*

$$\Delta p_{o,e} = G^2 \cdot \sigma \cdot (1-\sigma) \cdot v_l \cdot \left\{ \frac{(1-x)^2}{(1-\alpha)} + \left(\frac{v_v}{v_l} \right) \cdot \frac{x^2}{\alpha} \right\} \tag{4.8}$$

Here, G is the refrigerant mass flux in the flowchannels, and σ is the ratio of the total flowchannel area ($A_{p,tot}$) to the front area (A_{fr}) of the tube. For the present test tube, this ratio was

$$\sigma = \frac{A_{p,tot}}{A_{fr}} = 0.28 \tag{4.9}$$

The coefficient of contraction C_c depends on the contraction ratio defined by equation (4.9) Based on data for turbulent single-phase flow reproduced from Perry's (1963) by Collier and Thome (1994), the coefficient was estimated to

$$C_c \cong 0.6 \tag{4.10}$$

The void fraction (α) was estimated based on the model of Zivi (1964):

$$\alpha = \left[1 + \frac{1-x}{x} \cdot \left(\frac{\rho_v}{\rho_l} \right)^{\frac{2}{3}} \right]^{-1} \tag{4.11}$$

The refrigerant also flows through two 18.3 mm short sections at the ends of the heat transfer tube where no heat is transferred. The frictional pressure drop in these adiabatic parts of the tube was estimated by means of the Blasius single-phase friction factor

$$f = \frac{0.3164}{Re^{0.25}} \tag{4.12}$$

and an equivalent mass flux (G_{eq}) to account for two-phase flow, as proposed by Akers et al. (1959):

$$G_{eq} = G \cdot \left\{ (1-x) + x \cdot \left(\frac{\rho_l}{\rho_v} \right)^{\frac{1}{2}} \right\} \tag{4.13}$$

With these equations the 'adiabatic' pressure drop at the inlet ($\Delta p_{i,f}$) and at the outlet ($\Delta p_{o,f}$) could be calculated. Pressures were measured in the inlet and outlet manifolds, and any local pressure drops in the manifolds were neglected.

Finally, the net pressure drop in the heat transferring length of the test section (Δp_{ts}) could be calculated as:

$$\Delta p_{ts} = \Delta p_{meas} - \Delta p_{i,c} - \Delta p_{i,f} - \Delta p_{o,f} + \Delta p_{o,e} \tag{4.14}$$

Note that because of the horizontal installation of the test tube, there was no influence of gravity.

Finally, the frictional pressure drop in the heated part of the test section was found by subtracting the acceleration pressure drop from the above result. Acceleration pressure drop was estimated using Eq. (2.67), which over the change in vapour fraction x and void fraction α in the test section becomes

$$\Delta p_{ts,fric} = \Delta p_{ts} - G^2\left[\frac{x_2^2}{\alpha_2\rho_v} + \frac{(1-x_2)^2}{(1-\alpha_2)\rho_l} - \frac{x_1^2}{\alpha_1\rho_v} - \frac{(1-x_1)^2}{(1-\alpha_1)\rho_l}\right] \tag{4.15}$$

where index 1 and 2 indicates inlet and outlet of heated part of test tube, and the liquid and vapour density were assumed to be constant. The local void fraction was estimated using Eq. (4.11).

Finally, the pressure drop was found as:

$$\frac{dp}{dz} = -\frac{\Delta p_{ts,fric}}{L} \quad \text{Pa·m}^{-1} \tag{4.16}$$

where L is the heated length of the test tube, i.e. 0.5034 m.

4.7 Uncertainty analysis

4.7.1 General

Key results from the present study are refrigerant-side heat transfer coefficients, and refrigerant-side pressure drops. The CO_2 heat transfer coefficient (h_i) was determined based on a procedure for separating the overall heat transfer resistance ($1/U$) into its internal and external

components. Details of this procedure and the resulting uncertainty in h_i are presented in Chapter 5. In the present chapter, the uncertainty in U is found, as well as the uncertainty of the pressure drop (dp/dz) measurements. Uncertainties of other parameters that are included in the results or used in further processing of data are also needed. These parameters include the evaporating temperature (T), the refrigerant mass flux (G), the heat flux (q), the vapour fraction (x), and the water-side Reynolds and Prandtl numbers.

4.7.2 Principles of uncertainty analysis

Uncertainty δR in a computed result (R) can be estimated using propagation analysis, i.e. a root-sum-square combination of the effects of the individual parameters (Moffat, 1988):

$$\delta R = \left[\sum_{i=1}^{N} \left(\frac{\partial R}{\partial X_i} \delta X_i \right)^2 \right]^{1/2} \tag{4.17}$$

Here, δX_i is the uncertainty in the variable X_i, and the result R is calculated from a set of measurements using algorithms represented by

$$R = R(X_1, X_2, X_3, ..., X_N) \tag{4.18}$$

where $X_1..X_N$ are independent variables. The partial derivative is the *sensitivity coefficient* for the result R with respect to the measurement X_i. Each term in Eq. (4.17) represents the contribution made by the uncertainty in one variable (δX_i) to the overall uncertainty in the result (δR). Equation (4.17) applies as long as

1. Each of the measurements was independent
2. Repeated observations of each measurement, if made, would display Gaussian distributions
3. The uncertainty in each measurement was initially expressed with the same confidence

The validity of the first two assumptions is commented in the following text. All uncertainty data are discussed based on a confidence level of 95%

4.7.3 Uncertainty in evaporating temperature

The evaporating temperature T was based on pressure measurement at the test section inlet and pressure differential across the section. Compared to the uncertainty in the absolute pressure measurement, the uncertainty of differential pressure measurement is negligible. Temperature uncertainty is therefore calculated from the uncertainty in absolute pressure measurement:

$$\delta T = \left(\frac{\partial T}{\partial p} \right)_{sat} \delta p \tag{4.19}$$

From Table 4.3, the uncertainty in pressure measurement (δp with 95% confidence) was ±12.4 kPa. Owing to the non-linear saturation pressure curve, this uncertainty has a varying effect at different temperatures. Table 4.4 shows the uncertainties in T at the temperature levels used in the present tests.

Table 4.4 *Uncertainty in evaporating temperature*

T, °C	0	10	20	25
δT, K	±0.13	±0.11	±0.09	±0.08

4.7.4 Uncertainty in water temperatures

Water inlet and outlet temperatures were used to find the heat transfer rate in the test section, as well as the mean water temperature. The latter was needed in the determination of overall heat transfer coefficient U, and in the calculation of water Reynolds and Prandtl numbers.

From Table 4.3, the uncertainty of individual water temperature measurements was δT_i = ±0.064 K. Two independent sensors measured the test section inlet and outlet water temperature, respectively, and the average value at the inlet and outlet was used in further calculations. Thus, the uncertainty was improved compared to single measurements. Inlet and outlet water temperature was therefore measured with an uncertainty of

$$\delta T = \left[2\left(\frac{1}{2} \delta T_i \right)^2 \right]^{1/2} = \frac{1}{\sqrt{2}} \delta T_i = \pm 0.045 \text{ K} \tag{4.20}$$

The validity of this assumption may be discussed, since the water flow was split before the inlet measurement, and joined after the outlet temperature measurement. Thus, the inlet measurement is based on two independent measurements of the same parameter, but it may be argued that the average outlet temperature is instead based on two different physical locations. In order to assess the above assumptions, some data were extracted from a randomly chosen experiment at T=10°C, G=370 kgm^{-2}s^{-1}, q=10 kWm^{-2}, and x=0.57. Figure 4.10 shows an example of the frequency of measured water temperatures into and out of the test section, in a test with 26 measurements over a period of 26 minutes. Temperature bins of 0.01 K were used.

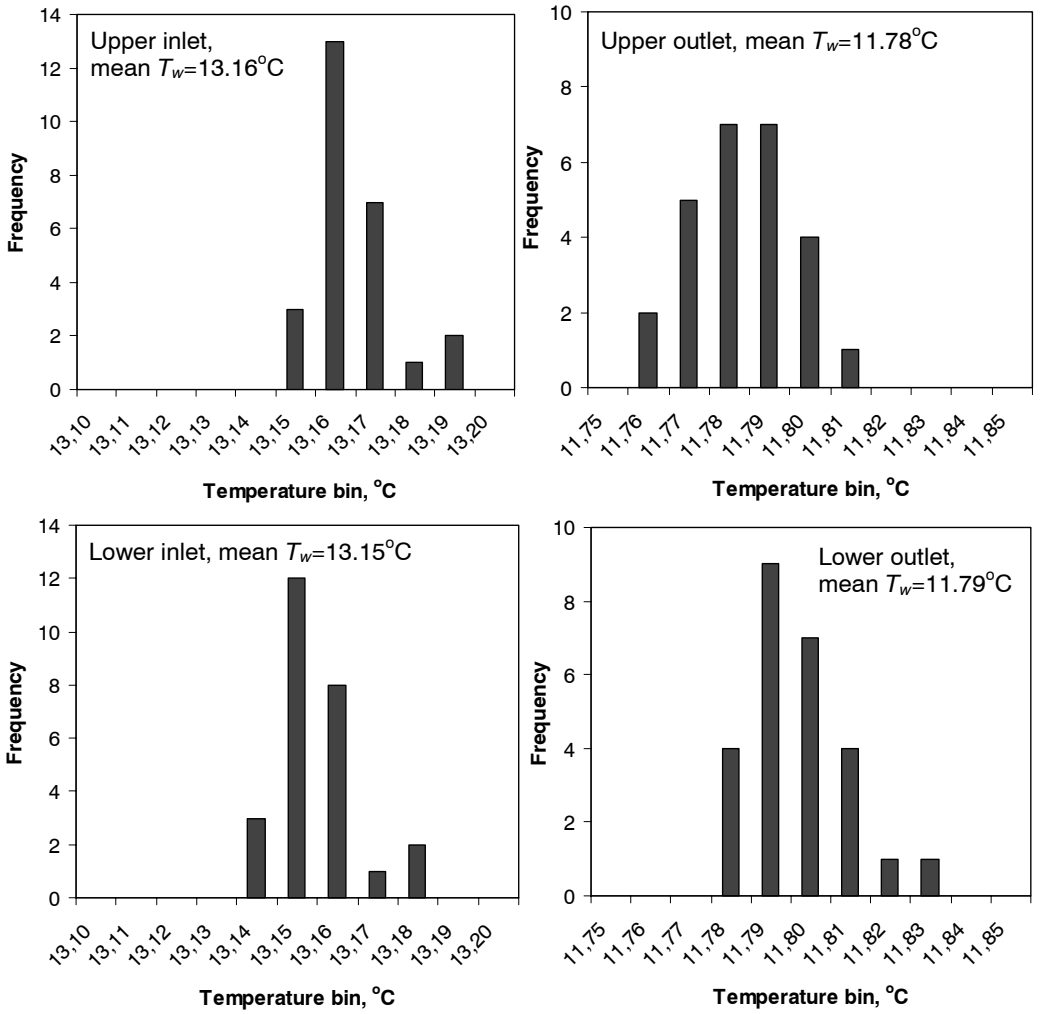

Figure 4.10 *Frequency of water temperature measurements at test section inlet and outlet, for 26 measurements. Bin size: 0.01 K. Test conditions are listed in the text*

As may be observed, the temperature data show a reasonably "normal" distribution, even though the range of scatter is small. There is very little difference between the two measurements at the inlet and outlet, respectively, and this was the situation in most experiments.

4.7.5 Uncertainty in refrigerant mass flux

The uncertainty in refrigerant mass flux is given by the mass flow meter uncertainty, and the uncertainty in the microchannel average diameter, which are independent measurements. From Section 4.4.1 and Table 4.3, these uncertainties are δD = ±0.01 mm and $\delta \dot{m}$ = ±0.00003 kg/s, respectively. The resulting uncertainty in mass flux was calculated by Eq. 4.22, with data as shown in Table 4.5. The relative uncertainty $\delta G/G$ ranges from 2.6 to 2.8%.

$$\delta G = \left[\left(\frac{\partial G}{\partial \dot{m}} \delta \dot{m} \right)^2 + \left(\frac{\partial G}{\partial A_f} \delta A_f \right)^2 \right]^{1/2} \tag{4.21}$$

$$\delta G = \left[\left(\frac{1}{A_f} \delta \dot{m} \right)^2 + \left(\frac{-\dot{m}}{A_f^2} \delta A_f \right)^2 \right]^{1/2} \tag{4.22}$$

Table 4.5 *Uncertainty in refrigerant mass flux*

G, kgm^{-2}s^{-1}	200	300	400	600
δG, kgm^{-2}s^{-1}	±5.6	±8.0	±10.5	±15.6

4.7.6 Uncertainty in heat transfer rate and heat flux

During vaporization tests, the heat transfer rate ($\dot{Q}$) was determined by a calorimeter balance on the water side:

$$\dot{Q} = \dot{m}_w c_p (T_2 - T_1) \tag{4.23}$$

Thus, the uncertainty in heat transfer rate is given by the uncertainty in water mass flow rate, temperature change, pressure change, and the uncertainty in water specific heat capacity $c_p(T,p)$. Heat leakage from the ambient air through the thermal insulation was not included in the uncertainty analysis. The minimum mean water temperature of 4°C, gave an estimated heat flow of about 0.5 W which can be neglected. The absence of heat leakage effects were also demonstrated by the calibration tests, where the difference between heat flow given off from the water and heat flow taken up by the single-phase CO_2 flow was generally less than 1%.

The contribution from uncertainty in c_p was found to be negligible compared to the other uncertainties, and the effect of δc_p was therefore not included in the calculations. As a result, the uncertainty in heat transfer rate was a function of three independent uncertainties:

$$\delta\dot{Q} = \left[\left(\frac{\partial \dot{Q}}{\partial \dot{m}_w} \delta \dot{m}_w \right)^2 + \left(\frac{\partial \dot{Q}}{\partial T_2} \delta T_2 \right)^2 + \left(\frac{\partial \dot{Q}}{\partial T_1} \delta T_1 \right)^2 \right]^{1/2} \tag{4.24}$$

Temperature uncertainties (δT_1 and δT_2) were both ±0.045 K (Section 4.7.4), and the uncertainty in water mass flow rate was ±0.2% of reading (Table 4.3). Partial derivation of Eq. (4.23) gives a sensitivity coefficient $\partial\dot{Q}/\partial T$ that depends on the water mass flow rate, and a sensitivity coefficient $\partial\dot{Q}/\partial\dot{m}_w$ that depends on the temperature change of the water: $T_2 - T_1$. The latter parameter generally varied between 1.5 and 3 K in the tests, and it has therefore been set to 2 K in the following uncertainty calculations. The resulting uncertainty for the heat transfer rate is shown in Table 4.6.

Table 4.6 *Uncertainty in test section heat transfer rate in evaporation tests.*

$\dot{m}_w$, kgs^{-1}	0.03	0.05	0.10	0.15
$\delta\dot{Q}$, W	±8	±13	±27	±40

During vaporization tests, the water flow rate ranged from 0.03 to 0.09 kgs^{-1}. Almost 80% of the tests were carried out with a water flow rate of around 0.05 kgs^{-1}. Since the uncertainty is constant for a given water mass flow rate, the relative (percent) uncertainty in test section heat transfer will be smaller the greater the heat load is.

The uncertainty in heat flux is influenced by the uncertainty in the inside heat transfer area, as shown by

$$\delta q = \left[\left(\frac{\partial q}{\partial \dot{Q}} \delta \dot{Q} \right)^2 + \left(\frac{\partial q}{\partial A_{ht}} \delta A_{ht} \right)^2 \right]^{1/2} \tag{4.25}$$

Based on the uncertainty in average diameter (±0.01 mm) and uncertainty in heated length of the test section (±0.5 mm), δA_{ht} is estimated to $\pm 3.96 \cdot 10^{-4}$ m^2, which is about 1.2% of the heat transfer surface area. Combining this with the uncertainty of heat transfer rate, the uncertainty of heat flux measurement (δq) can be found from Eq. (4.25). Table 4.7 gives the results.

Table 4.7 *Uncertainty in heat flux in evaporation tests.*

$\dot{m}_w$, kgs^{-1}	0.03		0.05		0.10	
q, kWm^{-2}	10	20	10	20	10	20
δq, Wm^{-2}	±279	±352	±424	±475	±852	±879
$\delta q/q$, %	±2.8	±1.8	±4.2	±2.4	±8.5	±4.4

4.7.7 Uncertainty in vapour fraction

The mean vapour fraction in the test section was calculated based on enthalpy and temperature data at the test section inlet and at locations along the test section. The "local" enthalpy values were found based on heat load and refrigerant mass flow rate. In principle,

$$x = x(h, T) \text{ and} \tag{4.26}$$

$$h = h_{ip}(T_{ip}, p_{ip}) + \frac{\dot{Q}_p}{\dot{m}} + F \cdot \frac{\dot{Q}}{\dot{m}} \tag{4.27}$$

where h_{ip} is the enthalpy at the preheater section inlet, and $\dot{Q}_p$ is the heat load in the preheater section. $\dot{Q}$ and $\dot{m}$ are the test section heat load and the refrigerant mass flow rate, respectively. F is a factor (less than 1) resulting from the averaging procedure to find the mean vapour fraction in the test section. In most cases, $F \approx 0.5$. As explained above, both enthalpy and pressure were assumed to depend on the cell number in a linear relationship. The averaging is therefore a matter of accounting for the varying length of the cells.

Uncertainty in the preheat section inlet enthalpy is

$$\delta h_{ips} = \left[\left(\frac{\partial h_{ip}}{\partial p} \delta p \right)^2 + \left(\frac{\partial h_{ip}}{\partial T} \delta T \right)^2 \right]^{1/2} \tag{4.28}$$

where the sensitivity coefficients varied with test section inlet pressure and temperature. Table 4.8 shows some typical data for the uncertainty in enthalpy at the evaporating temperature levels in the tests. A subcooling of 5 K, and a saturation pressure corresponding to the evaporation temperature was assumed.

Table 4.8 *Uncertainty in enthalpy at preheater section inlet*

T, °C	0	10	20	25
δh_{ips}, Jkg^{-1}	±36.7	±43.5	±59.8	±76.5

The expression for uncertainty of the "local" enthalpy in the test section can be derived from Eq. (4.27) ($\partial h/\partial h_{ip} = 1$):

$$\delta h = \left[\delta h_{ip}^2 + \left(\frac{\partial h}{\partial \dot{Q}_p} \delta \dot{Q}_p \right)^2 + \left(\frac{\partial h}{\partial \dot{Q}} \delta \dot{Q} \right)^2 + \left(\frac{\partial h}{\partial \dot{m}} \delta \dot{m} \right)^2 \right]^{1/2} \tag{4.29}$$

Table 4.9 shows calculated uncertainty of mean vapour fraction at varying refrigerant mass flux, heat flux, and evaporating temperature. A preheater heat load of 150 W was assumed for the q=10 kWm^{-2} data, and 300 W for the q=20 kWm^{-2} data. Uncertainty of preheater heat load was taken from Table 4.3 (±20 W), and uncertainty of refrigerant mass flow rate and test section heat load were taken from Tables 4.3 and 4.6, respectively.

Table 4.9 *Uncertainty in mean (local) vapour fraction in test section*
(T = 10°C, $\dot{m}_w$ = 0.05 kgs^{-1})

G, kgm^{-2}s^{-1}	200	300	400	600
q = 10 kWm^{-2}	±0.085	±0.057	±0.042	±0.028
q = 20 kWm^{-2}	±0.137	±0.091	±0.068	±0.045

The uncertainty in x is also shown graphically at varying mass flux in Figure 4.11.

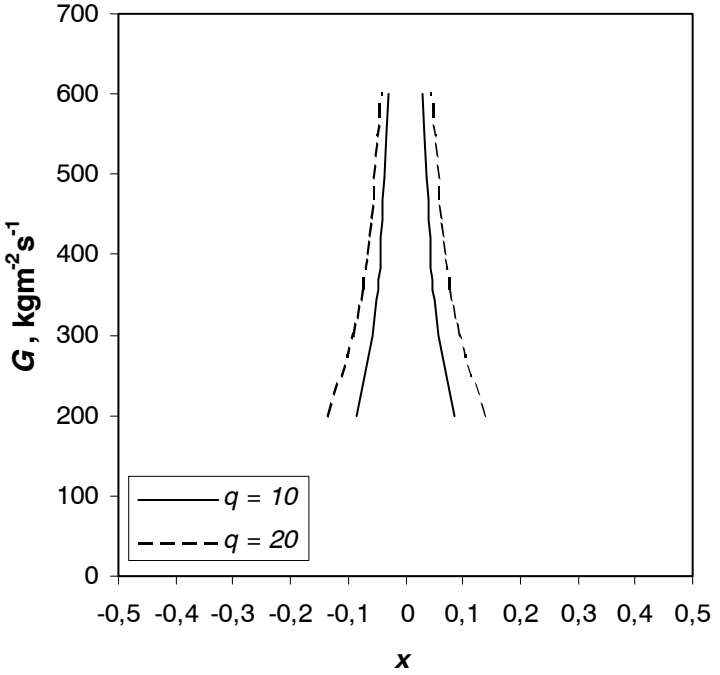

Figure 4.11 *Uncertainty in mean vapour fraction at varying mass flux and heat flux (q) 10 and 20 kWm^{-2}*

4.7.8 Uncertainty in pressure drop

The pressure drop dp/dz is measured by differential pressure across the length of the heated part of the test section. As explained above, corrections were made for inlet and outlet pressure losses/gains between the manifolds and the heat transfer tube, and for friction losses in the short unheated sections of the tube. These corrections did not exceed 5% of the total measured pressure drop in any experiment, and even though the models for two-phase flow pressure losses are inexact, it is estimated that the maximum contribution to the pressure drop uncertainty from these corrections was ±2.5% or 0.5 kPa. The latter corresponds to about ±1 kPa·m^{-1} for the pressure drop data, and this is neglected. From Table 4.3, the uncertainty of the pressure transducer was ±1 kPa, or ±2 kPa·m^{-1} for the test section pressure gradient. Thus, the total uncertainty in test section pressure drop was:

$$\delta\,(dp\ /\ dz) = \pm 2.2 \ \text{kPa·m}^{-1} \tag{4.30}$$

Table 4.10 shows some data for the relative uncertainty at varying pressure gradients.

Table 4.10 *Relative uncertainty in pressure drop*

dp/dz, kPa·m^{-1}	20	30	40	50
$\delta(dp/dz)/(dp/dz)$, %	±11.0	±7.3	±5.5	±4.4

4.7.9 Uncertainty in overall heat transfer coefficient

As may be seen from Eq. (4.2), the overall heat transfer coefficient U was determined by test section area (A), heat transfer rate ($\dot{Q}$), and temperature difference (ΔT). The expression for U may be written as

$$U = \frac{q}{\overline{T_w} - T_{CO2}} = \frac{q}{\Delta T} \tag{4.31}$$

with uncertainties defined as

$$\delta U = \left[\left(\frac{\partial U}{\partial q} \delta q \right)^2 + \left(\frac{\partial U}{\partial \Delta T} \delta \Delta T \right)^2 \right]^{1/2} \quad \text{and} \tag{4.32}$$

$$\delta \Delta T = \left[\left(\delta \overline{T_w} \right)^2 + \left(\delta T_{CO2} \right)^2 \right]^{1/2} \tag{4.33}$$

where q is the heat flux, $\overline{T}_w$ is the mean water temperature, and T_{CO2} is the mean temperature of CO_2 in the test section. Uncertainty in water temperature is discussed in Section 4.7.4, and Table 4.3 gives δT_{CO2}. Uncertainty in heat flux is given by Table 4.7, and the uncertainty in heat transfer surface is shown in Section 4.7.6: $\delta A_{hf} = \pm 3.96 \cdot 10^{-4}$ m^2.

The uncertainty of U varies with water mass flow rate, heat flux, temperature difference between water and CO_2, and evaporating temperature level. The uncertainty in temperature difference $\delta \Delta T$ based on Eq. (4.33) is shown in Table 4.11.

Table 4.11 *Uncertainty in temperature difference between water and CO_2 in evaporation tests*

T, °C	0	10	20	25
$\delta\Delta T$, K	±0.14	±0.12	±0.10	±0.09

Resulting uncertainty of U for normal tests is shown in Figures 4.12, 4.13, and 4.14. In the Figures, the relative uncertainty $\delta U/U$ is shown at varying U, for temperature levels (T) from 0 to 25°C, heat fluxes (q) 10 and 20 kWm^{-2}, and water mass flow rates ($\dot{m}_w$) of 0.03, 0.05 and 0.10 kgs^{-1}.

All the curves show an increase in relative uncertainty as U increases. This is due to the greater impact of the constant $\delta\Delta T$ as ΔT becomes smaller at higher U. The percent uncertainty in U is reduced as the heat flux is increased from 10 to 20 kWm^{-2}, due to the reduced relative uncertainty in heat flux. Also, relative uncertainty in U is reduced as the evaporating temperature is raised from 0 to 25°C, due to the reduced temperature uncertainty at higher temperature. In addition, uncertainty is reduced at reduced water mass flow rate. Most experiments were conducted with a water mass flow rate of 0.05 kgs^{-1}. Based on the above data, the typical uncertainty in U is δU = ±6% at a heat flux of 10 kWm^{-2}, and ±4% at a heat flux of 20 kWm^{-2}. Uncertainty of the CO_2 vaporization heat transfer coefficient is discussed in Chapter 6, based on the water-side heat transfer coefficient and its uncertainty, which is derived in Chapter 5.

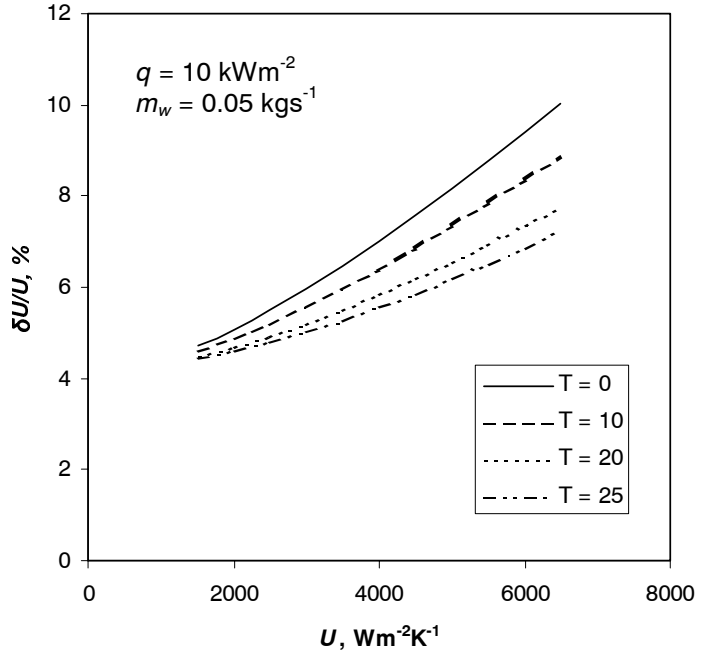

Figure 4.12 *Uncertainty of measured overall heat transfer coefficient (U), at evaporating temperature (T) of 0, 10, 20, and 25°C. Heat flux is 10 kWm-2 and water mass flow rate is 0.05 kgs-1.*

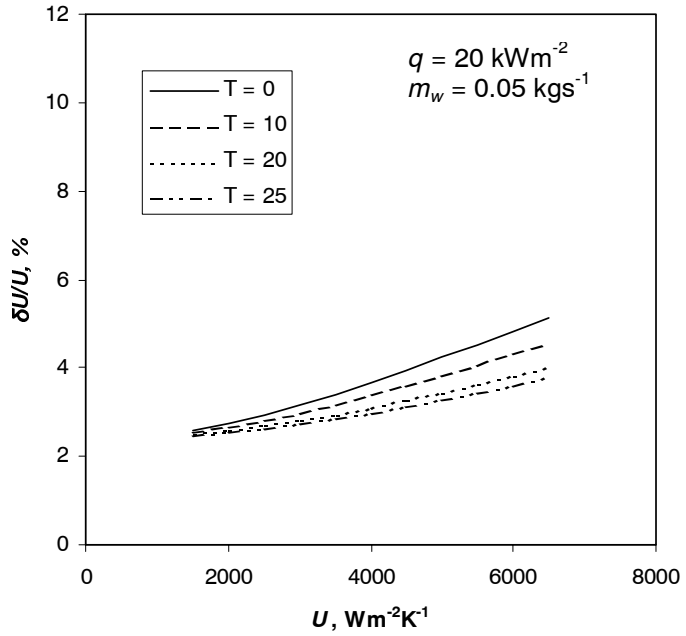

Figure 4.13 *Uncertainty of measured overall heat transfer coefficient (U), at evaporating temperature (T) of 0, 10, 20, and 25°C. Heat flux is 20 kWm-2 and water mass flow rate is 0.05 kgs-1.*

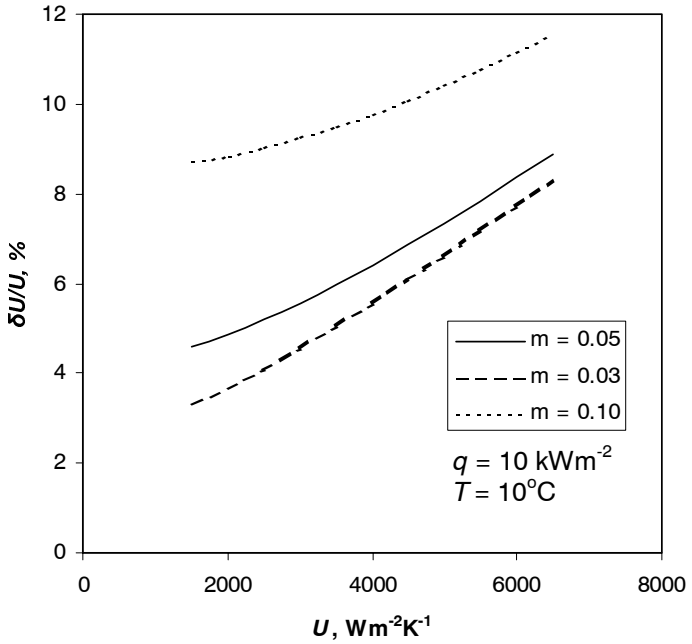

Figure 4.14 *Uncertainty of measured overall heat transfer coefficient (U), at varying water mass flow rate of 0.03, 0.05, and 0.10 kgs^{-1}.Evaporating temperature (T) is 10°C and heat flux is 10 kWm^{-2}.*

4.7.10 Uncertainty in water-side Reynolds and Prandtl numbers

The Reynolds and Prandtl numbers on the water side (at the mean water temperature and pressure), as well as the thermal conductivity of the water, are used in the determination of the expression for water-side heat transfer in the regression based on calibration tests, and to calculate water-side heat transfer coefficient in the ordinary tests.

The definitions are

$$Re = \frac{G_w \cdot D_h}{\mu} \tag{4.34}$$

$$Pr = \frac{c_p \cdot \mu}{k} \tag{4.35}$$

where G_w is water mass flux, D_h is hydraulic diameter of the flowchannel, μ is dynamic viscosity, and k is thermal conductivity. Based on the above definitions, the uncertainties are

$$\delta Re = \left[\left(\frac{\partial Re}{\partial G_w} \delta G_w \right)^2 + \left(\frac{\partial Re}{\partial D_h} \delta D_h \right)^2 + \left(\frac{\partial Re}{\partial \mu} \delta \mu \right)^2 \right]^{1/2} \tag{4.36}$$

$$\delta Pr = \left[\left(\frac{\partial Pr}{\partial c_p} \delta c_p \right)^2 + \left(\frac{\partial Pr}{\partial \mu} \delta \mu \right)^2 + \left(\frac{\partial Pr}{\partial k} \delta k \right)^2 \right]^{1/2} \tag{4.37}$$

The uncertainty of the mass flux is found based on similar methods as shown for the refrigerant side in Section 4.7.5. For property parameters μ, c_p and k, only the influence from uncertainty in water temperature was taken into account, since the pressure effects were negligible. The results are:

$$\delta D_h = 0.1\,\text{mm} \tag{4.38}$$

$$\delta \mu = \frac{\partial \mu}{\partial T_w} \delta T_w \tag{4.39}$$

$$\delta c_p = \frac{\partial c_p}{\partial T_w} \delta T_w \tag{4.40}$$

$$\delta k = \frac{\partial k}{\partial T_w} \delta T_w \tag{4.41}$$

The magnitudes of these uncertainties were found by entering incremental temperature changes corresponding to δT_w into the property calculation routines. As shown in Section 4.7.4, δT_w = 0.045 K. The uncertainty in flow area can be found in Table 4.2: $\delta A = 1.6 \cdot 10^{-6}$ m^2.

Resulting uncertainties in Pr, c_p and k caused by the temperature uncertainty were insignificant. Calculated uncertainties for these parameters were $\pm 1.5 \cdot 10^{-5}$ %, ±0.0012%, and ±0.013%, respectively. Uncertainty in μ was around ±0.11%, however, and this influence was included in the calculated Reynolds number uncertainty.

The uncertainty in Reynolds number was mainly affected by uncertainty in water mass flow rate measurement, and the percent uncertainty of *Re* thus did not vary much at different conditions. The following value represents the average for the 20 calibration tests:

$$\delta Re/Re = \pm 3.2\% \tag{4.42}$$

4.8 Distribution of two-phase flow into test section

Initially, the test section was supplied with CO_2 from one side of the manifold, i.e. an asymmetric flow. This could cause a separation of the liquid and vapour phase in the horizontal manifold, leading to non-uniform supply of liquid to the parallel ports of the test tube. This is shown schematically in Figure 4.15, which shows a possible solution as well.

It was decided to redesign the manifolds so that the fluid could enter and leave the test section symmetrically, i.e. through two inlets and two outlets. After the rebuilding the manifold connections, previous tests were repeated at an evaporation temperature of 10°C. Figure 4.16 shows the result for the modified test section with 'double inlet', in comparison with the initial results with 'single inlet'.

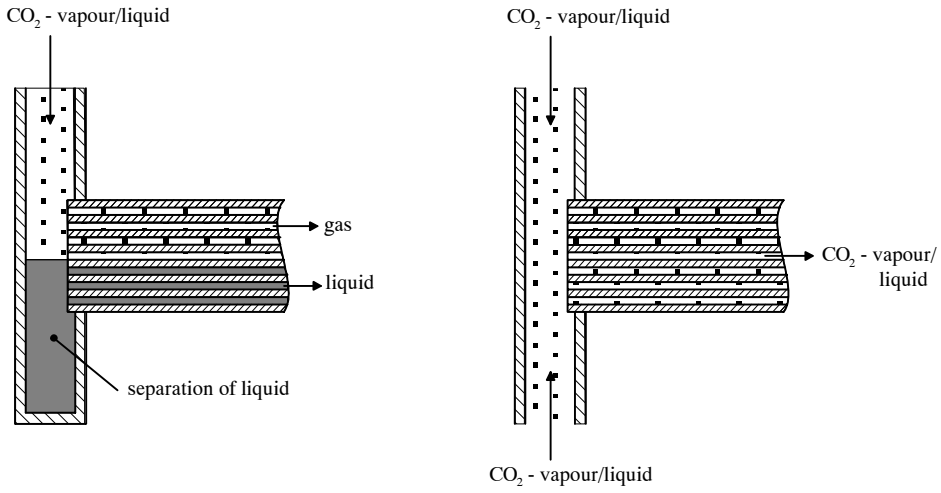

Figure 4.15 *Schematic drawing showing possible phase separation in manifold with inlet/outlet to/from one side only (left), and solution with inlet/outlet to/from both sides.*

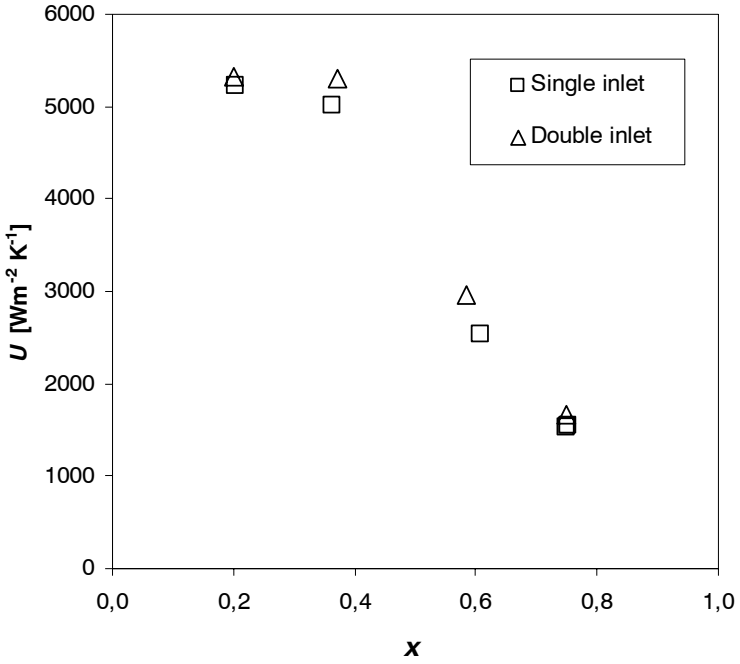

Figure 4.16 *Overall heat transfer coefficient depending on the vapour fraction with single and double refrigerant inlets/outlets. Conditions: Temperature 10°C, heat flux 20 kWm^{-2}, mass flux 600 kgm^{-2}s^{-1}.*

As can be seen from this Figure, there was no significant change, even at high vapour fraction. Thus the conclusion was drawn that both solutions gave uniform liquid supply to the ports, at least for this mass flux. All tests apart from the initial series at high mass flux were nevertheless done with two symmetric inlets and outlets.

4.9 Flow pattern visual observation rig

Detailed analysis of in-tube two-phase heat transfer and flow phenomena requires information about vapour/liquid flow patterns in the tube. This is of particular importance with CO_2, where results from earlier studies and from present heat transfer experiments indicate that dry-out phenomena play a significant role. It was thus decided that visual observations of two-phase flow patterns were needed. Since it was not practical to install any visual observation features in the heat transfer rig, a dedicated rig was built in order to observe and record two-phase flow pattern data.

4.9.1 Overview

In the design of an experimental rig to observe flow patterns in microchannels during vaporization of CO_2, a number of challenges had to be coped with:

a) Owing to the small tube diameter and high flow velocity, a magnified, high-speed recording was needed.
b) Owing to the high saturation pressure, special care was needed in the preparation of the test section to meet safety requirements without seriously impairing observation possibilities.
c) The phenomena to be observed were related to diabatic flow conditions, and the addition of heat flux to the observation tube was thus desired (again without impairing the observation possibilities).

A combination of a glass tube with sufficient wall thickness and a high-speed camera with magnifying optics was chosen. A "standard" quartz glass tube of ID/OD 0.98/6.35 mm was pressure tested and found capable of withstanding 25 MPa without breaking. It was thus decided to use this type of tube in the flow observations. Two different options for applying heat load to the observation tube were evaluated; a water jacket in a transparent outer tube, and a transparent resistive film coating on the glass tube. The last option gave the least effect on transparency, and was thus selected. In contrast to most earlier studies on flow pattern in evaporator tubes, where glass tube sections are installed after or between heated sections, this arrangement gives flow pattern observation inside the heated zone. This may not be of great importance in large tube diameters and when the vaporization is dominated by convective evaporation where the flow pattern is maintained through the adiabatic section. In microchannel flow, and especially when the heat transfer is dominated by nucleate-boiling, the use

of an unheated observation section that is very long compared to the tube diameter is not acceptable.

Since the refrigerant mass flow rate in a single tube would be quite small, it was decided to use an open circuit where CO_2 was taken from the liquid phase of a storage cylinder, through a control valve, preheated to reach the desired vapour fraction at the observation section, and finally expanded to atmospheric pressure and discharged from the circuit after passing through the observation tube.

The circuiting of the test system, and its instrumentation and components is shown in Figure 4.17. The instrumentation is also specified in Table 4.12.

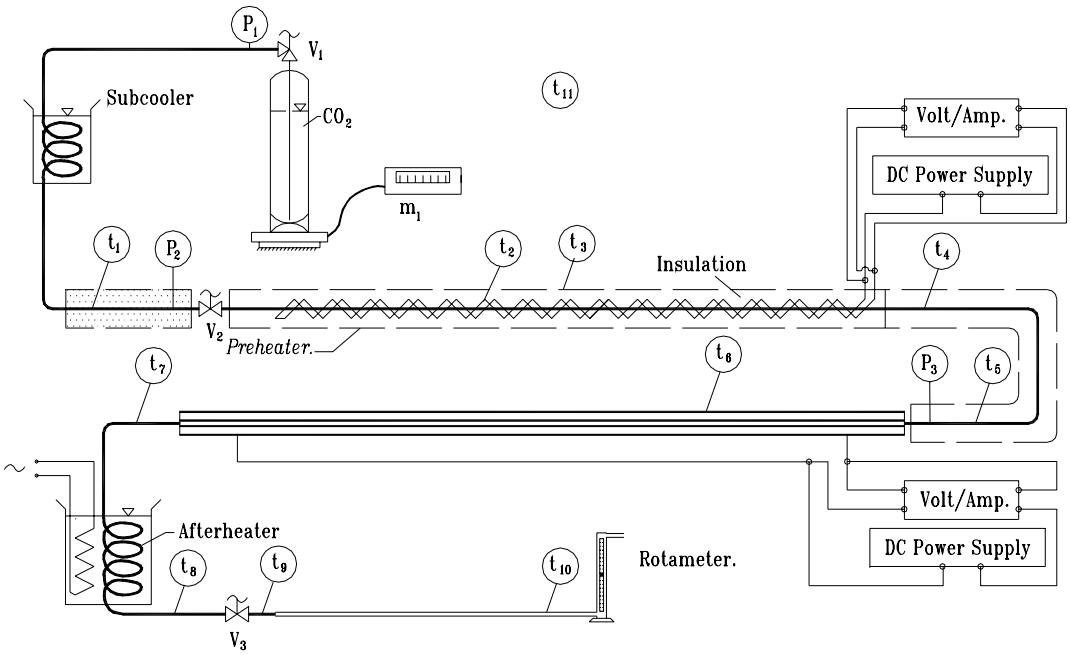

Figure 4.17 *Flow circuit and instrumentation of visual observation test rig*

A commercial CO_2 storage cylinder with internal riser tube was installed on a scale to measure average mass flow rate during the test period. A heater blanket wrapped around the cylinder controlled the temperature and maintained a slightly higher pressure than in the test section. A subcooling coil on the line from the CO_2 cylinder was submerged in ice/water to control the temperature at the inlet of the manual metering valve (V_2), which expanded the liquid CO_2 down to the evaporating pressure/temperature. The CO_2 flow then entered the preheater section, which consisted of a stainless steel tube with heating wires wrapped on it, all coated by thermal insulation. Heat load in the preheater was controlled by regulating the DC voltage and current applied to the heating wires. After the

preheater, the flow was taken through a thermally insulated return bend before it entered the test section.

After the test section, the refrigerant flow was taken through a coil submerged in heated water. This was done in order to evaporate any remaining liquid which otherwise could form dry ice in the final expansion valve (V_3) that reduced the pressure down to atmospheric pressure. Finally, a rotameter was used to monitor refrigerant flow rate.

The instrumentation consisted of surface thermocouples at the locations shown in Figure 4.17, and manometers at p_1, p_2 and p_3. The two latter manometers were calibrated. CO_2 mass flow rate was measured by a scale with a resolution of 1 g, and voltage/current to the preheater section and observation section were measured by multimeters.

Table 4.12 *Instrumentation of visual observation rig*

Pos-ition	Location	Type of instrument	Spec.
p_1	CO_2 cylinder	Manometer	Standard manom.
p_2	Inlet of valve V_2	Manometer, Bourdon Class 1	0-100 bar
p_3	Inlet of observation section	Manometer, Bourdon Class 1	0-100 bar
t_1	Inlet of valve V_2	Thermocouple, type T	0.5 mm
t_2	Preheater heating wires	Thermocouple, type T	0.5 mm
t_3	Preheater insulation (external)	Thermocouple, type T	0.5 mm
t_4	After preheater	Thermocouple, type T	0.5 mm
t_5	Inlet observation section	Thermocouple, type T	0.5 mm
t_6	Exterior of glass tube	Thermocouple, type T	0.2 mm
t_7	After observation section	Thermocouple, type T	0.5 mm
t_8	Before valve V_3	Thermocouple, type T	0.5 mm
t_9	After valve V_3	Thermocouple, type T	0.5 mm
t_{10}	Before rotameter	Thermocouple, type T	0.5 mm
t_{11}	Ambient air	Thermocouple, type T	0.5 mm
m_1	Weight of CO_2 cylinder	Mettler electronic scale	

4.9.2 Observation tube and camera equipment

The horizontal quartz glass observation tube was installed in a steel frame that supported the glass tube. Sealing between the glass tube and the steel frame was obtained by threaded packing glands from Conax. Main specifications of the observation tube are given in Table 4.13.

Table 4.13 *Test section data*

Tube inside/outside diameter	0.98 / 6.5	mm
Tube length	570	mm
Length of heated section	442	mm
Resistance of film	237	Ohm

Heating of the observation tube was achieved by applying DC voltage to a resistive coating film of transparent Indium Tin Oxide (ITO). The coating was carried out by BTE Bedampfungstechnik GmbH, Elsoff, Germany. Wires were strapped around the tube perimeter at each end of the ITO film to serve as electrical connectors.

A high-speed digital camera from Vision Research Inc. (Type Phantom 4.0 with a 25 mm F1.4 objective) recorded flow-patterns inside the observation tube at a location 65 mm downstream from the start of the heated part of the test section. A relatively short distance (but still corresponding to 66 tube diameters) was chosen to reduce the uncertainty in local x caused by heat loss to/from the observation tube. The camera had an observation angle 28 degrees above the horizontal, i.e. the images were taken slightly from above. Images were recorded for a test period of 1 second, and downloaded from the camera to a PC. For a recording rate of 4000 frames per second (fps), the recording image was 512x128 pixels. In some of the tests at higher mass flux, a recording rate of 8000 fps was used and only 50% of the image size could be recorded. The shutter speed was typically 15 microseconds.

Phantom 4.0 High Speed Camera Software was used in the processing of the images, including generation of still images, video clips, and measurements of dimensions and velocities.

4.9.3 Test principles

Almost all the flow-pattern recordings were taken at 20°C evaporating temperature, to reduce the uncertainties due to heat losses to/from the test section and the preheater, and to be able to focus on the temperature range where the dryout effects were of greatest importance.

Tests were conducted in series at constant mass flux, and increasing heat load in the preheater, thereby giving points of increasing vapour fraction in the observation tube. Once stable operating conditions were reached, temperatures, pressures, heat loads and mass flow data were recorded, and a flow pattern recording was made. Results from the recordings are presented in Section 6.6.

5. Heat exchanger data regression

5.1 Chapter overview

The purpose of this Chapter is to explain and document the principles and steps involved in finding a relation for the water-side heat transfer, based on special calibration tests under controlled conditions. The basic principles are outlined, and the calibration tests and resulting data are discussed. Two different water-side heat transfer models are tried in regression analysis based on calibration test data, and the best expression is found. Finally, the uncertainty of the water-side heat transfer coefficient is deduced, based on a rigorous uncertainty propagation procedure.

5.2 Basic relations

The overall heat transfer coefficient (U) and the mean refrigerant (evaporating) temperature (T) in the test section were experimentally determined as outlined in Chapter 4. U referred to the inside heat transfer surface (A_i) is defined as:

$$\frac{1}{U} = \frac{1}{h_i} + R_{cf} + \frac{1}{h_o}\left(\frac{A_i}{A_o}\right) \tag{5.1}$$

In order to determine the refrigerant-side heat transfer coefficient (h_i), the measured U must be separated into its individual components. The conduction and fouling resistance (R_{cf}) based on the inner tube area can be estimated as outlined later in this Chapter, and the area ratio is known from the tube geometry. Both heat transfer coefficients in Eq. (5.1) are unknown however, and an expression is needed for the outside (water side) heat

transfer coefficient (h_o) in order to find the inside coefficient based on U and R_{cf}.

In principle, single-phase heat transfer models from the literature could have been applied in order to estimate h_o, but such correlations typically have an uncertainty of ±15-20%, even for tube flow with fully developed velocity and temperature profiles. The complex geometry of the water ducts in the present test section is not covered by any standard well-proven correlation, and fully developed temperature and velocity profiles are not likely to be achieved. Most of the present water-side test data are in a transition region where fully developed turbulent flow is not reached, where uncertainties would be even greater. Thus, the use of standard correlations for h_o would give unacceptably large uncertainty in refrigerant-side heat transfer coefficient, which is a key result from the study.

Another approach is to conduct systematic "calibration" tests on the heat transfer tube, and then apply a regression scheme based on the test data to find a "calibrated" equation for the water-side heat transfer. If the heat transfer coefficient inside the test tube (h_i) is kept constant, and the water flow rate on the outside is varied systematically, an expression can be found for the water-side heat transfer coefficient (h_o). Such a regression depends on experimental data for U taken at controlled conditions, so that when U and R_{cf} are known, and h_i is constant, an equation can be fit that gives h_o at varying water flow rate and temperature. During later experiments, this equation can then be used to find h_i based on measured U. These principles were applied in the present tests.

5.3 Calibration test data

During the calibration experiments, the water-side Reynolds number was varied systematically by varying the water flow rate. The inside heat transfer coefficient h_i had to be constant during the experiments. Therefore, the following conditions were fulfilled:

- The calibration tests were conducted with single-phase supercritical-pressure flow of CO_2 inside the test tube, and the CO_2 flow rate (flow velocity) was constant.
- The mean CO_2 temperature and the CO_2 inlet and outlet temperatures and pressures were constant, in order to keep the amount of heat transferred and the thermophysical properties (viscosity, thermal conductivity, Prandtl number) constant.

- In order to keep the amount of heat transferred constant while varying the water flow rate, the water inlet and outlet temperature, and the mean temperature of the water had to be varied.

By conducting the calibration tests with supercritical CO_2 on the inside, the (constant) inside heat transfer coefficient h_i was quite high, thus giving better resolution in the determination of the variable h_o. This can be seen from Eq. (5.1) where increased h_i reduces the magnitude of the inside resistance term $(1/h_i)$. Even so, calibration tests were also needed in the high water-side Reynolds number range, where the outside resistance was diminished. This increased the accuracy in estimating the value of the constant inside resistance based on the data regression. In principle, the inside resistance was found as the asymptotic value of the total resistance minus wall/fouling resistance when $Re \rightarrow \infty$.

A total of 20 tests were conducted at varying water flow rate in order to obtain data for the regression analysis. The conditions on the inside (CO_2-side) were kept constant as shown in Table 5.1. Some key data for the water side for each test, and the measured overall heat transfer coefficient, are shown in Table 5.2.

Table 5.1 *Conditions on the inside (CO_2-side) during calibration tests*

Parameter	Nominal or average value	Observed variation range
p, MPa	9.1	±0.07
T, °C	11.3	±0.5
q, Wm^{-2}	19,380	19,086 – 19,805
G, $kgm^{-2}s^{-1}$	1890	1877 - 1901

During the calibration tests, the heat load on the test section was measured separately by flow rate and temperature difference on the water side (outside) and CO_2 side (inside). On average, the difference in measured heat load was 0.7%, and the maximum deviation was 1.6%.

Since calibration tests were conducted at one temperature level, there may be some concern about using the regression-based formula at other temperatures. By using "standard" correlations based on dimensionless groups containing fluid properties, these effects should be accounted for at least in a limited range of temperature around the calibrated level.

Table 5.2 *Water-side test data and measured overall heat transfer coefficient U for the test section in the calibration tests. Conditions on the CO_2-side are (nominally) constant as given in Table 5.1.*

Data point	$\dot{m}_w$ kgs^{-1}	$\overline{T}_w$ °C	*Re*	*Pr*	*k* Wm^{-1}K^{-1}	*U* Wm^{-2}K^{-1}
1	0.0286	16.85	2357	7.75	0.595	3002
2	0.0356	16.64	2914	7.79	0.595	3261
3	0.0417	16.39	3392	7.85	0.594	3468
4	0.0486	16.27	3938	7.88	0.594	3670
5	0.0555	16.13	4487	7.91	0.594	3846
6	0.0576	16.11	4652	7.91	0.594	3894
7	0.0595	16.04	4794	7.93	0.594	3959
8	0.0698	15.92	5610	7.95	0.594	4175
9	0.0714	16.25	5786	7.88	0.594	4233
10	0.0777	15.83	6230	7.97	0.593	4342
11	0.0780	15.90	6262	7.96	0.593	4347
12	0.0824	15.84	6608	7.97	0.593	4421
13	0.0913	15.77	7306	7.99	0.593	4576
14	0.0947	15.75	7578	7.99	0.593	4636
15	0.1047	15.71	8370	8.00	0.593	4752
16	0.1079	15.68	8620	8.01	0.593	4814
17	0.1171	15.62	9334	8.02	0.593	4899
18	0.1318	15.64	10511	8.02	0.593	5077
19	0.1445	15.61	11518	8.02	0.593	5189
20	0.1565	15.60	12475	8.03	0.593	5267

5.4 Constant resistances

5.4.1 Single-phase heat transfer resistance on refrigerant side

The single-phase heat transfer coefficient on the refrigerant side is one of the parameters determined from the regression using the calibration data. In order to assess its uncertainty and to evaluate the magnitude of the other fixed resistances, some calculations were made based on single-phase heat transfer correlations. Two types of correlations were used; the general single-phase models of Dittus and Boelter (1930), Pethukov (1970), and Gnielinski (1976), and special correlations for supercritical-pressure flow by Ghajar and Asadi (1986), Jackson and Fewster (1975), and Kakac (1987). Calculated heat transfer coefficients using the conditions of Table 5.1 are shown in Table 5.3.

Table 5.3 *Calculated CO_2 single-phase heat transfer coefficient during calibration tests, at conditions given in Table 5.1*

Model →	Dittus-Boelter	Gnielinski	Ghajar - Asadi	Jackson-Fewster	Kakac et al.	Pethukov
h, $Wm^{-2}K^{-1}$	10498	9775	10378	9878	9883	9988
Deviation from mean, %	+4,3	-2,9	+3,1	-1,9	-1,8	-0,8

All the calculated coefficients fall within a few percent deviation from the mean value of h=10067 $Wm^{-2}K^{-1}$. Thus, it is reasonable to assume that the CO_2-side heat transfer coefficient during the calibration tests should be approximately 10 $kWm^{-2}K^{-1}$.

5.4.2 Conduction and fouling resistance R_{cf}

The conduction resistance in the tube wall was calculated based on tube geometry and thermal conductivity. The test tube was extruded from aluminium alloy with 180 $Wm^{-2}K^{-1}$ conductivity, and the mean conduction length was calculated to 0.47 mm. Thus, the conduction resistance could be calculated to $2.6 \cdot 10^{-6}$ m^2KW^{-1} referred to the inside heat transfer area. Although the number is uncertain, the influence of this uncertainty on overall heat transfer is negligible due to the very small value.

Regarding fouling resistance, the situation is more complex. Inspection of the test tube and its jacketing after prolonged use shows a very slight deposit caused by ferrous corrosion products. Thus, some fouling resistance should be accounted for on the water side, even though distilled/deionised water was used. On the inside, fouling effects were assumed to be negligible due to the cleaning effect of pure CO_2 and the absence of substances that could cause fouling.

The most widely used design data for fouling were published by TEMA (Tubular Exchanger Manufacturers Association), based on "experience values" collected for many years. The TEMA data reproduced by Knudsen (1998) recommends a fouling resistance of $8.5 \cdot 10^{-5}$ m^2KW^{-1} for distilled or closed-cycle condensate water in shell-and-tube heat exchanger geometries. Cooper, Suitor and Usher (1980) studied fouling in plate and spiral heat exchangers, and found that due to higher turbulence level such heat exchangers had less tendency to fouling than shell-and-tube types. Flow geometry on the water side of the present test section had more in common with a plate or spiral heat exchanger than a shell-and-tube unit, and experience for plate units were therefore assumed to be valid also for the

test section. Specific data for water-side fouling in plate heat exchanger were given by Cross (1978), who recommended using a resistance between $2 \cdot 10^{-5}$ and $7.5 \cdot 10^{-5}$ m^2KW^{-1}. Since the test rig used distilled water in a sealed flow circuit, the fouling resistance should not be any higher than $2 \cdot 10^{-5}$ m^2KW^{-1}. Cooper and Usher (1998) recommended the use of values not greater than one-fifth of data for shell-and-tube units should be used for plate heat exchangers. Based on the above data from Knudsen (1998), the plate heat exchanger fouling resistance with distilled water should therefore be less than $1.7 \cdot 10^{-5}$ m^2KW^{-1}.

The calibration data do not provide any basis for separating between the fixed resistance caused by the constant internal heat transfer coefficient and the fixed resistance due to conduction and fouling. Total fixed resistance may be found, but the reduction of test data in ordinary experiments relies on having determined the value of combined conduction and fouling resistance. The only solution is then either to estimate fouling or to estimate inside heat transfer, and the latter was felt to be a safer estimate. Since the calibration tests were conducted with single-phase flow of "liquid" CO_2, it was possible to calculate the internal heat transfer coefficient with reasonable accuracy, as shown in the previous Section. Using the mean heat transfer coefficient of 10 $kWm^{-2}K^{-1}$ it was then possible to split the known overall fixed resistance into its two parts, thus finding a plausible number for the combined conduction and fouling resistance. After some initial trial and error using varying fouling resistance, it was found that the fouling and conduction resistance had to be approximately 10^{-5} m^2KW^{-1} in order to arrive at the above CO_2-side heat transfer coefficient from the regression. This fouling resistance was within the range of the lowest values from the literature, and it would not be unreasonable if low resistance was obtained considering the cleanliness of the water circuit, the moderate temperatures of operation, and the high water flow velocities. As a result, the following value was assigned to the total fixed resistance caused by conduction and fouling:

$$R_{cf} = 10^{-5} \ \text{m}^2\text{KW}^{-1} \tag{5.2}$$

5.5 Methods of regression

Several schemes for determining individual heat transfer coefficients based on the overall heat transfer are described in the literature. These methods, which are often termed *Wilson Plot Methods*, all rely on using regression based on experimental data to determine constants and exponents in mathematical

expressions for the heat transfer coefficient. The original method was developed by Wilson (1915), who found an expression for the tube-side (single phase) heat transfer coefficient in steam condensers. Tube-side heat transfer was expressed as a "reduced" flow velocity multiplied by a constant and raised to the power of 0.82. This "reduced" velocity has been shown to correspond to the Reynolds number. After including another constant to account for the wall resistance and the shell-side resistance (assuming that the latter was constant), a linear plot was fitted to the experimental data. Based on this plot, the two constants could be determined, thereby arriving at an expression for tube-side heat transfer. The original Wilson Plot method can be used only to determine one or two constants, and Wilson Plot methods in general rely on turbulent flow or flow situations where heat transfer varies with Reynolds number.

5.5.1 Categorization

A number of "modifications" of the original Wilson Plot method have been shown in the literature. These methods can be categorized based on the following criteria:

- *Number of expressions for heat transfer coefficient that need to be derived.* In some cases, expressions need to be derived for both the inside and outside heat transfer coefficient in the heat exchanger. This is typically the case when operating conditions are varied simultaneously on both sides. When calibrating the water-side of a test section, the conditions (temperature, pressure, flow rate) on the inside may be kept constant to reduce the number of unknowns.

- *Type of heat transfer expression(s).* Mathematical expressions for single-phase turbulent convective heat transfer coefficient are generally of the form

$$Nu = f(Re, Pr) \tag{5.3}$$

  where the functional relation typically have one or more constants and coefficients, and the Reynolds and Prandtl numbers may have exponents. Some common heat transfer models are discussed in the next Section.

- *Number of constants, coefficients and exponents that are determined.* A regression scheme can only determine a limited number of constants, coefficients and exponents, but the ability of the model

to reproduce test data may be better when more such parameters can be fitted.

- *Type of regression scheme applied.* In most cases linear regression schemes have been used, in accordance with the original Wilson Plot Method. In some cases, three unknowns need to be determined, a task that cannot be solved by linear regression. Briggs and Young (1969) developed a procedure for solving this problem by using two linear regressions with iteration to avoid the added complexity of a non-linear regression scheme. Later on, Khartabil and Christensen (1992) developed a nonlinear regression scheme that was claimed to be more robust with respect to convergence. In general, any non-linear regression software may be used, provided that the desired form of Equation (5.3) can be handled.

5.5.2 Heat transfer models for the water side

The most common heat transfer expression used in relation to Wilson plot methods is the Dittus and Boelter (1930) type of equation, i.e.

$$Nu_{DB} = C \cdot Re^{m} Pr^{n} \tag{5.4}$$

This type of expression is generally valid only for Reynolds numbers above the transition regime, i.e. above 10,000. In relation to a Wilson-plot regression, the coefficient C and the exponents m and n can be regarded as unknown, or one or more values can be assigned based on standard assumption. The Prandtl number exponent n in Eq. (5.4) is usually defined as 0.4 for heated flow and 1/3 for cooled flow, as in our case. The standard Reynolds number coefficient in Eq. (5.4) is m=0.8, and the standard C for fully developed turbulent flow in *straight* circular tubes is 0.023.

Kattan (1996) instead used the Gnielinski (1976) expression for single-phase heat transfer, both inside the test tube and for the external annulus. This heat transfer model is given as

$$Nu_{G} = \frac{\left(\frac{f}{8}\right)(\mathrm{Re} - 1000)\mathrm{Pr}}{1 + 12.7\left(\frac{f}{8}\right)^{1/2}\left(\mathrm{Pr}^{2/3} - 1\right)} \tag{5.5}$$

where the Darcy friction factor (f) is estimated from the expression of Filonenko (1954) for isothermal flow in smooth tubes.

$$f = \left[1.82 \cdot \log_{10}(\mathrm{Re}) - 1.64\right]^{-2} \tag{5.6}$$

One important feature of the Gnielinski (1976) model is its claim of higher accuracy for Reynolds numbers in the transition region, i.e. between 2300 and 10,000. The Gnielinski correlation only needs one additional constant to account for flow in non-circular cross section, and short tube length. Even though the use of this correlation may seem promising, a statistical comparison made by Kattan (1996) based on his test data showed that the use of a "Dittus-Boelter" type of model generally gave smaller deviations.

All types of Nusselt number correlations may be refined by a multiplier that accounts for variation in viscosity (or Prandtl number) from film (tube wall) to bulk conditions. For liquids, this multiplier is often calculated as (Kays and Crawford, 1993):

$$\frac{Nu}{Nu_{CP}} = \left(\frac{\mu_w}{\mu_b}\right)^n \tag{5.7}$$

where subscript *CP* refers to the constant-property result, and subscripts *w* and *b* refer to wall (film) and bulk conditions. For cooled flow, *n* can be assumed to be -0.25, according to Kays and Crawford (1993) quoting Pethukov (1970). In the present calibration tests, the temperature difference between wall and bulk on the water side varies from about 1 K to 4 K, which gives a correction factor Nu/Nu_{CP} varying from 1.006 to 1.025. This variation is regarded as small enough to be neglected.

As shown in Chapter 4, the water flow channels in the test section are short straight ducts with abrupt 180° bends between each pass. Heat transfer takes place only on one (flat) side of the duct. The length of a straight section is about 5.8 times the duct hydraulic diameter. This situation may come closer to developing flow along a flat plate than tube flow, especially considering the temperature profile development. Another observation is that the bend may be abrupt enough to give flow separation over the edge of the test tube. In case of flow along a flat plate, the Reynolds number is evaluated based on plate length in the flow direction (*L*), and turbulence requires $Re_L > 10^5$. Based on this limit, all water-side data in the present test would be in the laminar region, if the inlet velocity profile was regular. This is probably not the case due to the flow around the abrupt tube edge, but it may still be of interest to consider a model for heat transfer in laminar flow along a flat plate based on the *Pohlhausen* solution for $Pr > 0.5$ (Kays and Crawford, 1993):

$$Nu_L = 0.664 \cdot Re^{1/2} Pr^{1/3} \tag{5.8}$$

This Nusselt number represents the average over the length of the plate (L). This equation is similar to Eq. (5.4) with n=1/3, even though the constant and the Reynolds number exponent m are different. According to Briggs and Young (1969), m varies from about 0.6 at low Reynolds numbers (less than 1000) to approximately 0.9 at high Re.

It seemed reasonable to try both a "Gnielinski" type model and a "Dittus-Boelter" type model in the regression analysis. The latter model may also be relevant if the flow situation resembles developing flow along a flat plate.

5.6 Linear regression using Gnielinski model

5.6.1 Principles

The Gnielinski model promises good accuracy at transition flow. Unless one wishes to modify any of the terms in Eq. (5.5), e.g. by changing the friction factor formula or exponent, or by changing other constants, only one single constant C need to be fitted in the expression for the water-side heat transfer coefficient:

$$h_o = C \cdot Nu_G \frac{k}{D} \tag{5.9}$$

Since the Gnielinski model was regarded as "fixed" and the outcome of changing the expression was uncertain, only the "constant-multiplier" approach was used. This was also the approach used by Kattan (1996). The Nusselt number Nu_G is calculated from Equations (5.5) and (5.6), based on the known Re and Pr for the water flow. Inserting Eq. (5.9) into Eq. (5.1) and rearranging, we get

$$\left(\frac{1}{U} - R_{cf}\right) = \frac{1}{C}\frac{1}{Nu_G}\frac{D}{k}\left(\frac{A_i}{A_o}\right) + \frac{1}{h_i} \tag{5.10}$$

This is a linear equation of the form

$$Y = A \cdot X + B \tag{5.11}$$

where the slope A equals

$$A = \frac{1}{C} \tag{5.12}$$

the independent variable is

$$X = \frac{1}{Nu_G} \cdot \frac{D}{k}\left(\frac{A_i}{A_o}\right) \tag{5.13}$$

the intersection with the y-axis (B) equals

$$B = \frac{1}{h_i} \tag{5.14}$$

and the dependent variable (Y) is

$$Y = \left(\frac{1}{U} - R_{cf}\right) \tag{5.15}$$

The variables and parameters in Eq. (5.13) are known from geometry data, calculated Nusselt number (Eq. 5.5), and fluid properties, thus making a calculation of X possible. Furthermore, the overall heat transfer coefficient (U) is known from the experiment, and the conduction and fouling resistance (R_f) was estimated to $1 \cdot 10^{-5}$ m^2KW^{-1} in Section 5.4.2. With both variables in Eq. (5.15) known, the dependent variable Y is also known. A regression is then possible to find A and B to fit a linear curve.

5.6.2 Results and discussion

Figure 5.1 shows the data points from Table 5.2 converted to X-Y coordinates based on Eq. (5.13) and (5.15). The diagram also shows a linear regression line fitted to the data points using the Gnielinski model, with the interception of the ordinate axis marked.

The slope A based on the N=20 data points (X,Y) was based on a normal *Gaussian* least-squares method of linear regression

$$A = \frac{N\sum_{j=1}^{N} X_j Y_j - \left(\sum_{j=1}^{N} X_j\right)\left(\sum_{j=1}^{N} Y_j\right)}{N\sum_{j=1}^{N} X_j^2 - \left(\sum_{j=1}^{N} X_j\right)^2} \tag{5.16}$$

The following constants were derived:

$$A = 0{,}2709$$
$$B = 1{,}6041 \cdot 10^{-4}$$

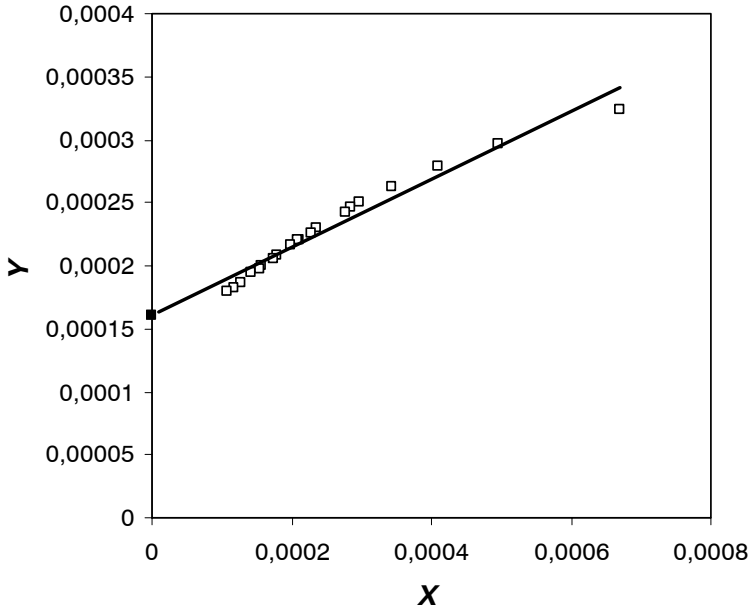

Figure 5.1 *Data points and regression line based on the Gnielinski model*

This gives:

$$C = 3.692$$
$$h_i = 6234$$

Thus, the Nusselt number calculated from Equations (5.5) and (5.6) has to be multiplied by a factor of almost 4 to fit the test data. Some increase may

be explained by the short flow-channels on the water side of the test section. The correction factor given by Gnielinski (1976) is

$$1+\left(\frac{d}{L}\right)^{2/3} \tag{5.17}$$

where d and L are channel hydraulic diameter and length, respectively. This correction would give only about 30% increase in Nu, however.

The ordinate-axis interception B gives a constant internal heat transfer coefficient of about 6200 $Wm^{-2}K^{-1}$, which is almost 40% lower than the calculated coefficients in Section 5.4.1. This indicates that the regression-based h_i is too low.

Another problem is the deviation between the regression line and the data points, as may be observed in Figure 5.1. Using Eq. (5.9) with C=3.69, and inserting h_i=6234 into Eq. (5.1), U may be calculated and compared to the experimental U. This comparison is shown in Figure 5.2, and the deviation between the measured and calculated U-values is shown in Figure 5.3.

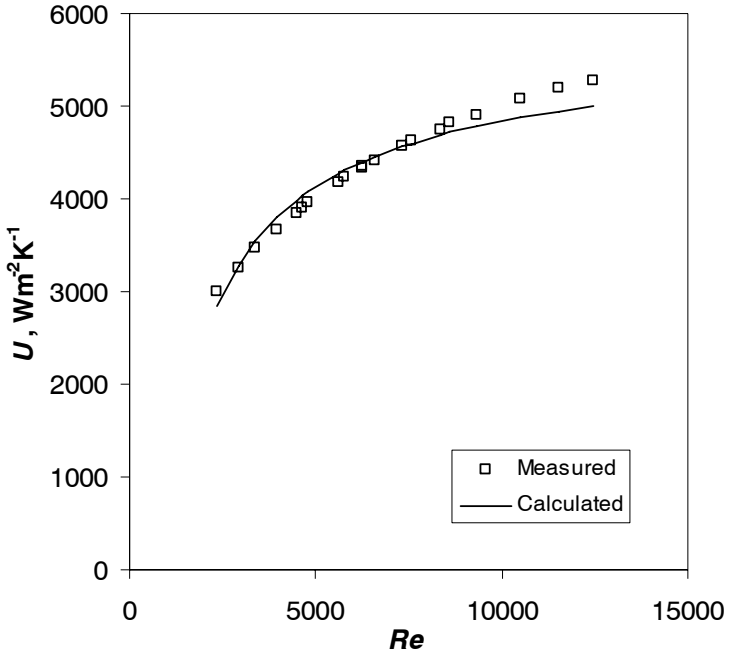

Figure 5.2 *Measured and calculated overall heat transfer coefficient U, using a Gnielinski heat transfer model on the water side*

As may be observed from Figures 5.2 and 5.3, there is considerable deviation between the calculated and measured data, and the calculated curve does not reproduce the shape of the curve given by the experimental data. Based on Figure 5.3 it seems like the Gnielinski model gives a systematic or "non-random" deviation from the experimental data. The present model is not acceptable for processing of test data in order to find h_i based on measured U.

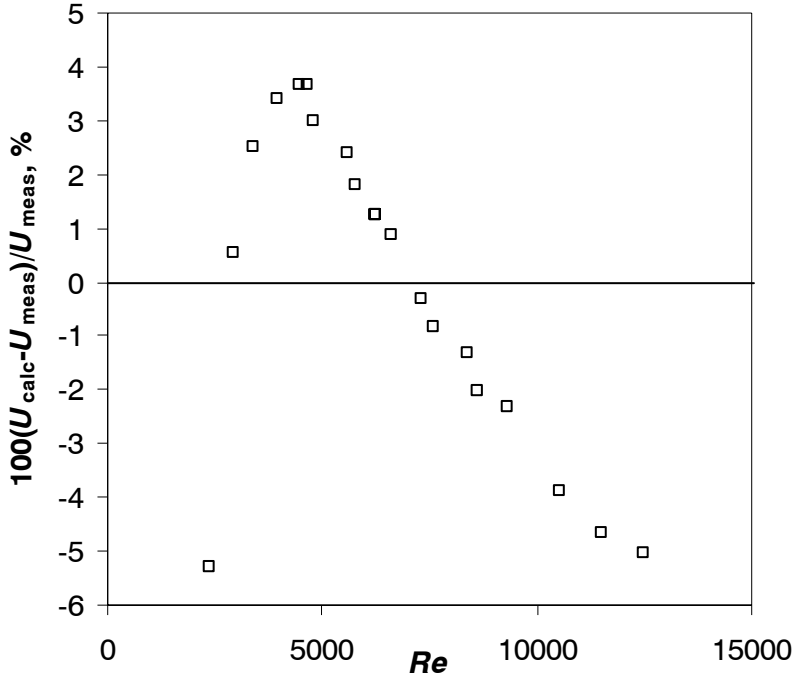

Figure 5.3 *Deviation between measured and calculated overall heat transfer coefficients in Figure 5.2*

This outcome may have been changed by introducing modifications in the Gnielinski expression, as suggested above. In order to limit the efforts needed, and since the simpler Dittus-Boelter model gave a good fit (see next Section) it was decided to not spend more time on modifying Eq. (5.5), however.

5.7 Regression using Dittus-Boelter model

5.7.1 Principles

As explained above, both Eq. (5.4) and Eq. (5.8) are of the same type, i.e. with *Re* and *Pr* having exponents that can be assumed known or adapted by regression, as well as a constant that should be determined by regression. This type of model is termed "Dittus-Boelter", although we are talking more of a type of equation than a specific model. Compared to the Gnielinski correlation this type of equation has the advantage of being more easily "adaptable" to test data.

Equation (5.4) provides an expression for the water-side heat transfer coefficient:

$$h_o = \frac{k}{D} C \cdot Re^m Pr^n \tag{5.18}$$

Combining this with Eq. (5.1), and rearranging, we get

$$\left(\frac{1}{U} - R_{cf} \right) \cdot \frac{A_o}{A_i} = \frac{1}{\left(C \cdot Re^m \cdot Pr^n \cdot \frac{k}{D} \right)} + \frac{A_o}{h_i \cdot A_i} \tag{5.19}$$

This equation has four unknowns: h_i, C, m and n. The Prandtl number exponent n may be assigned the standard value for cooled flow, n=1/3, but still there are three unknowns, thus making linear regression impossible. There are then two possible solutions; either to use non-linear regression, or to use two linear regressions (one based on transformed data) and iteration, as devised by Briggs and Young (1969) and adapted to computer program use by Farrell et al. (1991). The linear/iterative method may give convergence problems, however, and the linear "Logarithmic Wilson Plot" is famous for the large uncertainty involved in finding the slope and ordinate axis intersection from transformed data points clustered together far away from the ordinate axis. Another important argument for using non-linear methods is the better possibility to analyse uncertainties in the derived model, as shown later in this Chapter.

Eq. (5.19) can be written as

$$\left(\frac{1}{U}-R_{cf}\right)\frac{A_o}{A_i}=\frac{1}{C}\cdot Re^{-m}Pr^{-1/3}\cdot\frac{D}{k}+\frac{1}{h_i}\frac{A_o}{A_i} \tag{5.20}$$

This is an equation on the form

$$Y=a\cdot X_1^b\cdot X_2+K\cdot c \tag{5.21}$$

where the dependent variable is

$$Y=\left(\frac{1}{U}-R_{cf}\right)\cdot\frac{A_o}{A_i} \tag{5.22}$$

the independent variables are

$$X_1=Re \tag{5.23}$$

$$X_2=Pr^{-1/3}\cdot\frac{D}{k} \tag{5.24}$$

and the parameters to be fitted are

$$a=\frac{1}{C} \tag{5.25}$$

$$b=-m \tag{5.26}$$

$$c=\frac{1}{h_o} \tag{5.27}$$

The constant is

$$K=\frac{A_o}{A_i}=0.852 \tag{5.28}$$

5.7.2 Results and discussion

The commercial software package *DataFit* v. 7.1.44 by *Oakdale Engineering* was used to conduct a non-linear least-squares data regression based on the data in Table 5.2. The program used a Levenberg-Marquardt (iterative) method to find the optimum solution. The following initial values were used:

$$C_{initial} = 0.02 \quad \Rightarrow \quad a_{initial} = 50$$
$$m_{initial} = 0.8 \quad \Rightarrow \quad b_{initial} = -0.8$$
$$h_{i,\,initial} = 10000 \quad \Rightarrow \quad c_{initial} = 0.0001$$

Convergence was obtained after 13 iterations, with the following results:

$$C = 0.1820$$

$$m = 0.6352$$

$$h_i = 9840$$

Variation in the initial values did not give significant changes in the result, and the derived numbers seemed plausible, so it was concluded that the desired solution had been found. The water-side heat transfer coefficient could thus be calculated as:

$$Nu = 0.182 \cdot Re^{0.635} Pr^{1/3} \tag{5.29}$$

A Reynolds number exponent m of 0.635 is significantly lower than the usual value of 0.8 for turbulent tube flow. Since the range of Re generally is in the transition region, a somewhat lower value can be expected. Also, following the arguments given in Section 5.5.2, the exponent can be expected to be close to 0.5-0.6. It is also interesting to note that if the constant in Eq. (5.8) is corrected by the ratio of length-based and cross-section based hydraulic diameter, the value becomes 0.114, which is much closer to the C=0.182 found from the regression than the usual value of 0.023 used in tube flow.

Figure 5.4 shows a plot of the data points and the regression-based model, in $X_1/X_2/Y$-coordinates. The plane representing the fitted model reproduces the data points with a coefficient of multiple determination (R^2) of 0.99954. The single experimental point that deviates from the general trend in Figure 5.4 was caused by a slightly higher water temperature than nominally. This gave a Prandtl number that deviated from the trend in the experimental points.

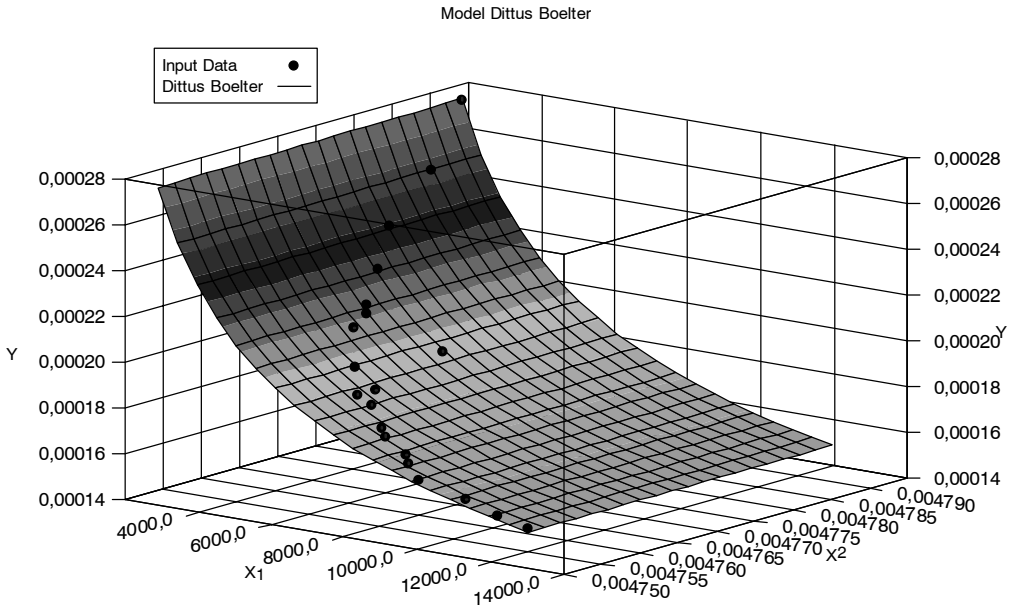

Figure 5.4 *Plot of data points and model from non-linear regression*

Figure 5.5 shows a comparison between the measured U and the calculated U using Eq. (5.29) for the water side, and assuming an internal (CO_2-side) heat transfer coefficient of 9,840 $Wm^{-2}K^{-1}$. In comparison to Figure 5.2, the fit of the model has been greatly improved. The improved accuracy can also be observed from Figure 5.6, showing the percent difference between measured and calculated U. In this case, the deviation is much smaller and of a much more random nature than in Figure 5.3. Most of the deviation in Figure 5.6 can be attributed to experimental scatter.

The mean absolute difference between measured and calculated U is reduced from 2.50 % with the Gnielinski model to 0.29% with the Dittus-Boelter model. In the present study, Equation (5.29) based on the Dittus-Boelter model is therefore used to calculate water-side heat transfer in the processing of test data to find the CO_2-side heat transfer coefficient.

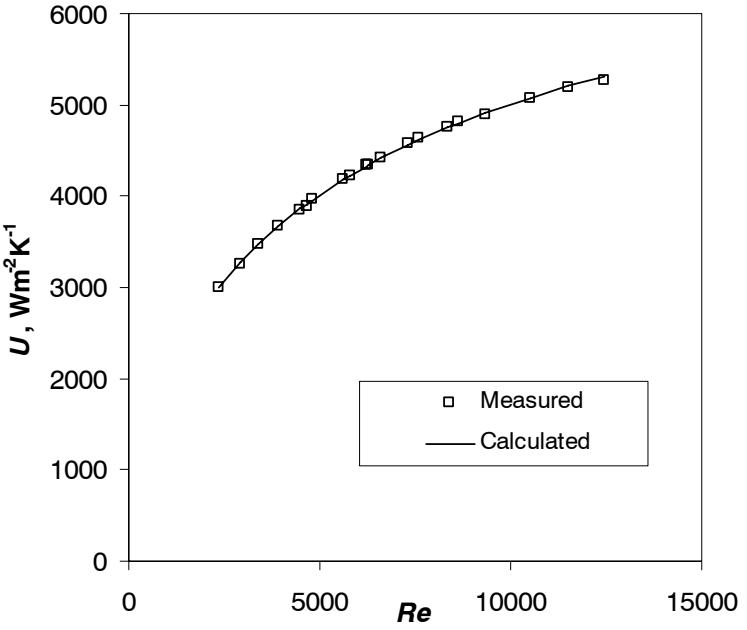

Figure 5.5 *Measured and calculated overall heat transfer coefficient U, using Eq. (5.29) to model water-side heat transfer*

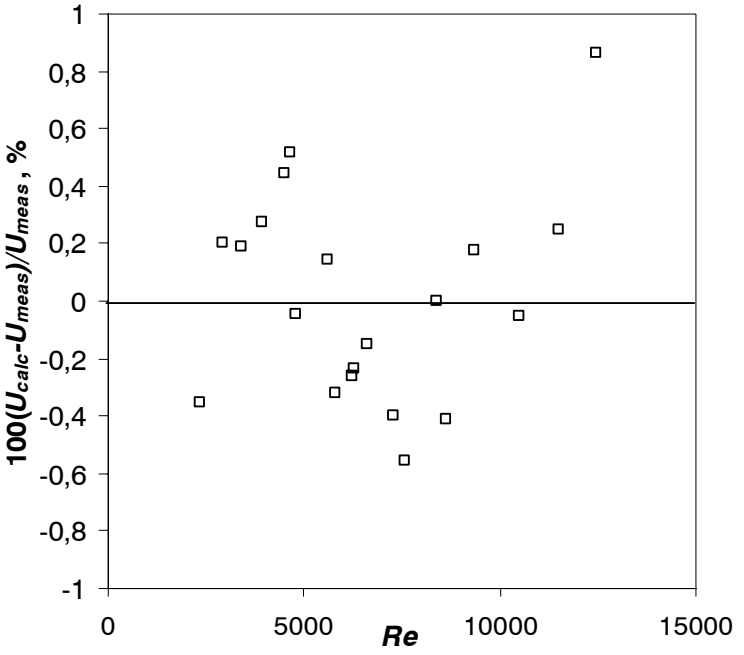

Figure 5.6 *Deviation between measured and calculated overall heat transfer coefficients in Figure 5.5*

5.8 Uncertainties of Wilson plot method

5.8.1 General

Many authors have stressed the fact that Wilson plot methods can give large uncertainties. Based on the discussion of Shah (1990), the following restrictions apply:

1. Fluid flow rate and log-mean average temperature on the constant-resistance side (in our case: the inside) must be constant during calibration, so that the thermal resistance is truly constant.

2. The Reynolds number on the variable-resistance side (in our case: the outside) is not known initially and needs to be determined.

3. All test data must be in one flow region (e.g. turbulent flow) on the variable-resistance side.

4. Fluid-property variation on the variable-resistance side must be taken into account.

5. Tube wall (and fin) thermal resistance must be taken into account.

6. During calibration and testing, fouling on either fluid side must be avoided or kept constant.

The present methods have taken these restrictions into account, even though the fouling influence gave some uncertainty. In order to get an indication of possible changes in fouling resistance over time, the same test series was repeated three times in a time span of 16 months with extensive use of the test rig. Figure 5.7 shows measured heat transfer coefficients at an evaporating temperature of 20^{o}C, a mass flux of 300 kgm^{-2}s^{-1} and a heat flux of 10 kWm^{-2}, recorded at three different times during the test program. Heat transfer coefficients were derived using the methods described in this Chapter. The deviation was relatively small (well within experimental uncertainty) and did not show any consistent tendency, and it was therefore concluded that variable fouling effects were not significant.

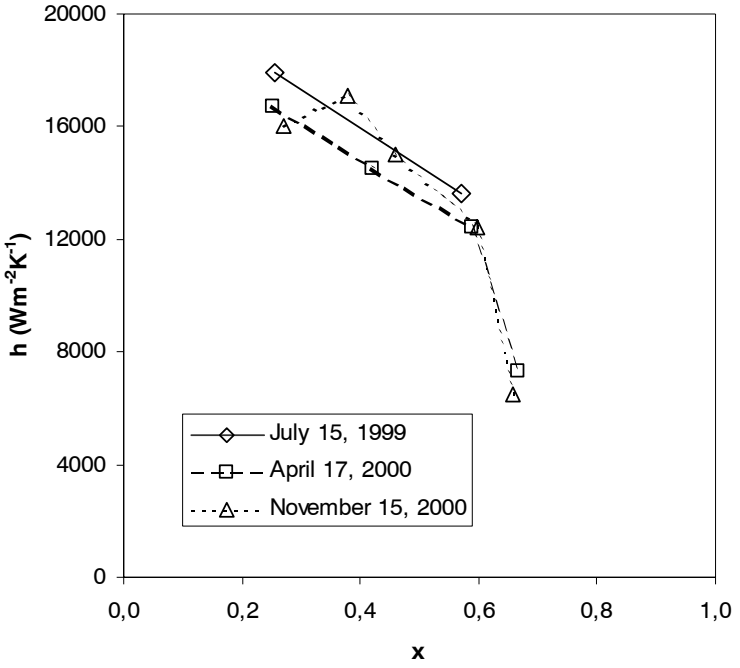

Figure 5.7 *Repeated measurements of CO_2-side heat transfer coefficient at varying vapour fraction, at the following conditions: Evaporating temperature 20°C, mass flux 300 kgm^{-2}s^{-1}, and heat flux 10 kWm^{-2}*

5.8.2 Uncertainty analysis of calibration data

In the calibration tests that were used to derive the water-side heat transfer equation, the test section heat load was determined by two independent measurements; calorimeter balances on the water side and a similar balance on the CO_2 side (single-phase CO_2 flow). Thus, accuracy could be improved by using the average value of the two capacities. As mentioned in Section 5.3, the difference between the two measured heat loads was 0.7% on average, and the maximum deviation was 1.6% or 10.1 W.

The CO_2 mass flow rate, inlet/outlet temperature and pressure was maintained constant during the calibration tests. Thus, the heat load as measured on the CO_2-side was constant, given by

$$\dot{Q} = \dot{m}_{CO2}\left[h_2(T_2, p_2) - h_1(T_1, p_1)\right] \tag{5.30}$$

with uncertainty

$$\delta\dot{Q} = \left[\left(\frac{\partial \dot{Q}}{\partial \dot{m}} \delta \dot{m} \right)^2 + \left(\frac{\partial \dot{Q}}{\partial h_2} \delta h_2 \right)^2 + \left(\frac{\partial \dot{Q}}{\partial h_1} \delta h_1 \right)^2 \right]^{1/2} \tag{5.31}$$

Both refrigerant enthalpies were measured with the same uncertainty, given by

$$\delta h = \left[\left(\frac{\partial h}{\partial T} \delta T \right)^2 + \left(\frac{\partial h}{\partial p} \delta p \right)^2 \right]^{1/2} \tag{5.32}$$

The enthalpy uncertainties at inlet temperature (5°C) and outlet temperature (15°C) were found by perturbing the input data to the thermodynamic property functions. The results are

$$\delta h_1 = \pm 147 \text{ Jkg}^{-1} \text{ at } 5^\circ\text{C and } 9.0 \text{ MPa}$$

$$\delta h_2 = \pm 164 \text{ Jkg}^{-1} \text{ at } 15^\circ\text{C and } 9.0 \text{ MPa}$$

Resulting uncertainty in measured heat load on the CO_2 side was $\delta\dot{Q} = \pm 23$ W, which, combined with water-side uncertainty data from Table 4.6, gives uncertainties of the averaged heat load during calibration tests as shown in Table 5.4.

Table 5.4 *Uncertainty in test section heat transfer rate in calibration tests.*

$\dot{m}_w$, kgs^{-1}	0.03	0.05	0.10	0.15
$\delta\dot{Q}$, W	±12	±13	±18	±23

Figure 5.8 shows typical distribution of heat transfer rate measured on the CO_2-side and the water side in a calibration experiment (Data point 4 in Table 5.2). A total of 21 measurements were taken over 21 minutes, and the two capacities calculated for each point. As may be observed from the diagrams, both measurements experience scatter with a reasonably "normal" distribution. Since the measurements were independent and the distributions "normal", the averaging was believed to reduce uncertainty.

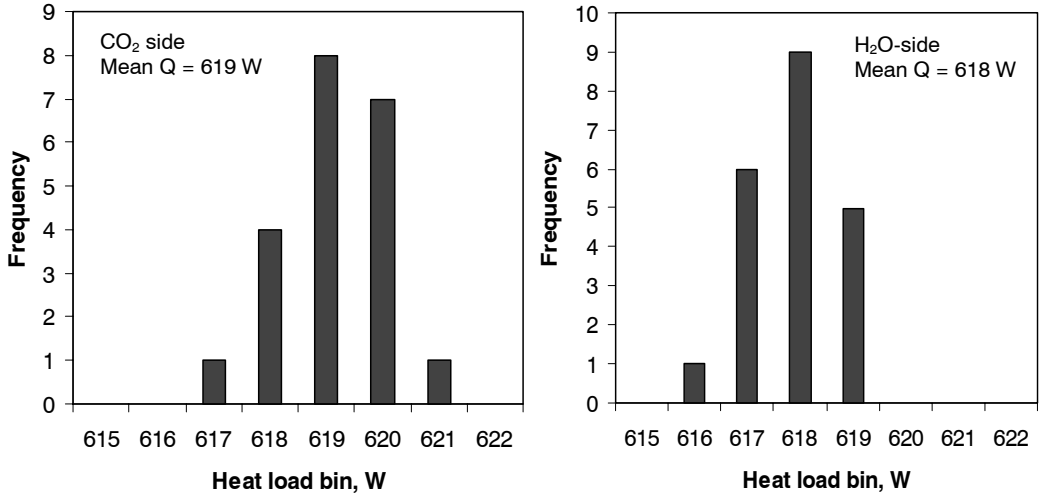

Figure 5.8 *Typical distribution of individual heat load measurements on CO_2 side and water side.*

The uncertainty in mean temperature difference between water and CO_2 (ΔT) was calculated based on Eq. (4.33), using $\delta\overline{T}_w$ = 0.045 K (Eq. 4.20), and δT_{CO2} = ±0.064 K (Table 4.3), giving

$$\delta\Delta T = \pm 0.078\ \mathrm{K} \tag{5.33}$$

The heat flux uncertainty δq was then calculated for the calibration tests, using heat load uncertainty data from Table 5.4. Table 5.5 shows some results.

Table 5.5 *Uncertainty in heat flux in calibration tests.*

$\dot{m}_w$, kgs^{-1}	0.03		0.05		0.10		0.15	
q, kWm^{-2}	10	20	10	20	10	20	10	20
δq, Wm^{-2}	±395	±449	±424	±475	±576	±614	±729	±760

Using the same methods as shown in Section 4.7.9, the uncertainty in overall heat transfer coefficient (δU) was calculated for each of the calibration tests. In addition, the uncertainty in Reynolds number was calculated. Results are shown in Table 5.6.

The percent uncertainty in mass flux and Reynolds number were more or less constant at $\delta G_w/G_w$ = ±2.6% and $\delta Re/Re$ = ±3.2%, respectively. The uncertainty in U increased from ±2.6% to ±4.5% as the Reynolds number increased from 2,400 to 12,500. On average, $\delta U/U$ was ±3.4%.

Table 5.6 *Water-side test data and calculated uncertainties in the calibration tests. Uncertainty in water temperature was* $\delta\overline{T}_w = \pm 0.045$ *K in all tests, and uncertainty in mass flow rate was* $\delta\dot{m}_w = \pm 0.2\%$ *of* $\dot{m}_w$

Data point	$\dot{m}_w$ kgs^{-1}	G_w kgm^{-2}s^{-1}	δG_w kgm^{-2}s^{-1}	$\overline{T}_w$, °C	Re	δRe	U Wm^{-2}K^{-1}	δU Wm^{-2}K^{-1}
1	0.0286	459.3	±11,8	16.85	2357	±74	3002	±77
2	0.0356	571.7	±14,7	16.64	2914	±92	3261	±88
3	0.0417	669.7	±17,3	16.39	3392	±107	3468	±96
4	0.0486	780.5	±20,1	16.27	3938	±125	3670	±105
5	0.0555	891.3	±23,0	16.13	4487	±143	3846	±114
6	0.0576	925.1	±23,8	16.11	4652	±148	3894	±117
7	0.0595	955.6	±24,6	16.04	4794	±153	3959	±120
8	0.0698	1121.0	±28,9	15.92	5610	±180	4175	±131
9	0.0714	1146.7	±29,6	16.25	5786	±184	4233	±138
10	0.0777	1247.9	±32,2	15.83	6230	±200	4342	±144
11	0.0780	1252.7	±32,3	15.90	6262	±201	4347	±144
12	0.0824	1323.4	±34,1	15.84	6608	±213	4421	±150
13	0.0913	1466.3	±37,8	15.77	7306	±236	4576	±161
14	0.0947	1520.9	±39,2	15.75	7578	±245	4636	±165
15	0.1047	1681.5	±43,3	15.71	8370	±270	4752	±179
16	0.1079	1732.9	±44,7	15.68	8620	±272	4814	±182
17	0.1171	1880.7	±48,5	15.62	9334	±296	4899	±194
18	0.1318	2116.7	±54,6	15.64	10511	±333	5077	±209
19	0.1445	2320.7	±59,8	15.61	11518	±365	5189	±227
20	0.1565	2513.4	±64,8	15.60	12475	±395	5267	±239

5.8.3 Uncertainty analysis of regression-based water-side heat transfer coefficient

In order to derive uncertainty data for the regression-based heat transfer coefficient for the water side, a comprehensive propagation analysis was made. Since the heat transfer correlation was derived through regression, the analysis had to include the propagation of uncertainties through the regression scheme.

The heat transfer coefficient was regarded as a function of three variables:

$$h_o = h_o(U, Re, R) \tag{5.34}$$

where R is the sum of the fixed resistances, i.e. conduction/fouling, and convective heat transfer on the inside during calibration.

$$R = R_{cf} + R_i \tag{5.35}$$

Thus, the uncertainty in water-side heat transfer coefficient is:

$$\delta h_o = \left[\left(\frac{\partial h_o}{\partial U} \delta U \right)^2 + \left(\frac{\partial h_o}{\partial Re} \delta Re \right)^2 + \left(\frac{\partial h_o}{\partial R_{fixed}} \delta R_{fixed} \right)^2 \right]^{1/2} \tag{5.36}$$

In other words, the underlying procedure of regression was regarded as a functional relation for h_o based on U, Re, and R. In this respect, U and Re were independently measured parameters, and R was a parameter that resulted partly from the assumptions on fouling and conduction resistance shown in Section 5.4, partly from the original (baseline) regression, and partly from calculated single-phase CO_2 heat transfer, as shown in Section 5.4.1.

Khartabil and Christensen (1992) discussed a scheme for calculation of uncertainties in heat exchanger regressions. With some modifications, this comprehensive procedure has been used to calculate the uncertainties in h_o caused by δU and δRe from Table 5.6. The following steps were involved:

1. For the first data point in Table 5.6, the original U was perturbed in a positive direction by its uncertainty δU, while Re remained unchanged.

2. A regression was conducted based on the data set having the perturbed U point with the remaining points unchanged, finding a new expression for the water-side heat transfer coefficient h_o. The difference between the new h_o and the original h_o was then computed for every Re in the calibration series, giving values of Δh_o for each Re. Since the constants C and m are not independent, these could not be assessed individually.

3. The same procedure as in 1. and 2. was carried out with a negative perturbation of U by δU for the first data point. The average of the absolute values of the two Δh_o was then used as the representative value at each Re. Perturbations in both directions were used since the relations were not linear.

4. The procedure in 1., 2., and 3. was then repeated for each of the 20 data points, i.e. 40 regressions, with one data point perturbed at a time. This finally gave a set of 20 Δh_o-values for each Re. The parameter $(\partial h_o/\partial U)\delta U$ at each Re was then taken as the root-mean-square of all 20 Δh_o.

5. A similar procedure as 1. to 4. was then repeated with perturbations of Re (from Table 5.6) instead, keeping U constant. This gave variations ΔRe for each data point. In the same way as above, after 40 regressions, this eventually gave the factor $(\partial h_o/\partial Re)\delta Re$ at each Re as the root-mean-square of the individual factors from each regression.

The above procedure differs from the one proposed by Khartabil and Christensen (1992) in that actual uncertainties of U and Re were used for each data point, and not average relative uncertainties.

Uncertainty in the fixed resistance R was calculated by a different scheme. The combined fouling and conduction resistance (R_{cf}), which was calculated/estimated to 10^{-5} m^{2}KW^{-1} in Section 5.4, was assumed to have a large uncertainty. Thus it would be reasonable to assume that it could vary between 0.5 and 1.5 times the calculated value, i.e. an uncertainty of ±50% or

$$\delta R_{cf} = \pm 0.5 \cdot 10^{-5} \text{ m}^2\text{KW}^{-1}$$

The fixed internal resistance (R_i) of 1/9840 m^{2}KW^{-1} due to convective heat transfer between CO_2 and the tube wall was based partly on regression and partly by prediction using common single-phase flow models. Normally, such predictions would be expected to have an uncertainty of around ±15-20% (Gnielinski, 1976). Due to the good correspondence between several models (Section 5.4.1), it was assumed that uncertainty was somewhat better, at ±10%. Thus, the uncertainty in internal resistance in the calibration tests was

$$\delta R_i = \pm 1.02 \cdot 10^{-5} \text{ m}^2\text{KW}^{-1}$$

The resulting total uncertainty of the fixed resistance was calculated as the root-mean-square of the two parts:

$$\delta R = \left[\delta R_{cf}^2 + \delta R_i^2\right]^{1/2} = 1.14 \cdot 10^{-5} \text{ m}^2\text{KW}^{-1} \qquad (5.37)$$

In order to evaluate the effect of this uncertainty, Eq. (5.20) was rewritten as:

$$\left(\frac{1}{U}-(R+\frac{1}{h_i})\right)\frac{A_o}{A_i}=\frac{1}{C}\cdot Re^{-m}Pr^{-1/3}\cdot\frac{D}{k} \tag{5.38}$$

where

$$R_{cf}+\frac{1}{h_i}=R_{cf}+R_i=R \tag{5.39}$$

Now, perturbations of R could be introduced in the regressions, based on similar principles as above. In this case, however, only one regression was needed in the negative and positive direction, respectively, since δR was constant for all Reynolds numbers. Table 5.7 gives a summary of the uncertainty data, including the total uncertainty in water-side heat transfer coefficient (δh_o) based on Eq. (5.36). As may be observed from the Table, the uncertainty in fixed resistance dominates among the three terms that contribute to uncertainty in the heat transfer coefficient

As shown by Figure 5.9, the uncertainty δh_o is an almost linear function of the Reynolds number. Figure 5.10 shows the relative uncertainty.

The uncertainty can be expressed as the following linear function:

$$\delta h_o=\pm(0.241Re-235)\quad \mathrm{Wm^{-2}K^{-1}} \tag{5.40}$$

Most evaporation tests were conducted at Reynolds numbers ranging from 3000 to 6000, where the relative uncertainty $\delta h_o/h_o$ was between 8% and 13%.

Uncertainty of the vaporization heat transfer coefficient is discussed in Chapter 6, together with the experimental data.

Table 5.7 *Uncertainty data for water-side heat transfer coefficient in the calibration tests.*

Data point	Re	$(\partial h_o/\partial U)\cdot \delta U$ $Wm^{-2}K^{-1}$	$(\partial h_o/\partial Re)\cdot \delta Re$ $Wm^{-2}K^{-1}$	$(\partial h_o/\partial R)\cdot \delta R$ $Wm^{-2}K^{-1}$	h_o $Wm^{-2}K^{-1}$	δh_o $Wm^{-2}K^{-1}$	$\delta h_o/h_o$ %
1	2357	197	82	244	5268	324	6,2
2	2914	279	100	349	6036	458	7,6
3	3392	350	121	440	6658	575	8,6
4	3938	432	151	544	7327	711	9,7
5	4487	514	177	648	7967	846	10,6
6	4652	539	186	679	8154	887	10,9
7	4794	560	194	706	8314	922	11,1
8	5610	682	240	860	9195	1123	12,2
9	5786	706	249	890	9356	1163	12,4
10	6230	774	276	976	9833	1275	13,0
11	6262	778	277	981	9861	1282	13,0
12	6608	829	297	1046	10208	1367	13,4
13	7306	931	338	1175	10885	1537	14,1
14	7578	971	353	1225	11143	1603	14,4
15	8370	1086	399	1370	11872	1793	15,1
16	8620	1122	413	1416	12098	1853	15,3
17	9334	1225	454	1545	12731	2024	15,9
18	10511	1392	520	1756	13727	2300	16,8
19	11518	1534	577	1935	14550	2535	17,4
20	12475	1667	630	2103	15309	2757	18,0

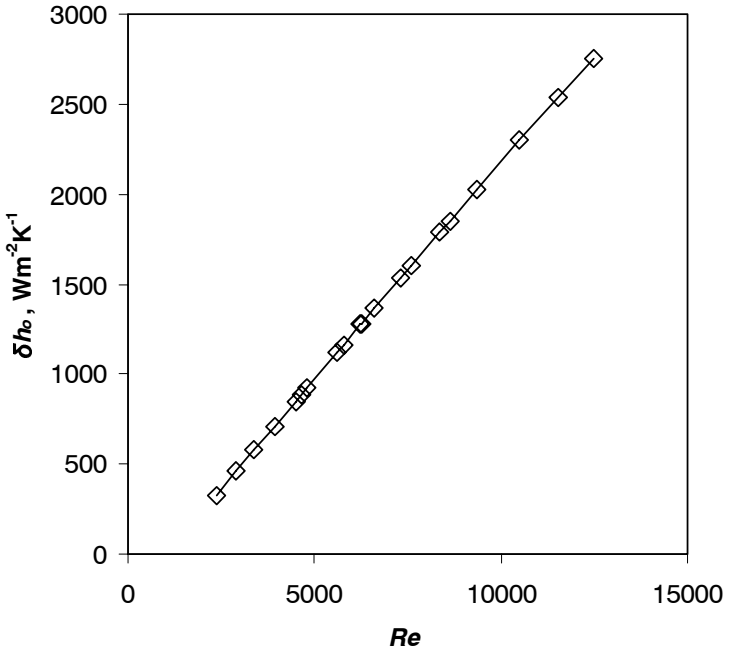

Figure 5.9 *Uncertainty in water-side heat transfer coefficient at varying Reynolds number.*

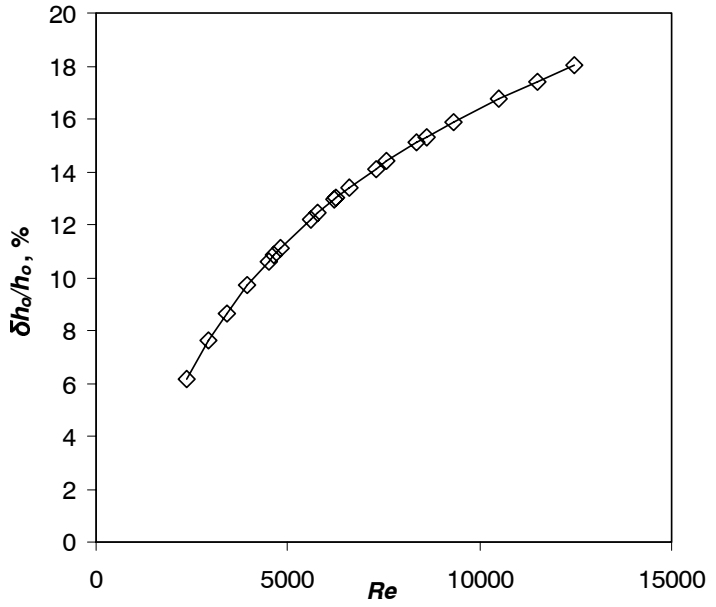

Figure 5.10 *Relative uncertainty in water-side heat transfer coefficient at varying Reynolds number*

5.8.4 Temperature fluctuation effects

Wojs and Tietze (1997) showed that temperature interference (fluctuation, oscillation, or random variation) could have a significant effect on the heat transfer coefficient determined by Wilson-plot methods. By introducing random temperature variation using a normal-distribution interference with zero average and known variance, they found the influence of a RMS[h] deviation of σ=0.01, 0.1 and 1.0 K, respectively. This variation was introduced to the hot and cold fluid outlet temperatures from the test section, while the fluid flow rate on the variable-resistance side was varied. The σ=0.01 K deviation was found to influence the resulting heat transfer coefficient by less than 2%, while a deviation of σ=0.1 K gave an uncertainty of about 20%. The 1.0 K case gave unacceptable and sometimes unphysical results.

In the present calibration tests, the standard deviation of measured water and CO_2 outlet temperatures from the test section were calculated for each test run (at a given water flow rate). Results from one test were taken as mean values from 20-30 data points logged during 20-30 minutes at steady-state conditions. Typically, the standard deviation for such a measured temperature point was about 0.02 K. These data are not directly comparable to the "interference data" used by Wojs and Tietze (1997), because only individual data points are characterized in the present results. The standard deviation calculated from all the water and CO_2 outlet temperature variance data for the 21 calibration tests is about 0.01 K. It thus seems like temperature fluctuations should not introduce significant (more than 5%) uncertainties in the present heat transfer data.

[h] Root Mean Square, in this case over a range of fluid flow rate on the variable-resistance side

6. Test data and observations

6.1 Chapter overview

This Chapter gives an overview of test data and observations from heat transfer measurements, pressure drop measurements, and two-phase flow pattern observations. In the first part of the Chapter, the test program is outlined, including a discussion on test conditions and parameters. Next, the change in x through the test section is shown at varying heat and mass flux. The uncertainty of heat transfer data is then shown, before the heat transfer test data are presented at varying heat flux, mass flux, and evaporating temperature. A special section is devoted to nucleate boiling heat transfer data. Pressure drop recordings are then presented for the same conditions. Finally, the flow pattern observations results are explained, in series at constant G and varying x, and the results are shown in flow regime charts.

6.2 Heat transfer and pressure drop test program

6.2.1 Test conditions

Microchannel heat transfer tubing for CO_2 will most likely be used primarily in compact heat exchangers for vehicle or residential air conditioners and heat pumps. From an engineering point of view, flow vaporization heat transfer and pressure drop test data are therefore needed for temperatures in the range 0 to 15°C for air conditioning, and –30 to 0°C for heat pump applications. Owing to the low critical temperature of CO_2 (31.1°C), properties like surface tension, liquid-to-vapour density difference, and evaporation enthalpy, departs considerably from those of conventional refrigerants at air conditioning evaporation temperatures. The primary interest from a scientific point of view would therefore be to study

evaporation heat transfer at near-critical temperatures, to see the effects of these peculiar properties. Also, from an experimental point of view, it is simpler to operate close to normal room temperature, since heat losses into the test section become less of an issue, and water can be used as secondary fluid. The use of water is practical, and it is also reduces experimental uncertainty compared to other fluids, e.g. alcohols. Owing to the high heat transfer coefficient of water, maximum resolution and accuracy is obtained in the determination of refrigerant-side heat transfer coefficients. Focus of the present study has therefore been on evaporating temperatures between 0 and 25°C.

Other experimental parameters include mass flux (G), heat flux (q) and vapour fraction (x). Relevant range was assumed for each variable, reflecting the conditions of operation that are likely to be encountered in actual compact evaporators. Vapour fraction was generally varied from slightly above zero to almost one in each experimental series. Table 6.1 provides an overview of the test condition range.

Table 6.1 *Range of nominal test conditions*

Parameter	Symbol	Unit	Range
Mass flux	G	$kgm^{-2}s^{-1}$	190 - 570
Heat flux	q	Wm^{-2}	5,000 – 20,000
Evaporating temperature	T	°C	0 - 25

A few tests were conducted at higher heat flux than shown in the Table, see Section 6.4.4. In total, 143 test points were recorded, one point being a recording of heat transfer coefficient and pressure drop gradient at a combination of the above parameters (x, G, q, T).

During a typical test, slightly subcooled CO_2 was pumped into the preheater section, where the liquid was partly evaporated to achieve the desired vapour fraction at the test section inlet. In the test section, further vaporization occurred by absorbing heat from the water. The test section outlet vapour fraction was adjusted by water temperature and flow rate, in order to get the desired mean vapour fraction. After the test section, the two-phase flow entered the condenser, where the vapour was liquefied.

6.2.2 Change in vapour fraction through test section

In contrast to tests where local heat transfer coefficients are measured by wall temperatures, the present test rig provided data based on mean values for the test section length. As explained in Section 4.6.1, the mean value was based on geometric length ("length-averaging") of local x as shown by Eq. (4.6). The change in x through the test section depended on heat flux and

mass flux, as well as evaporation enthalpy. Figures 6.1 and 6.2 show the change in x from test section inlet to outlet at some typical test conditions. The abscissa shows change in x below and above the mean point for the test. As may be observed, the change in x (Δx) is larger above the mean value than below it. This is caused by the mean-value calculation scheme. Since water flows in the opposite direction of CO_2 in the test section, the necessary tube length is larger from the refrigerant inlet and up to the mean point, than from the mean point to the outlet where the temperature difference is larger. Due to the "length-averaging" procedure, the mean x will be located nearer the refrigerant inlet. In reality, the degree of "eccentricity" varies from test to test due to variation in water flow rate and -temperature. In the present test program, the Δx above the mean value was between 1% and 25% larger than the Δx below the mean. In the diagrams, the average ratio of 16% difference was used.

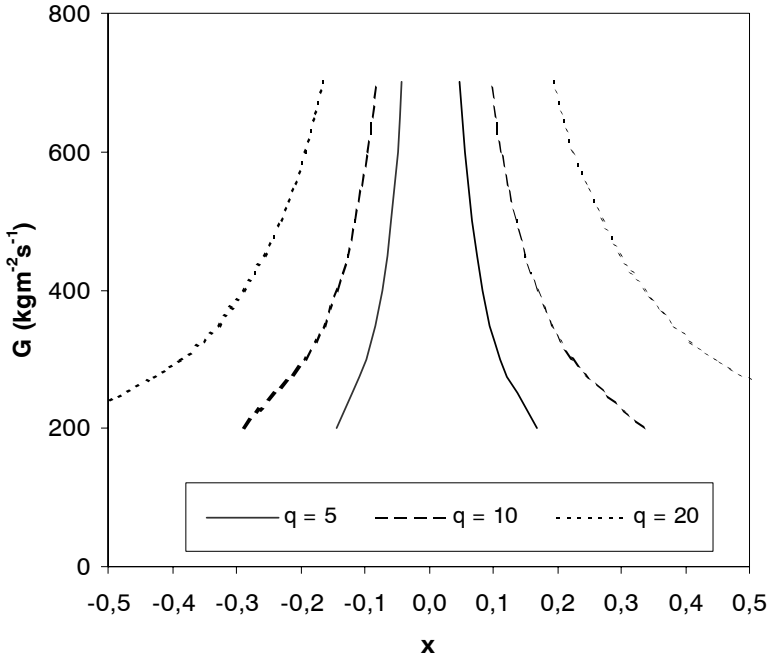

Figure 6.1 *Range of x in the test section below and above the mean value at varying mass flux (G) and heat flux (q). Heat flux curves are shown for 5, 10 and 20 kWm^{-2}. The evaporation temperature is maintained constant at 10°C*

As may be observed from Figure 6.1, combinations of high heat flux and low mass flux are not possible due to x becoming subcooled or superheated. A similar effect can be seen in Figure 6.2 as the evaporation enthalpy drops at higher temperature. The diagrams give some idea about the range of x that is possible without entering the subcooled liquid or superheated vapour region, depending on the operating conditions.

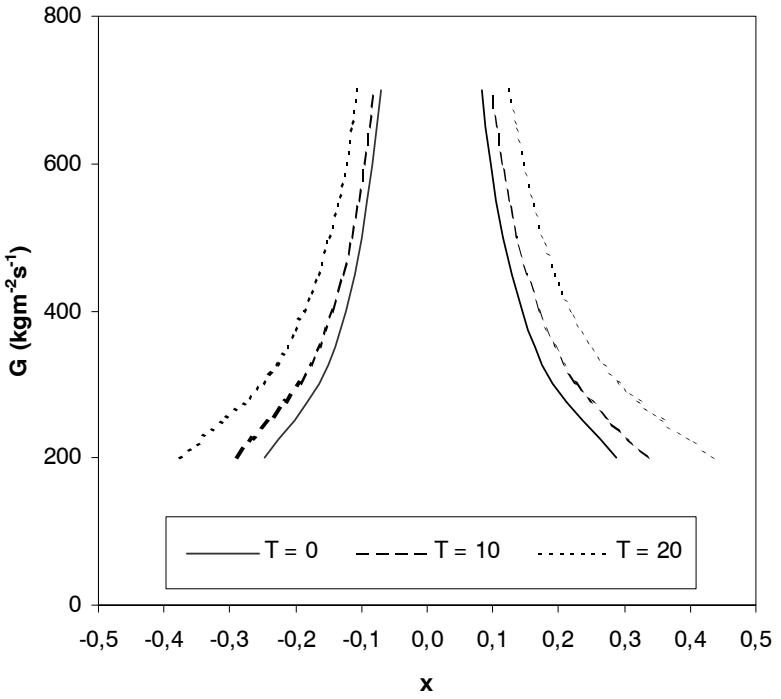

Figure 6.2 *Range of x in the test section below and above the mean value at varying mass flux (G) and evaporating temperature (T). Temperature curves are shown for 5, 10 and 20°C. The heat flux is maintained constant at 10 kWm-2*

6.3 Uncertainty of heat transfer coefficients

Uncertainty of the measured heat transfer coefficient has been calculated based on data and principles from Chapters 4 and 5. Equation (5.1) can be rewritten as

$$\frac{1}{h_i} = \frac{1}{U} - R_{cf} - \frac{1}{h_o}\left(\frac{A_i}{A_o}\right) \tag{6.1}$$

or

$$h_i = \frac{1}{\frac{1}{U} - R_{cf} - \frac{1}{h_o}\left(\frac{A_i}{A_o}\right)} \tag{6.2}$$

where

$$h_o = h_o(Re, Pr) \tag{6.3}$$

as defined by Eq. (5.29). Uncertainty data for U are given in Figures 4.12 to 4.14, and uncertainty data for h_o at varying Reynolds numbers are given in Table 5.7. The uncertainty in Prandtl number and its influence on h_o is negligible. On this basis, the uncertainty of the CO_2 side heat transfer coefficient can be calculated from

$$\delta h = \left[\left(\frac{\partial h}{\partial U} \delta U \right)^2 + \left(\frac{\partial h}{\partial h_o} \delta h_o \right)^2 \right]^{1/2} \tag{6.4}$$

In Equation (6.4) and the following text, the CO_2-side heat transfer coefficient is designated with the symbol "h " without a subscript.

Figure 6.3 shows the relative uncertainty of h (in %) at varying level of measured heat transfer coefficient and varying evaporating temperature, for a heat flux of 10 kWm^{-2} and a water mass flow rate of 0.05 kgs^{-1}. As pointed out in Chapter 4, most tests were carried out with this water mass flow rate.

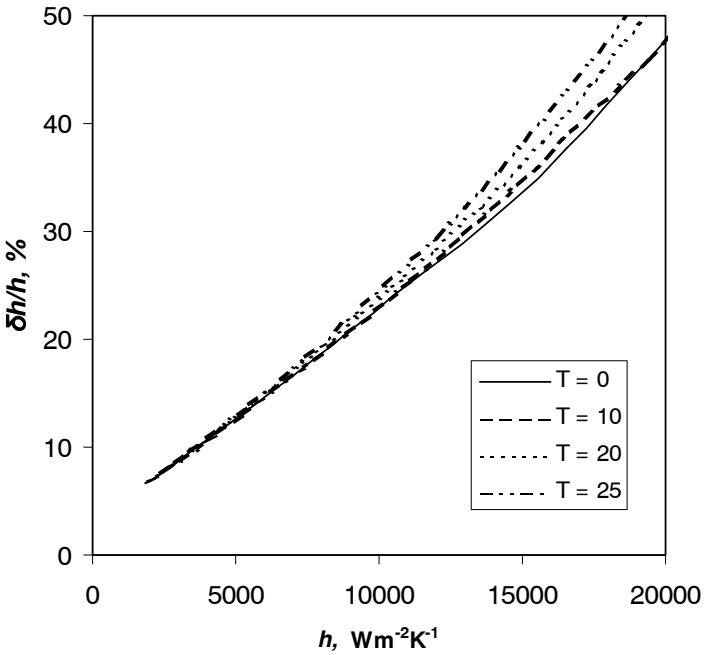

Figure 6.3 *Relative uncertainty of CO_2 vaporization heat transfer coefficient, at a heat flux of 10 kWm^{-2} and a water-side mass flow of 0.05 kg/s.*

As may be observed, the relative uncertainty in measured vaporization heat transfer coefficient is an almost linear function of the coefficient itself, increasing from about ±13% at a measured h of 5000 $Wm^{-2}K^{-1}$, to almost ±40% if the heat transfer coefficient is 15000 $Wm^{-2}K^{-1}$. Uncertainty increases a bit with evaporating temperature. As shown by Figure 6.4, the uncertainty is reduced when the heat flux is increased to 20 kWm^{-2}, giving a typical uncertainty of ±30% at h=15000 $Wm^{-2}K^{-1}$.

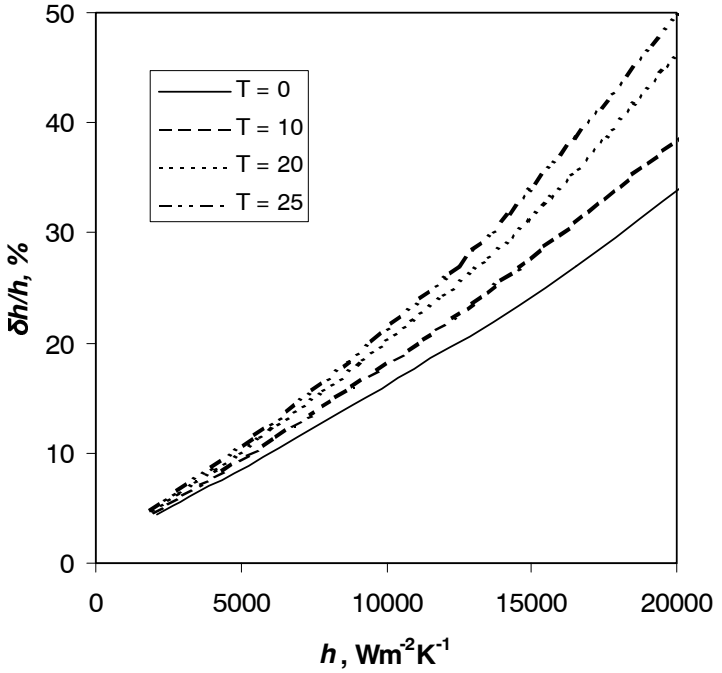

Figure 6.4 *Relative uncertainty of CO_2 vaporization heat transfer coefficient, at a heat flux of 20 kWm^{-2} and a water-side mass flow of 0.05 kg/s.*

Figure 6.5 shows the effect of varying water flow rate on the relative uncertainty, for a temperature of 10°C and a heat flux of 10 kWm^{-2}. Increased water mass flow rate gives a noticeable increase in the uncertainty.

Increased relative uncertainty at higher h is caused by two primary reasons:

- As h increases, the importance of water-side resistance becomes larger, and thus also the importance of uncertainty in water-side resistance. When h is high, the relative impact of δh_o thus becomes very large.

- The influence of the constant uncertainty in temperature difference between water and CO_2 becomes large when ΔT becomes small, i.e. when h is high. This effect was also observed in the uncertainty of U shown in Figures 4.12 to 4.14.

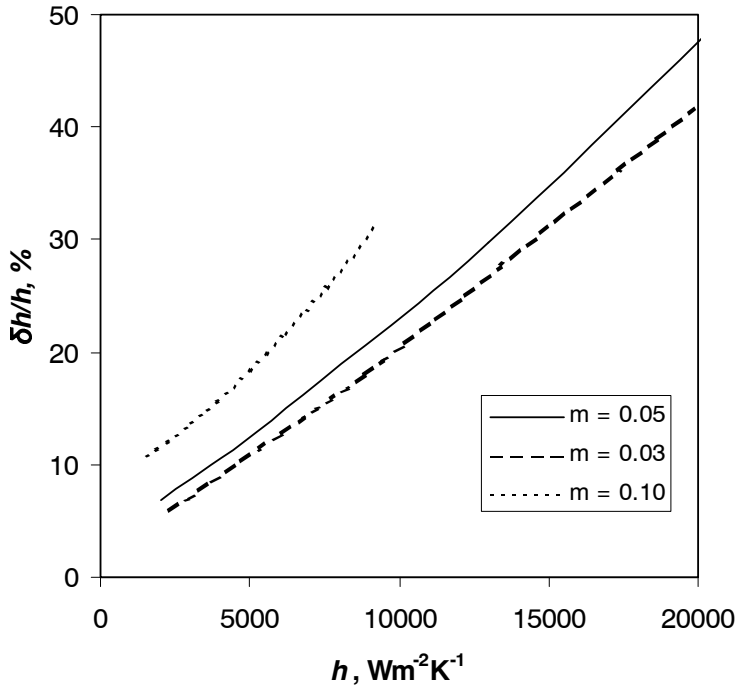

Figure 6.5 *Relative uncertainty of CO_2 vaporization heat transfer coefficient, at heat flux 10 kWm^{-2}, temperature 10°C, and water mass flow of 0.03, 0.05 and 0.10 kg/s.*

Uncertainty in h increases as the heat flux is reduced, because the constant (absolute) uncertainty in q becomes more important at lower heat flux.

In contrast to the U-uncertainty data, where $\delta U/U$ was reduced at higher evaporating temperature, $\delta h/h$ instead increases with temperature. A higher evaporating temperature leads to higher water temperature and higher water-side Reynolds number (for a given water mass flow rate), which gives larger uncertainty in the water-side heat transfer coefficient. This increased uncertainty leads to increased uncertainty in h as well, since h is the result of subtracting the water-side resistance ($1/h_o$) from the total resistance ($1/U$).

Experimental uncertainty for the heat transfer coefficient becomes very high as the measured coefficient increases above 15,000-20,000 Wm^{-2}K^{-1}. Some improvement may be possible by reducing the uncertainty of the fixed resistance (mainly fouling), and/or by improving heat transfer on the water side. The use of wall temperature measurement is not likely to give lower uncertainty, as pointed out earlier. To a certain extent, large uncertainty must therefore be accepted in this range of geometry and heat transfer efficiency. Some of the nucleate boiling data at high temperature should be considered as very uncertain, though.

6.4 Heat transfer results

6.4.1 Heat transfer at varying heat flux

Figure 6.6 shows test data taken at evaporating temperature T=10°C and a mass flux (G) of 300 kgm^{-2}s^{-1}. The heat flux (q) was varied between three different levels; 5, 10 and 15 kWm^{-2}. In this diagram, lines ("error bars") are included, showing the range of x from the test section inlet to the outlet. Since these lines make the diagrams difficult to read, they are omitted in the remaining figures. The reader should keep in mind that all data points are based on mean values for x and h in the test section, and consult Figures 6.1. and 6.2 for information on the actual range of x in each experiment.

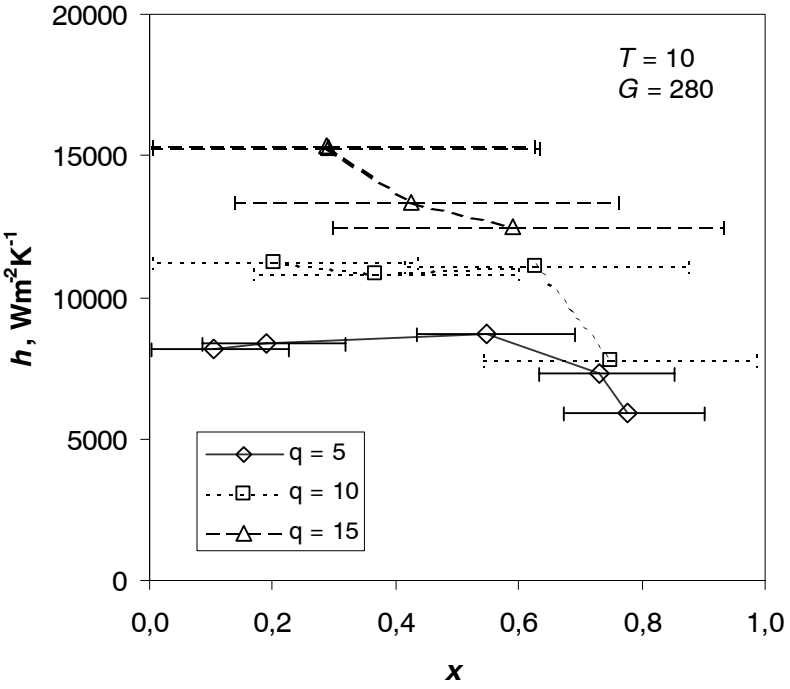

Figure 6.6 *Measured heat transfer coefficient (h) at varying vapour fraction (x), for heat fluxes (q) 5, 10 and 15 kWm^{-2}. Evaporating temperature is 10°C and mass flux is G=280 kgm^{-2}s^{-1}.*

Varying heat flux has a significant effect on heat transfer at low and moderate vapour fraction, while the curves seem to fall closer together at higher vapour fraction. This behaviour indicates a dominance of nucleate boiling in the low/moderate vapour fraction region, and a dominance of other mechanisms such as dryout or convective evaporation at higher x.

Figure 6.7 shows test data taken at the same evaporating temperature (10°C), but slightly higher heat fluxes 10 and 20 kWm^{-2}, and a higher mass flux of G=570 kgm^{-2}s^{-1}. The same tendencies as in Figure 6.6 can be observed here. Again, the heat flux has a major influence on heat transfer at low/moderate x, while the influence is quite small at higher x. Heat transfer coefficients in the low x range are at the same level as in Figure 6.6, despite the twice as high mass flux. This is another indicator that nucleate boiling dominates at low x.

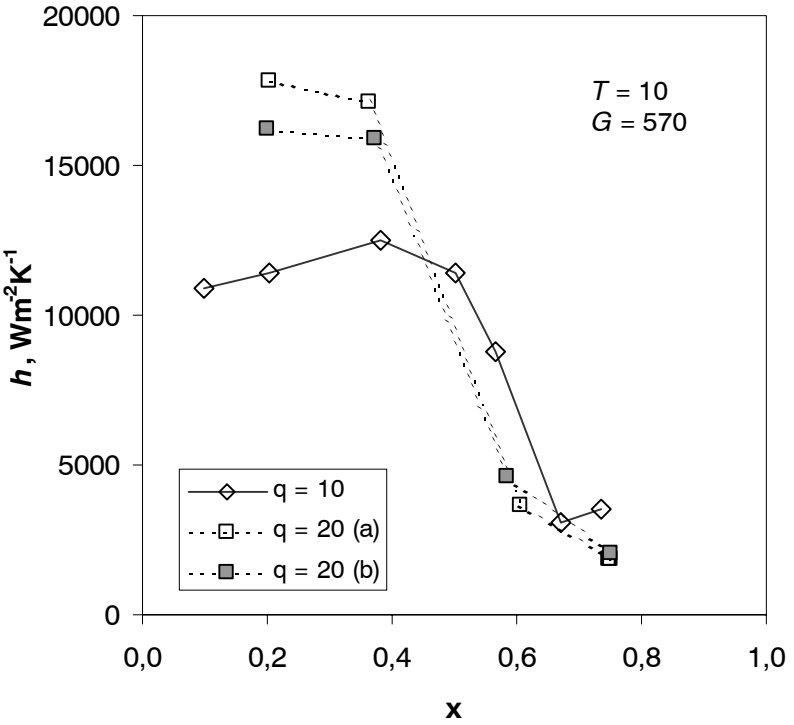

Figure 6.7 *Measured heat transfer coefficient (h) at varying vapour fraction (x), for heat fluxes (q) 10 and 20 kWm^{-2}. Evaporating temperature is 10°C and mass flux is G=570 kgm^{-2}s^{-1}. Results (a) and (b) are from different test series.*

Figure 6.8 shows test data at G=280 kgm^{-2}s^{-1} and an evaporating temperature of 20°C, i.e. the same conditions as in Figure 6.6 but a higher temperature. A higher temperature apparently gives higher heat transfer coefficients, but the data points are too few to make definite comments on the general tendency. Since the points are quite close even at a moderate x around 0.4 it may seem like convective evaporation becomes dominant at a lower vapour fraction than in Figure 6.6.

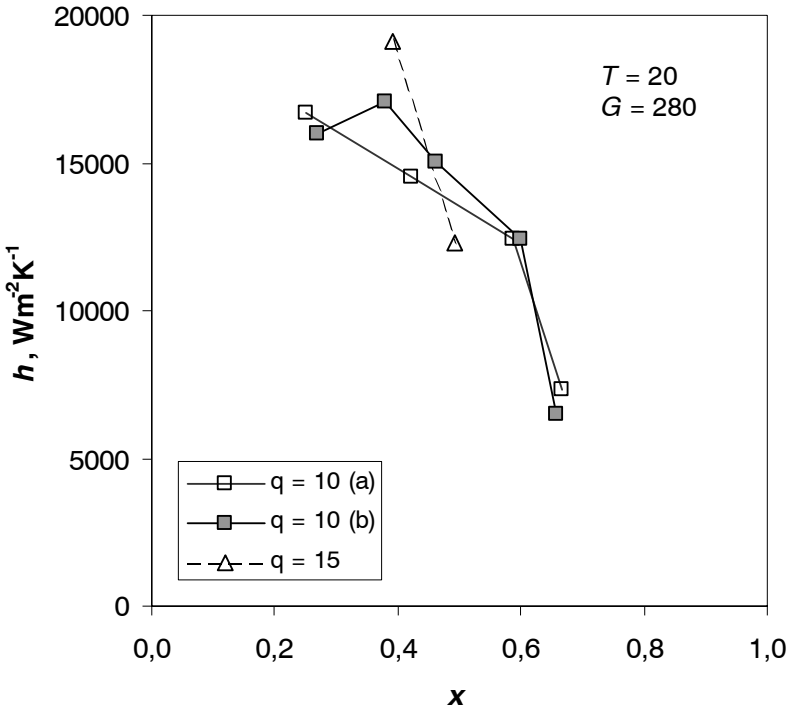

Figure 6.8 *Measured heat transfer coefficient (h) at varying vapour fraction (x), for heat fluxes (q) 10 and 15 kWm^{-2}. Evaporating temperature is 20°C, and mass flux is G=280 kgm^{-2}s^{-1}. Results (a) and (b) are from different test series.*

6.4.2 Heat transfer at varying mass flux

Figure 6.9 shows the influence on measured heat transfer coefficient by varying mass flux (G), at an evaporating temperature of 0°C and a heat flux of q=10 kWm^{-2}.

Varying mass flux and vapour fraction (both related to flow velocity) has little or no influence on heat transfer over a wide range of x. At 0°C a drop in heat transfer at x>0.6 is observed for the highest mass flux.

In Figure 6.10, data are shown for the same conditions, but at a temperature of 10°C. Both figures show how variation in mass flux and x has little or no influence on heat transfer at low/moderate x, again indicating a dominance of nucleate boiling. As observed before, the nucleate boiling heat transfer coefficients increase with temperature, like shown when comparing Figure 6.9 and 6.10. The most striking observation is the sudden drop in heat transfer coefficient at a vapour fraction of 0.5 to 0.7.

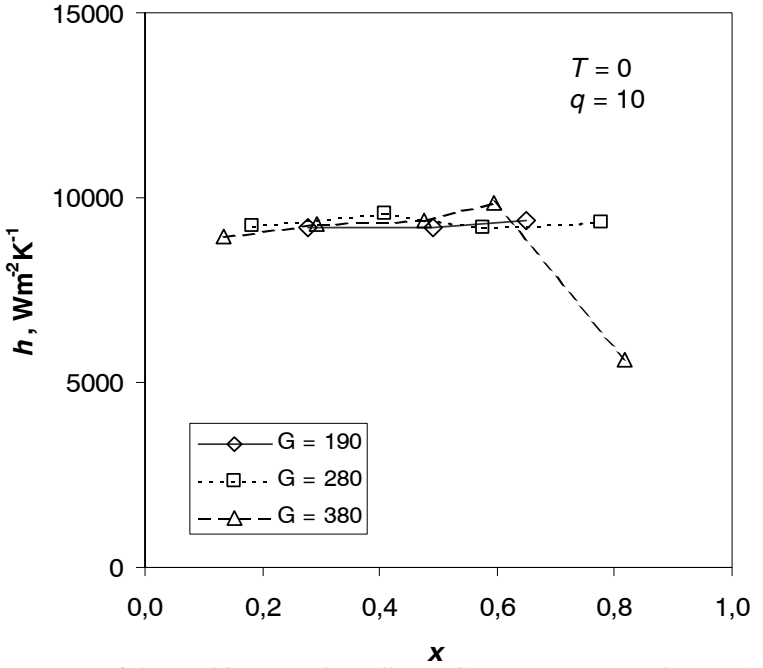

Figure 6.9 *Measured heat transfer coefficient (h) at varying vapour fraction (x), for mass fluxes (G) 190, 280 and 380 kgm^{-2}s^{-1}. Evaporating temperature is 0°C, and heat flux is q=10 kWm^{-2}.*

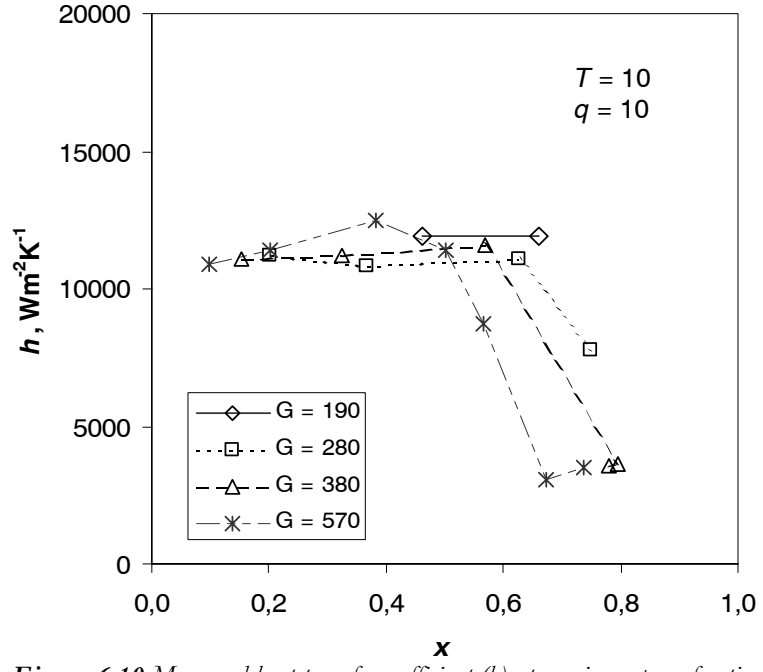

Figure 6.10 *Measured heat transfer coefficient (h) at varying vapour fraction (x), for mass fluxes (G) 190, 280 and 570 kgm^{-2}s^{-1}. Evaporating temperature is 10°C, and heat flux is q=10 kWm^{-2}.*

This behaviour is quite similar to the dryout effects observed by Hihara (2000) and Sun and Groll (2001), referred to in Chapter 3. Increased mass flux seems to move the onset of dryout to lower x, thus indicating that the flow velocity may play a role in defining the inception of dryout. In Figures 6.11 and 6.12, the evaporating temperature has been further increased to 20 and 25°C, respectively.

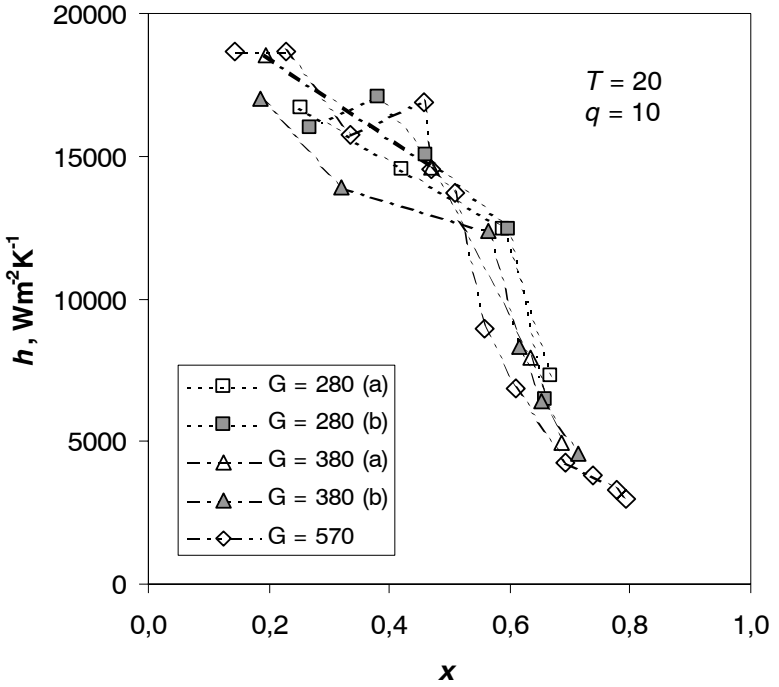

Figure 6.11 *Measured heat transfer coefficient (h) at varying vapour fraction (x), for mass fluxes (G) 280, 380, and 570 kgm^{-2}s^{-1}. Evaporating temperature is 20°C, and heat flux is q=10 kWm^{-2}. Results (a) and (b) are from different test series.*

At these higher temperatures, the measured nucleate boiling heat transfer coefficients become extremely high, and limitations in the test rig prevented testing at lower vapour fractions than shown. Still the tendencies observed in the earlier diagrams are present: Very rapid decrease in h beyond a certain critical x, and earlier onset of dryout at higher G. From Figures 6.11 and 6.12 it seems like the mass flux has little or no influence on heat transfer near the completion of dryout. Finally, the onset of dryout seems to occur at lower x at higher evaporating temperature.

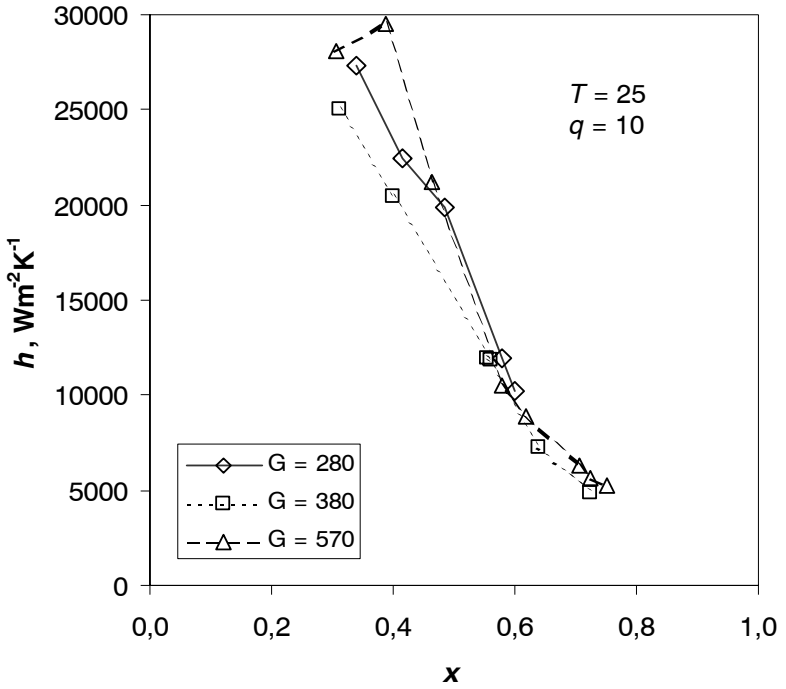

Figure 6.12 *Measured heat transfer coefficient (h) at varying vapour fraction (x), for mass fluxes (G) 280, 380, and 570 kgm^{-2}s^{-1}. Evaporating temperature is 25°C, and heat flux is q=10 kWm^{-2}.*

6.4.3 Heat transfer at varying evaporating temperature

Figure 6.13 shows test data recorded at mass flux 280 kgm^{-2}s^{-1}and heat flux 10 kWm^{-2}, with evaporating temperature ranging from 0 to 25°C. As may be observed, heat transfer behaviour is a strong function of evaporating temperature. In the low/moderate vapour fraction region, the nucleate boiling heat transfer is strongly affected by the temperature level. Dryout effects apparently play a much greater role as temperature increases; at 0°C the heat transfer is almost constant independent of x, while at higher temperatures the dryout effects become more and more dominant. Onset of dryout is a function of temperature, apparently starting even below x=0.4 at 25°C. At high vapour fraction, the convection-dominated heat transfer coefficients apparently become lower as temperatures increases. This may be explained by reduced flow velocity at higher temperatures due to higher vapour density, and possibly due to non-equilibrium effects caused by poor heat transfer between vapour and droplets. Figure 6.14 shows the influence of varying evaporating temperature at higher heat and mass flux: q=20 kWm^{-2} and G=570 kgm^{-2}s^{-1}.

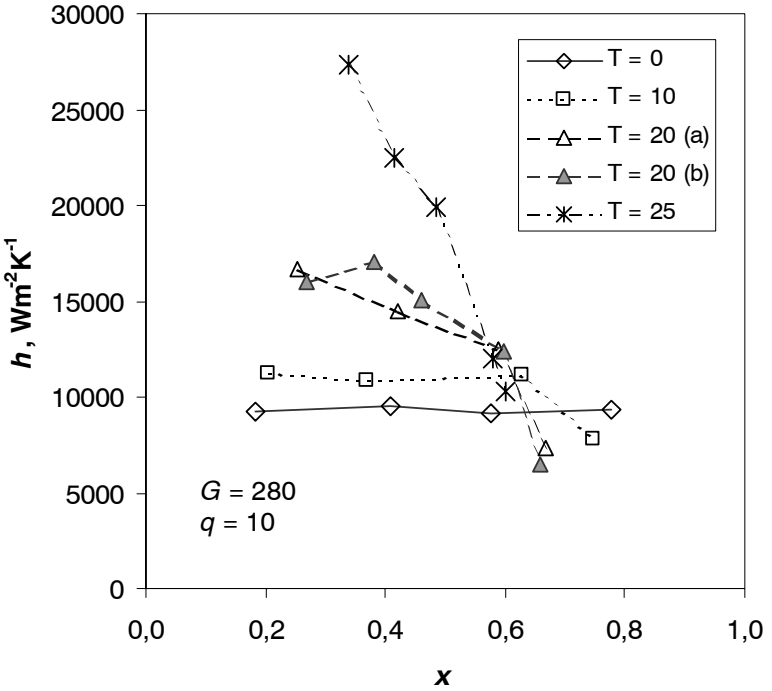

Figure 6.13 *Measured heat transfer coefficient (h) at varying vapour fraction (x), for evaporating temperatures (T) of 0, 10, 20 and 25°C. Mass flux is G=280 kgm⁻²s⁻¹, and heat flux is q=10 kWm⁻². Results (a) and (b) are from different test series*

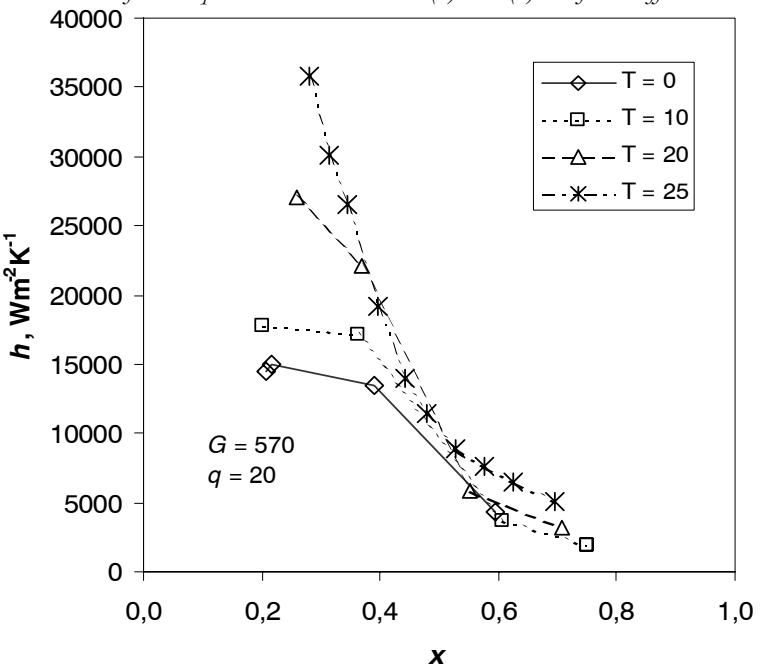

Figure 6.14 *Measured heat transfer coefficient (h) at varying vapour fraction (x), for evaporating temperatures (T) of 0, 10, 20 and 25°C. G=570 kgm⁻²s⁻¹, q=20 kWm⁻².*

At q=20 kWm^{-2}, there is a drop in heat transfer coefficient with increasing x also at 0°C. The onset of dryout again seems to occur at lower x as the temperature increases. In contrast to the curves in Figure 6.13, the heat transfer coefficient at higher vapour fraction seems to fall into the same range, regardless of temperature level. It should be remembered that the uncertainty of the heat transfer coefficient is quite large in the range of h from 15,000 Wm^{-2}K^{-1} and up (Figure 6.4), where relative uncertainty becomes larger than 30%.

Summing up the heat transfer test results, nucleate boiling dominates at low/moderate vapour fraction, with heat transfer coefficients increasing with heat flux and temperature. Dryout effects become more pronounced at increasing mass flux and temperature, with dryout inception moving to lower x. Post-dryout heat transfer is not much affected by heat flux and mass flux, but low flow velocity (low G and/or high T) may give reduced heat transfer due to non-equilibrium effects.

6.4.4 Heat transfer tests at constant inlet and outlet vapour fraction

Some tests were conducted in order to investigate the effect of varying mass flux when both the inlet and outlet vapour fraction to the test section were maintained constant. In order to achieve this, the heat flux also had to be varied simultaneously. Two such test series were conducted, at conditions as shown in Table 6.2, and results as shown in Figure 6.15.

Table 6.2 *Test conditions in Figure 6.12*

Series	x_{inlet}	x_{outlet}	q, kWm^{-2}	G, kgm^{-2}s^{-1}	T, °C
A	0.3	0.9	9.5 – 25.2	189 - 552	10
B	0.0	0.9	14.0 – 41.6	185 - 574	10

Normally, the heat transfer coefficient would be expected to increase with mass flux and heat flux, but the experimental data show that the coefficient actually has a maximum around G=300 kgm^{-2}s^{-1}. The B series gives somewhat higher coefficients, probably because a larger part of the heat transfer takes part in the nucleate boiling region.

Again these results confirm that heat transfer deteriorates at higher mass flux (and heat flux), most likely because of dry-out of the liquid film. Increased liquid entrainment at higher mass flux may explain the negative effect of higher flow velocity, and increased heat flux may also give more entrainment caused by increased bubble transport and film turbulence.

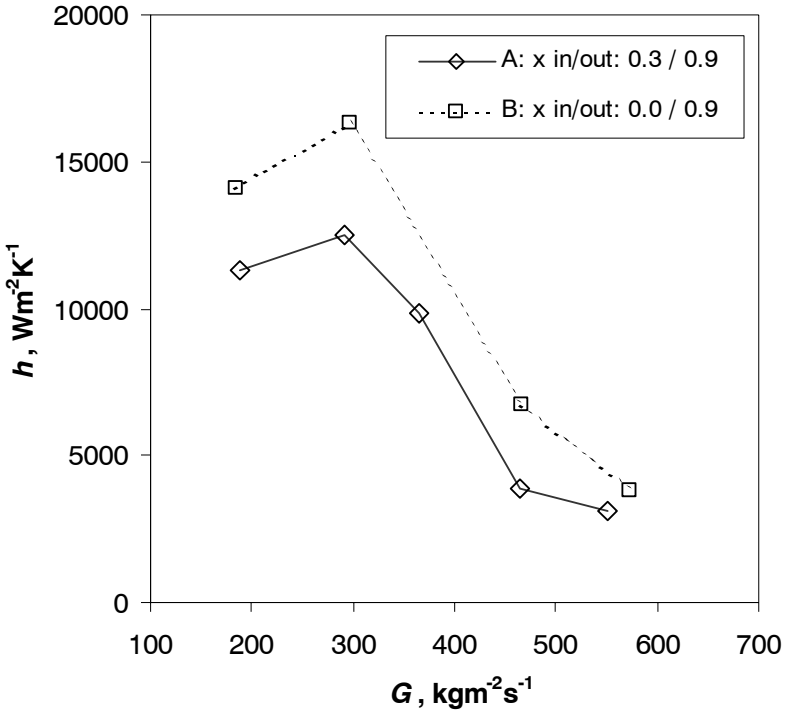

Figure 6.15 *Measured mean heat transfer coefficient at varying mass flux and heat flux, with constant test section inlet and outlet vapour fraction as indicated. Evaporating temperature 10°C.*

6.4.5 Nucleate boiling heat transfer

Figure 6.16 shows the measured relation between wall superheat and heat flux based on test data where nucleate boiling is expected to dominate, i.e. at low vapour fraction where heat transfer was not affected by varying G and x. The wall superheat ΔT is the difference between surface temperature inside the tube (T_w) and the local refrigerant temperature (saturation temperature, T_{sat}). ΔT was estimated by the relation

$$\Delta T = T_w - T_{sat} = \frac{q}{h} \tag{6.5}$$

As would be expected, the data points for a given temperature fall together along a curve. Within a narrow range of heat flux and wall superheat, the curve may be approximated by a linear relationship as shown. Also as expected, increased boiling temperature gives smaller superheat for a given

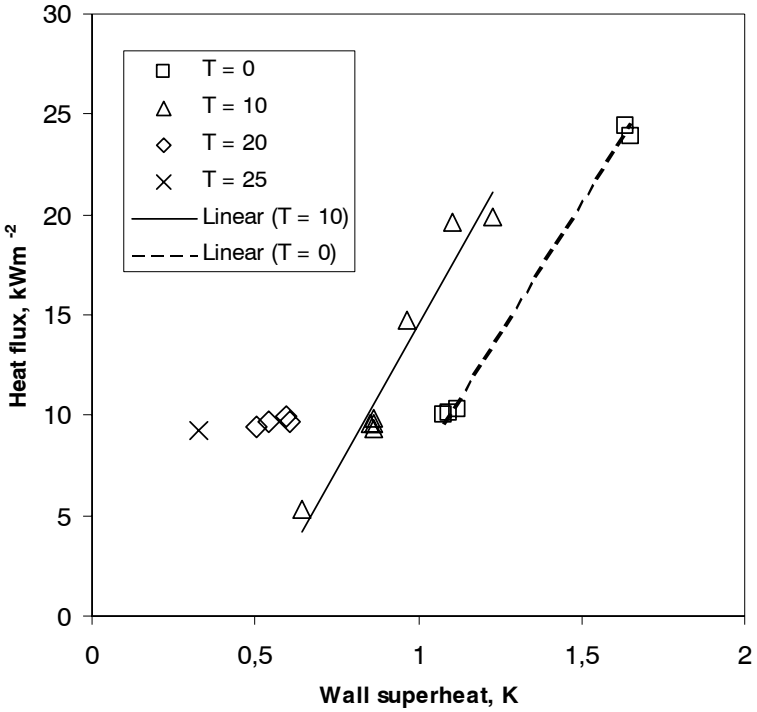

Figure 6.16 *Relation between heat flux and calculated wall superheat based on Eq. (6.1), at evaporating temperature 0, 10, 20, and 25°C. Mass flux varies from 190 to 570 kgm^{-2}s^{-1}. Linear least-square regression lines are shown for 0 and 10°C*

heat flux. Even though data points at each temperature and heat flux were taken at mass fluxes varying over a wide range, they collapse into clusters of data points in the diagram, thus confirming that the heat transfer mechanism is more or less pure nucleate boiling, i.e. unaffected by varying mass flux and convective evaporation. In most cases where several data points are shown in one group, the range of mass flux is 280-570 kgm^{-2}s^{-1} or 190-380 kgm^{-2}s^{-1}.

6.5 Pressure drop measurements

6.5.1 Pressure drop at varying mass flux

Figure 6.17 shows measured pressure drop at evaporating temperature 0°C and heat flux 10 kWm^{-2}, i.e. based on the same test series as shown in Figure 6.9. The mass flux is varied from 190 to 380 kgm^{-2}s^{-1}. As expected, the pressure drop is a strong function of mass flux and vapour fraction, both

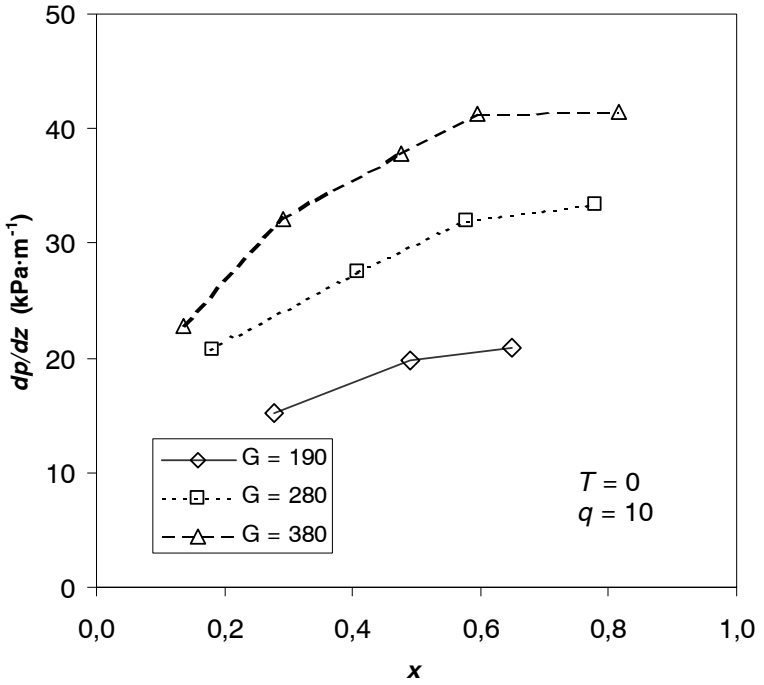

Figure 6.17 *Pressure drop gradient (dp/dz) at varying vapour fraction (x), for mass fluxes (G) 190, 280 and 380 kgm^{-2}s^{-1}. Evaporating temperature is 0°C, and heat flux is q=10 kWm^{-2}.*

characterizing the refrigerant flow velocity. When comparing the pressure drop data to the heat transfer data of Figure 6.9 it is interesting to note that although the pressure drop rises, there is not much gain in heat transfer by increasing the mass flux due to the dominating role of nucleate boiling.

Figure 6.18 shows pressure drop data at 10°C, for the same heat flux and mass fluxes, plus data at mass flux 570 kgm^{-2}s^{-1}. For given G and x, the pressure drop is lower, due to the reduced vapour volume (higher saturation pressure). Heat transfer data corresponding to this Figure are shown in Figure 6.10. Again, the higher mass flux and pressure drop does not lead to higher heat transfer. Dryout also sets in at higher x when G is reduced, thus diminishing the negative impact of dryout.

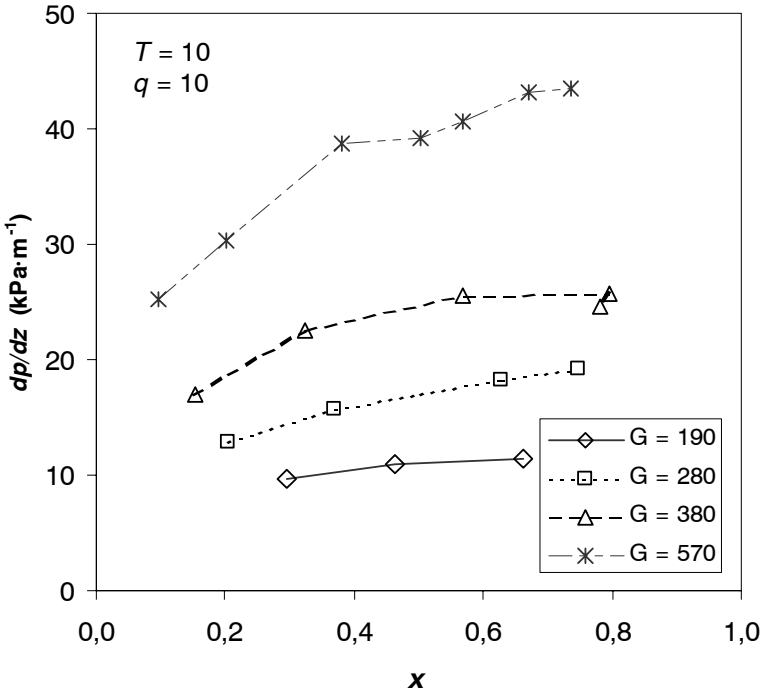

Figure 6.18 *Pressure drop gradient (dp/dL) at varying vapour fraction (x), for mass fluxes (G) 190, 28, 380, and 570 kgm^{-2}s^{-1}. Evaporating temperature is 10°C, and heat flux is q=10 kWm^{-2}.*

6.5.2 Pressure drop at varying heat flux

Figure 6.19 shows pressure drop test results at 10°C and 280 kgm^{-2}s^{-1} for heat fluxes 5, 10, and 15 kWm^{-2}. Apparently, heat flux does not have a major influence on the pressure drop gradient. The results at 5 and 10 kWm^{-2} fall on the same line, while there is a slight increase when the flux is further increased to 15 kWm^{-2}. The corresponding heat transfer data are shown in Figure 6.6.

Figure 6.20 shows pressure drop data at a higher mass flux (570 kgm^{-2}s^{-1}). The tendency is the same – varying heat flux does not have a major influence on pressure drop gradient. Heat transfer data corresponding to this diagram are shown in Figure 6.7.

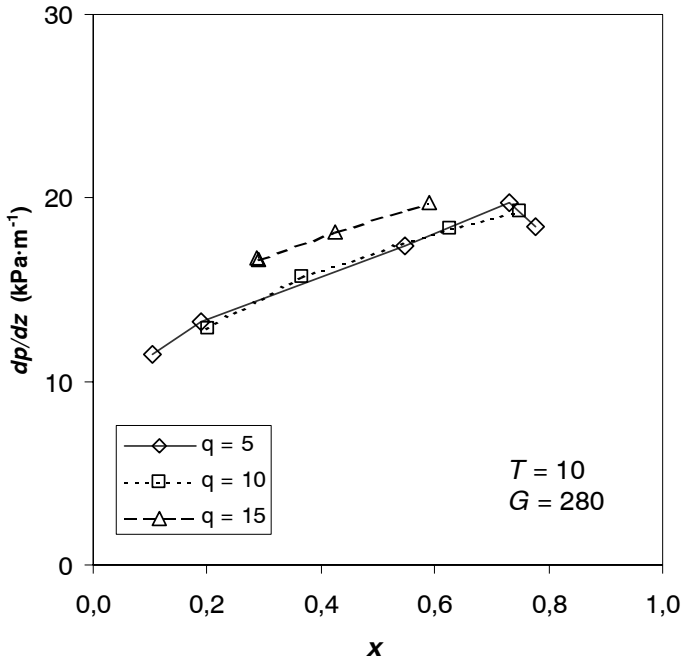

Figure 6.19 *Pressure drop gradient (dp/dL) at varying vapour fraction (x), for mass fluxes (q) 5, 10, and 15 kWm^{-2}. T=10°C, G=280 kgm^{-2}s^{-1}.*

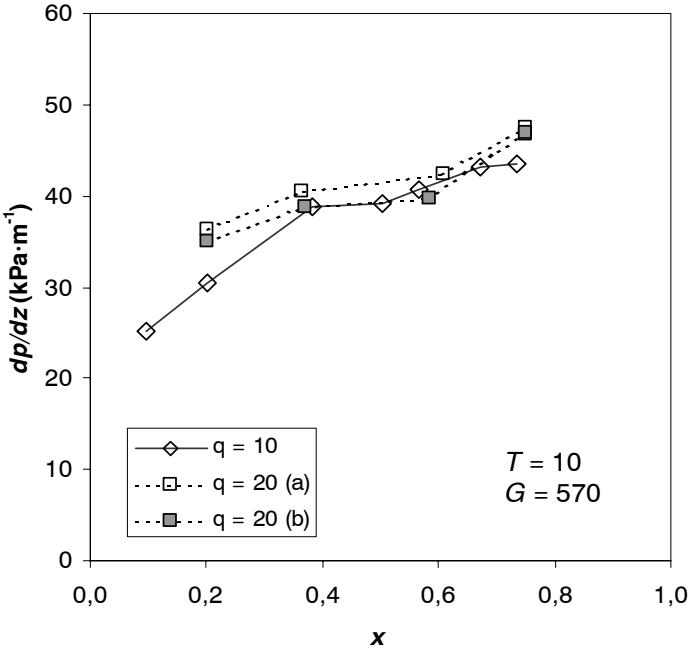

Figure 6.20 *Pressure drop gradient (dp/dL) at varying vapour fraction (x), for heat fluxes (q) 10 and 20 kWm^{-2}. T=10°C, G=570 kgm^{-2}s^{-1}. Results (a) and (b) are from different test series.*

6.5.3 Pressure drop at varying evaporating temperature

Increased temperature and saturation pressure gives reduced vapour volume, and thereby reduced flow velocity. The pressure drop is therefore reduced as temperature increases for a given heat and mass flux, as shown in Figure 6.21 (G=280 kgm^{-2}s^{-1}, q=10 kWm^{-2}).

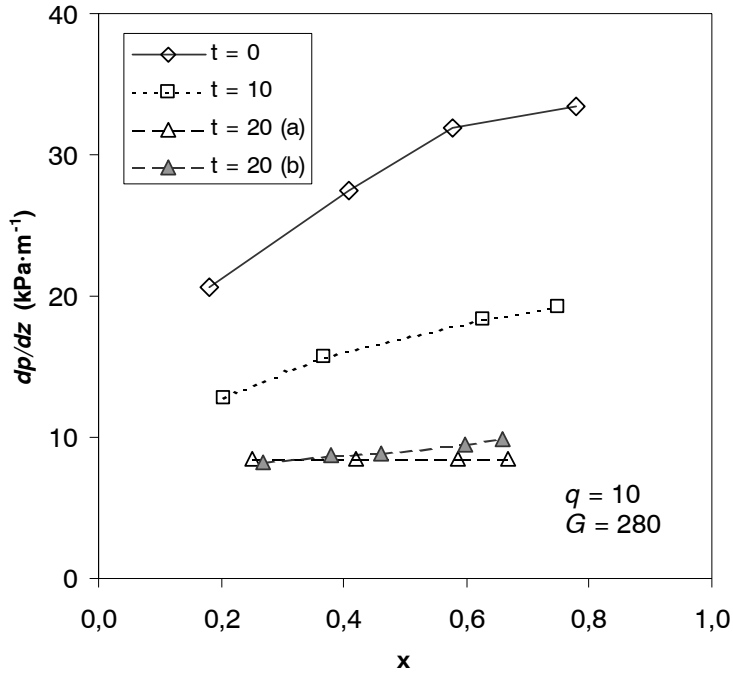

Figure 6.21 *Pressure drop gradient (dp/dz) at varying vapour fraction (x), for evaporating temperatures (T) 0, 10 and 20 °C. Heat flux is 10 kWm^{-2} and mass flux is G=280 kgm^{-2}s^{-1}. Results (a) and (b) are from different test series.*

In summary, the pressure drop measurements show expected behaviour of higher gradient at lower temperature, higher mass flux and increasing vapour fraction. In most cases, the gradient does not increase linearly with x, but shows a declining tendency at high vapour fraction, maybe because of change in flow pattern.

6.6 Two-phase flow pattern studies

The present Section outlines the results from recordings of flow patterns inside the glass test tube, using the equipment described in Section 4.9. Forty-one recordings were made, at varying vapour fraction and mass flux. Detailed observations and photos, as well as flow pattern charts, are discussed in the following text.

6.6.1 Overview

In order to separate between the different flow patterns that were observed, a classification system was used, as shown in Table 6.3. The degree of detail that can be illustrated in flow regime charts is limited, and only the major flow regimes are identified in the charts. In Table 6.4, however, the patterns in most flow situations are characterized in some more detail, using the flow pattern terminology of Table 6.3. The term "droplet" flow could have been replaced by "mist" flow, but since the liquid droplets were quite large compared to the tube diameter, the pattern did not associate well with "mist" even though the droplets had a diameter only of a fraction of a millimetre.

Table 6.3 *Classification of flow regimes*

Major flow regime	Flow pattern
Stratified	*Smooth*
	Wavy
Intermittent	*Bubble*
	Elongated bubble
	Slug
Annular	*Smooth*
	Wavy
	(E) - With entrainment
Dispersed	*Bubble*
Droplet	

Table 6.4 shows the conditions at each of the recordings that gave useful results. All tests except No 21 and 41 were conducted at an evaporating temperature of 20°C. Text in *italics* indicate tests where conditions depart from the "standard" of q=13 kWm^{-2} and T=20°C.

Table 6.4 *Outline of flow pattern tests*

Test	G, kgm^{-2}s^{-1}	q, kWm^{-2}	T, °C	x	Flow regime	Flow pattern
1	*252*	*0*	*19*	*0.13*	*Intermittent*	*Elongated bubble*
2	244	13	19	0.22	Intermittent	Elongated bubble
3	259	13	20	0.23	Intermittent	Elongated bubble
4	263	13	20	0.27	Intermittent	Slug
5	274	13	20	0.29	Intermittent	Slug
6	255	13	20	0.35	Intermittent	Slug
7	266	13	20	0.45	Annular	Wavy (E)
8	255	13	20	0.53	Annular	Wavy (E)
9	248	13	20	0.58	Annular	Wavy (E)
10	256	13	20	0.59	Annular	Wavy (E)
11	263	13	20	0.63	Annular	Wavy (E)
12	292	13	20	0.62	Annular	Wavy (E)
13	266	13	21	0.82	Annular	Smooth (E)
14	*540*	*0*	*19*	*0.20*	*Uncertain: Annular/ Dispersed*	
15	584	12	20	0.31	Annular	Wavy (E)
16	581	12	20	0.40	Annular	Wavy (E)
17	529	12	20	0.52	Annular	Wavy (E)
18	544	12	20	0.62	Annular	Wavy (E)
19	522	12	20	0.77	Droplet	
20	502	12	21	0.93	Droplet	
21	*229*	*12*	*-1*	*0.42*	*Annular*	*Smooth (E)*
25	*99*	*0*	*20*	*0.23*	*Intermittent*	*Elongated bubble*
26	135	13	20	0.16	Intermittent	Elongated bubble
27	93	13	20	0.58	Intermittent	Slug
28	128	13	20	0.48	Intermittent	Slug
29	109	13	20	0.78	Annular	Smooth
30	119	13	20	0.87	Annular	Smooth
31	*115*	*0*	*20*	*0.78*	*Stratified*	*Smooth*
32	*367*	*0*	*20*	*0.04*	*Intermittent*	*Bubbly*
33	360	13	20	0.12	Dispersed	Bubble
34	371	13	21	0.56	Annular	Wavy (E)
35	382	13	20	0.72	Annular	Wavy (E)
36	378	13	20	0.84	Annular	Wavy (E)
37	387	13	20	0.99	Droplet	
38	398	13	20	0.98	Droplet	
39	253	13	21	1.00	Droplet	
40	557	13	21	1.08	Droplet	
41	*379*	*12*	*0*	*0.72*	*Annular*	*Wavy (E)*

6.6.2 Recordings at mass flux 250 $kgm^{-2}s^{-1}$

Figure 6.22 shows a picture of the flow pattern in Test 1, at a nominal mass flux of 250 $kgm^{-2}s^{-1}$, a vapour fraction of 0.13 and zero heat flux. Direction of flow is from right to left, as shown by the arrow. The diameter of the tube can be clearly observed, and the length of the image is about 7.5 mm. In this test, no heat load was applied to the flow in neither the preheater nor the observation tube. The apparent upward inclination of the tube was caused by the camera position being slightly out of horizontal. The tube was horizontal, however.

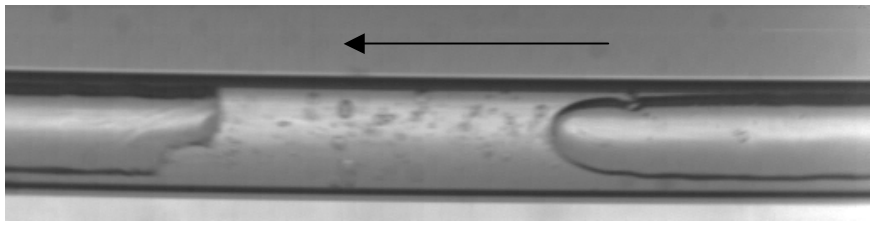

Figure 6.22 *Flow pattern in Test 1($G=252 kgm^{-2}s^{-1}$, $x=0.13$, $q=0$)*
Flow direction is from right to left

As may be observed from the picture, the flow regime was elongated bubble or slug flow, with some smaller vapour bubbles in the liquid phase. In general, the bubbles had a regular rounded front, and the interfaces were quite smooth. According to Tong and Tang (1997), this flow pattern would fall into a *plug flow* category due to the "staircase" hydraulic jumps at the tails of the gas pockets. The elongated bubbles moved at a velocity of about 0.5 ms^{-1}.

Figure 6.23 shows the conditions at a slightly higher vapour fraction (x=0.22), this time with a heat load of 13 kWm^{-2} applied to the observation tube. In this case, the flow pattern could be described slug flow.

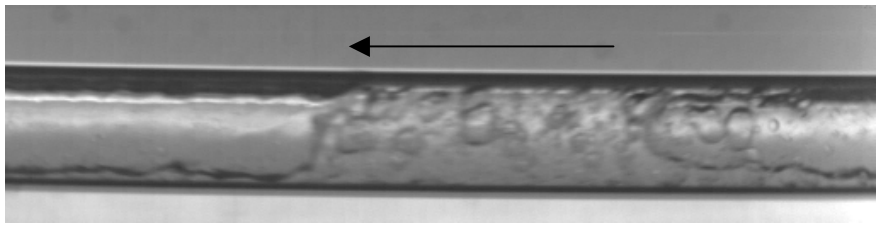

Figure 6.23 *Flow pattern in Test 2 ($G=244 kgm^{-2}s^{-1}$, $x=0.22$)*

The addition of heat flux and a slightly higher vapour fraction gave a quite different flow pattern. In this case, there was a large amount of smaller vapour bubbles in the liquid phase, and the shape of the elongated bubbles was quite irregular. The differences were clear at the front of elongated bubbles, and in the annular film interface along the bubbles. The liquid film was irregular, and large waves occurred on the film surface. These irregularities were probably caused by bubble nucleation and growth along the tube wall. In the lower right corner of Figure 6.23, the dark "patches" along the tube wall are probably small vapour bubbles. On the recorded images, these patches could be observed growing and entering the liquid film. In the part of the film that was observed further up the sides of the tube, bubbles could be seen growing in the film and collapsing at the vapour interface. The elongated bubbles moved at a velocity slightly above 0.6 ms^{-1}. In some cases, the front of a liquid slug formed a rounded oblong front that protruded into the vapour space, as shown in Figure 6.24

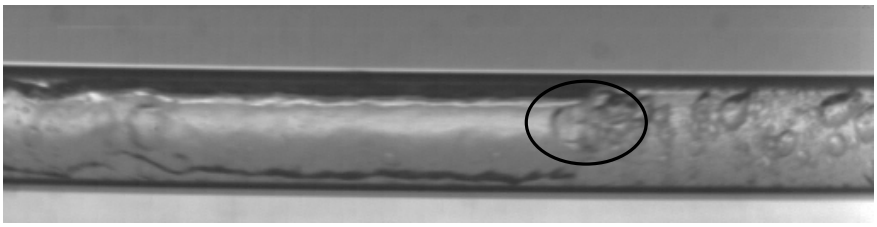

Figure 6.24 *Liquid front shape in Test 2 (G=244 $kgm^{-2}s^{-1}$, x=0.22)*

Figure 6.25 shows an image from Test 4, at a vapour fraction of x = 0.27. The liquid slugs became less frequent at these conditions, and vapour bubbles seemed to take up more of the liquid slug volume. In some periods, the flow showed more of an annular/wavy flow pattern. Velocity of the vapour plugs was about 0.7 ms^{-1} at these conditions. The liquid film was very wavy in periods.

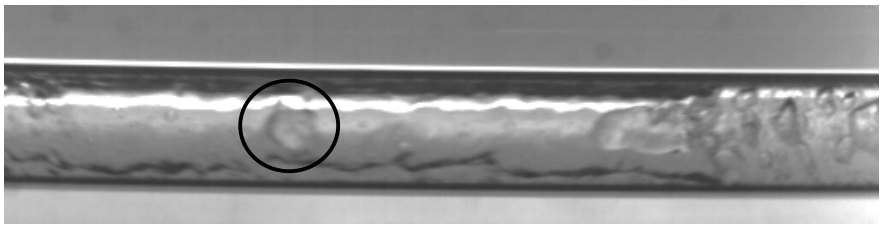

Figure 6.25 *Flow pattern in Test 4 (G=263 $kgm^{-2}s^{-1}$, x=0.27)*
"Large" droplet inside circle

Figure 6.25 also shows a further development of the phenomenon observed in Figure 6.24. The front of the slug (in the right part of the picture) developed a protrusion apparently moving in the centre of the tube. In

addition, a larger droplet of liquid that seemed to originate from this slug was flowing in the vapour core about 2.3 mm in front of the slug (to the left of the centre of the picture).

In Test 6 (x=0.35), the flow pattern became even more annular and wavy in its nature, Figure 6.26. Slugs of liquid filling the entire diameter were now very rare. It was difficult to judge from the images if stratification occurred, i.e. if the film was thinner in the top of the tube. Apparently, the upper part of the tube had less liquid than the bottom, but it was often swiped by waves extending to the top. These waves had a "sawtooth" shape, and liquid droplets seemed to enter the vapour core from the tips of such waves. An important feature of the flow pattern was the large amount of entrained droplets, as well as larger drops of liquid. In Figure 6.26, a larger drop that was torn off from the advancing wave can be observed in the centre of the picture. The velocity of advancing slugs of liquid was around 0.7 ms^{-1}.

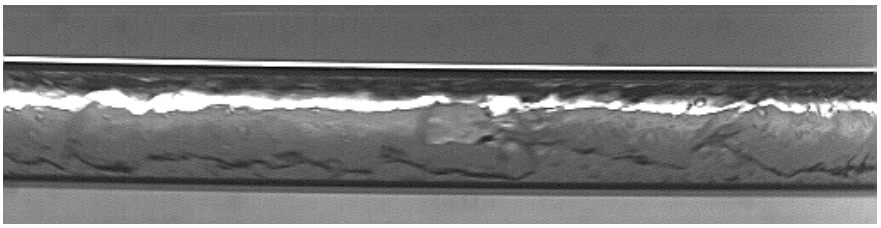

Figure 6.26 *Flow pattern in Test 6, with liquid drop torn off from wave front (G=255 $kgm^{-2}s^{-1}$, x=0.35). (The picture has been processed to get a sharper image)*

In Test 8 (x=0.53), the tendencies observed so far continued, as shown in Figure 6.27. Now the flow did not have any slugs at all, and the flow pattern was purely annular, possibly with more liquid in the bottom of the tube than in the top. The waves in the wavy annular flow pattern had a marked "sawtooth" or "rippled" shape. The liquid film seemed thinner than in previous tests, and there was a visible difference in speed between the liquid film, moving at about 0.6 ms^{-1} and the core flow, moving at about 1 ms^{-1}. Considerable amounts of liquid was entrained in the core, with droplets of varying size and larger drops having diameters around 0.2 to 0.4 mm, i.e. 20-40 % of the tube diameter.

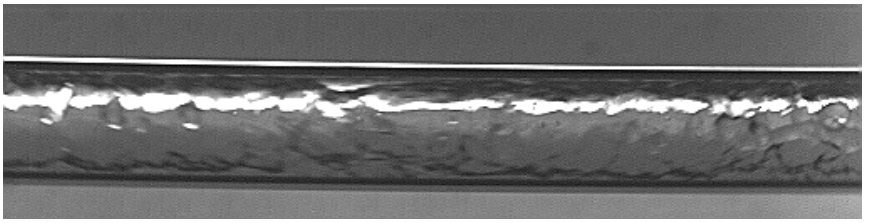

Figure 6.27 *Flow pattern in Test 8 (G=255 $kgm^{-2}s^{-1}$, x=0.53)*

The tendencies of ever more regular (although wavy) annular flow continued as the vapour fraction was increased in Tests 9, 10 and 11. Figure 6.28 shows a typical situation from Test 11, at a vapour fraction of x = 0.63.

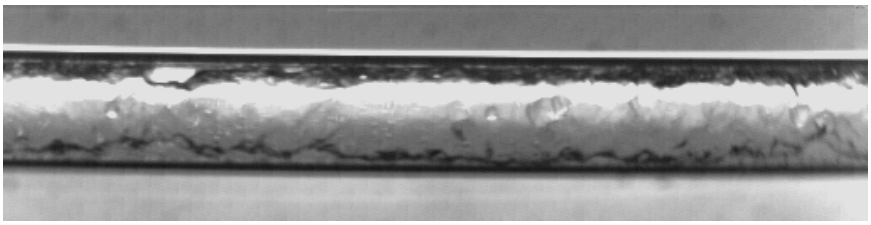

Figure 6.28 *Flow pattern in Test 11 (G=263 kgm^{-2}s^{-1}, x=0.63)*

The liquid film was continuously getting thinner as the vapour fraction increased, and measurements on the recorded images indicated a film thickness between the waves of less than 0.1 mm in test 11.

In Test 13, at a vapour fraction of x = 0.82, there was only an almost invisible liquid film in the lower part of the tube, as shown in Figure 6.29. Small liquid droplets were entrained in the vapour flow, moving at about 1.1-1.3 ms^{-1}. The liquid film was moving at a quite low velocity, in the order of 0.2 ms^{-1}.

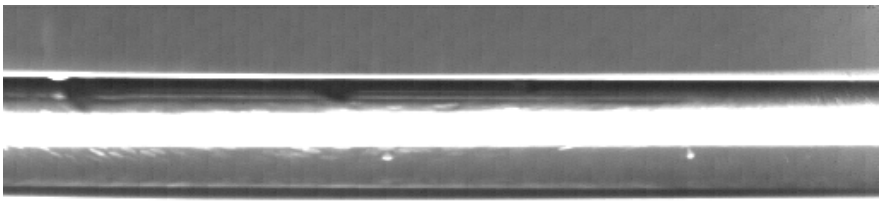

Figure 6.29 *Flow pattern in Test 13 (G=266 kgm^{-2}s^{-1}, x=0.82)*

Going back to Figure 6.11, it is clear that the major reduction in measured heat transfer coefficient occurred around x=0.6 (0.5-0.7) for a mass flux of 280 kgm^{-2}s^{-1}. Based on the observations in Figures 6.28 and 6.29, this range of x give a dryout of (parts of) the liquid film on the tube wall, and a transition to entrained droplet flow.

6.6.3 Recordings at mass flux 550 $kgm^{-2}s^{-1}$

In Tests 14 to 20, the mass flux was increased to a nominal value of about 550 $kgm^{-2}s^{-1}$, and the vapour fraction was varied over a similar range as in the above tests. Figure 6.30 shows an image taken from Test 14, at a mass flux of 540 $kgm^{-2}s^{-1}$ and x=0.20. In this case, no heat flux was applied neither in the preheater nor the glass tube.

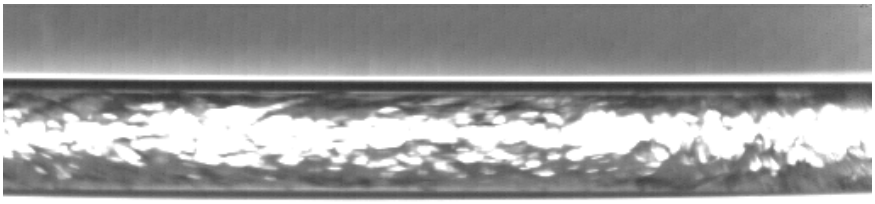

Figure 6.30 *Flow pattern in Test 14 (G=540 $kgm^{-2}s^{-1}$, x=0.20, q=0)*

Owing to the high flow velocity and the high turbulence inside the tube, it was quite difficult to evaluate the flow pattern. In addition, the light was concentrated by the liquid film, making the image less clear. Most likely, the flow was annular, but with significant entrainment of liquid droplets in the core, and with large waves on the liquid film surface.

Figure 6.31 shows a recorded image from Test 15, at a vapour fraction of 0.31 and a mass flux of 584 $kgm^{-2}s^{-1}$. The video film clearly indicated annular flow with considerable entrainment in the core flow. The entrained liquid phase looks finely dispersed, and there is only a small amount of light coming through the tube due to the scattering effect by the droplet mist. As may be observed, the liquid film thickness on the tube wall was quite thin, even at this moderate vapour fraction.

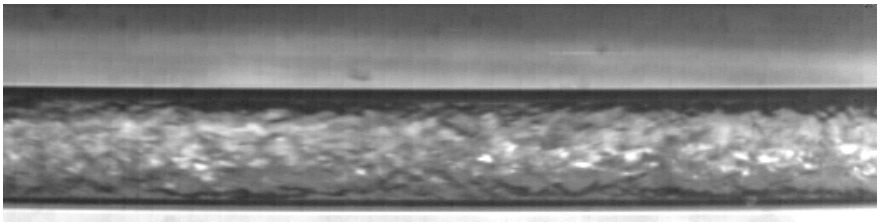

Figure 6.31 *Flow pattern in Test 15 (G=584 $kgm^{-2}s^{-1}$, x=0.26)*

Due to the high flow velocity, it was difficult to observe droplet movement from one frame to the next with a recording rate of 4000 frames per second. In the subsequent tests the rate was therefore increased to 8000 frames per second. As a result, the number of image pixels had to be reduced by 50%.

At this higher recording rate, a significant difference in flow velocity could be observed between the film on the wall and the entrained liquid droplets. In Test 17 (x=0.52), the droplet speed was measured to about 2.2 ms^{-1}, increasing to about 2.4 ms^{-1} in Test 19 (x=0.77). Figures 6.32 and 6.33 show the change in flow pattern between Test 17 and Test 19. In the first picture, a very thin liquid film can still be observed on the tube wall, while in the latter test, the liquid film seems to be concentrated mainly in the bottom of the tube. A reduction in the amount of entrained liquid droplets can also be observed.

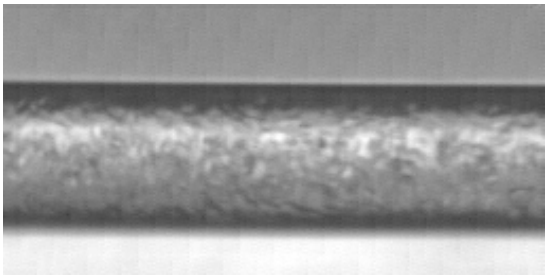

Figure 6.32 *Flow pattern in Test 17 (G=529 $kgm^{-2}s^{-1}$, x=0.52)*

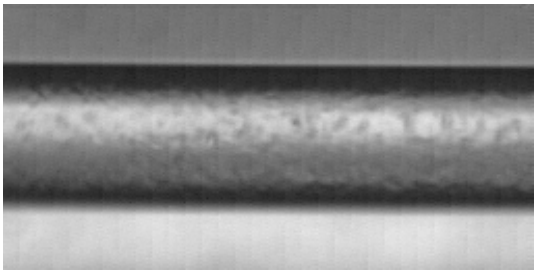

Figure 6.33 *Flow pattern in Test 19 (G=522 $kgm^{-2}s^{-1}$, x=0.77)*

The heat transfer test data in Figure 6.11 indicates that dryout occurred at a vapour fraction around 0.5, i.e. at conditions corresponding to the above images. Again, it seems plausible that onset of dryout was caused by liquid film thinning and removal due to entrainment.

Figure 6.34 shows the dramatic change in flow pattern that occurred when the vapour fraction was raised to 0.93 in Test 20. In this case, the liquid film completely dried up and the flow pattern became entrained/droplet flow. The droplet speed was measured to about 2.7 ms^{-1}.

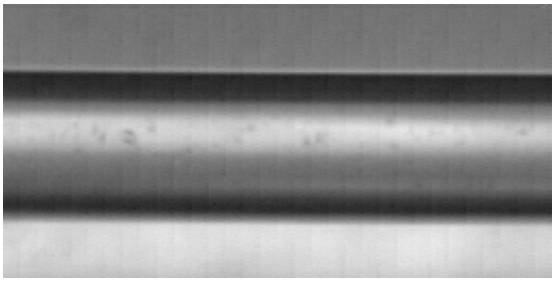

Figure 6.34 *Flow pattern in Test 20 (G=502 kgm^{-2}s^{-1}, x=0.93)*

6.6.4 Recordings at mass flux 100 kgm^{-2}s^{-1}

Even though heat transfer measurements had not been conducted at mass flux below 200 kgm^{-2}s^{-1}, the flow pattern situation at low mass flux conditions was of some interest. Flow pattern observations were therefore made at a nominal mass flux of 100 kgm^{-2}s^{-1}. Figure 6.35 shows an image from Test 26, at G=135 kgm^{-2}s^{-1} and x=0.16, with flow pattern in the bubble regime. The vapour plugs moved at a velocity of only about 0.2 ms^{-1} and bubble growth and detachment could therefore be clearly observed for the nucleate boiling occurring in the liquid phase. Bubbles typically detached from the tube wall at a diameter of 0.12-0.15 mm

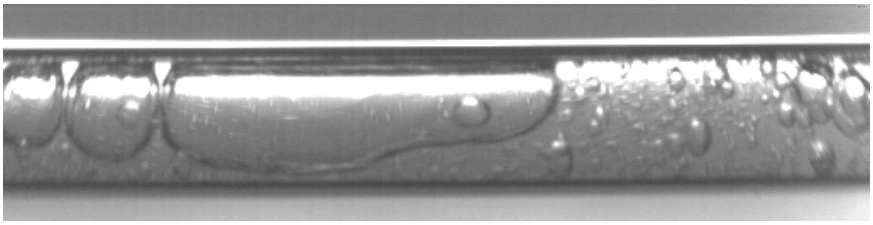

Figure 6.35 *Flow pattern in Test 26 (G=135 kgm^{-2}s^{-1}, x=0.16)*

An interesting observation in Test 26 was the apparent suppression of nucleate boiling in the film under the vapour plug. In the above picture, bubbles cannot be observed under the elongated bubble in the left part of the photo. This phenomenon was also observed at higher vapour fraction, as may be seen in Figure 6.36 from Test 28 at x=0.48. The liquid film flow velocity was about 0.3 to 0.4 ms^{-1}, but with quite some fluctuation. In the left part of the picture, where the film is thinner, there are very few, if any, visible bubbles.

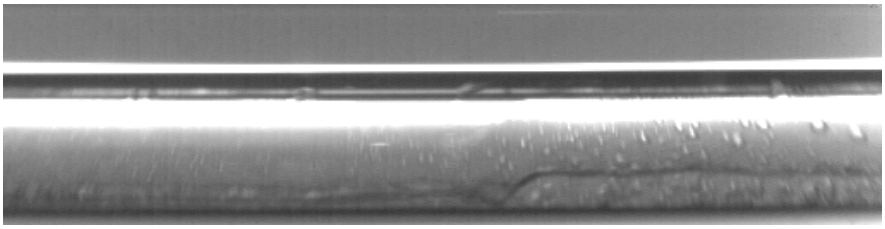

Figure 6.36 *Flow pattern in Test 28 (G=128 kgm^{-2}s^{-1}, x=0.48)*

Another observation in the *G*=100 tests was the apparent lack of entrained liquid droplets. At this low flow rate, the relative velocity between vapour and liquid may not be high enough to give significant (observable) entrainment.

As the vapour fraction was increased beyond 0.5, the flow pattern stayed in the annular regime, and vapour bubbles could generally be observed in the film. By comparing images from tests 29 and 31, the effect of removing the heat flux could be observed, Figure 6.37 and 6.38.

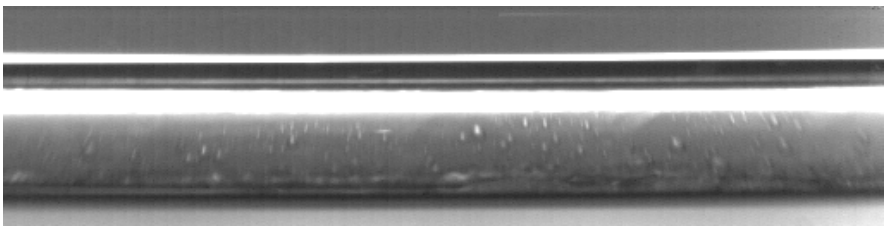

Figure 6.37 *Flow pattern in Test 29 (G=109 kgm^{-2}s^{-1}, x=0.78), q=13 kWm^{-2}*

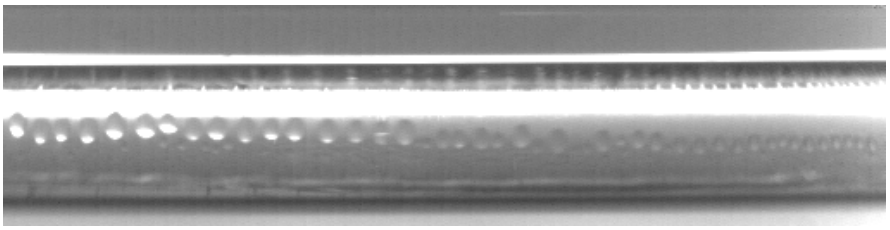

Figure 6.38 *Flow pattern in Test 31 (G=115 kgm^{-2}s^{-1}, x=0.78), q=0*

In test 29, the flow pattern was annular with a thin film towards the top of the tube, and nucleate boiling in the film along the tube wall. In test 31, however, the flow pattern was stratified, and no liquid film could be observed on the sides of the tube. The row of drops on the tube wall could not be easily explained, though. This may be lubricant from the CO_2 supply cylinder, or it may be evidence of the "rivulet flow" pattern found by

Barajas and Panton (1993) for liquid/surface combinations giving large contact angle.

6.6.5 Recordings at mass flux 380 $kgm^{-2}s^{-1}$

Finally, a series of tests were made at a nominal mass flux of 380 $kgm^{-2}s^{-1}$. Figure 6.39 shows a bubble flow pattern at zero heat flux. This test was made to check the correspondence between observed near-zero vapour fraction and resulting calculated vapour fraction. Recorded/calculated x was 0.04, which shows good correspondence to the observed situation. Observed bubble velocity was 0.5 ms^{-1}, and the calculated liquid flow velocity at x=0 for the given mass flux was 0.473 ms^{-1}.

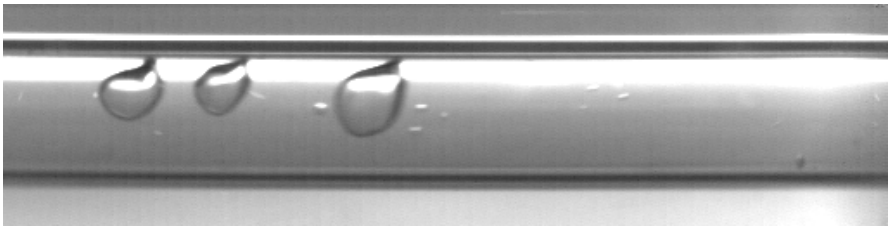

Figure 6.39 *Flow pattern in Test 32 (G=367 $kgm^{-2}s^{-1}$, x=0.04), with q=0*

In test 33, at x=0.12, the flow pattern was dispersed bubbly flow, a regime that was not observed in the other tests. Figure 6.40 shows the flow pattern in Test 33.

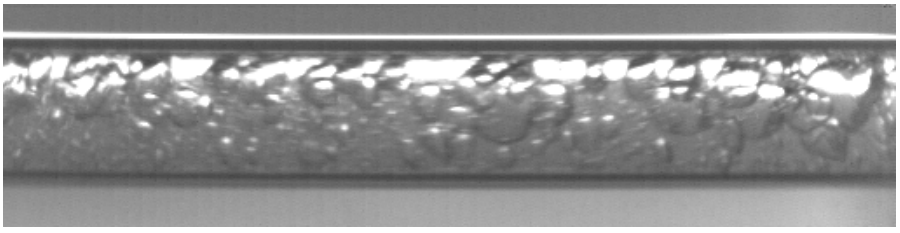

Figure 6.40 *Flow pattern in Test 33 (G=360 $kgm^{-2}s^{-1}$, x=0.12)*

6.6.6 Effects of reduced evaporating temperature

In order to get some indications on the effect of evaporating temperature, two experiments (Test 21 and 41) were conducted at a nominal temperature of 0°C. The nominal mass flux was 250 $kgm^{-2}s^{-1}$ in Test 21, i.e. at conditions comparable to Test 7 at 20°C, and the mass flux was 400 $kgm^{-2}s^{-1}$ in test 41,

i.e. at conditions comparable to Test 35 . An image from Test 21 is shown in Figure 6.41. As may be observed, the flow was annular, with a quite smooth liquid film having only small waves.

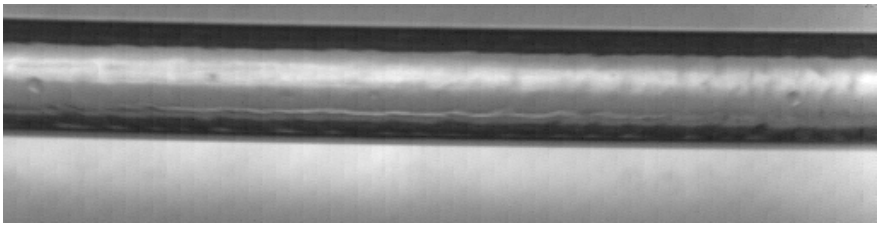

Figure 6.41 *Flow pattern in Test 21 (T=-1°C, G=229 kgm^{-2}s^{-1}, x=0.42)*

A few small entrained drops could be observed. The flow pattern fluctuated quite a bit over the 1-second recording time, with a large variation in film thickness, and fronts of liquid entering intermittently. This could have been caused by flow instabilities in the test rig. The occurrence of liquid droplets was also intermittent. Droplet speed was measured to about 2.5 ms^{-1}, and liquid film speed was about 0.3 ms^{-1}. Apparently, there was not much bubble formation in the liquid film.

Compared to the flow pattern in Tests 6, 7 and 8 at similar x and G but at higher temperature, the pattern was quite different. While Figures 6.26 and 6.27 showed very unstable liquid/vapour interface, and large entrained drops, the reduced-temperature test had a much more stable smooth wavy interface even though the vapour velocity and the slip velocity was more than twice as high.

A similar comparison at higher mass flux gave the same tendencies. Figure 6.42 shows an image from Test 41 with a mass flux of 379 kgm^{-2}s^{-1} at a temperature of 0°C (x=0.72), and Figure 6.43 shows the flow pattern at the same G and x at 20°C. The liquid surface was smoother at the lower temperature, the vapour core contained much less entrained drops/droplets, and the droplets were generally smaller.

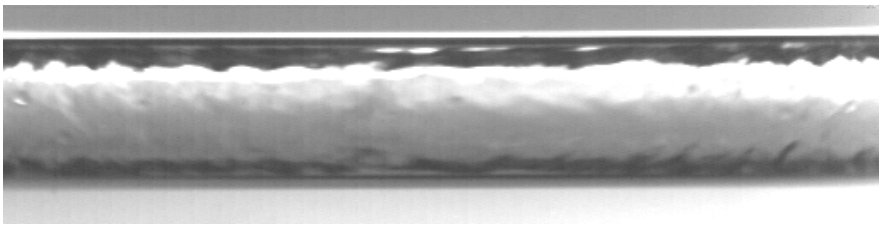

Figure 6.42 *Flow pattern in Test 41 (T=0°C, G=37 kgm^{-2}s^{-1} 9, x=0.72)*

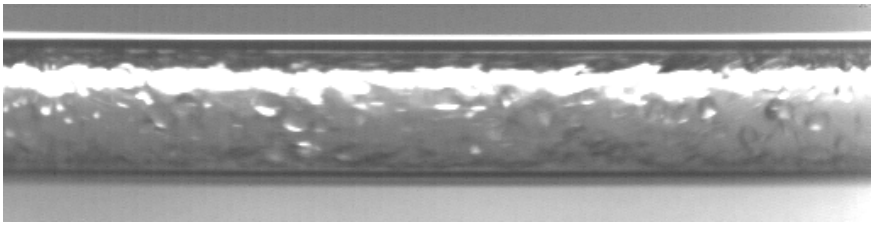

Figure 6.43 *Flow pattern in Test 35 (T=20°C, G=382 kgm^{-2}s^{-1}, x=0.72)*

6.6.7 Control of *x*=1.0

Two tests, at G=250 and 550 kgm^{-2}s^{-1} were conducted in order to check the correspondence between the observed situation where x should be close to 1.0 based on the images, and the measured equilibrium x based on heat balance and measured mass flow rate in the test rig. Figure 6.44 shows a recorded image from Test 40, at a mass flux of 557 kgm^{-2}s^{-1}, and a measured equilibrium x of 1.08. This correspondence was regarded as satisfactory. Probably, the vapour was somewhat superheated and even though liquid droplets could be observed, the equilibrium x was at or slightly above 1.0. Measured droplet speed was about 2.5 ms^{-1}, and the calculated vapour flow velocity for equilibrium x=1 was 2.74 ms^{-1}. The same procedure in Test 39 gave x=1.00, observed droplet velocity 1.1 ms^{-1}, and calculated vapour flow velocity 1.275 ms^{-1}.

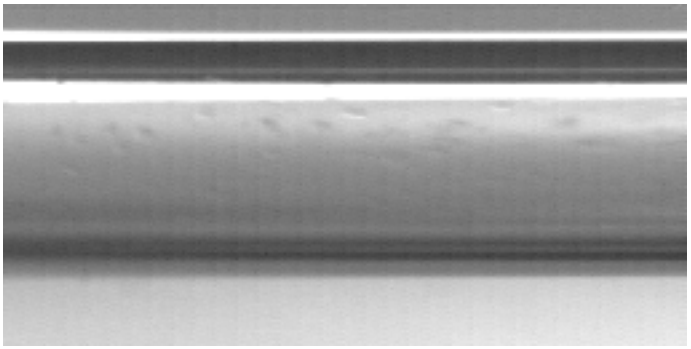

Figure 6.44 *Flow pattern in Test 40 (G=557 kgm^{-2}s^{-1}, x=1.08)*

6.6.8 Flow regime maps

A flow chart based on superficial vapour and liquid flow velocity is probably the most common type of diagram for showing two-phase flow pattern observations. Some charts of this type for air/water flow in small-diameter tubes are presented in Chapter 2. All observations at T=20°C and q=13

kWm^{-2} in the present study are shown in (superficial vapour and liquid velocity) j_v/j_l-coordinates in Figures 6.45 (linear scale) and 6.46 (logarithmic scale). In contrast to low-pressure systems, the range of vapour flow velocity is quite limited due to the high vapour density, and a linear scale is probably more appropriate than the more common logarithmic scale.

The series of tests at increasing x for a constant G can be seen as points on diagonal paths in the linear diagram, with increasing vapour fraction from upper left to lower right. Lines drawn into the diagram mark the approximate location of transition between intermittent and annular flow, and between annular and droplet flow. These lines are of course very approximate, since transitions occur in a region and not at a specific point, and since more observations are needed to confirm the actual location of the lines.

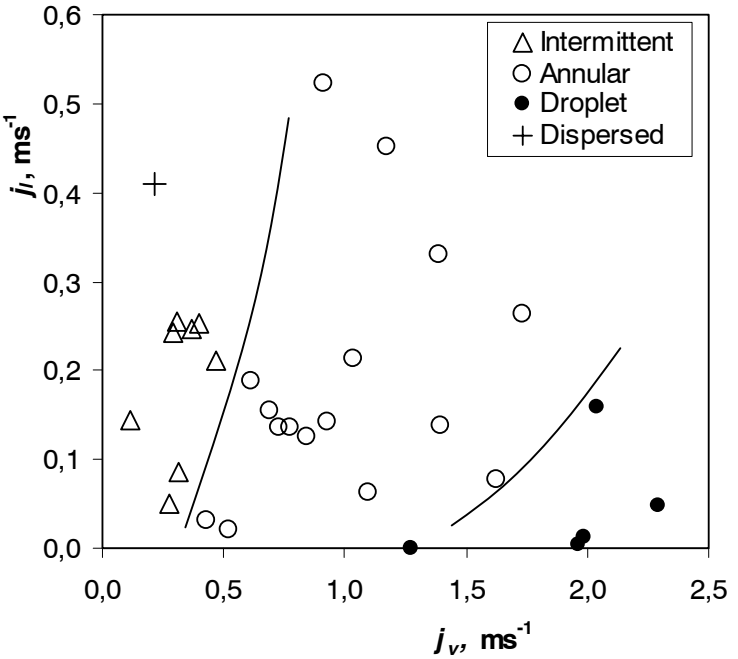

Figure 6.45 *Flow pattern observations plotted against vapour and liquid superficial velocities in linear scale. Conditions: D=0.98 mm, T=20°C, q=13 kWm^{-2}.*

Kattan et al. (1998a) preferred a more practical or "useful" representation of the flow chart, with x as abscissa and G as ordinate. Thus, the development of flow pattern along an evaporator tube for given G could be easily observed. The present observations are shown in x/G-coordinates in Figure 6.47, including approximate lines of transition. Again, more observations would be needed to have a firm basis for locating the transition lines.

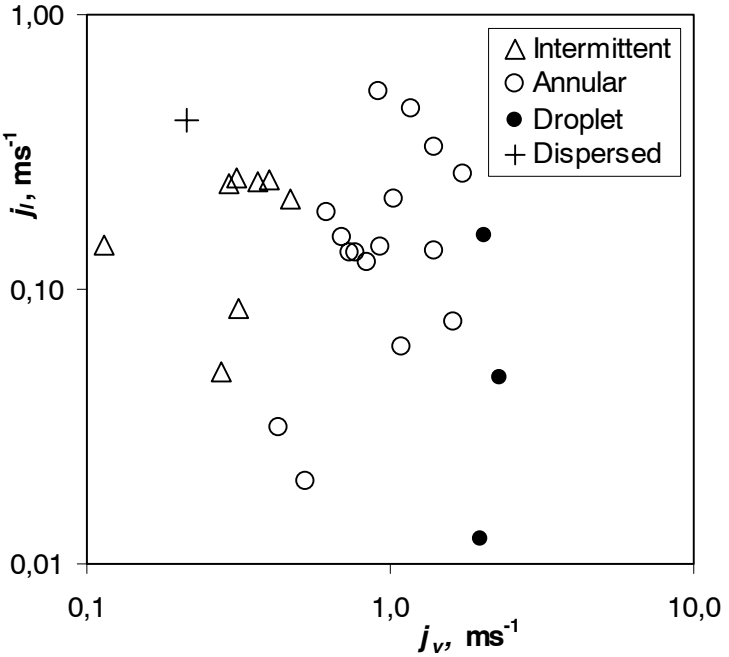

Figure 6.46 *Flow pattern observations plotted against vapour and liquid superficial velocities in logarithmic scale. Conditions: D=0.98 mm, T=20°C, q=13 kWm^{-2}.*

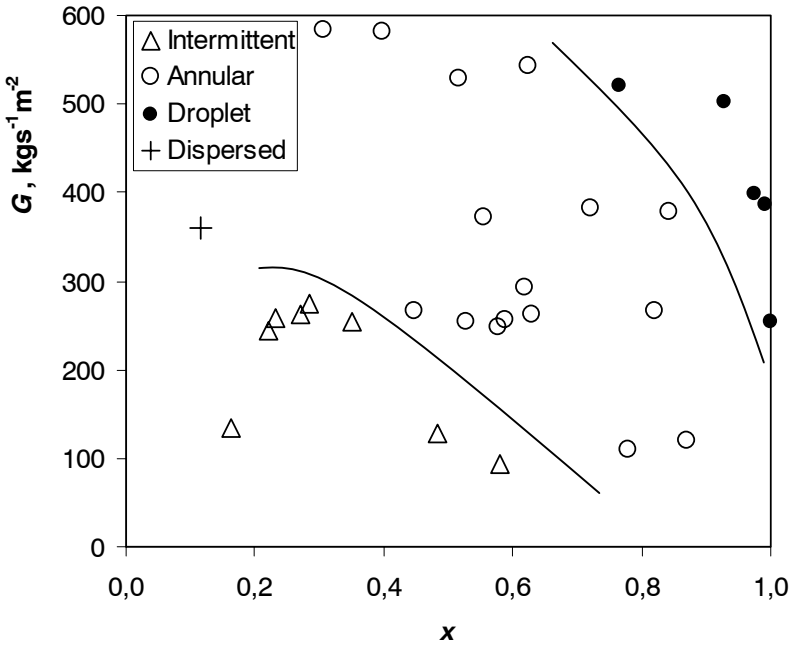

Figure 6.47 *Flow pattern observations plotted at varying vapour fraction and mass flux, including approximate transition lines. D=0.98 mm, T=20°C, q=13 kWm^{-2}.*

Both diagram types above show the dominance of annular flow in the tested system, and Figure 6.47 shows how intermittent flow becomes less dominant at increasing mass flux, while mist/droplet flow (post-dryout) becomes more important. Stratified flow was not observed in tests at the above conditions (20°C), even at the low mass flux of 100 $kgm^{-2}s^{-1}$.

URN:NBN:no-2319

7. Analysis and discussion of results

7.1 Nucleate boiling heat transfer

7.1.1 Conditions for Onset of Nucleate Boiling (ONB)

Results shown in Chapter 6 indicate a clear dominance of nucleate boiling heat transfer at low/moderate vapour fractions, up to the onset of dryout. As explained in Section 2.5.3, the threshold conditions for onset of nucleate boiling (ONB) can be predicted, using the model of Frost and Dzakowic (1967), Eq. (2.38).

Figure 7.1 shows results from calculations for CO_2 based on this model, at three saturation temperatures: -10, 0 and 10°C, giving predicted regimes of nucleate boiling and heat transfer without boiling. The diagram shows threshold conditions for ONB at varying surface superheat. For a given wall superheat (i.e. given wall temperature since T_{sat} is constant), the lines show the maximum heat flux that allows nucleate boiling. More relevant is the use of the diagram for a given heat flux, where the lines show minimum wall superheat required for ONB. Thus, ONB is favoured by increasing superheat.

As may be observed, a very low wall superheat is required for ONB at the heat flux levels of the present study (5-25 kWm^{-2}). A wall superheat of 0.1-0.2 K is only a small fraction of the actual wall superheat found in the test data, and conditions should therefore be well beyond those required for ONB in most if not all experiments.

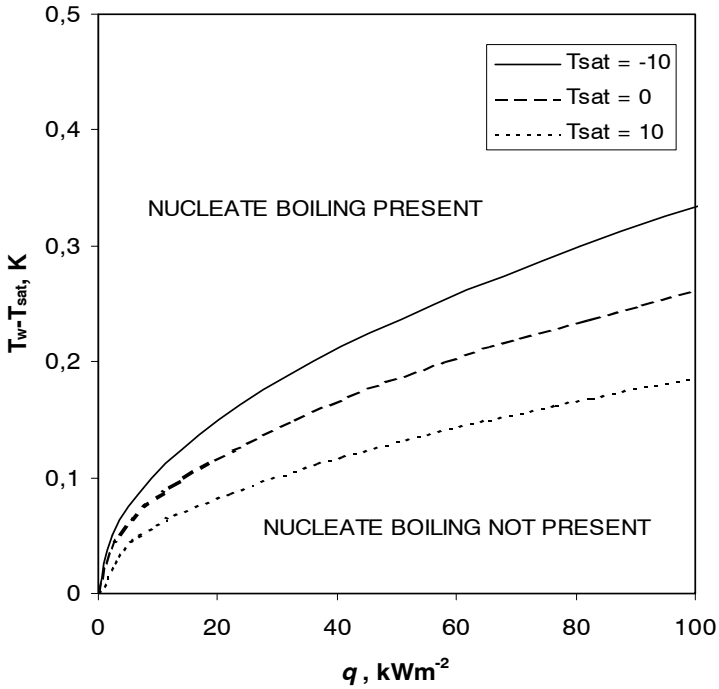

Figure 7.1 *Predicted conditions for onset of nucleate boiling (ONB) in CO_2, based on the model of Frost and Dzakowic (1967).*

7.1.2 Analysis of nucleate boiling results

Experimental data for heat transfer dominated by nucleate boiling are presented in Section 6.4.5 (Figure 6.16). This heat transfer mechanism plays an important role in CO_2 flow vaporization at the tested range of temperature, and these data are therefore analysed in some detail in relation to other published data and in comparison to nucleate boiling correlations.

In Figure 7.2 the low-x heat transfer data of Hihara and Tanaka (2000) are shown together with data from the present study. Hihara and Tanaka (2000) conducted experiments with constant heat flux on a 1 mm ID stainless steel tube at 15°C evaporating temperature. Their results follow the same trend as in the present experiments, but at a lower level. By interpolating between the 10°C and 20°C data from the present study, and drawing a line through the data points at this temperature, a comparison can be made to the data of Hihara and Tanaka (2000). The result is that the data of Hihara and Tanaka generally have about 30% lower heat flux for a given wall superheat, i.e. about 30% lower heat transfer coefficient.

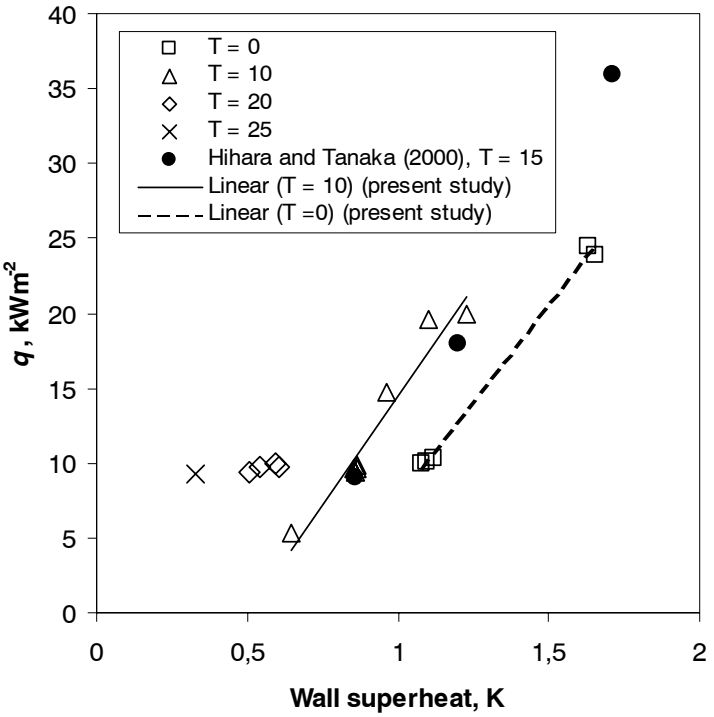

Figure 7.2 *Nucleate boiling heat transfer data of the present study at varying temperature (T,°C),and data taken from Hihara and Tanaka (2000) for ID=1mm electrically heated tube at 15°C evaporating temperature*

There are numerous possible reasons why the data are different, including experimental uncertainty, influence of convective heat transfer, differences in heat supply and wall temperature conditions (electric heating instead of fluid heating), tube surface properties, confinement effects, and presence of small lubricant concentrations. Hihara and Tanaka (2000) used a stainless steel test tube that may have surface properties that differ from those of aluminium, and their test loop had a compressor. Thus, small amounts of lubricant could influence their experimental data. These effects are known to have a significant influence on nucleate boiling.

Heat transfer data dominated by nucleate boiling have also been extracted from test data published by Yun et al. (2001) for flow boiling in a 6 mm ID tube at 5°C, Figure 7.3. Again, the values are in the order of 30-40% lower than in the present study, but the data also gives a slightly different slope of the $q/\Delta T$-curve. The above comments regarding differences are relevant also in this case, except for the lubricant issue since this system used a pump that did not introduce lubricant into the test circuit. A few data points from unpublished test data of Pettersen (2001) in a 2.5 mm ID stainless steel tube are also shown in Figure 7.3. These data were taken at 0°C in a fluid-heated

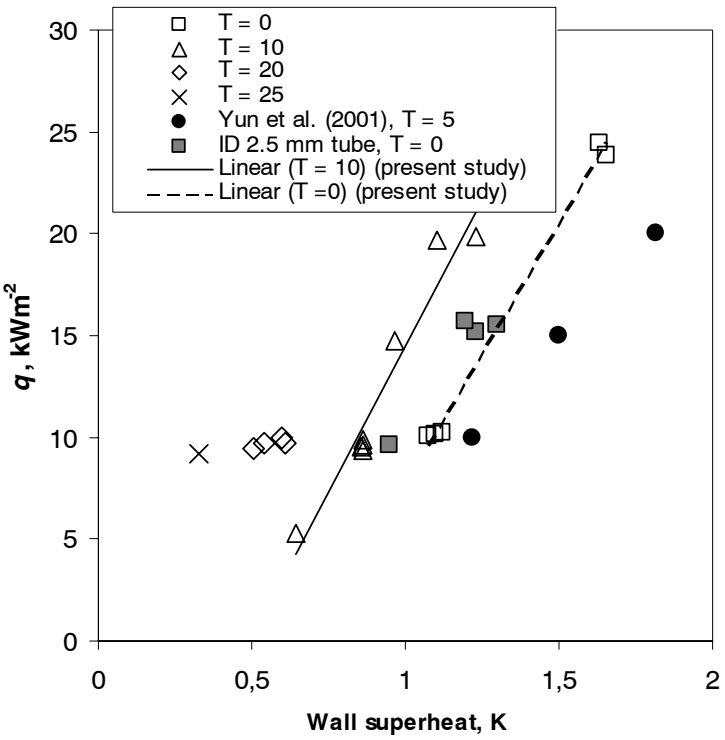

Figure 7.3 *Nucleate boiling heat transfer data of the present study at varying temperature (T,°C),data taken from Yun et al. (2001) for ID=6mm electrically heated stainless steel tube at 5°C evaporating temperature, and data for ID=2.5 mm fluid-heated test tube at 0°C.*

test section. As may be observed from the diagram, the data points fall quite close to and somewhat above the ID=0.81 mm results at 0°C from the present study. This indicates that confinements effects are not significant.

The experimental data of Koyama et al. (2001) indicates a heat transfer coefficient of approximately 22 $kWm^{-2}K^{-1}$ for nucleate boiling-dominated heat transfer at a heat flux of 31.2 kWm^{-2} at 10°C (4.5 MPa saturation pressure) in a ID 1.79 mm electrically heated tube. This corresponds to a temperature difference of 1.4 K, and the data of Koyama et al. (2001) thus correspond well to the level in the present tests. The test system of Koyama et al. (2001) circulated CO_2 in an open circuit from a storage cylinder with discharge into the atmosphere, and lubricant effects should thus not be present.

In summary, data from other tests give coefficients that are in the same range as in the present experiments, and it is not possible to conclude if the data are consistently lower or higher than data from others. Figure 7.4

shows the present test data together with lines of constant heat transfer coefficient. The nucleate boiling test data cover a range of heat transfer coefficient from about 10000 $Wm^{-2}K^{-1}$ to almost 30000 $Wm^{-2}K^{-1}$. The experimental uncertainty in this range of heat transfer coefficient is quite high with any test method. From Figures 6.3 to 6.5, the uncertainty in the present test rig is more than ±25% at these high coefficients. Thus, it is not possible to draw clear conclusions based on differences in level of about ±30% compared to the very limited data published by others.

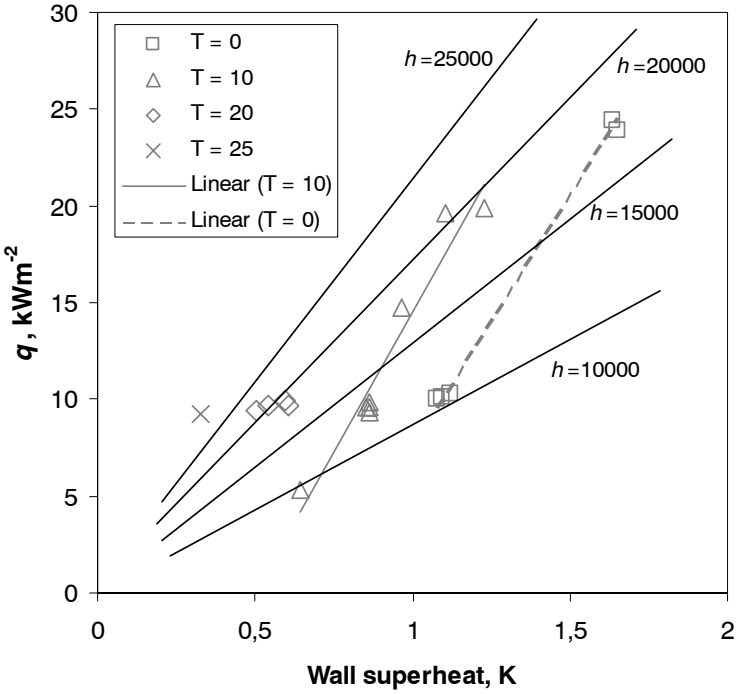

Figure 7.4 *Lines of constant heat transfer coefficient (h) shown in relation to experimental data from the present tests*

7.1.3 Correlation of nucleate boiling data

Experimental data from tests dominated by nucleate boiling (Figure 6.16) have been compared to the pool boiling correlations discussed in Chapter 2. Figure 7.5 shows the percent deviation between experimental and calculated heat transfer coefficients based on the Cooper (1984) correlation (Eq. 2.46). The test data are the points shown in Figure 6.16 and in Section 6.4.5. From the data points in this and later diagrams it may seem like there is some systematic "declining" tendency within each group of points at a given temperature, but it has not been possible to identify any plausible reason

why this should be the case. For all the data points in Figure 7.5, the Cooper correlation predicts lower heat transfer coefficient than measured, and the average deviation is –28%. There is no clear general tendency regarding effects of temperature level, and the deviation seems to be of the same magnitude at all the tested temperatures. The single point at the highest temperature (25°C) shows largest deviation, and this is also the point with largest experimental uncertainty. It is interesting to note that the Cooper (1984) correlation seem to agree well with the data of Hihara and Tanaka (2000).

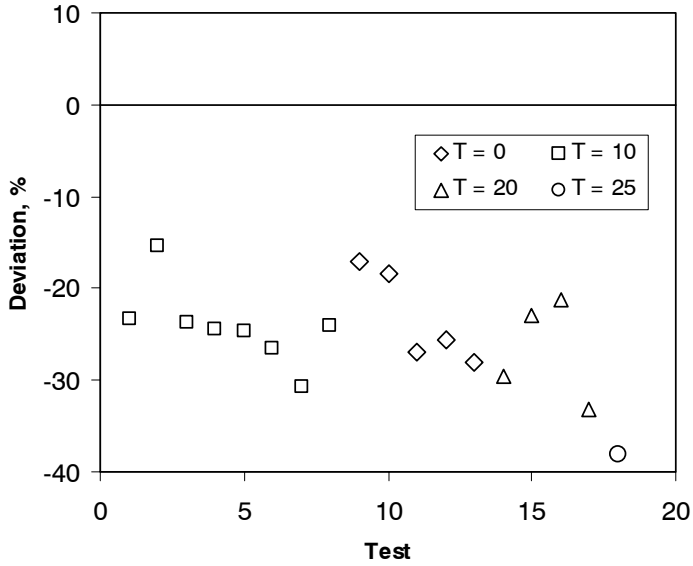

Figure 7.5 *Deviation (in %) between experimental data in the nucleate boiling region and calculated pool boiling heat transfer using the Cooper (1984) correlation (Eq. 2.46)*

Comparison of experimental data to the Borishanski (1969) correlation (Eq. 2.39), using fluid-constant and reduced-pressure functions of Mostinsky (1963) (Eqs 2.40 and 2.41), gave an average deviation of 60.2%. This is an unacceptably large deviation.

By replacing the reduced-pressure function of Mostinsky (1963) with the model of Bier et al. (1976) (Eq. 2.42), the deviation was reduced considerably, Figure 7.6. Owing to the different shape of $F(p)$ at high reduced pressure (Figure 2.9), the coefficients calculated based on Bier et al. (1976) are much closer to the experimental data, with an average deviation of –7.6 % and a mean deviation of 8.8%. The Bier et al. (1976) reduced-pressure function was developed using experimental data over a full range of reduced pressure, including points at $p_r \rightarrow 1$. With this function, the correlation of Borishanski (1969) gave better correspondence to the present

CO_2 data, which were taken at reduced pressures ranging from 0.47 at 0°C to 0.87 at 25°C.
A comparison was also made to pool boiling coefficients calculated with the correlation of Gorenflo (1993), Eqs. (2.43) to (2.45), using reference heat transfer coefficients (h_o) of 5100 and 4170 $Wm^{-2}K^{-1}$, respectively, as explained in Chapter 2. Results from the comparisons are shown in Figures 7.7 and 7.8.

In Figure 7.7, using the 5100 coefficient, the correlation on average predicts 31.5 % higher heat transfer coefficient than the experimental data, a rather surprising result considering the general tendency of underprediction observed so far, and the well-established basis for the Gorenflo (1993) correlation. By replacing the reference heat transfer coefficient with the 4170 coefficient, however, the situation improves, as may be observed in Figure 7.8. In this case, the average deviation is reduced to 7.6%, and the mean deviation to 7.9%. Among the tested pool boiling correlations, this model gives best correspondence to the present test data.

As outlined in Section 2.5.6, a special correlation for nucleate flow boiling in small-channels was developed by Tran et al. (1997) Eq. (2.65), using experimental data for fluorocarbon refrigerants. The confinement number (N_{conf}), Eq. (2.2) was believed to be significant for small-channel boiling, accounting for bubble size in relation to channel size. The confinement number for CO_2 boiling in a 0.81 mm ID tube at varying temperature is shown in Figure 7.9. Based on the criterion that confinement effects become important for $N_{conf} > 0.5$, boiling at temperatures below 22.5°C could be influenced by channel size for this particular diameter.

Using regression based on their experimental data, Tran et al. (1997) found the three coefficients c_1, c_2 and c_3 in Eq. (2.65), arriving at the following correlation:

$$Nu = \frac{hD}{k_l} = 770 \left(Bo \cdot Re_l \cdot N_{conf} \right)^{0.62} \left(\frac{\rho_g}{\rho_l} \right)^{0.297} \tag{7.1}$$

where Re_l is the liquid Reynolds number based on the superficial liquid velocity, tube diameter, and liquid viscosity. Figure 7.10 shows the deviation between the present experimental data and Eq. (7.1), using the same data points as in the earlier figures. Eq. (7.1) with the coefficients derived by Tran et al. (1997) does not predict the heat transfer coefficients of CO_2 in nucleate boiling well, and the model gives calculated coefficients significantly above the test data. The correlation also fails to predict the relative change in heat transfer coefficient at varying temperature level, thus giving an increasing deviation as the boiling temperature drops. This confirms the observation made by several investigators, who have concluded that nucleate boiling heat transfer correlations need to account

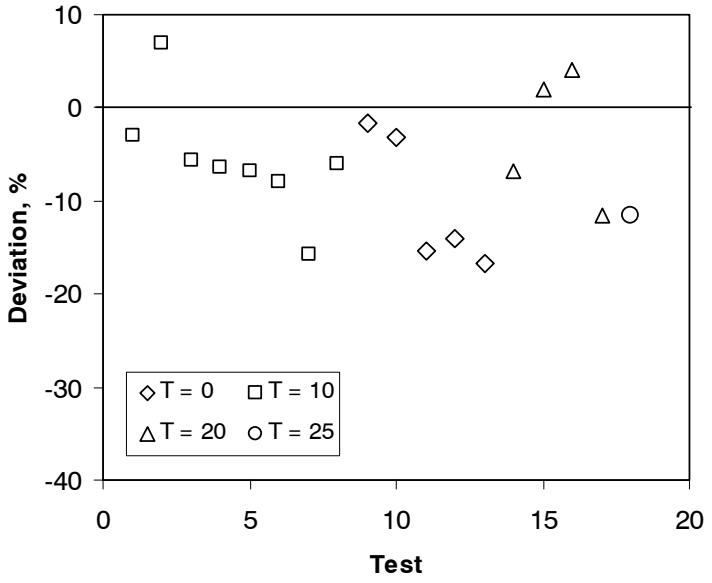

Figure 7.6 *Deviation (in %) between experimental data in the nucleate boiling region and calculated pool boiling heat transfer using the Borishanski (1969) correlation and the Bier et al. (1976) reduced-pressure function*

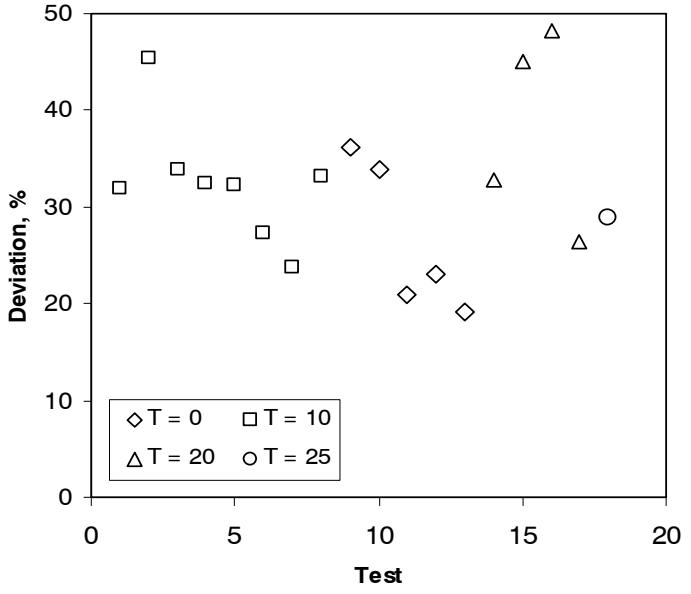

Figure 7.7 *Deviation (in %) between experimental data in the nucleate boiling region and calculated pool boiling heat transfer using the Gorenflo (1993) correlation with a reference heat transfer coefficient of 5100 $Wm^{-2}K^{-1}$*

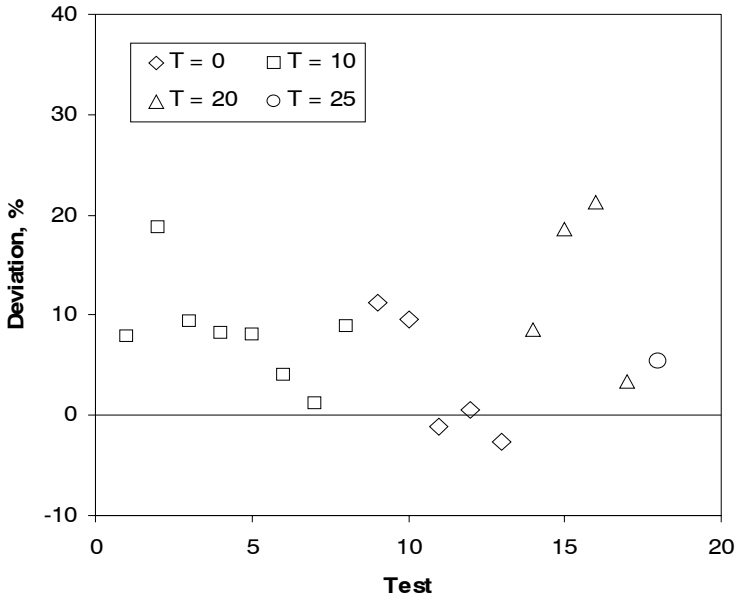

Figure 7.8 *Deviation (in %) between experimental data in the nucleate boiling region and calculated pool boiling heat transfer using the Gorenflo (1993) correlation with a reference heat transfer coefficient of 4170 $Wm^{-2}K^{-1}$*

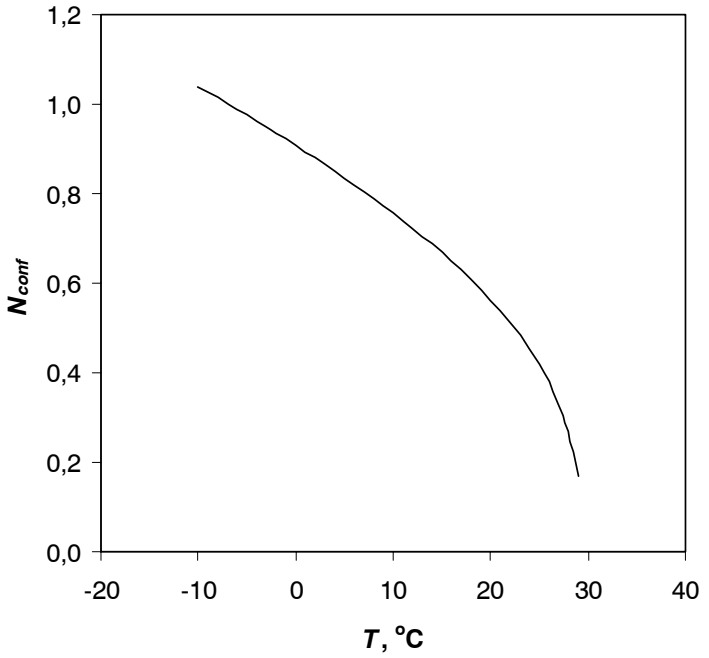

Figure 7.9 *Confinement number (Eq. 2.2) for CO_2 nucleate flow boiling in 0.81 mm ID tube.*

for varying (reduced) pressure in order to reproduce the physics of the boiling process. The correlation of Tran et al. (1997) does not have the necessary features for prediction of nucleate boiling heat transfer over a wide range of conditions.

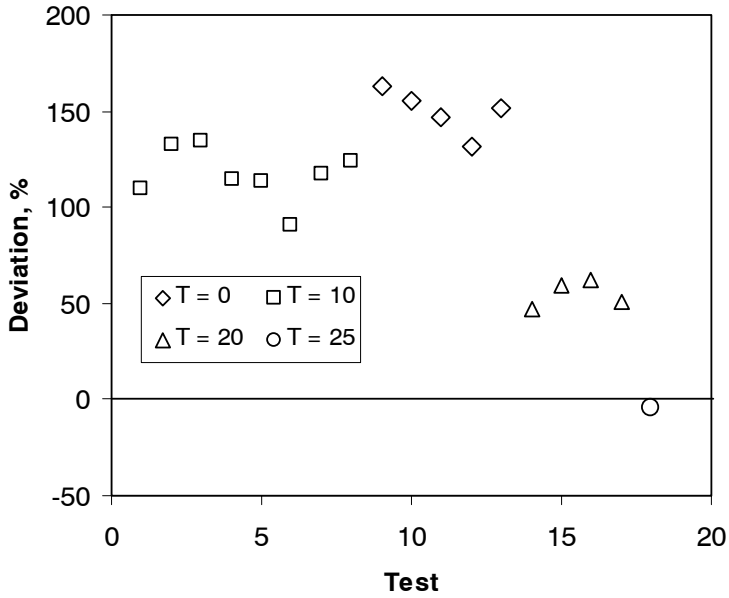

Figure 7.10 *Deviation (in %) between experimental data in the nucleate boiling region and calculated "confined" nucleate flow boiling heat transfer using the correlation of Tran et al. (1997), Eq. (7.1)*

Based on the above comparison of current test data to other published data and to various pool boiling correlations, the situation is evaluated as follows:

- Compared to published data from other studies, the measured heat transfer coefficients in the region dominated by nucleate boiling seem to be comparable or somewhat high in the present study. A conservative assessment would be to conclude that the present coefficients are about 30% higher than the "average" level from other studies.
- Nucleate boiling heat transfer correlations with "reduced-pressure" features reproduce the experimental data in a satisfactory way. The correlation of Gorenflo (1993) with a reference coefficient of 4170 $Wm^{-2}K^{-1}$ gives the best correspondence to test data, while the Cooper (1984) correlation predicts about 30% lower coefficients. Again, a conservative approach would be to use the Cooper correlation in heat transfer models.

- The small-diameter nucleate boiling correlation of Tran et al. (1997) did not fit the present experimental data, and also fails to follow the observed trends at varying temperature.

7.2 Convective evaporation

As outlined in Section 2.5.2, Kattan et al. (1998b) proposed a correlation for convective evaporation in annular flow using a turbulent single-phase model with coefficients adapted to their test data. Since annular flow is a dominating flow pattern in pre-dryout vaporization of CO_2 in microchannels, this model may also be adapted to CO_2. Although the exponents and coefficients of Eq. (2.34) may have to be adjusted to CO_2 results, a first approach would be to use this model for convective heat transfer in annular flow. In a more refined model, the effect of entrainment and onset of annular flow will have to be accounted for.

Figure 7.11 shows calculated local convective coefficients for CO_2 at two temperatures (0 and 20°C) and two mass fluxes (200 and 600 $kgm^{-2}s^{-1}$), based on Eq. (2.35). Film thickness was estimated using the void fraction correlation of Rouhani and Axelsson (1970, Eq. (2.33), neglecting entrainment.

In practice, film dryout will occur before the convective heat transfer coefficient reaches the very high values at x beyond 0.7-0.8, especially at high mass flux and high temperature. Nevertheless, the above data provide a basis for a model of combined nucleate and convective heat transfer in the annular flow regime up to the critical x.

Depending on the relative magnitude of convective evaporation and nucleate boiling heat transfer, it may be necessary to check for possible suppression of nucleate boiling. By using an asymptotic model (Eq. 2.28) the contributions from nucleate boiling and convective evaporation can be combined into a total pre-dryout heat transfer coefficient. Figure 7.12 shows calculated coefficients at 0°C using an asymptotic model with n=3, and the Cooper (1984) correlation for nucleate boiling (Eq. 2.46).

At the lower mass flux the predicted effect of the convective heat transfer is quite small, while at higher mass flux the convective contribution is significant. In practice, dryout is likely to occur from a vapour fraction of 0.7-0.9. A heat transfer coefficient of 25 $kWm^{-2}K^{-1}$ corresponds to a wall superheat of 0.4 and 0.8K at q=10 and 20 kWm^{-2}, respectively. From Figure 7.1, this wall superheat is well beyond the requirements for ONB, and

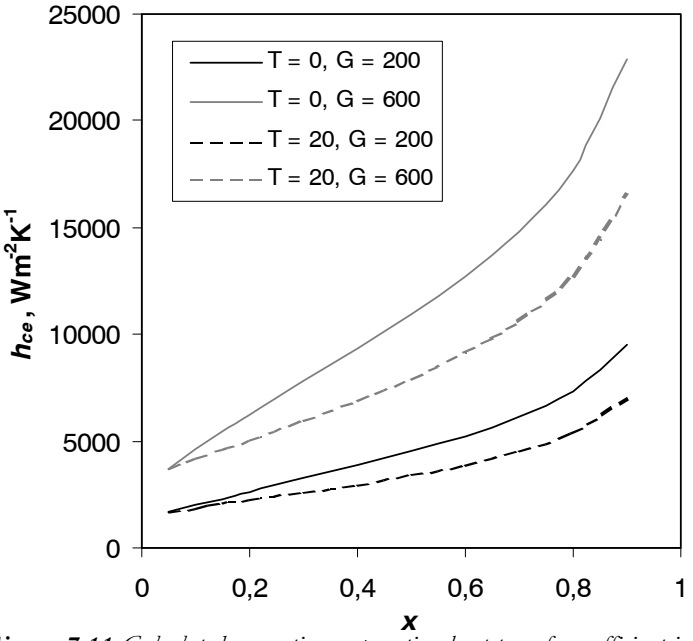

Figure 7.11 *Calculated convective evaporation heat transfer coefficient in annular flow (without entrainment) in 0.81 mm ID tube, based on the correlation of Kattan et al. (1998b) (Eq. 2.34), for combinations of mass flux G (in $kgm^{-2}s^{-1}$) and saturation temperature T (in ^{o}C).*

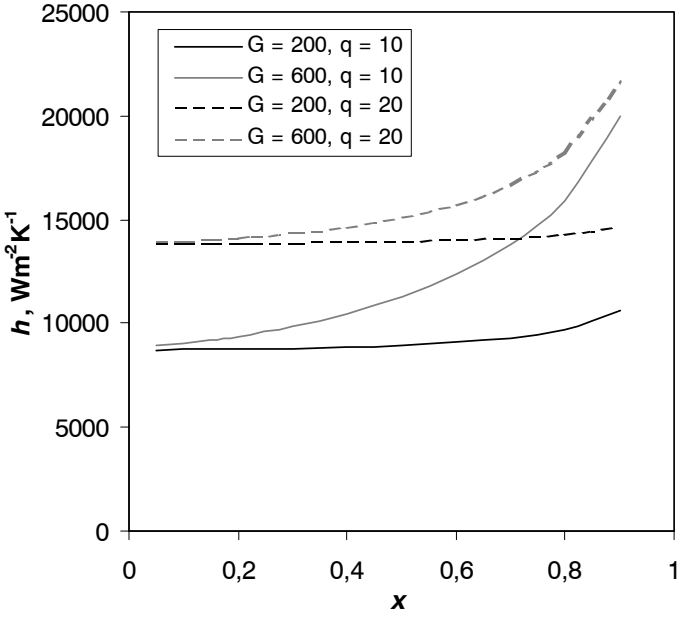

Figure 7.12 *Calculated vaporization heat transfer coefficient (not considering dryout) using asymptotic model (Eq.2.29) with n=3, and nucleate boiling and convective evaporation heat transfer coefficients from Equations (2.46) and (2.34), respectively. Conditions: T=0^{o}C, D=0.81 mm, G=200 and 600 $kgm^{-2}s^{-1}$, q= 10 and 20 kWm^{-2}.*

suppression of nucleate boiling is not likely to occur. This situation may change at lower temperature and higher mass flux, however.

Predictions using the above model for vaporization heat transfer in the pre-dryout regime are compared to the local measurements of Hihara and Tanaka (2000) in Figure 7.13.

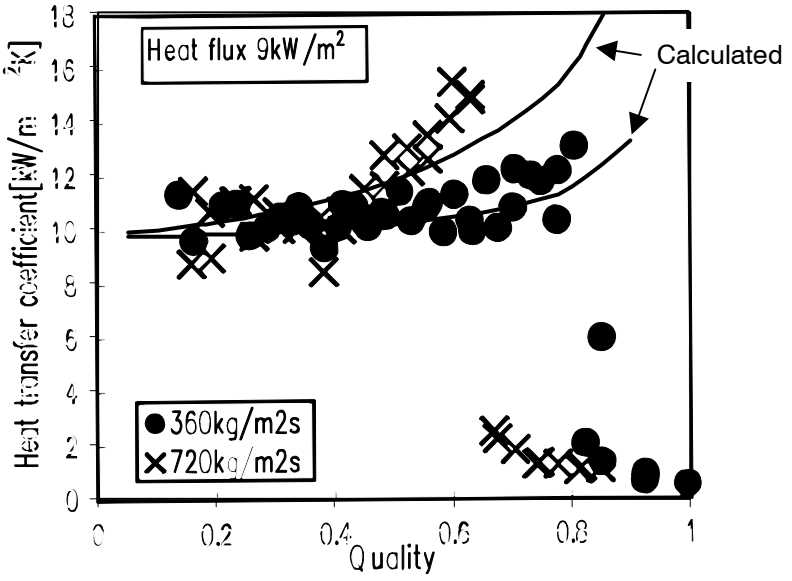

Figure 7.13 *Calculated pre-dryout heat transfer coeffcient using the asymptotic model explained above, compared to test data points of Hihara and Tanaka (2000). Conditions: D=1mm, T=15°C, q=9 kWm⁻², G=360 and 720 kgm⁻²s⁻¹.*

The level and trends of the model give reasonably good correspondence with the local heat transfer test points of Hihara and Tanaka (2000). For the highest mass flux, the convective contribution seems to be a bit underpredicted, though.

7.3 Dryout

7.3.1 Analysis of results

Nearly all the heat transfer experimental data shown in Chapter 6 are affected by dryout, particularly in tests with high mass flux and/or at high evaporating temperature. Even though the experimental rig did not allow true local measurements of heat transfer coefficient at varying vapour

fraction, the tendencies are clear, and even the "averaged" coefficient is sensitive enough to show the significant drop at increasing x.

It is possible to identify approximate x before onset and after completion of dryout for some of the test series shown in Chapter 6. In this way, the range of x where dryout occurs can be bracketed. Figure 7.14 shows results taken from Figures 6.7 and 6.10, at evaporating temperature 10°C and heat flux 10 and 20 kWm^{-2}, respectively. As may be observed from the diagram, dryout occurs at lower vapour fraction as the mass flux increases, and although only one observation is shown at the high heat flux, there also seems to be some effect of increasing q. Unfortunately, most test series in Chapter 6 did not allow this type of observation, because the data did not show completion of dryout, or the rig could not be operated at low enough x, or the data points were too few.

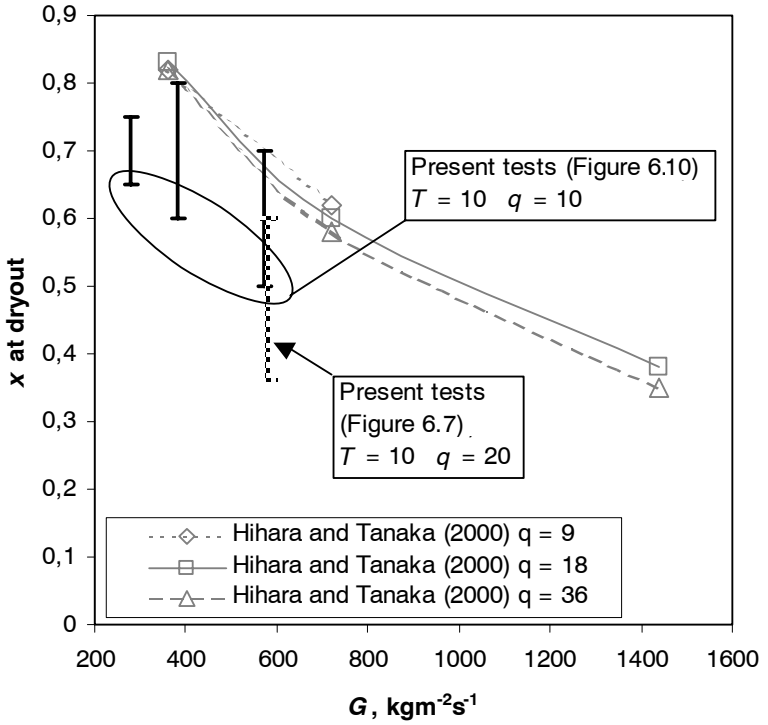

Figure 7.14 *Vapour fraction before and after dryout as observed in present tests at 10°C, compared to x giving onset of dryout in the experimental data of Hihara and Tanaka (2000) in a 1mm ID tube at 15°C.*

The local heat transfer measurements of Hihara and Tanaka (2000) in a 1 mm tube at 15°C allow accurate determination of the onset of dryout. Data taken from the published diagrams of Hihara and Tanaka (2000) are included in Figure 7.14 to serve as reference data. The same general

tendency can be observed, although data from the present tests indicates earlier onset of dryout and larger dependency on heat flux. Considering the somewhat higher temperature level and the slightly larger tube diameter in the tests of Hihara and Tanaka (2000), dryout would be expected to occur earlier than in the present tests.

There are a number of possible reasons for differences in dryout x. Heat is supplied with different methods in the two rigs, with Hihara and Tanaka (2000) using electric resistance heating in the tube wall. Upstream flow history is also known to play a role, especially with subcooled inlet as in the case of the Hihara/Tanaka system. Another possible source of difference is effects of flow maldistribution between the parallel channels in the present tests. Tube surface characteristics are also known to play a role. Tong and Tang (1997) refer to experiments conducted by Jansson et al. (1963), showing considerable reduction in CHF at high vapour fraction as the surface roughness was increased. Roughening of the heated surface was believed to increase the liquid re-entrainment in annular flow, thus reducing the film thickness and reducing the CHF.

Finally, flow instabilities and flow oscillations give reduced critical heat flux and lower critical vapour fraction for a given heat flux. Two-phase flow in parallel channels as in the present test section is known to give flow oscillations. Umekawa et al. (1999) showed that the critical heat flux is significantly reduced due to the periodic dryout and rewetting that occurs under oscillatory flow conditions. Compared to the single test tube of Hihara and Tanaka (2000), where the flow is more stable, the present "multi-channel" test tube is likely to give earlier onset of dryout. Even though the flow oscillations give an uncontrollable test parameter, the results from the present test tube should be closer to the behaviour in a real heat exchanger.

7.3.2 Correlation of dryout results

Section 2.3.7 discusses methods for predicting onset of dryout in forced convection vaporization. In principle, the methods shown by Govan et al. (1988) and Hewitt and Govan (1990) have the potential to predict dryout accurately, by modelling the mechanisms of film evaporation, droplet entrainment and depostion along the tube. These methods are important in analysis of dryout phenomena and in the development of predictive tools. In relation to heat transfer correlations for engineering evaporator design purposes, however, methods that require detailed modelling and integration of the two-phase flow along the tube from inlet to dryout conditions may

become too complex. The second best solution is then to use empirical correlations that can predict critical x based on flow parameters, geometry and operating conditions.

In absence of a general dryout prediction correlation for a wide range of fluids, the only available option is to use dryout data for water systems and to convert those data to CO_2 by a scaling method. As shown in Chapter 2, Ahmad (1973) devised a fluid-to-fluid scaling method that may be used. Figure 7.15 shows calculated dryout data for CO_2, based on the water data of Kon'kov (1965). Curves for temperatures 0/10°C and heat flux 10/20 kWm^{-2} are shown. The "error bars" show predicted onset of dryout at the top of the tube (low x) and at the bottom (high x).

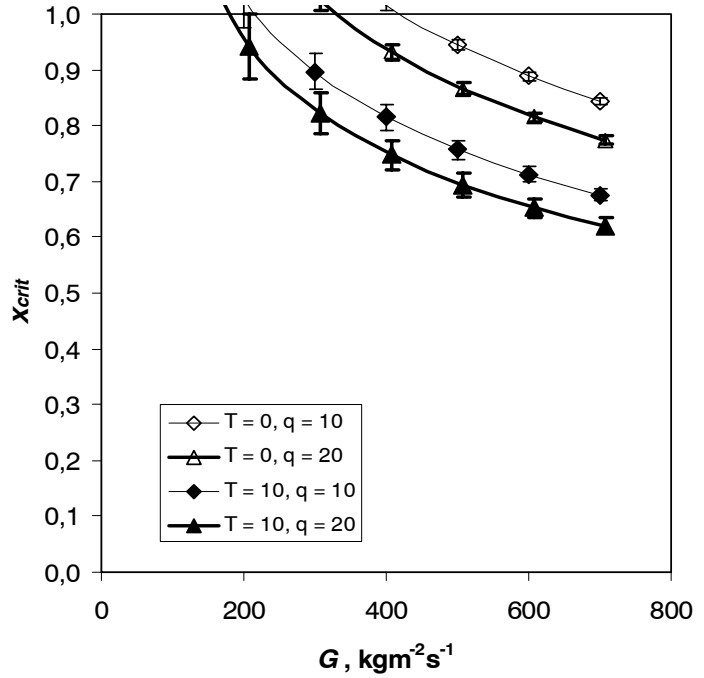

Figure 7.15 *Predicted onset of dryout at varying mass flux in CO_2 evaporator tube with ID 0.81 mm and temperature/ heat flux as shown. Based on water dryout data by Kon'kov (1965) and scaled to CO_2 by the method of Ahmad (1973). Error bars show predicted dryout at top and bottom of tube (Auracher et al., 1993).*

The curves follow the general trend observed in the tests, and as expected the dryout occurs earlier at higher evaporating temperature. The model of Kon'kov (1965) also predicts some influence of heat flux. Noticeable stratification effects giving different dryout in top and bottom of the tube are predicted only at low mass flux levels. This factor is somewhat questionable, though, since stratification is not well predicted by a Froude number parameter only, which is the basis for this model (Eq. 2.17 to 2.20).

In addition, the correlation of Kon'kov (1965) is only valid for tube diameters above 4 mm.

Use of the Ahmad (1973) method is also questionable for this range of parameters, considering the limitations shown in Table 2.2. The density ratio limit of $\rho_l/\rho_v < 7$ restricts the method to CO_2 saturation temperatures below 7°C, and the minimum value of the scaling factor ψ of 5 restricts the method to very high mass flux levels (from about 1300 $kgm^{-2}s^{-1}$ and up), owing to the small tube diameter in the present study. Another restriction is the vapour fraction at channel inlet, which is specified to negative values, i.e. subcooled inlet. Inlet conditions to the test section are always at positive x in the present study, even though the preheater has a subcooled inlet. Finally, the test section tube length/diameter ratio of 620 is well above the maximum limit of 310 in Table 2.2.

Thus, both the water data and the scaling method are extended well beyond their intended range, and high accuracy of prediction can therefore not be expected. Figure 7.16 shows a comparison between predicted dryout and observations from the test data.

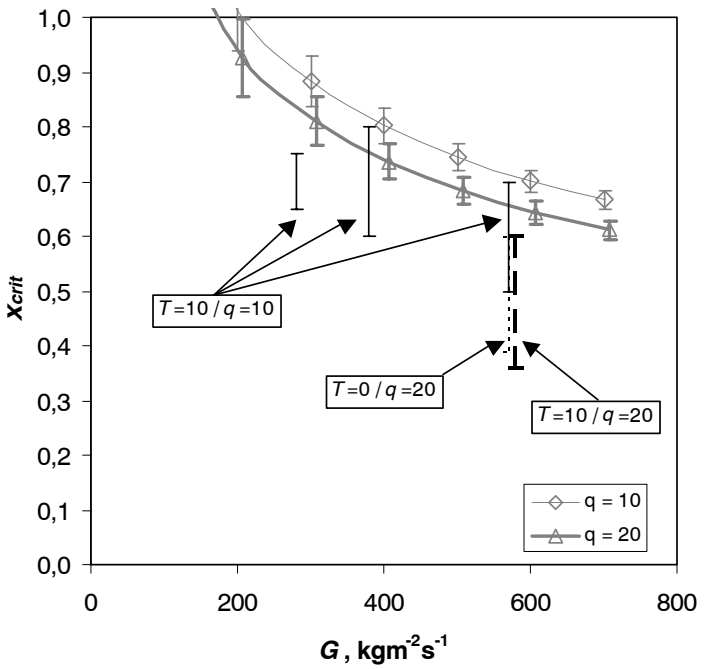

Figure 7.16 *Dryout observations from test data compared to predicted dryout curves at 10°C from Figure 7.15.*

The observed range of x at dryout corresponds reasonably well to the predictions, especially at 10°C, but the general tendency seems to be that

dryout occurs earlier than predicted. One issue in relation to the level of the predicted curves is the use of two alternative formulations for the Ahmad (1973) scaling factor ψ. As shown by Equations (2.12) and (2.13) the scaling factor can be calculated using a Weber-Reynolds number or a Barnett number, which is supposed to give similar results. Figure 7.17 shows that this is not the case, and the choice of formula has a major effect on the dryout prediction. Results so far have been based on the *We-Re* factor (Eq. 2.12).

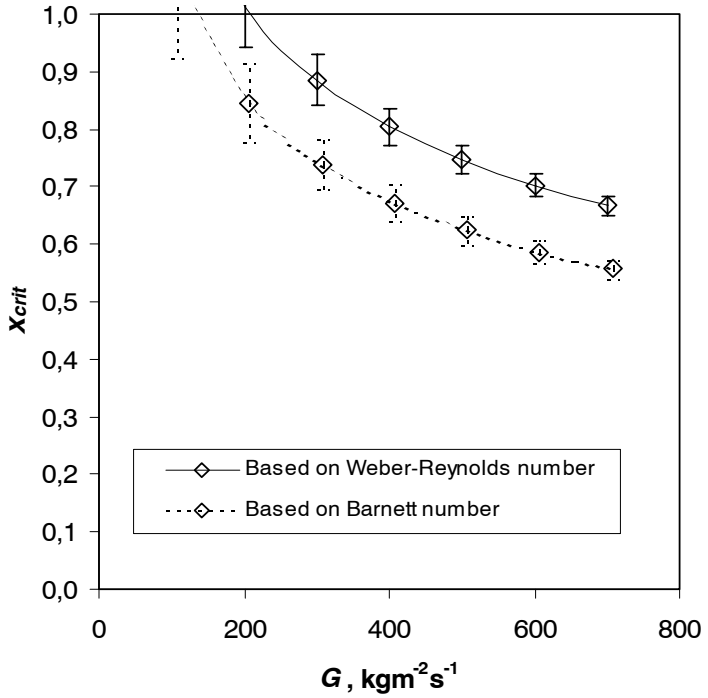

Figure 7.17 *Dryout predictions at T=10°C and q=20 kWm^{-2} using Kon'kov (1965) water data and Ahmad (1973) scaling factor based on Weber-Reynolds number (Eq. 2.12) and Barnett number (Eq. 2.13).*

The Barnett number method was originally introduced as a simplification due to scarcity of surface tension data, and since saturation density data were more readily available for various fluids. Consulting the paper of Ahmad (1973), it is clear that the scaling parameter should preferably be based on the *We-Re*-group. It is then a paradox that in all literature, the Barnett number method has been established as the only approach. It may be noted that Barnett number scaling gives improved correspondence between measured and predicted x at dryout in the present tests. In comparison to the dryout data of Hihara and Tanaka (2000) however, the *We-Re*-method provides the best prediction at high mass flux, even though the predicted x_{cr} values at moderate and low mass flux are too low, as shown by Figure 7.18.

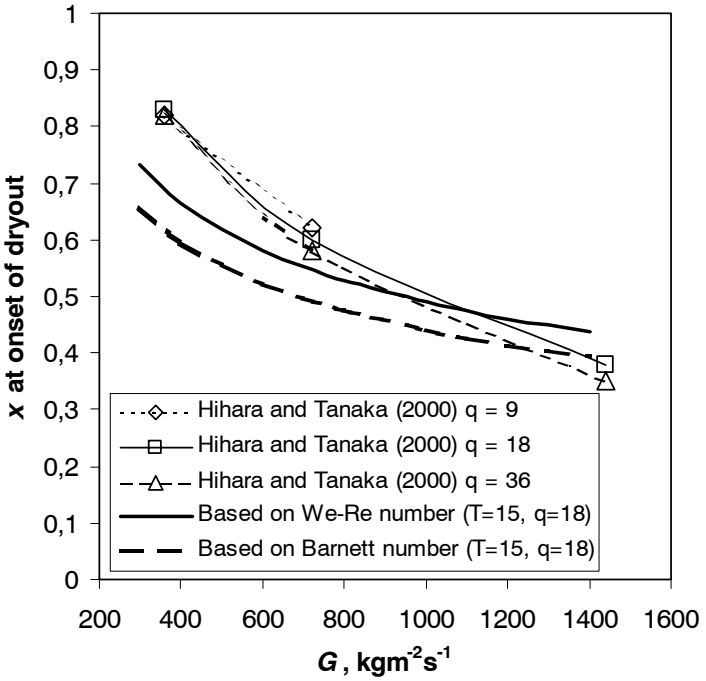

Figure 7.18 *Predicted dryout x for flow at varying mass flux at 15°C in a 1 mm ID tube, using Kon'kov (1965) and Ahmad (1973) method, compared to experimental dryout data from Hihara and Tanaka (2000)*

In the above results, all predictions were made using the Kon'kov (1965) empirical dryout correlation for water. Figure 7.19 shows the effect of replacing this correlation by the model of Levitan and Lantsman (1975) for critical x in vaporization of water (Eq. 2.21). A correction is done for the change in diameter from 8 mm to 1 mm as explained in Chapter 2. The Levitan and Lantsman (1975) correlation does not include any effect of varying heat flux. Although the prediction curves follow the trend of the experimental data in a better way than above, the predicted level of dryout x is too high.

Provided that the experimental data of Hihara and Tanaka (2000) can be trusted as being typical of dryout behaviour of CO_2 in microchannel flow, a simple correction can be made to the Levitan and Lantsman (1975) correlation by reducing the constant term from 0.39 to 0.24. The adapted equation for water dryout thus becomes

$$x_{cr} = \left[0.24 + 1.57\left(\frac{p}{98}\right) - 2.04\left(\frac{p}{98}\right)^2 + 0.68\left(\frac{p}{98}\right)^3\right]\left(\frac{G}{1000}\right)^{-0.5} \qquad (7.2)$$

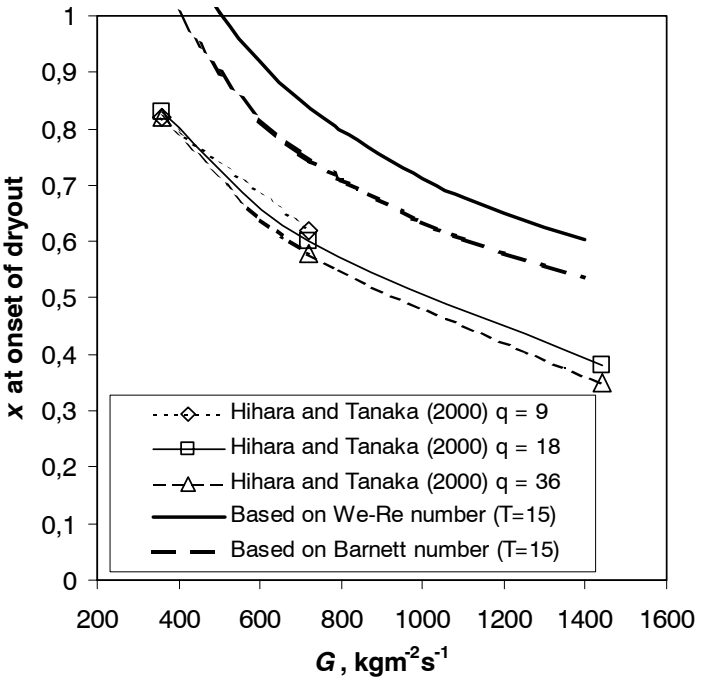

Figure 7.19 *Predicted dryout x for flow at varying mass flux at 15°C in a 1 mm ID tube, using Levitan and Lantsman (1975) dryout data for water and the Ahmad (1973) scaling model, compared to experimental dryout data from Hihara and Tanaka (2000)*

The fit to experimental data (using the *We-Re*-group in the scaling) is then improved, as shown in Figure 7.20. Even though the adapted equation may seem like a good choice for prediction of CO_2 dryout, the range of equivalent mass flux is partly below the range for the Levitan and Lantsman (1975) correlation, and until more dryout data for CO_2 becomes available this model should be used only if the predictions can be checked.

Some general CHF prediction methods from literature were also tested in relation to the available data. The correlation of Katto and Ohno (1984), which is regarded as the best generalized model, predicts the critical heat flux as

$$q_c = q_{co}\left(1 + K\frac{h_{l,sat} - h_{in}}{h_{lv}}\right) \tag{7.3}$$

where q_{co} is the critical heat flux at zero subcooling at the tube inlet (saturated inlet), K is a non-dimensional parameter, and ($h_{l,sat}$ - h_{in}) is the amount of inlet subcooling expressed as enthalpy difference. CHF for satu-

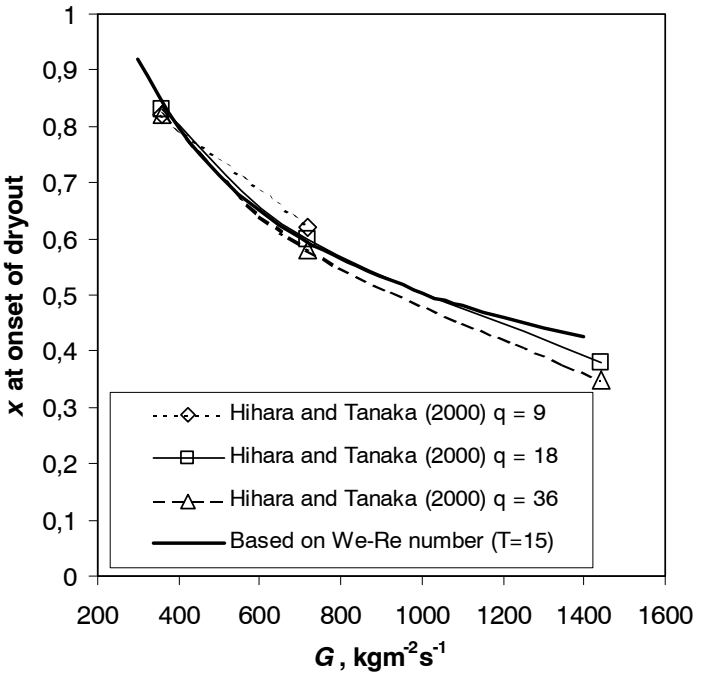

Figure 7.20 *Predicted dryout x for flow at varying mass flux at 15°C in a 1 mm ID tube, using Eq. (7.2) and Ahmad (1973) scaling model (based on We-Re), compared to experimental dryout data from Hihara and Tanaka (2000*

rated inlet (q_{ci}) is estimated based on vapour/liquid density ratio, liquid Weber number, L/D, mass flux, and enthalpy of evaporation. The upper curves in Figure 7.21 shows predicted x_{cr} for saturated inlet, using the correlation of Katto and Ohno (1984). Since the heat flux is a given parameter in the experiments, the boiling length L is varied with mass flux, and the critical x is found at the length that gives $q_{ci}=q$. The lower curves were obtained by extrapolating the inlet condition into the saturated region, i.e. using a negative enthalpy difference in Eq. (7.3). Neither of the two methods reproduce the observed behaviour. Results similar to the lower curves in Figure 7.21 were obtained by using the CISE dryout correlation (Bertoletti et al., 1965). The general CHF correlation of Shah (1987), and the lookup table method of Groeneveld et al. (1986) were tested as well, but these methods also failed to reproduce the observed dryout behaviour in the CO_2 tests.

In summary, the only practical method for estimating dryout x seems to be by scaling of water data using the Ahmad method. Future experiments on CO_2 dryout and/or development of advanced two-phase models for CO_2 flow may change this. The best fit to present data was obtained using the Barnett number in the Ahmad scaling factor.

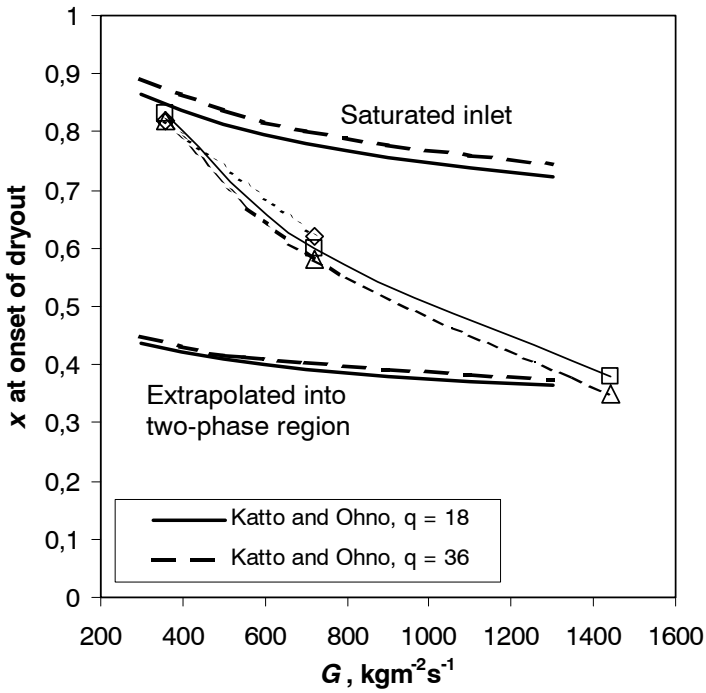

Figure 7.21 *Predictions of dryout using the correlation of Katto and Ohno (1984), compared to the dryout data of Hihara and Tanaka (2000). The upper curves are based on saturated inlet, and the lower curves are based on extrapolation of the method into the two-phase area.*

7.4 Post-dryout heat transfer

Heat transfer coefficients measured in the present study are not truly local, since they result from averaging over the length of the test section. Thus, no data were measured that enable a detailed discussion of local post-dryout heat transfer coefficient. Some trends may be observed in the test data of Chapter 6, however. In Figure 6.7, for instance, the heat transfer coefficient seems to be approaching a level of about 2000 $Wm^{-2}K^{-1}$ from a vapour fraction of 0.7-0.8. These data were taken at 10°C evaporating temperature and a mass flux of 570 $kgm^{-2}s^{-1}$. Also in Figure 6.11, the coefficient seems to approach this level at higher vapour fractions, in this case at a temperature of 20°C. The mass flux does not seem to have a major influence on the heat transfer coefficients at higher x in this diagram. In Figure 6.13, however, the post-dryout heat transfer coefficient was lower at higher temperature, possibly due to direct effects of smaller flow velocity, but possibly also due to non-equilibrium effects.

Based on the correlations for mist flow heat transfer outlined in Chapter 2, the expected level of heat transfer coefficients in the post-dryout regime can be estimated. Using the correlation of Dougall and Rohsenow (1963), Eq. (2.49), calculations were made at saturation temperatures 0 and 20°C and mass fluxes 100 and 600 $kgm^{-2}s^{-1}$, thus encompassing the range of conditions in the present study. A tube diameter of 0.81 mm was used. Results are shown in Figure 7.22, with calculated heat transfer coefficients from x=0.3 to x=1.0. As pointed out in Chapter 2, the Dougall and Rohsenow (1963) correlation becomes equal to the Dittus-Boelter single-phase correlation for x=1. As a reference, heat transfer using superficial vapour velocity in the Dittus Boelter correlation was also calculated for T=0°C, G=600 $kgm^{-2}s^{-1}$. The two models meet at x=1, but at x=0.3 the Dougall and Rohsenow (1963) correlation predicts about 20% higher heat transfer coefficient due to the presence of entrained droplets. This difference becomes larger at higher temperature, becoming 45% at 20°C due to the effect of the density ratio in Eq. (2.49).

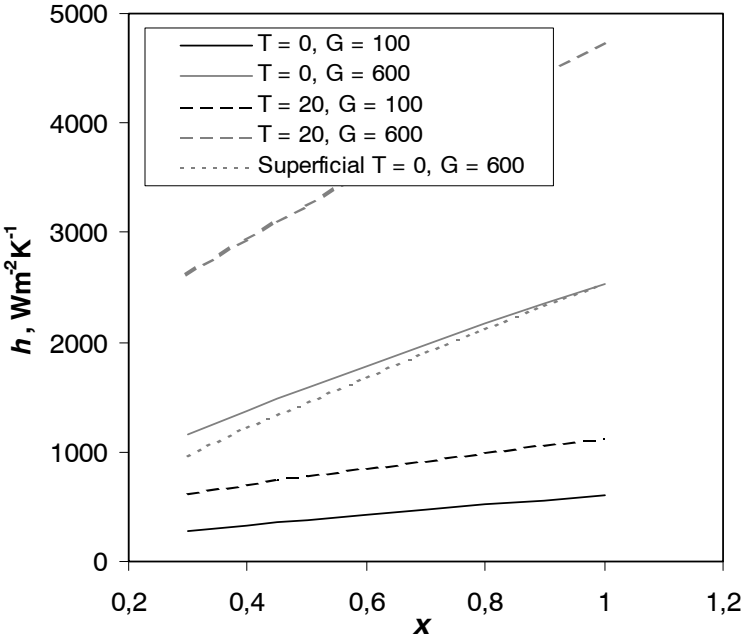

Figure 7.22 *Calculated mist-flow heat transfer coefficient at varying vapour faction based on the Dougall and Rohsenow (1963) correlation, for combinations of saturation temperature (T, °C) and mass flux (G, $kgm^{-2}s^{-1}$).The "superficial" curve is calculated using $Nu=0.023Re^{0.8}Pr^{0.4}$, where Re is based on vapour-only superficial velocity, and Re, Pr and Nu are based on vapour properties.*

A common feature of all equlibrium correlations is the predicted steady increase in heat transfer coefficient at increasing x, due to the increased flow velocity as the vaporization of droplet proceeds.

Models that account for non-equilibrium effects consider the limited heat transfer between vapour and droplets. The resulting departure from equilibrium gives rising vapour temperature and delayed evaporation of droplets. The test data of Hihara and Tanaka (2000) include local post-dryout heat transfer coefficients for mass flux 360, 720, and 1440 $kgm^{-2}s^{-1}$ at 15°C, as shown in Figure 3.2. Even though there is quite some scatter in the test data, it is clear that the measured trends are different from the steady rise in heat transfer predicted at equilibrium. At 360 and 720 $kgm^{-2}s^{-1}$ the measured coefficient actually drops after dryout completion, and continues at a low level at increasing x.

Figure 7.23 shows calculated heat transfer coefficients at conditions corresponding to the Hihara and Tanaka (2000) tests, using various models. The equilibrium model of Dougall and Rohsenow (1963) (D&R) predicts steady increase in h, while the non-equilibrium model of Groeneveld and Delorme (1976) (G&D) predicts a rising coefficient at a much lower level. Calculations were only done at 720 $kgm^{-2}s^{-1}$ using this model. The correlation of Shah and Siddiqui (2000) (S&S) predicts a quite different behaviour, with a sudden drop after dryout completion for G=720 $kgm^{-2}s^{-1}$, and a near-equilibrium trend up to x=0.75 and then a rapid drop at higher x for G=1440 $kgm^{-2}s^{-1}$.

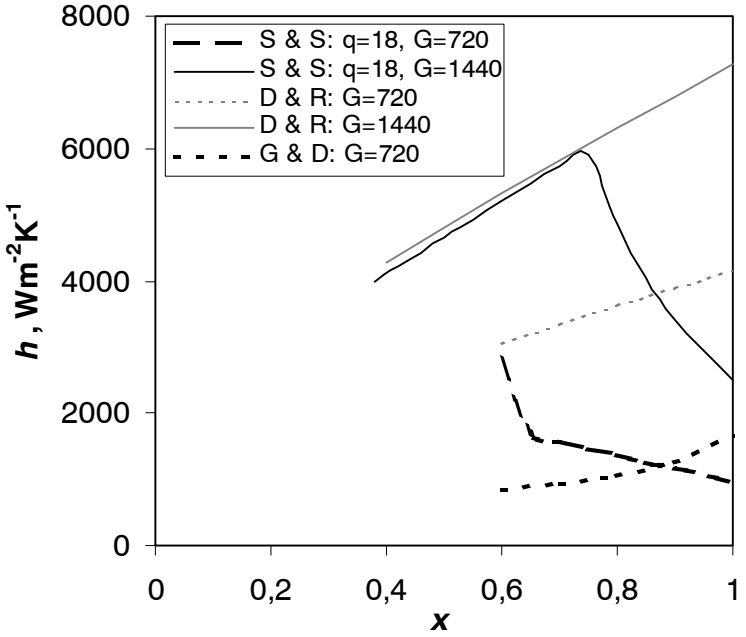

Figure 7.23 *Calculated post-dryout heat transfer coefficients using the "non-equilibrium" models of Shah and Siddiqui(2000)(S&S), and Groeneveld and Delorme (1976)(G&D), and the equilibrium model of Dougall and Rohsenow (1963)(D&R). Conditions:D=1mm, T=15°C, q=18 kWm^{-2}, G=720 and 1440 $kgm^{-2}s^{-1}$.*

Figure 7.24 shows the predictions using the correlation of Shah and Siddiqui (2000) drawn into the diagram of Hihara and Tanaka (2000), with a very good correspondence between test data on post-dryout heat transfer and predicted behaviour.

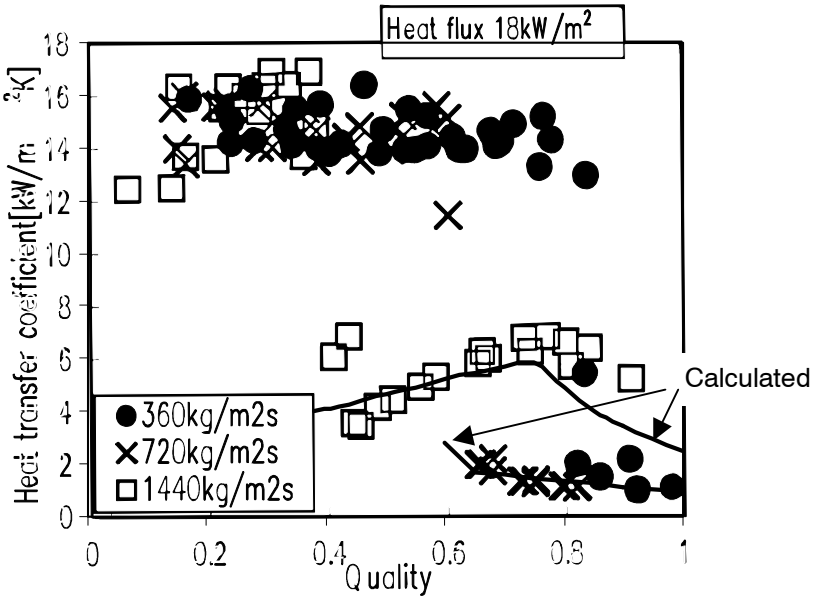

Figure 7.24 *Calculated post-dryout heat transfer coeffcient using the correlation of Shah and Siddiqui(2000) compared to the test data points of Hihara and Tanaka (2000). Model conditions:D=1mm, T=15°C, q=18 kWm⁻², G=720 and 1440 kgm⁻²s⁻¹.*

At 1440 $kgm^{-2}s^{-1}$ the behaviour is close to thermal equilibrium after dryout completion, due to the high turbulence and good heat transfer between vapour and droplets. The predicted and measured drop from around x=0.8 could not have been predicted with an equilibrium model, however. At 720 $kgm^{-2}s^{-1}$ there is considerable departure from equilibrium, which is correctly predicted by the Shah and Siddiqui (2000) correlation. As shown in Figure 7.23, the use of an equilibrium model here would have given overprediction by several hundred percent compared to the actual heat transfer coefficient.

A preliminary conclusion from modelled and experimental post-dryout heat transfer data is that non-equilibrium effects seem to be of quite some significance, even at the relatively high mass flux of 720 $kgm^{-2}s^{-1}$. Heat transfer in this regime is apparently well predicted by the model of Shah and Siddiqui (2000). At lower mass flux, the non-equilibrium effects are likely to be even more significant. At lower temperature the higher vapour flow velocity may compensate for this, however.

One question in relation to the above results is the effect of heat flux boundary conditions. The test data of Hihara and Tanaka (2000) and the correlation of Shah and Siddiqui (2000) are based on constant wall heat flux. In the above data, this gives a wall superheat of more than 15 K at a mass flux of 720 $kgm^{-2}s^{-1}$. These conditions may not be comparable to the situation in a fluid-heated tube, where wall superheat would be prevented from reaching this level. Some caution must therefore be exercised in the use of the above model in heat exchangers with small temperature difference and limited possibilities for surface superheating.

7.5 Discussion of flow pattern observations

7.5.1 General

Flow pattern observations and flow charts for the heated 0.98 mm ID glass tube are presented in Section 6.6. A majority of observations were done at 20°C to reduce the heat transfer from/to the test tube to/from ambient air, and to make sure that dryout effects were present due to high temperature. Two-phase flow characteristics in CO_2 evaporator tubes are unusual due to the high vapour density, and at 20°C this effect becomes very clear. Figure 7.25 shows calculated void fraction using the Rouhani-Axelsson (1970) vapour void fraction correlation (Eq. 2.33).

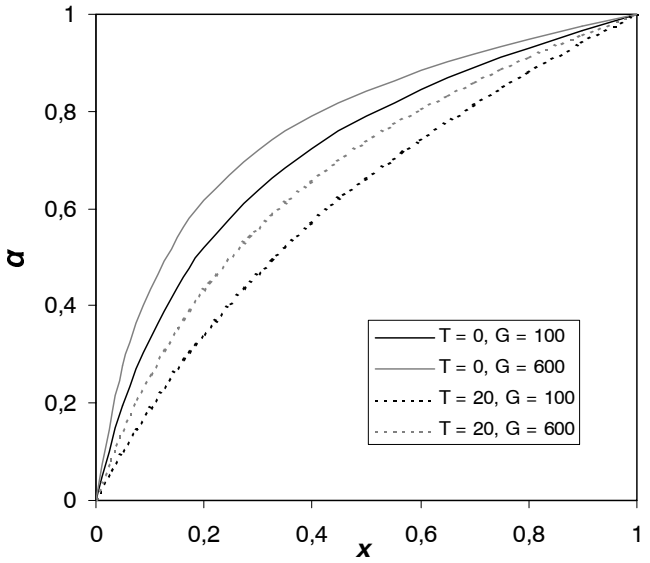

Figure 7.25 *Void fraction at varying vapour fraction, at temperatures(T) 0 and 20°C and mass fluxes (G) 100 and 600 $kgm^{-2}s^{-1}$, based on the correlation of Rouhani and Axelsson (1970).*

Already at 0°C the curve is much more linear than usual for common refrigerants, and at 20°C, the vapour volume increases almost linearly with *x*. This behaviour, plus the particularly low surface tension, should be kept in mind while discussing the flow pattern results. An additional parameter that may affect the flow patterns is the contact angle between liquid and wall, especially at low flow conditions. Here, the flow may behave differently in a glass tube than in a metal (aluminium) tube.

7.5.2 Superficial velocity chart

In analysing the flow pattern observations, a key question is whether the transitions between flow regimes can be predicted by any of the generalized chart types and transition lines discussed in Chapter 2. In addition, the observations can be compared to published charts based on experiments in small-diameter air/water flow, as shown in Chapter 2. Figures 7.26 and 7.27 show two of the transition lines proposed by Weisman et al. (1979); for transition between intermittent and annular flow, and for transition into the dispersed flow regime at increasing liquid superficial velocity.

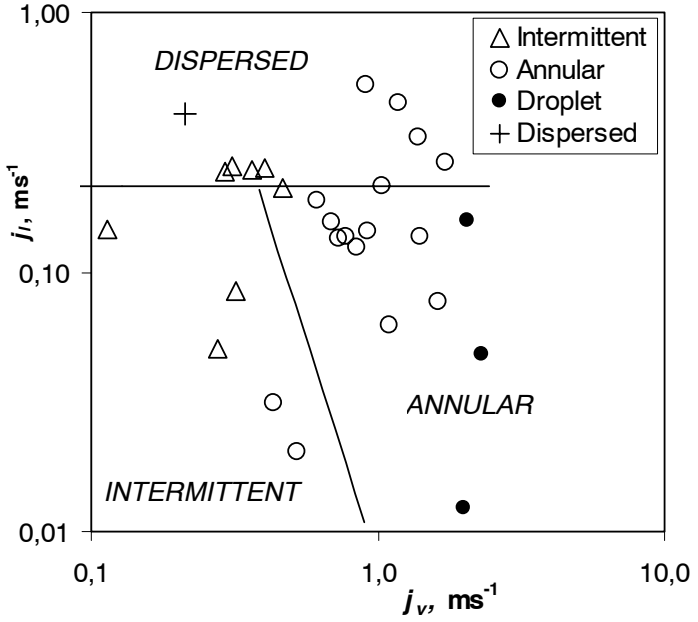

Figure 7.26 *Flow pattern observations for CO_2 (Chapter 6) in relation to transition lines proposed by Weisman et al., (1979) (regime names in CAPITAL ITALICS).*

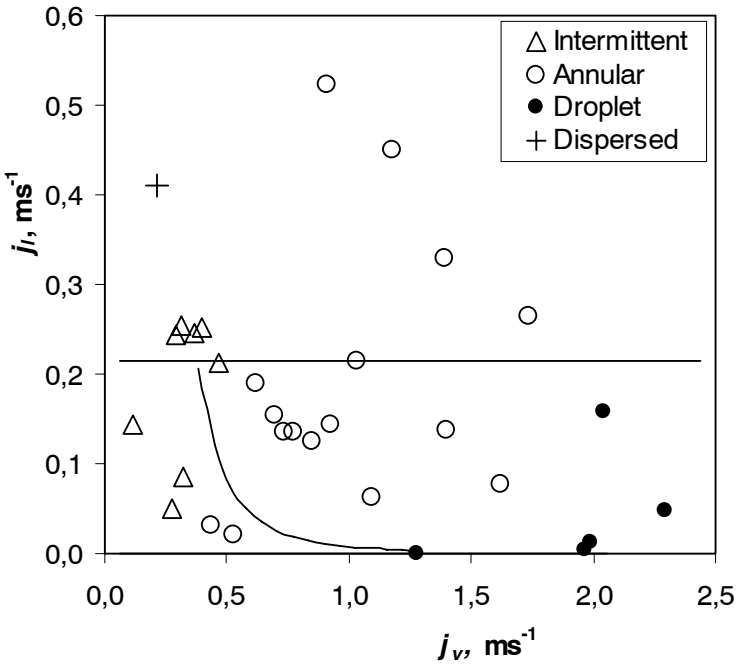

Figure 7.27 *Flow pattern observations for CO_2 (Chapter 6) in relation to transition lines proposed by Weisman et al., (1979).*

The intermittent/annular transition line of Weisman et al. (1979) is close to predicting the observed behaviour, even though a few points fall on the "wrong" side of the line and the slope apparently should have been in the opposite direction. Coleman and Garimella (1999) also noted that this transition line was close to their experimental air/water observations in a 1.3 mm ID tube. The Weisman transition line into dispersed flow does not fit the data, however, predicting transition at a moderate liquid superficial velocity (0.22 ms^{-1}). Coleman and Garimella (1999) observed the opposite tendency, so this transition prediction seems questionable as a general tool.

Weisman at al. (1979) also gives a transition line into stratified flow, giving a horizontal line at a liquid superficial velocity of 0.00006 ms^{-1}, which gives a liquid flow rate that probably can not be observed in practice. The possible occurrence of stratified flow below this j_l has no practical significance, since x will be equal to 1.0. As mentioned above, stratified flow was not observed in the experiments with q>0.

Compared to the observed transitions of Damianides and Westwater (1988) (Figure 2.13), and Coleman and Garimella (1999) (Figure 2.14), the present observations show some important differences. The air-water two-phase flow map of Damianides and Westwater (1988) show transition from

intermittent (slug) flow to annular flow at vapour superficial velocity of 20-40 ms^{-1}, i.e. almost two decades higher than in the present study. They observed transition to dispersed flow with air/water at about 0.5 ms^{-1}, which seems to be at about the same level as in the present CO_2 tests. Stratified flow was not observed by Damianides and Westwater (1988). Coleman and Garimella (1999) observed transition from intermittent to wavy annular flow at about j_v=6 ms^{-1} in a 1.3 mm ID tube with air/water flow, and transition to annular flow at about 20 ms^{-1} for a wide range of liquid superficial velocity. Stratified flow was not observed. The absence of stratified flow and the transition to dispersed flow show some similarities to the present observations on CO_2, while transition to annular flow occurs at much lower vapour velocity with CO_2 than with air/water at low pressure. Another difference is the absence of droplet or mist flow patterns in the air/water tests. Several authors have claimed that surface tension effects were responsible for absence of stratified flow, but this factor should not play an important role with CO_2 considering the much lower surface tension than of water.

A few observations of CO_2 flow were made also at $0^{o}C$/13 kWm^{-2} and at $20^{o}C$/0 kWm^{-2}, to see the effects of temperature and heat flux on the flow pattern. Results from these additional observations are shown as grey markers in Figure 7.28. At a temperature of $0^{o}C$, annular flow was maintained up to a much higher superficial vapour velocity. This indicates that the entrained amount of liquid is smaller at low temperature, thus leaving more liquid in the annular film. At q=0, one observation of stratified flow was made, at conditions that gave annular flow when heat flux was added. The other observations at q=0 gave flow patterns that matched observation with positive heat flux (intermittent or annular flow).

The stratified flow observation at zero heat flux is quite interesting, indicating an influence of heat flux in determining the flow pattern. It is not clear what mechanism that gives annular flow when heat is added, but the presence of small vapour bubbles may alter the flow characteristics of the liquid phase by changing the effective density and viscosity.

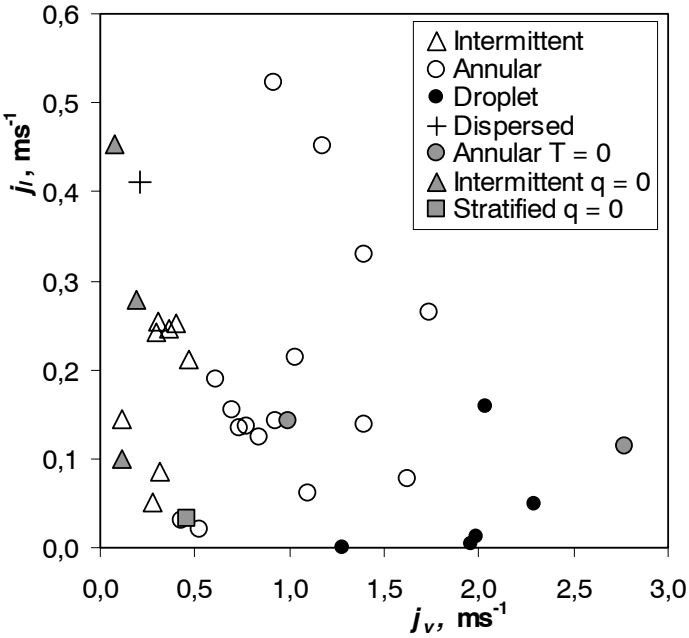

Figure 7.28 *Flow pattern observations for CO_2 including points at 0°C and at zero heat flux.*

7.5.3 Vapour fraction / mass flux chart

Based on the equations and procedures for drawing transition lines in the flow pattern chart of Kattan et al. (1998a), a chart for CO_2 flow in a 0.98 mm diameter tube at 20°C was generated. Figure 7.29 shows the resulting chart, with the present observations plotted into the coordinate system. The generalized transition lines give a poor prediction of the actual situation, with droplet ("mist") flow observations in the predicted annular regime, and a majority of the annular observations in the predicted intermittent regime.

The transition into bubbly flow is predicted to occur at mass flux around 600 kgm^{-2}s^{-1}, while transition into mist flow is predicted from a mass flux of 1500 kgm^{-2}s^{-1} and upwards, which is well above the range where mist flow (entrained droplet flow) was observed in the present tests. It is clear that the concept of the transition lines in this map does not match the present data. The flow chart of Kattan et al. (1998b) was based on earlier charts by Taitel and Dukler (1976) and Steiner (1993), all of which were adapted to larger diameter flow and quite different fluid properties than of CO_2.

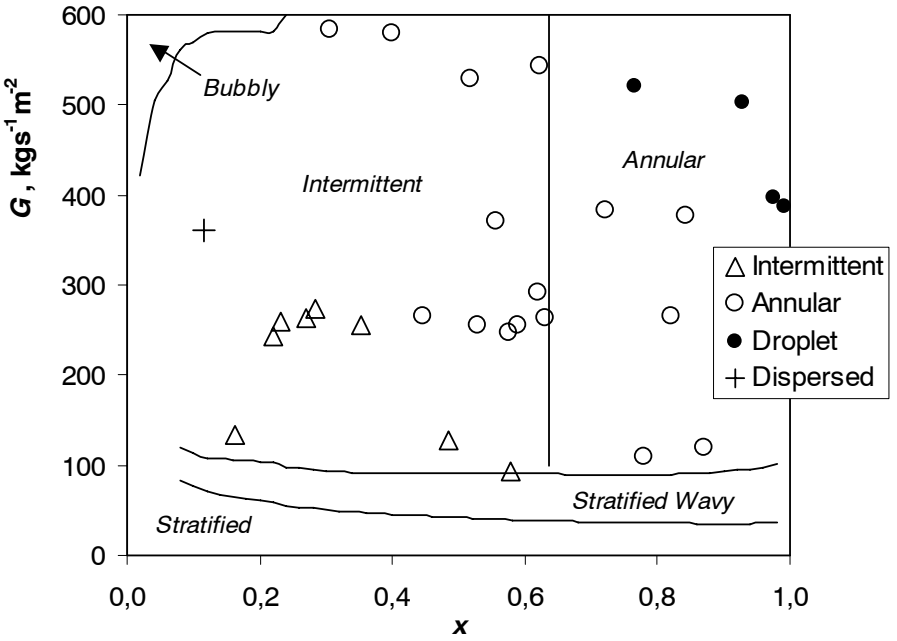

Figure 7.29 *Flow pattern observations for CO_2 (Chapter 6) in relation to transition lines proposed by Kattan et al.(1998a). Predicted flow chart regimes are shown in Italics*

Onset of partial dryout in the flow pattern map of Kattan et al. (1998a) was based on identifying the conditions that would give a transition from annular flow to stratified-wavy flow. By modifying the Weber- and Froude number influence on the stratified-wavy flow boundary in the Steiner (1993) flow map, transition to partial dryout could be accounted for. In the present tests, the dryout mechanism is not related to stratification of the flow, and liquid entrainment seems to have much more influence on the dryout occurrence. In the experiments that constitute the basis for the Kattan et al. (1998a) flow map, annular to mist flow transitions occurred only at very high mass flux, due to the properties of the refrigerants studied, and the relatively low pressures. Entrainment effects and models were not considered by Kattan et al. (1998a). In the present system, however, the annular to mist transition and liquid entrainment effects on dryout are of great importance, and have to be accounted for. As an example of the possible shape of the annular-droplet transition line, the predicted occurrence of dryout based on the Kon'kov/Ahmad method (Chapter 2) is indicated in Figure 7.30. Even though transition from annular to droplet flow was generally observed at higher x, the line seems to follow the observed tendency of earlier onset of droplet flow at higher mass flux.

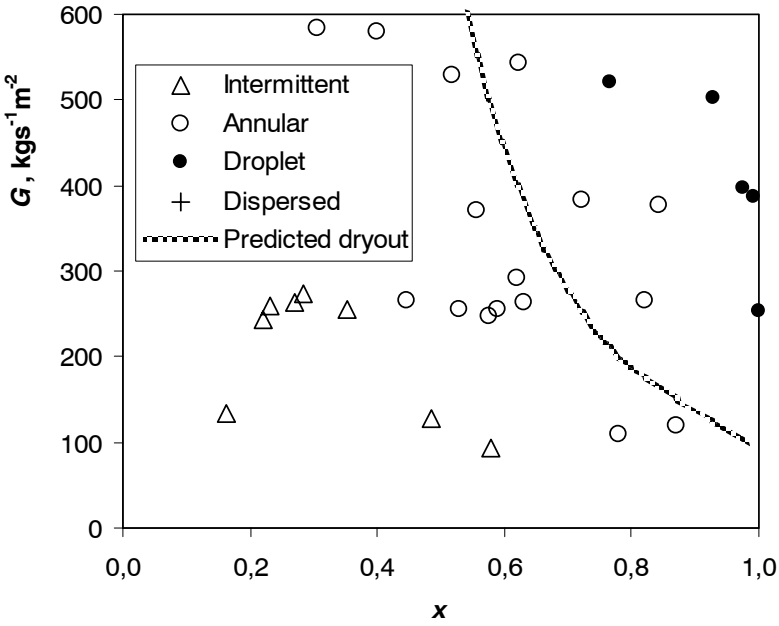

Figure 7.30 *Predicted onset of dryout shown as a possible indicator of transition from annular to droplet flow. The dryout curve is based on water dryout data by Kon'kov (1965) scaled to CO_2 by the method of Ahmad (1973).*

7.5.4 Inception of entrainment

Equation (2.5) (Utsuno and Kaminaga, 1998) and Figure 2.10 predicted inception of entrainment at a superficial vapour flow velocity of about 0.4 ms^{-1} at a temperature of 20°C. Table 7.1 shows results from flow pattern observations that indicate conditions when entrainment could/could not be observed in the video recordings. Superficial velocity data are based on measured mass flux and vapour fraction.

Table 7.1 *Entrainment observations in tests*

Test	G, $kgm^{-2}s^{-1}$	x	j_v, ms^{-1}	j_l, ms^{-1}	Entrainment
29	109	0.78	0.43	0.03	no
30	119	0.87	0.53	0.02	no
7	266	0.45	0.62	0.19	yes
11	263	0.63	0.85	0.13	yes
13	266	0.82	1.10	0.06	yes

From the above observations, the inception of entrainment seems to occur at a superficial vapour velocity between 0.5 and 0.6, thus indicating that the

inception criterion of Eq. 2.5 is close to the actual situation. The thicker liquid film in tests 7 and 11 than in tests 29 and 30 also contributes to onset of entrainment, since higher film Reynolds number is known to increase entrainment.

In summary, the flow pattern observations on CO_2 did not fit any of the generalized maps or transition lines, including the map proposed by Kattan et al. (1998a). Only the intermittent-annular transition prediction of Weisman et al. (1979) was close to the observed behaviour. Compared to small-diameter observations with air/water at low pressure, the transition into annular flow occurred at much lower superficial vapour velocity (superficial velocity of approximately 0.5 ms^{-1}). Observed inception of entrainment at 0.5-0.6 ms^{-1} superficial vapour flow velocity was close to the predicted onset at 0.4 ms^{-1}.

7.6 Pressure drop

All pressure drop measurements presented in Chapter 6 have been compared to the correlations outlined in Chapter 2, including the general models and the special correlations for small-diameter flow. A total of 95 test points were considered. Frictional pressure drop data were obtained as shown in Section 4.6.2, by subtracting inlet/outlet pressure drops, frictional pressure drops in unheated inlet/outlet, and acceleration pressure drop, from the measured total pressure drop between the test section manifolds.

7.6.1 Comparison with general friction pressure drop correlations

Two versions of the Friedel (1979) correlation were tried, the first one using equivalent two-phase density and corresponding Froude and Weber numbers, as shown in Section 2.6.2. Instead of the turbulent friction factor formula given by Friedel for the liquid-only flow (Eq. 2.77), an explicit expression by Haaland (1983) was used

$$f = \left\{ 1.8 \log_{10} \left[\frac{6.9}{Re} + \left(\frac{r}{3.7D} \right)^{1.11} \right] \right\}^{-2} \tag{7.4}$$

Here, r is the wall roughness of the tube, which was assumed to be 10^{-6} m. Correspondence between measured and calculated pressure drops using this correlation is shown in Figure 7.31 (left). Average deviation is –15.3% and mean deviation is 25.3%. Especially at small pressure drops, the model greatly underpredicts the experimental data. The right-hand side part of Figure 7.31, shows results using the other version of the Friedel correlation using single-phase liquid density, Froude- and Weber numbers, and the original single-phase friction factor models by Friedel. The accuracy is slightly improved, with a mean deviation of 22.3%, but the tendency of underprediction is increased slightly, giving an average deviation of -17.4%. Also Friedel (1979) commented the slightly better accuracy of the "liquid-property" version of the correlation.

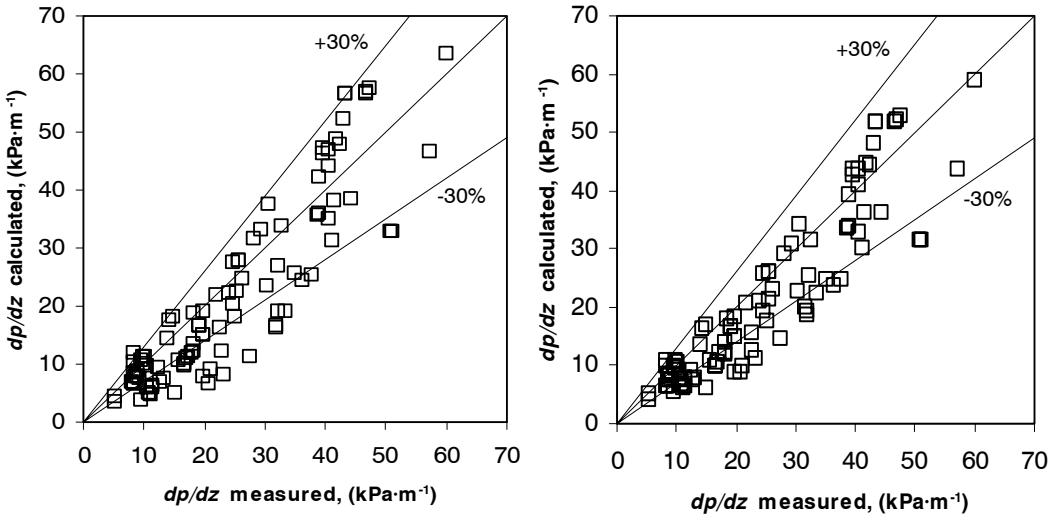

Figure 7.31 *Correspondence between measured and calculated friction pressure drop using the correlation of Friedel (1979). The left diagram was based on two-phase density, We and Fr, and friction factor from the Haaland (1983) model, and the right diagram was based on single phase liquid density, We and Fr, and the original Friedel friction factor expression.*

Figure 7.32 shows the results obtained using the CESNEF-2 correlation of Lombardi and Carsana (1992), as given in Section 2.6.2. Accuracy was markedly improved compared to the Friedel model, giving an average deviation of –1.1% and a mean deviation of 16.4%, which is very good.

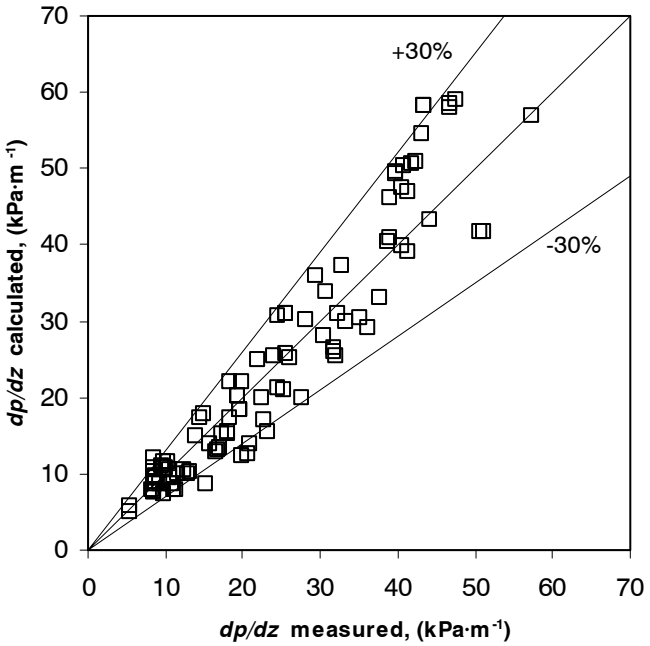

Figure 7.32 *Correspondence between measured and calculated friction pressure drop using the CESNEF-2 correlation of Lombardi and Carsana (1992)*

A number of other correlations were also tried, including the modified Chisholm correlation of Wambsganss et al. (1992), which gave a mean deviation of 103.5%, and the model developed by Grønnerud (1971), with a mean deviation 45.3%. The correlation of Fuchs (1975), without using the Froude number correction, gave better results with average deviation of minus 16.8% and mean deviation of 29.0%.

7.6.2 Comparison with small-tube correlations

Figure 7.33 shows results using the correlation of Tran et al. (1999), which is a specially developed model for small-diameter tubes. The correlation fails to reproduce the test data, with average/mean deviation of 74.5% and 80.4%, respectively.

Another small-tube correlation that was tried is the "adapted" version of the Friedel model as proposed by Zhang and Webb (2001), Figure 7.34.

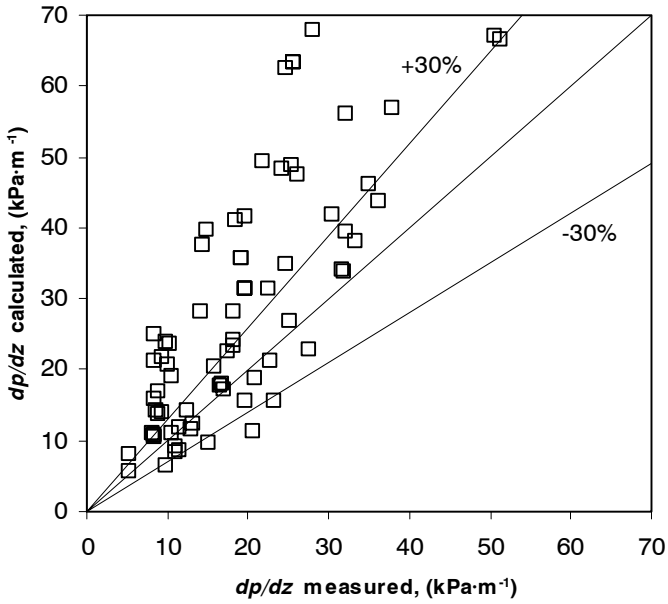

Figure 7.33 *Correspondence between measured and calculated friction pressure drop using the small-tube correlation of Tran et al. (1999)*

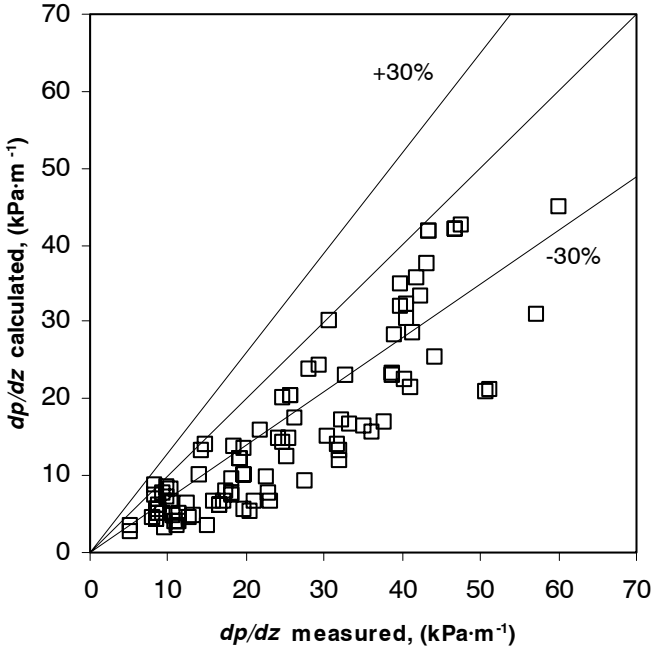

Figure 7.34 *Correspondence between measured and calculated friction pressure drop using the small-tube correlation of Zhang and Webb (2001)*

The correlation of Zhang and Webb (2001) works slightly better than the other small-tube model, but at average/mean deviation of –40.5 / 40.5% the accuracy is not very good. A paradox here is that the original Friedel model does a better job in relation to the present small-tube test data than the "adapted" model by Zhang and Webb (2001). The same authors claimed that the Friedel (1979) correlation overpredicts the pressure drops in small diameter tubes, especially for high reduced pressures. The above data and results show that this general statement is incorrect.

7.6.3 Evaluation of correlations by Friedel (1979) and Lombardi and Carsana (1992)

In order to evaluate the characteristics of the two best models, and to study the deviation between calculated and measured pressure drops in some more detail, predictions using the Friedel (1979) and Lombardi/Carsana (1992) correlations have been compared to some experimental data points shown in diagrams in Chapter 6. Figures 7.35 and 7.36 show results for varying mass flux at 0°C evaporating temperature and heat flux 10 kWm^{-2}, with experimental data as presented in Figure 6.17.

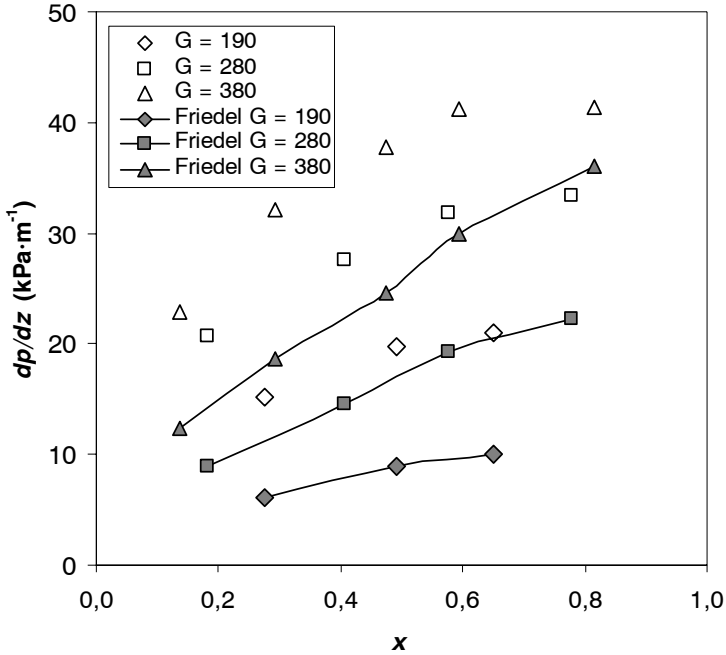

Figure 7.35 *Measured and predicted pressure drop gradient (dp/dz) using the Friedel (1979) correlation, for mass fluxes (G) 190, 280 and 380 kgm^{-2}s^{-1}. Evaporating temperature is 0°C, and heat flux is q=10 kWm^{-2}.*

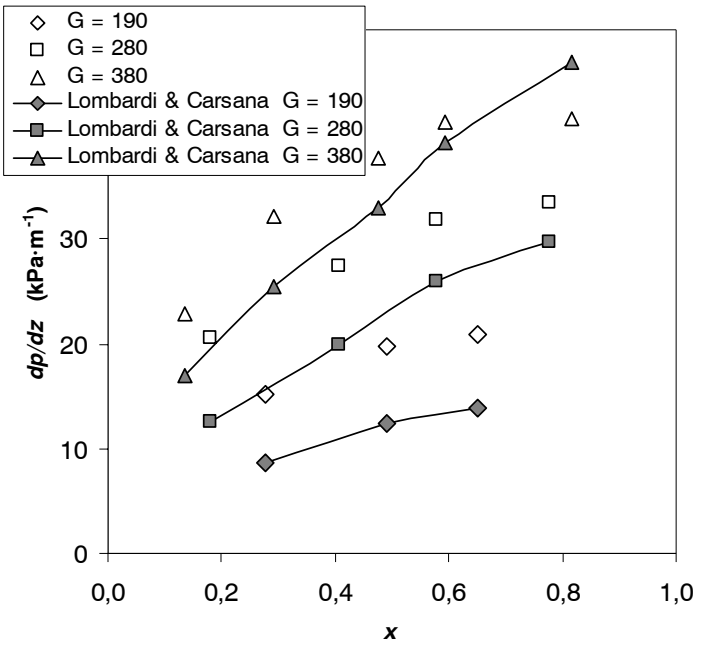

Figure 7.36 *Measured and predicted pressure drop gradient (dp/dz) using the correlation of Lombardi and Carsana (1992), for mass fluxes (G) 190, 280 and 380 kgm^{-2}s^{-1}. Evaporating temperature is 0°C, and heat flux is q=10 kWm^{-2}.*

As already observed, the Friedel correlation underpredicts the experimental data considerably, with increasing difference at lower mass flux. The Lombardi and Carsana (1992) correlation also gives increasing underprediction at lower mass flux, as shown in Figure 7.36, but the difference is smaller. Both correlations predict a steady increase in pressure drop at higher vapour fraction for the highest mass flux, while the experimental data indicate a more moderate increase in pressure drop at the highest vapour fractions.

At higher evaporating temperature, the deviation between calculated and measured data is smaller, as shown in Figure 7.37 for the Friedel (1979) correlation and in Figure 7.38 for the Lombardi/Carsana correlation. The evaporating temperature is 10°C, heat flux is 10 kWm^{-2}, and the range of mass flux is from 190 to 570 kgm^{-2}s^{-1}.

Again, the deviation is larger for the Fiedel (1979) correlation. Both models give better predictions as the mass flux is increased. Accuracy is improved compared to the data at 0°C, however, and the Lombardi/Carsana correlation gives data very close to the measured points.

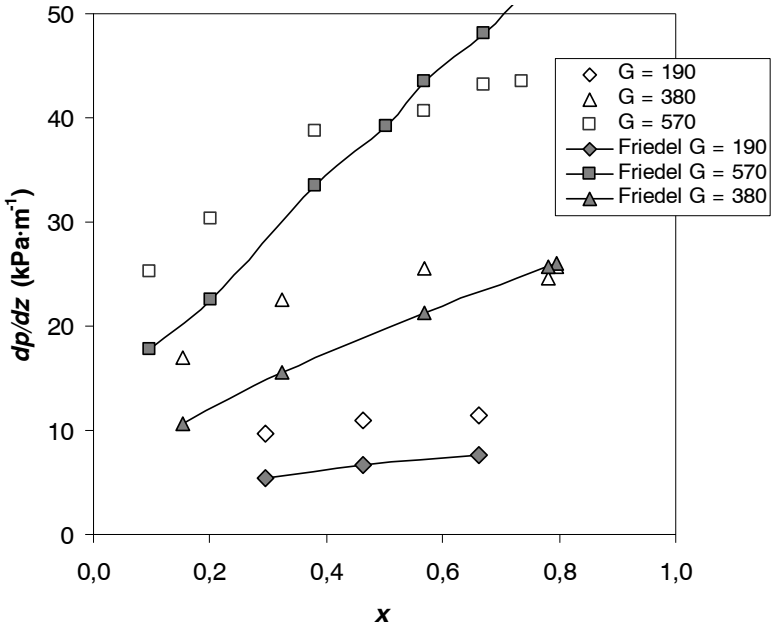

Figure 7.37 *Measured and predicted pressure drop gradient (dp/dz) using the Friedel (1979) correlation, for mass fluxes (G) 190, 380 and 570 kgm^{-2}s^{-1}. Evaporating temperature is 10^{o}C, and heat flux is q=10 kWm^{-2}*

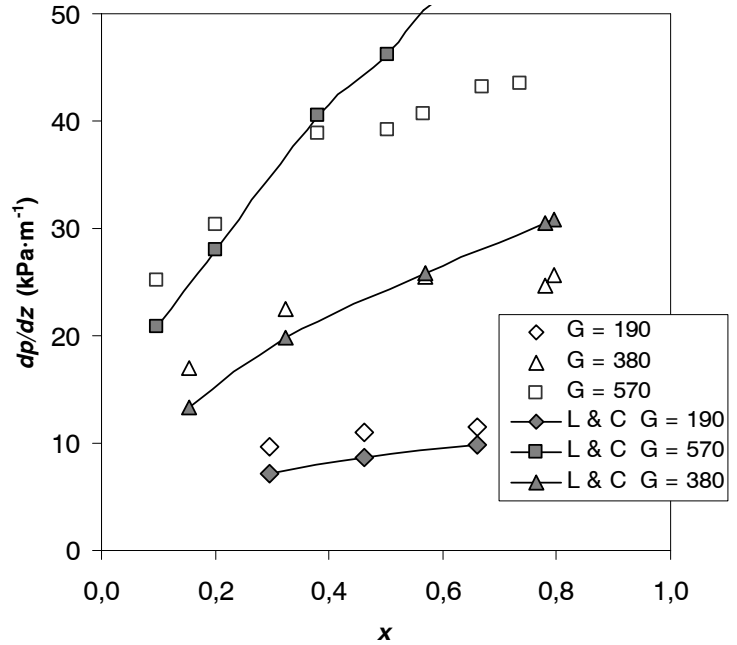

Figure 7.38 *Measured and predicted pressure drop gradient (dp/dz) using the Lombardi and Carsana (1992) correlation, for mass fluxes (G) 190, 380 and 570 kgm^{-2}s^{-1}. Evaporating temperature is 10^{o}C, and heat flux is q=10 kWm^{-2}*

As commented above, both correlations predict a steady increase in pressure drop at increasing *x*, especially at high vapour fraction and high mass flux, while the test data show a declining trend at higher *x*. As a result, the correlations overpredict the measured pressure drop data at high mass flux and high vapour fraction. A possible reason for this may be a change in flow pattern, giving less increase in *dp/dz* as *x* increases.

The above observations indicate that prediction accuracy changes with evaporating temperature, which is confirmed by Figures 7.39 and 7.40, showing data at temperatures 0, 10 and 20°C, at a heat flux of 10 kWm^{-2} and a mass flux of 280 kgm^{-2}s^{-1}.

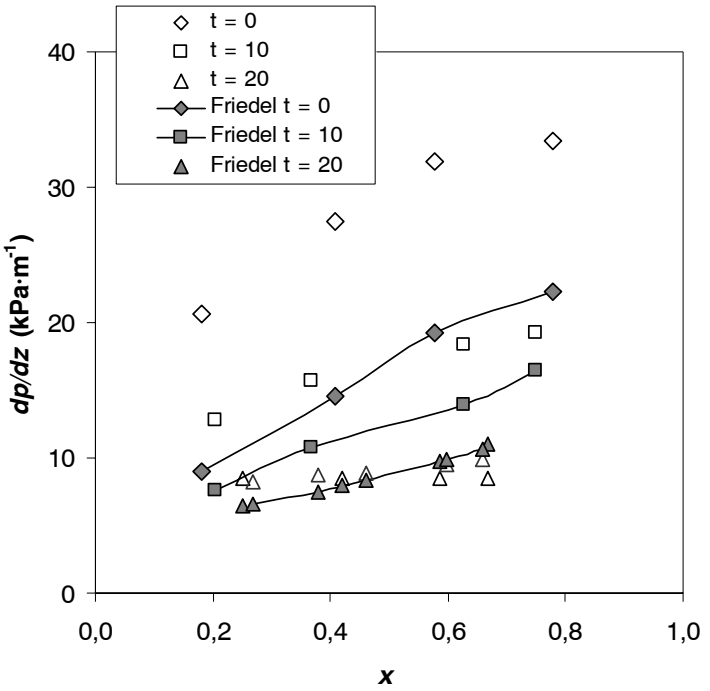

Figure 7.39 *Measured and predicted pressure drop gradient (dp/dz) using the Friedel (1979)correlation at varying vapour fraction (x), for evaporating temperatures (T) 0, 10 and 20 °C. Heat flux is q=10 kWm^{-2} and mass flux is G=280 kgm^{-2}s^{-1}.*

Both correlations predict well at 20°C, with increasing deviation at low temperature, again showing larger deviations with the Friedel (1979) model. The test data at 20°C indicate just a small increase in dp/dz at rising *x*, but the calculated data show more effect of *x*.

Since both correlations were developed using data mainly at moderate to low reduced pressure, it is somewhat surprising that prediction accuracy is

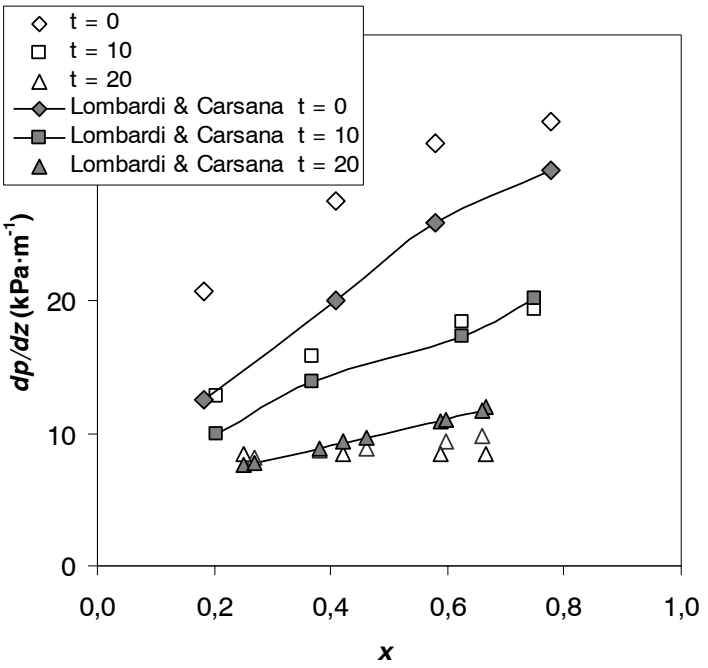

Figure 7.40 *Measured and predicted pressure drop gradient (dp/dz) using the Lombardi and Carsana (1992) correlation at varying vapour fraction (x), for evaporating temperatures (T) 0, 10 and 20 °C. Heat flux is q=10 kWm^{-2} and mass flux is G=280 kgm^{-2}s^{-1}*

improved as $p_r \rightarrow 1$ and not the other way around. Also, the above results are quite opposite to the observation of Zhang and Webb (2001), which found that the Friedel (1979) correlation overpredicted friction pressure losses in small tubes.

To summarize, the analysis of pressure drop data and correlations have shown that

- Among the tested correlations, experimental data on two-phase frictional pressure drop are best reproduced by the correlation of Lombardi and Carsana (1992). Second best prediction accuracy was obtained using the Friedel (1979) correlation using liquid-phase *We*, *Fr* and density.
- Prediction accuracy of the above correlations is reduced at lower evaporating temperature and lower mass flux, where the underprediction may be considerable. At high mass flux and high *x*, the correlations may overpredict the pressure drop

- None of the tested special small-tube correlations reproduced the experimental data well.

7.6.4 Pressure drop converted into temperature drop

In order to assess the consequences of refrigerant side pressure drop in evaporators, dp/dz can be converted into its equivalent in terms of drop in saturation temperature (dT/dz). Based on this parameter, the loss in total temperature difference caused by pressure drop and by heat transfer resistance can be compared. Figure 7.41 shows the pressure drop data of Figure 6.21 converted to temperature drop. Owing to the exponential shape of the saturation pressure curve, a given pressure drop has a larger effect at low temperature than at higher temperature. Heat transfer test data taken at the same conditions as these pressure drop recordings are shown in Figure 6.13.

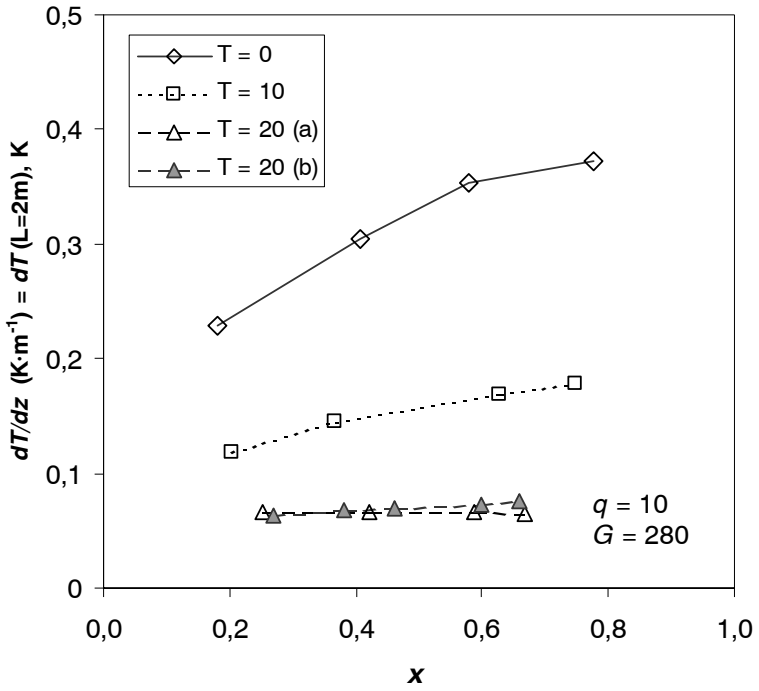

Figure 7.41 *Temperature gradient (dT/dz) at varying vapour fraction (x), for evaporating temperatures (T) 0, 10 and 20 °C. Heat flux is 10 kWm^{-2} and mass flux is G=280 kgm^{-2}s^{-1}. Results (a) and (b) are from different test series. For a tube length of 2 m, the ordinate gives temperature loss in K.*

Figure 7.42 shows the local temperature difference between tube wall and saturation temperature, calculated based on the heat transfer test data of Figure 6.13, i.e. at the same conditions as Figure 7.41.

From these two diagrams, the effects of pressure drop and heat transfer resistance can be observed and compared in terms of the common parameter of temperature difference. Since the temperature points in Figure 7.41 represent gradients, some information regarding circuit length is needed.

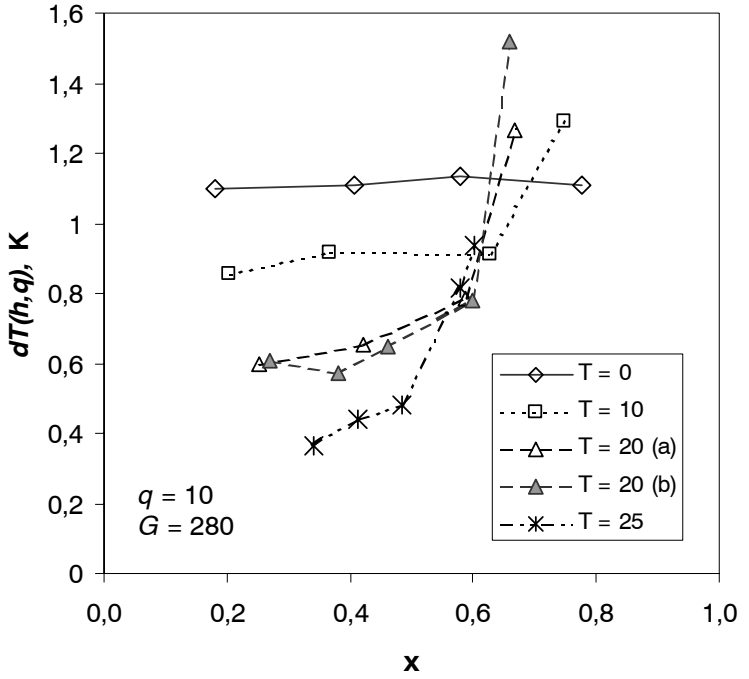

Figure 7.42 *Local temperature difference (=q/h) at varying vapour fraction (x), for evaporating temperatures (T) 0, 10 and 20 °C. Heat flux is 10 kWm^{-2} and mass flux is G=280 kgm^{-2}s^{-1}. Results (a) and (b) are from different test series.*

Assuming a circuit length of 2 m, the values of Figure 7.41 represent the mean reduction in temperature difference over the circuit length due to pressure drop. For the conditions in these diagrams, the loss in temperature difference due to pressure drop is smaller than the effect of finite heat transfer coefficient, and the influence by pressure drop becomes smaller at higher temperature even though the local heat transfer coefficient increases.

Since heat transfer dominated by nucleate boiling is not much improved by increased mass flux, and since the dryout problems are much aggravated by increased mass flux, there is actually no benefit of increasing G and dp/dz. From this it follows that conventional evaporator optimisation strategies

using a trade-off between ΔT caused by heat transfer and ΔT caused by pressure drop does not apply, at least not for the geometry and range of conditions investigated by this study. The optimum evaporator design based on the data shown here would have low mass flux and flooded operation, using efficient nucleate boiling, and avoiding the penalties of dryout, poor post-dryout heat transfer, and temperature loss due to pressure loss.

8. Correlation of heat transfer data

8.1 Basis for correlation development

In order to predict heat transfer behaviour of CO_2 in microchannel fllow vaporization, a number of mechanisms need to be accounted for and correlated:

- Nucleate boiling heat transfer
- Convective evaporation heat transfer
- Model for combining nucleate and convective components
- Dryout inception and completion
- Post-dryout heat transfer

Earlier Chapters have described experimental data and shown comparisons between data and various models for these mechanisms, thus establishing a basis that can be used in the development of a heat transfer correlation. Based on the analysis and discussion in Chapter 7, the models shown in Table 8.1 seem to have the potential for use in a heat transfer correlation for CO_2 flow vaporization in microchannels.

Experimental observations and predictions show that flow stratification is not likely to occur in microchannel flow vaporization of CO_2.in horizontal tubes. Effects of stratification and partial wetting on heat transfer and dryout behaviour are therefore not included in the proposed correlation.

Annular flow is likely to dominate up to dryout in heat exchanger tubes with two-phase inlet, such as in evaporators for refrigeration, air conditioning and heat pump systems. The proposed correlation therefore assumes annular flow pattern up to the estimated x for onset of dryout.

Table 8.1 *Models that constitute a basis for correlation development*

Mechanism	Model	Shown in
Nucleate boiling	Cooper (1984) Gorenflo (1993)	Eq. (2.46) Eq. (2.43-45)
Convective evaporation	Kattan et al. (1998b)	Section 2.5.2
Model for combining nucleate and convective heat transfer	Asymptotic model, with n=3	Eq. (2.28)
Dryout inception	Kon'kov (1965) data scaled from H_2O to CO_2 using Ahmad (1973)[a]	Section 2.3.7
Post-dryout heat transfer	Shah and Siddiqui (2000)	Section 2.5.5

a: Using scaling factor that can be based on Weber-Reynolds number (Eq. 2.12) or Barnett number (Eq. 2.13)

As shown in Chapter 7, the Cooper (1984) model underpredicts the nucleate boiling data from the present tests by approximately 30%, while the Gorenflo (1984) model gives a slight overprediction.

Dryout inception is predicted at lower x using the Barnett number version of the Ahmad (1973) scaling factor, than with the original factor based on Weber-Reynolds number. The first model seems to give better correspondence to the critical x measured in the present tests.

From Table 8.1, there are two choices that need to be made; selection of nucleate boiling correlation, and selection of scaling factor in the Ahmad model. Owing to the limited number of data and the still incomplete understanding of CO_2 vaporization heat transfer behaviour, no attempts have been made to derive additional empirical factors or multipliers that could improve the fit between observed and predicted data. Since the present test data are not truly local, this would in any case be questionable.

8.2 Comparison between test data and correlations

8.2.1 Principles of comparison

Comparisons between test data and correlations have been made using three different combinations of the above models:

(a) Using the Cooper (1984) nucleate boiling correlation, and the Weber-Reynolds number scaling factor. This model would give the best fit to the published data of Hihara and Tanaka (2000).

(b) Using the Cooper correlation and the Barnett number scaling factor.

(c) Using the Gorenflo (1993) nucleate boiling correlation, and the Barnett number scaling factor.

The models for convective evaporation, combination of nucleate/convective contributions, and post-dryout heat transfer are as shown in Table 8.1.

In order to get a correct comparison between measured and correlated data, the mean heat transfer coefficient for the range of x in the test section need to be calculated. By calculating a mean coefficient, the predicted result for each test can be directly related to the experimental data presented in Chapter 6.

A special procedure was applied in calculation of the mean coefficient, using the measured G, q, and T. Based on the measured inlet and outlet x to the test section, the mean heat transfer coefficient was calculated for ten "sub-sections" using the following scheme:

$$h_{calc} = \frac{1}{10}\sum_{i=1}^{10} h(x_i) \tag{8.1}$$

where

$$x_i = x_{in} + \frac{i - 0{,}5}{10}(x_{out} - x_{in}) \tag{8.2}$$

x_{in}/x_{out} was the measured inlet and outlet vapour fraction in the test section in each test. The mean vapour fraction was assumed to be the x found in the experimental data reduction (Eq. 4.6).

8.2.2 Correlation using Cooper nucleate boiling correlation and Weber-Reynolds number in dryout scaling

Figure 8.1 shows the correspondence between measured and calculated heat transfer coefficient when using the models shown in Table 8.1 and in point (a) in Section 8.2.1. The average deviation is 14.6% and the mean deviation is 52.5%.

Two types of deviation can be observed in the Figure; a general underprediction at all levels of heat transfer, and significant scatter and overprediction in the lowest range of coefficients. These observations will be discussed in relation to "local" data in the following text.

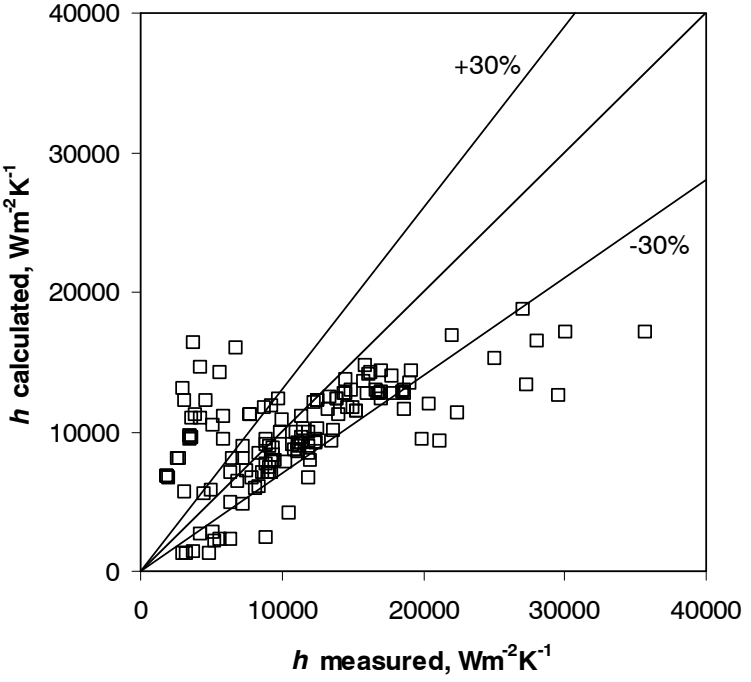

Figure 8.1 *Comparison of measured and calculated heat transfer coefficients using a combination of models given in point (a) in Section 8.2.1.*

Figure 8.2 shows a comparison of test data and calculated data at q=10 and 20 kWm^{-2}, T=10^{o}C, and G=570 kgm^{-2}s^{-1}, i.e. data as shown in Figure 6.7. At low/moderate vapour fraction, the correlation underpredicts the heat transfer coefficient, as may be expected when using the Cooper (1984) nucleate boiling model. The predicted drop in h due to dryout apparently occurs too late to match the experimental data, and this may also be

expected when using the *We-Re*-based scaling factor in the Ahmad (1973) model. As a result, a peak in the heat transfer coefficient is predicted for q=10 kWm^{-2} that is not reflected in the experimental data. This peak may also be influenced by a too high predicted convective coefficient.

Figure 8.3 shows heat transfer data and predictions for varying mass flux, at a temperature of 0°C and a heat flux of 10 kWm^{-2}, i.e. corresponding to Figure 6.9. Again, the nucleate boiling coefficients are too low, the convective contributions are too high, and predicted dryout occurs too late at G=380 kgm^{-2}s^{-1}

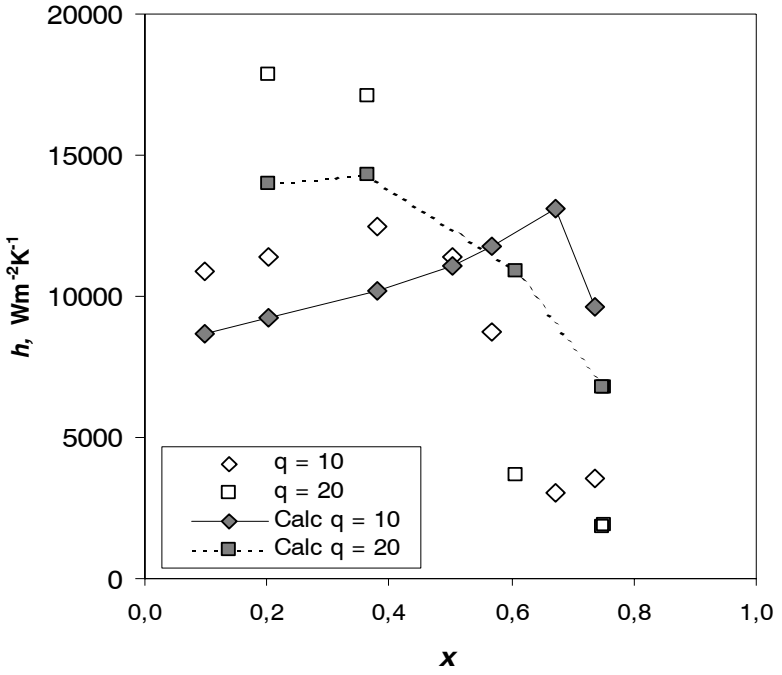

Figure 8.2 *Measured and calculated ("calc", using the (a) combination of models) heat transfer coefficients at q=10 and 20 kWm^{-2}, G=570 kgm^{-2}s^{-1} and T=10°C*

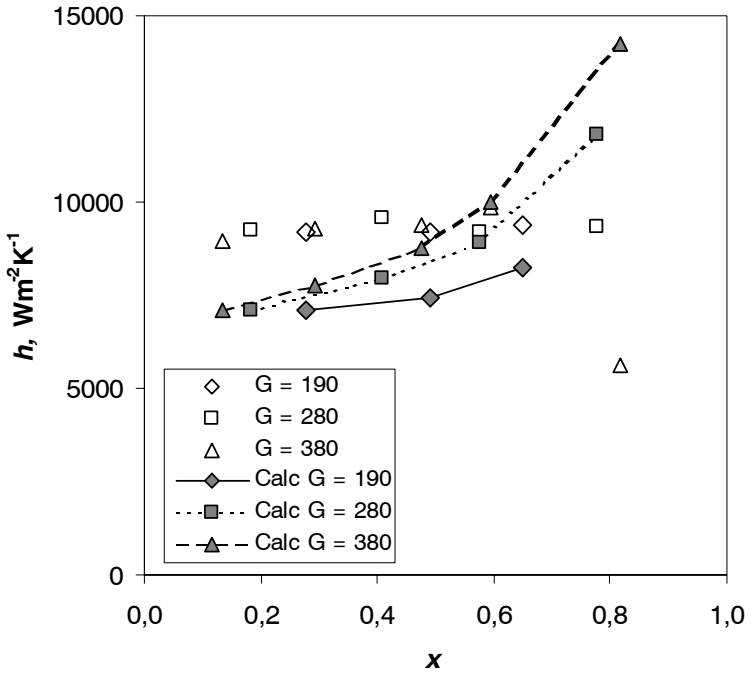

Figure 8.3 *Measured and calculated ("calc", using the (a) combination of models) heat transfer coefficients at q=10 kWm^{-2}, G=190-380 kgm^{-2}s^{-1} and T=0°C*

The reasons for a general underprediction using this correlation thus seems to be an effect of the Cooper correlation, while the scatter and overprediction at low measured coefficients may be due to heat transfer being predicted in the pre-dryout regime, while the test data are in the post-dryout regime.

By using the Barnett number scaling parameter instead, dryout will be predicted at lower x, and the effects of this is shown in the next Section.

8.2.3 Correlation using Cooper nucleate boiling model and Barnett number in dryout scaling

Figure 8.4 shows the overall comparison between measured and calculated heat transfer using the (b) correlation in Section 8.2.1. Compared to Figure 8.1, the situation is significantly improved, with average deviation reduced to only 7.7% and mean deviation to 35.1%.

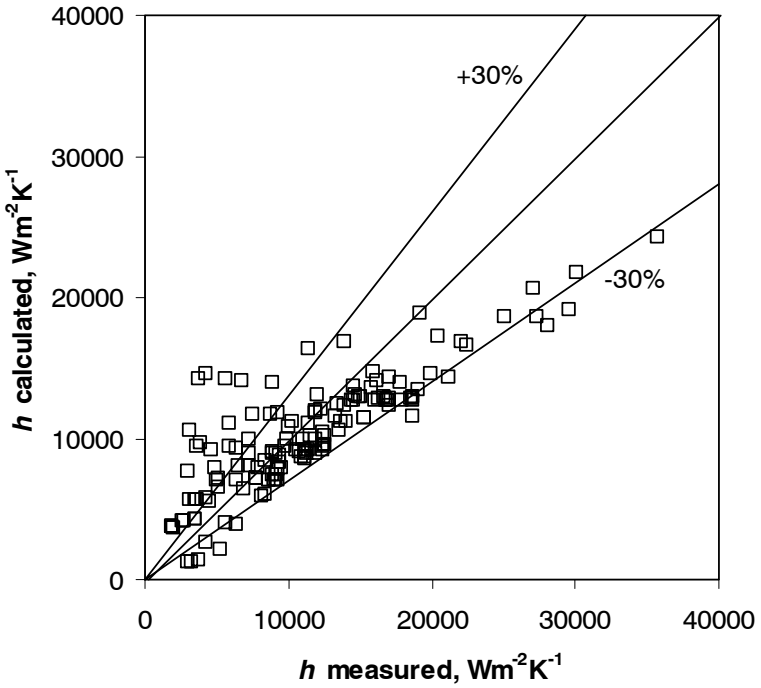

Figure 8.4 *Comparison of measured and calculated heat transfer coefficients using a combination of models given in point (b) in Section 8.2.1.*

Still, a slight underprediction can be observed, but very few data points now fall below the –30% line. The overprediction at low heat transfer coefficients has also been reduced, even though there is still potential for improvement in this range of data.

Figure 8.5 shows a comparison between test data and predictions for the same points as shown in Figure 8.2, i.e. at q=10 and 20 kWm^{-2}, T=10°C, and G=570 kgm^{-2}s^{-1}. Compared to Figure 8.2, the predicted drop in heat transfer due to dryout now falls closer to the experimental data, even though the predicted x_{cr} still seems a bit too high.

Since dryout is not predicted in the range of experimental data of Figure 8.3 even with the changed dryout scaling model, the results are unchanged at these conditions (0°C).

Figure 8.6 shows results at varying mass flux for a temperature of 10°C, and a heat flux of 10 kWm^{-2}. The experimental data are underpredicted at low x, and the convective effect seems a bit too large. Dryout location is reasonably well predicted, even though at a slightly high x compared to the observations.

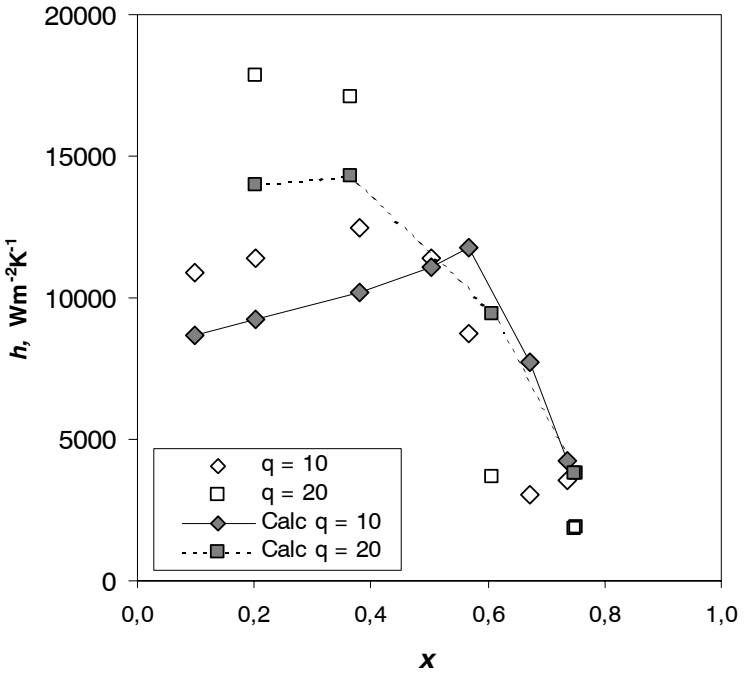

Figure 8.5 *Measured and calculated ("calc", using the (b) combination of models) heat transfer coefficients at q=10 and 20 kWm^{-2}, G=570 kgm^{-2}s^{-1} and T=10°C*

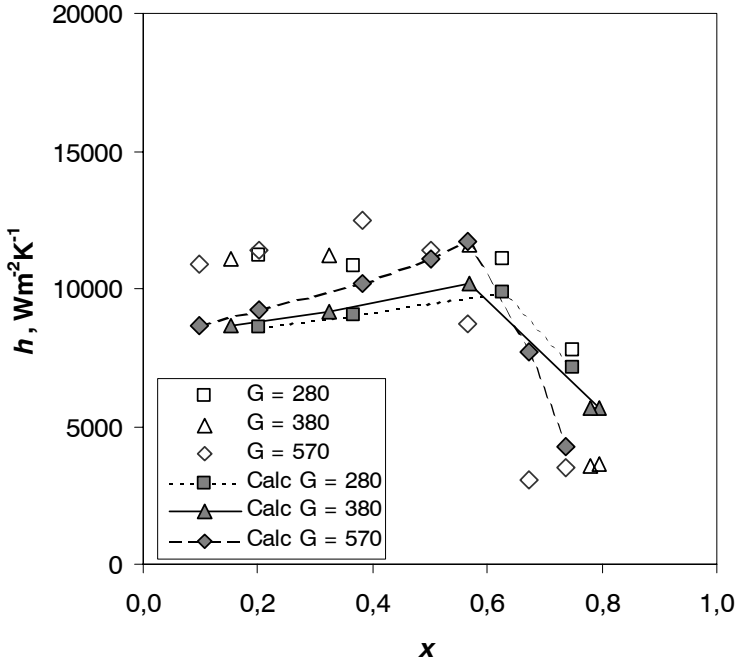

Figure 8.6 *Measured and calculated ("calc", using the (b) combination of models) heat transfer coefficients at q=10 kWm^{-2}, G=280-570 kgm^{-2}s^{-1} and T=10°C*

Figure 8.7 shows a comparison between experimental data at varying temperature and the "(b)" correlation, for a mass flux of 380 $kgm^{-2}s^{-1}$ and a heat flux of 10 kWm^{-2}. Again, the underprediction is noticeable at low x, while the fit is reasonably good at moderate/high x apart from the failure of the model to predict dryout at 0°C.

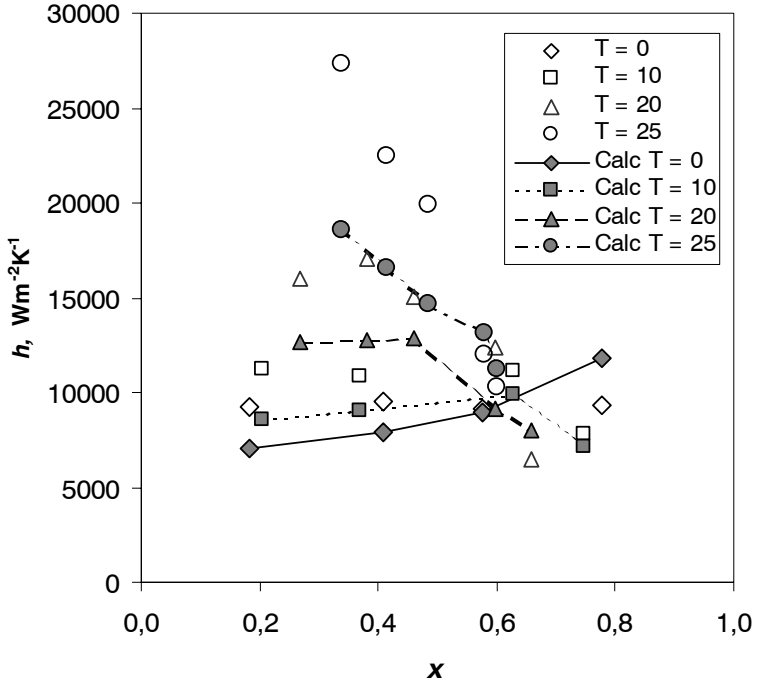

Figure 8.7 *Measured and calculated ("calc", using the (b) combination of models) heat transfer coefficients at q=10 kWm^{-2}, G=280 $kgm^{-2}s^{-1}$ and T=0-25°C*

8.2.4 Correlation using Gorenflo nucleate boiling model and Barnett number in dryout scaling

In the above comparisons, the experimental nucleate boiling heat transfer coefficients were underpredicted, and this effect could be avoided by instead using the Gorenflo (1993) nucleate boiling correlation, i.e. model (c) in Section 8.2.1. The dryout scaling is still based on the Barnett number.

Overall results are shown in Figure 8.8, where the average deviation between experimental and predicted data is 47.2%, and the mean deviation is 51.4%. The much higher calculated nucleate boiling coefficients give a consistent overprediction of the test data.

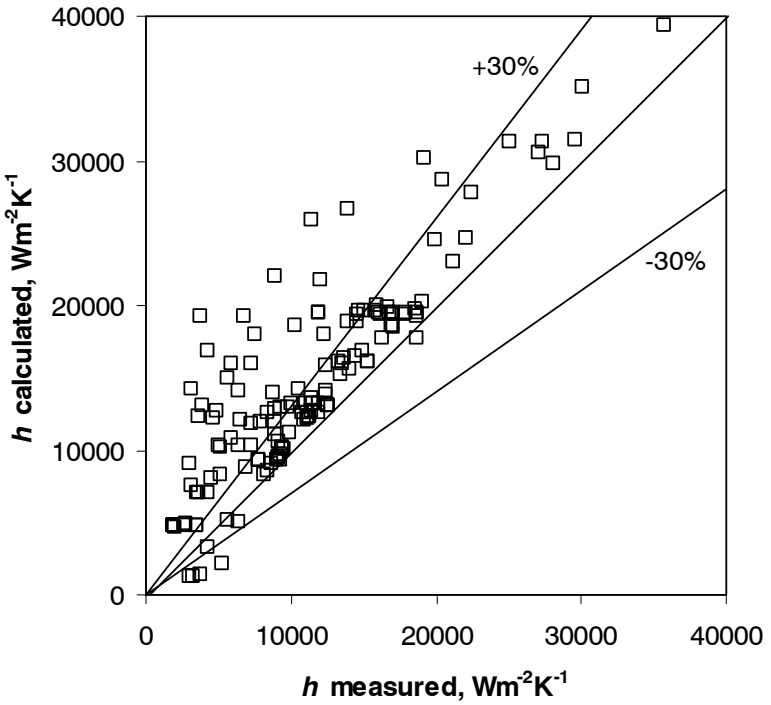

Figure 8.8 *Comparison of measured and calculated heat transfer coefficients using a combination of models given in point (c) above.*

A slight overprediction of low/medium-x heat transfer data can be observed in Figure 8.9, showing the same experimental data points as discussed in relation to the (a) and (b) correlations above. The percent deviation between measured and predicted pre-dryout heat transfer is smaller than with the Cooper model, but the change from underprediction to overprediction increases the effect of the "delayed" predicted dryout inception, thus giving too high heat transfer also at higher x.

Figure 8.10 shows how the prediction gives good correspondence at low x and 0°C, but too steep increase in heat transfer with increasing x, probably due to the combined effect of too high predicted convective heat transfer, and prediction of dryout at too high x.

Finally, Figure 8.11 shows how the overprediction of nucleate boiling heat transfer apparently becomes larger at higher evaporating temperature.

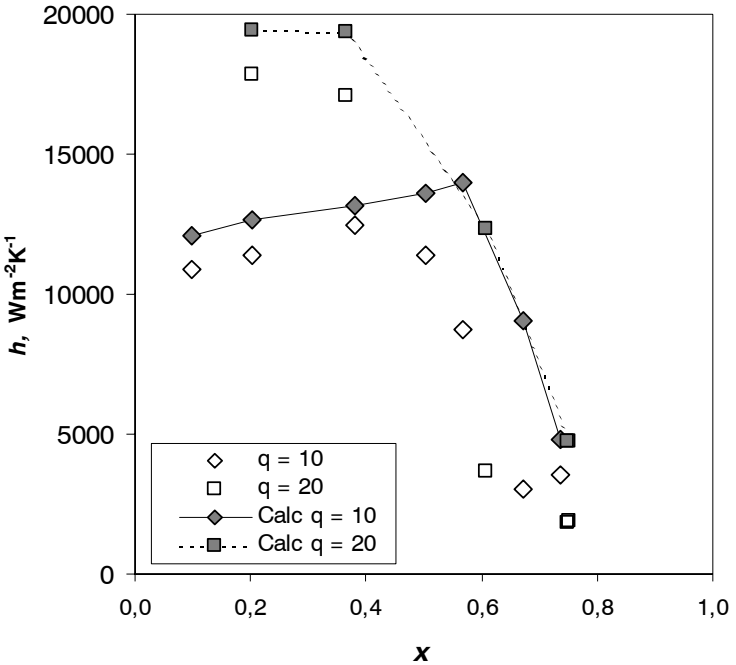

Figure 8.9 *Measured and calculated ("calc", using the (c) combination of models) heat transfer coefficients at q=10 and 20 kWm^{-2}, G=570 kgm^{-2}s^{-1} and T=10°C*

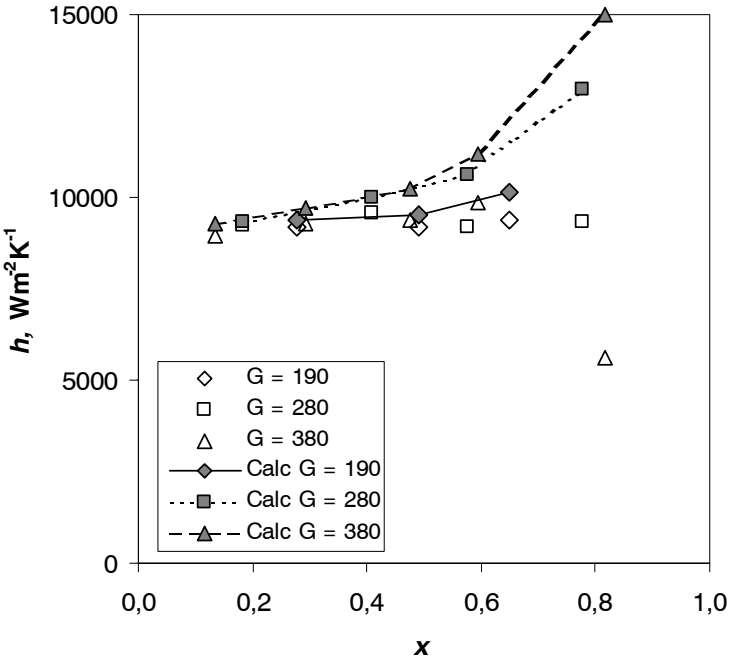

Figure 8.10 *Measured and calculated ("calc", using the (c) combination of models) heat transfer coefficients at q=10 kWm^{-2}, G=190-380 kgm^{-2}s^{-1} and T=0°C*

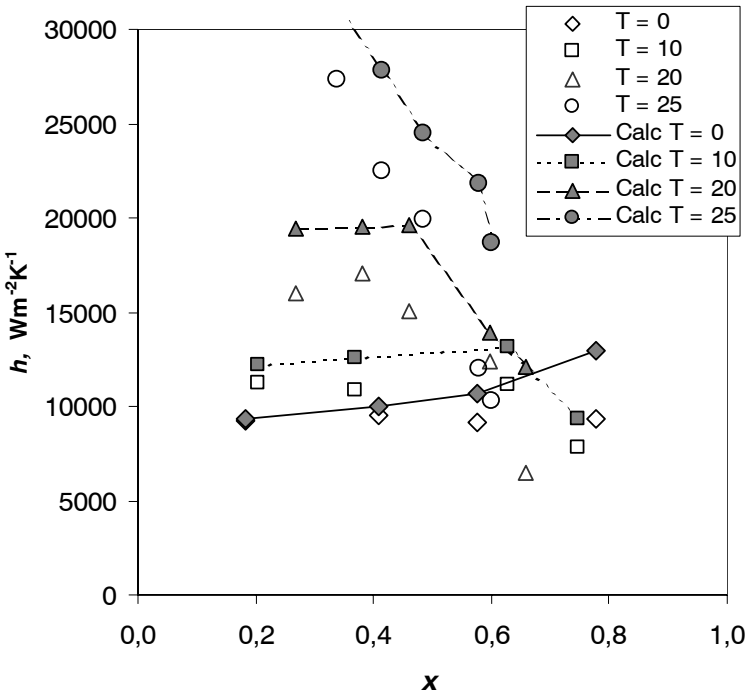

Figure 8.11 *Measured and calculated ("calc", using the (c) combination of models) heat transfer coefficients at q=10 kWm^{-2}, G=280 kgm^{-2}s^{-1} and T=0-25°C*

8.2.5 Concluding remarks

The above comparisons have shown that a combination of existing models for pre-dryout heat transfer (nucleate and convective), a model for dryout inception, and a model for post-dryout heat transfer can provide a reasonably good overall correlation for CO_2 flow-vaporization heat transfer in microchannels, even in situations where heat transfer varies dramatically due to dryout and post-dryout effects.

Very few results have been reported so far from other studies on CO_2 microchannel flow vaporization. Earlier attempts to correlate experimental data have largely been based on using existing "standard" correlations without looking into the more fundamental models for nucleate boiling, convective vaporization, dryout, post-dryout heat transfer, and the combination of these into a correlation. The range of temperature and mass flux in earlier studies has been more limited, thus providing less of a basis for discussing characteristics and for developing correlations. The present work has pointed out a possible correlation concept, reproducing the trends

and magnitudes of experimental heat transfer coefficients. Owing to the extreme and abrupt changes in heat transfer between regimes of nucleate-boiling and post-dryout heat transfer, the correlation of data is difficult.

The present study has also measured and correlated frictional pressure drop, a factor that has largely been ignored by earlier studies. Experimental heat transfer and pressure drop data in the present study were determined under fluid heating conditions and not with constant heat flux as in earlier work. Also, the test tube was of a relevant type and material for heat exchanger service, including parallel flowchannels. Thus, the present results should be as close as possible to the behaviour in real compact heat exchanger geometries. Earlier studies have generally used a single stainless-steel tube with resistance heating. Implications of experimental data and findings in this work are discussed in Chapter 6.

Further refinement of test data and models is clearly needed, especially regarding dryout prediction, and modelling of the convective evaporation heat transfer component prior to dryout. Compared to earlier studies using existing "standard" correlations, the present correlation with mean deviation of 35% gives improved prediction accuracy. The accuracy compared to present test data could have been further improved by introducing empirical factors and/or multipliers derived through regression of experimental data, but this would have introduced more uncertainty regarding general applicability of the correlation.

Thus, the recommended correlation for engineering prediction is model "(b)" above, as long as the system is similar to the present test tube, i.e. with parallel microchannel tubes having inlet/outlet manifolds, and flow of pure CO_2 at similar conditions of mass flux, heat flux and temperature.

Further studies in this area should extend the range of test conditions and flow observations, e.g. to lower temperature and lower mass flux, and to other tube diameters. In order to provide the necessary foundation for correlation development, true local heat transfer data will be needed. This will necessitate improved experimental concepts using wall temperature measurements. Effects of lubricant on heat transfer and pressure drop also needs to be investigated. Lubricant may have considerable influence especially on nucleate boiling heat transfer, and may also play a role in the post-dryout regime.

Further developments in modelling and prediction should consider the potential of using a detailed two-phase flow model with local correlations for entrainment and deposition as a basis, not just for dryout prediction but also as a basis for heat transfer modelling. As shown by some published studies on water/steam systems, this type of model can give good accuracy

in prediction of critical vapour fraction, and can also aid the modelling of pre- and post-dryout heat transfer.

Notation and Definitions

Symbol	Description	Unit
A	Area	m^2
A^*	Fluid dependent constant (Eq. 2.39)	-
A_f	Flow area	m^2
b	Weight function (Eq. 2.87)	-
c_f	Friction factor (Fanning)	-
A_i	Inside heat transfer surface	m^2
A_o	Outside heat transfer surface	m^2
B	Constant	-
c_p	Isobaric specific heat	$Jkg^{-1}K^{-1}$
C	Constant	-
C_c	Coefficient of contraction	-
D	Diameter	m
E	Enhancement factor	-
F	Two-phase convection multiplier	-
E	Entrainment rate	$kgm^{-2}s^{-1}$
f	Friction factor (Darcy)	-
F	Factor	-
F_{dc}	Parameter defined by Eq. (2.53)	-
$F(p)$	Function of reduced pressure	-

F_{PF}	Function of reduced pressure	-
G	Mass flux (mass velocity)	$kgm^{-2}s^{-1}$
g	Acceleration due to gravity	ms^{-2}
h	Heat transfer coefficient	$Wm^{-2}K^{-1}$
h	Specific enthalpy	Jkg^{-1}
h_{lv}	Enthalpy of evaporation	Jkg^{-1}
j	Superficial velocity	ms^{-1}
k	Thermal conductivity	$Wm^{-1}K^{-1}$
K	Constant	-
L	Length	m
$\dot{m}$	Mass flow rate	kgs^{-1}
M	Molecular mass	$kg{\cdot}mol^{-1}$
N	Number	-
n	Exponent	-
nf	Exponent	-
p	Pressure	Pa (Nm^{-2})
p_r	Reduced pressure ($=p/p_{cr}$)	-
q	Heat flux	Wm^{-2}
$\dot{Q}$	Heat load	W
r	Radius	m
R	Thermal resistance	m^2KW^{-1}
R_{cf}	Conduction and fouling resistance	m^2KW^{-1}

R_p	Surface rougness	m
S	Suppression factor	-
T	Temperature	^oC, K
T_r	Reduced temperature ($=T/T_{cr}$)	-
U	Overall heat transfer coefficient	$Wm^{-2}K^{-1}$
v	Specific volume	m^3kg^{-1}
x	Vapour (mass) fraction (quality)	-
x_A	Actual (non-equilibrium) vapour fraction	-
x_E	Equilibrium vapour fraction	
X	Lockhart-Martinelli parameter (Eq.2.22)	-
X	Independent variable	
Y	Dependent variable	
Y	Parameter defined by Eq. (2.48)	
z	Length	m
Z	Number	-

Greek

α	Void fraction	
δ	Film thickness	m
γ	Parameter defined by Eq. (2.14)	
μ	Dynamic viscosity	Pa·s
ρ	Density	kgm^{-3}
σ	Surface tension	Nm^{-1}

σ	Flow area ratio	-
ψ	Mass flux scaling factor	Eq. (2.12), (2.13)
θ	Wetting angle	Radians
Φ_{lo}	Two-phase frictional multiplier (Eq. 2.68)	-

Dimensionless numbers

Ce		Eq.(2.84)
Bo	Boiling number	Eq.(2.15)
Co	Convection number	Eq.(2.31)
Fr	Froude number	
Lo	Lombardi number	Eq.(2.83)
N_{conf}	Confinement number	Eq.(2.2)
N_{μ}	Viscosity number	Eq (2.7)
Nu	Nusselt number	
Re	Reynolds number	
We	Weber number	

Subscripts

b	bulk
c	critical
ce	convective evaporation
cr	critical
CP	constant property

CR	critical
dry	dry part
eq	equivalent
f	friction
fr	front
fric	frictional
g	gravity
gas	vapour/gas
h	hydraulic
i	inside
in	inlet
l	liquid
liq	liquid
lo	liquid only
m	momentum (acceleration)
m	mixture (homogeneous)
meas	measured
nb	nucleate boiling
nbp	pool boiling
ONB	onset of nucleate boiling
out	outlet
p	preheater

sat	saturated
tp	two-phase
ts	test section
v	vapour
vo	vapour only
w	wall
w	water
wet	wetted part
o	reference value
o	outside

Superscripts

m	exponent
n	exponent

Vapour and liquid superficial flow velocity:

$$j_v = \frac{Gx}{\rho_v} \tag{N.1}$$

$$j_l = \frac{G(1-x)}{\rho_l} \tag{N.2}$$

Darcy (or Moody) friction factor for circular tube:

$$f = \frac{2D\rho}{G^2}\left(-\frac{dp}{dz}\right) \tag{N.3}$$

Fanning friction factor for circular tube:

$$c_f = \frac{D\rho}{2G^2}\left(-\frac{dp}{dz}\right) \tag{N.4}$$

Average deviation (*AD*) and **mean deviation** (*MD*) are used in the assessment of the fit between calculated data for parameter *P* (P_{calc}) and measured data for parameter *P* (P_{meas}). The data set contains *n* points.

The deviations are defined as

$$AD = \frac{1}{n}\sum_n \frac{(P_{calc} - P_{meas})}{P_{meas}} \tag{N.5}$$

$$MD = \frac{1}{n}\sum_n \left|\frac{(P_{calc} - P_{meas})}{P_{meas}}\right| \tag{N.6}$$

References

Ahmad, S. Y., 1973. Fluid to fluid modeling of critical heat flux: A compensated distortion model. *Int. J. Heat Mass Tranfer*. Vol 16, pp. 641-662.

Akers, W. W., Deans, H. A., and Crosser, O. K., 1959. Condensing heat transfer within horizontal tubes, *Chemical Engineering Progress Symposium Series,* Vol 55 No 29, pp. 171-176.

Angus, S., Armstrong, B. and DeReuck, K.M., Altunin, V. V., Gadetskii, O. G., Chapela, G. A., and Rowlinson, J. S. 1976. International Thermodynamic Tables of the Fluid State – Carbon Dioxide. International Union of Pure and Applied Chemistry (IUPAC), Pergamon Press.

ASHRAE, 1986. Guide for Engineering Analysis of Experimental Data. ANSI/ASHRAE Guideline 2-1986. American Society of Heating, Refrigerating and Air-Conditioning Engineers, Inc.

Auracher, H., Drescher, G., Hein, D., Katsaounis, A., Kefer, V., Köhler, W., and Ulrych, G. 1993. Critical boiling states in flowing liquids. Chapter Hbc 1 in VDI Heat Atlas, English translation of VDI –Wärmeatlas, 6. auflage. Edited by VDI Gesellschaft Verfahrenstechnik und Chemieingenieurwesen. VDI-Verlag.

Baker, O., 1954. Simultaneous flow of oil and gas. *Oil and Gas J.* Vol 53, pp. 185-195.

Barajas, A. M., and Panton, R. L., 1993. The effects of contact angle on two-phase flow in capillary tubes, *Int. J. Multiphase Flow,* Vol 19 No 2, pp. 337-346.

Barnea, D., Luninski, Y., and Taitel, Y., 1983. Flow pattern in horizontal and vertical tw-phase flow in small diameter pipes, *Canadian J. Chem. Eng.,* Vol 61, pp. 617-620.

Bennett, D. L., and Chen, J. C., 1980. Forced convective boiling in vertical tubes for saturated pure components and binary mixtures, *AIChE J.,* Vol 26, pp. 454-461.

Bertoletti, S., Gaspari, G.S., Lombardi, C., Peterlongo, G., Silvestri, M., and Tacconi, F. A., 1965. Heat Transfer Crisis with Steam-Water Mixtures, *Energia Nucleare,* Vol 12 No 3, pp. 121-172.

Borishanski, V.M., 1969. Correlation of the Effect of Pressure on the Critical Heat Flux and Heat Transfer Rates Using the Theory of Thermodynamic Similarity, in *Problems of heat Transfer and Hydraulics of Two-Phase Media.* Ed. S. S. Kutateladze, pp. 16-37, Pergamon.

Bier, K., Engelhorn, H., and Gorenflo, D., 1976. Wärmeübergang an tiefsidende Halogenkältemittel, *Klima Kälte Ing.,* Vol 11, pp. 399-406.

Bredesen, A. M., Hafner, A., Pettersen, J., and Aflekt, K. 1997. Heat transfer and pressure drop for in-tube evaporation of CO_2. International Conference on Heat Transfer Issues in 'Natural' Refrigerants, Sponsored by IIR, ASHRAE and CEEE, University of Maryland, November. Preprints pp. 1-15.

Briggs, D. E., and Young, E. H. 1969. Modified Wilson Plot Techniques for Obtaining Heat Transfer Correlations for Shell and Tube Heat Exchangers. *Chemical Engineering Progress Symposium series,* Vol 65, No 92, pp. 35-45.

Carey, V. P. 1992. Liquid-Vapor Phase-Change Phenomena, Hemisphere Publishing Company.

Carey, V. P., Tervo, P. and Shollenberger, K. 1992. Partial Dryout in Enhanced Evaporator Tubes and Its Impact on Heat Transfer Performance. SAE Technical Paper 920551, SAE International Congress and Exposition, Detroit, Michigan, USA, Feb. 24-28.

Chen, J. C., 1966. A Correlation for Boiling Heat Transfer to Saturated Fluids in Convective Flow, *Ind. Eng. Chem., Process Design and Development*, Vol 5, No 3, pp. 322-329.

Cichelli, M. T., and Bonilla, C. F., 1945. Heat Transfer to Liquids Boiling Under Pressure, *Trans AIChE*, Vol 45, p. 755-787.

Coleman, J. W., and Garimella, S., 1999. Characterisation of two phase flow patterns in small diameter round and rectangular tubes. *Int. J. Heat Mass Trans.,* Vol 42, pp 2869-2881

Collier, J. G., and Thome, J. R. 1994. Convective Boiling and Condensation. 3rd Edition, Oxford University Press, Oxford Engineering Science Series.

Cooper, M. G., 1984. Heat flow rates in saturated nucleate pool boiling – a wide-ranging examination using reduced properties, *Advances in Heat Transfer*, Vol 16, pp. 157-239.

Cooper, A., Suitor, J.W., and Usher, J.D. 1980. Cooling Water Fouling in Plate Heat Exchangers. *Heat Transfer Engineering.* Vol 1, No 1, pp. 50-55.

Cooper, A., and Usher, J. D. 1998. Fouling. In: Heat Exchanger Design Handbook, Section 3.7.9. Begell House, Inc., G. F. Hewitt, Executive Editor.

Cross, P. H. 1978. Preventing Fouling in Plate Heat Exchangers. *Chemical Engineering*. Vol 86 No 1, pp. 87-90.

Damianides, C. A., and Westwater, J. W., 1988. Two-phase flow patterns in a compact heat exchanger and in small tubes, Proceedings of 2nd UK National Conference on Heat Transfer, Glasgow, Scotland, Vol II, pp. 1257-1268.

Davis, E.J., and Anderson, G.H. 1966.The incipience of nucleate boiling in forced convection flow, *AIChE J*, Vol 12, pp. 774-780.

Dukler, A. E., and Taitel, Y. 1991. Flow Pattern Transitions in Gas-Liquid Systems (Chap. 3), Modelling Two-phase Annular Flow (Chap. 5), and Modelling Upward Gas-Liquid Flow (Chap. 7), in *Two-Phase Gas-Liquid Flow: A Short Course on Principles of Modelling Gas-Liquid Flow and on Modern Measuring Methods*. University of Houston, TX.

Farrell, P., Wert, K., and Webb, R. 1991. Heat Transfer and Friction Characteristics of Turbulator Radiator Tubes. *SAE Transactions*, Vol 100, No 5, pp. 218-230.

Filonenko, G. K., 1954. Hydraulic Resistance in Pipes (in Russian). *Teploenergetika* 1, No 4, pp. 40-44.

Friedel, L., 1979. Improved friction pressure drop correlations for horizontal and vertical two-phase pipe flow, Presented at the European Two-phase Flow Group Meeting, Ispra, Italy, paper E2, June.

Frost, W., and Dzakovic, G. S., 1967. An extension of the methods of predicting incipient boiling on commercially finished surfaces. ASME paper 67-HT-61, presented at the 1967 National Heat Transfer Conference, Seattle, WA, USA

Fuchs, P. H. 1975. Trykkfall og varmeovergang ved strømning av fordampende væske i horisontale rør og bend. Doctoral dissertation (in Norwegian). Department of Refrigeration Engineering, NTH, Trondheim.

Garimella, S., and Bandhauer, T. M., 2001. Measurement of Condensation Heat Transfer Coefficients in Microchannel Tubes, *Proc 2001 ASME Int. Mech. Eng. Congr. and Expo.,* November 11-16, New York, Paper HTD-24221

Ghajar, A. T., and Asadi, A. 1986. Improved Forced Convective Heat Transfer Correlation for Liquids in the Near Critical Region, *AIAA Journal,* Vol 24 No 12, pp. 2030-2037.

Gnielinski, V., 1976. New equations for heat and mass transfer in turbulent pipe and channel flow. *International Chemical Engineering*, Vol 16 No 2, pp 359-368.

Gorenflo, D. 1993. Pool Boiling. Chapter Ha in VDI Heat Atlas, English translation of VDI –Wärmeatlas, 6. auflage. Edited by VDI Gesellschaft Verfahrenstechnik und Chemieingenieurwesen. VDI-Verlag.

Govan, A. H., Hewitt, G. F., Owen, D. G., and Bott, T. R., 1988. An improved CHF modelling code. Second UK National Conference on Heat Transfer, IMechE/University of Strathclyde, 14-16 September, Vol 1, pp. 33-48.

Groeneveld, D. C., 1973. Post-dryout heat transfer conditions at reactor operating conditions, National Topical Meeting on Water Reactor Safety, Paper AECL-4513, ANS, Salt Lake City, Utah, 26-28 March.

Groeneveld, D. C., and Delorme, G. G. J. 1976. Prediction of Thermal Non-Equilibrium in the Post-Dryout Regime. *Nuclear Engineering and Design,* Vol 36, pp. 17-26.

Groeneveld, D.C., Kiameh, B.P., and Cheng, S.C., 1986. Prediction of Critical Heat Flux (CHF) for Non-Aqueous Fluids in Forced Convective Boiling. *Proc 8th Int. Heat Transfer Conf.,* New York, Vol 5, Hemisphere, pp. 2209-2214.

Grønnerud, R. 1971. Undersøkelse av resirkulasjonsfordamper. Hovedarbeid ved den tekniske licentiatgrad. Institutt for kjøleteknikk, NTH. Doctoral dissertation (in Norwegian)

Gungor, K. E., and Winterton, R. H. S., 1986. A General Correlation for Flow Boiling in Tubes and Annuli, *Int. J. Heat Mass Transfer,* Vol 29, No 3, pp. 351-358

Gungor, V., and Winterton, R. H. S., 1987. Simplified General Correlation for Saturated Flow Boiling and Comparison of Correlations with Data, *Chem Eng. res. Des.,* Vol 65, March, pp. 148-156.

Haaland, S. E., 1983. Simple and explicit formulas for the friction factor in turbulent pipe flow. *J. Fluids Eng.,* Vol 195, pp. 89-90.

Hadaller, G., and Banerjee, S., 1969. Heat Transfer to Superheated Steam in Round Tubes, AECL unpublished report, quoted by Groeneveld and Delorme (1976)

Hewitt, G. F., and Govan, A. H., 1990. Phenomenological modelling of non-equilibrium flows with phase change, *Int. J. Heat Mass Transfer*, Vol 33, No 2, pp. 229-242.

Hihara, E. 2000. Heat Transfer Characteristics of CO_2. IEA Annex 27 Workshop on Selected Issues on CO_2 as Working Fluid in Compression Systems, Trondheim, September.

Hihara, E., and Tanaka, S. 2000. Boiling Heat Transfer of Carbon Dioxide in Horizontal Tubes. Preliminary Proceedings of the IIR Gustav Lorentzen Conference on Natural Working Fluids, Purdue University, W. Lafayette, IN, USA, July. pp. 279-284.

Hoyer, N., 1998. Calculation of Dryout and Post-Dryout Heat Transfer for Tube Geometry, *Int. J. Multiphase Flow,* Vol 24, No 2, pp. 319-334.

Høgaard Knudsen, H. J., and Jensen, P. H. 1997. Heat Transfer Coefficient for Boiling Carbon Dioxide, Workshop Proceedings – CO_2 Technology in Refrigeration, Heat Pump and Air Conditioning Systems. IEA-IIR Workshop, Trondheim, Norway, May. Report HPC-WR-19, pp. 319-328.

Høgaard Knudsen, H. J. 1998. Varmeovergang og trykfald ved fordampning av kuldioxid. DTI Temadag: Kuldioxid i køle- og varmepumpeanlæg. November.

Ishibashi, E., and Nishikawa, K. 1969. Saturated Boiling Heat Transfer in Narrow Spaces. *Int J heat Mass Transfer,* Vol.12, pp. 863-894.

Ishii, M, and Mishima, K., 1981. Correlation for liquid entrainment in annular two-phase flow of low viscous fluid. Argonne National Laborator Report, ANL/RAS/LWR 81-2.

Jackson, J. D., and Fewster, J., 1975. Forced convection data for supercritical pressure fluids, HTFS 21540

Kandlikar, S. G., 1983. An Improved Correlation for Predicting Boiling Heat Transfer in Horizontal and Vertical Tubes, in *Heat Exchangers for Two-Phase Flow Applictions,* ASME

Kandlikar, S. G., 1990. A General correlation for Saturated Two-Phase Flow Boiling Heat Transfer Inside Horizontal and Vertical Tubes, *ASME J. Heat Transfer*, Vol 112, pp. 219-228.

Kandlikar, S. G., and Alves, L. 1999. Effects of Surface Tension and Binary Diffusion on Pool Boiling of Dilute Solutions: An Experimental Assessment. *Trans. ASME Journal of Heat Transfer*, Vol 121, May, pp. 488-493.

Kaszra, K. E., Didascalou, T., and Wambsganss, M. W. 1997. Microscale Flow Visualization of Nucleate Boiling in Small Channels: Mechanisms Influencing Heat Transfer: Mechanisms Influencing Heat Transfer. Proc. International Conference on Compact Heat Exchangers for the Process Industries, Snowbird, Utah, USA, June 22-27, pp. 343-352.

Kattan, N. 1996. Contribution to the heat Transfer Analysis of Substitute Refrigerants in Evaporator Tubes with Smooth or Enhanced Tube Surfaces. Thése No. 1498 (1996), École Polytechnique Fédérale de Lausanne (EFPL).

Kattan, N., Thome, J. R., Favrat, D., 1998a. Flow Boiling in Horizontal Tubes : Part 1 – Development of a Diabatic Two-Phase Flow Pattern Map. *Trans. ASME, J. Heat Transfer*, Vol 120, pp. 140-147.

Kattan, N., Thome, J. R., Favrat, D., 1998b. Flow Boiling in Horizontal Tubes : Part 3 – Development of a New Heat Transfer Model Based on Flow Pattern. *Trans. ASME, J. Heat Transfer*, Vol 120, pp. 156-165.

Katto, Y., 1981. On the relation between CHF and outlet flow pattern of forced convection boiling in uniformly heated vertical tubes. *Int. J. Heat Mass Transfer*, Vol 24, pp. 533-539.

Katto, Y and Ohno, H., 1984. An improved version of the generalized correlation for critical heat flux for the forced convection boiling in uniformly heat vertical tubes, *Int J. Heat Mass Transfer*, Vol 27, pp. 1641-1648.

Kefer, V. 1989. Strömungsformen und Wärmeübergang in Verdampferrohren unteschiedlicher Neigung. Dissertation Tech. Univ. Munich.

Kakac, S, Shah, R. K., and Aung, W. 1987 *Handbook of Single-Phase Convective Heat Transfer*, John Wiley & Sons.

Kays, W. M. and Crawford, M. E. 1993. Convective Heat and Mass Transfer, 3rd Edition, McGraw-Hill, Inc.

Kew, P. A. and Cornwell, K., 1994. Confined Bubble Flow and Boiling in Narrow Spaces. 10th International Heat Transfer Conference, Brighton, UK, Vol 7.

Khartabil, H. F., and Christensen, R. N., 1992. An Improved Scheme for Determining Heat Transfer Correlations from Heat Exchanger Regression Models with Three Unknowns. *Experimental Thermal and Fluid Science*, Vol 5, pp. 808-819.

Knudsen, J. G. 1988. Recommended fouling resistances for design. In: Heat Exchanger Design Handbook, Section 3.17.7. Begell House, Inc., G. F. Hewitt, Executive Editor.

Kon'kov, A. S., 1965. Experimental Study on the Conditions under which Heat Exchange Deteriorates when a Steam-Water Mixture Flows in heated Tubes. *Teploenergetika*, Vol 13, No 12, pp. 77.

Koyama, S., Kuwahara, K., Shinmura, E., and Ikeda, S. 2001. Experimental Study on Flow Boiling of Carbon Dioxide in a Horizontal Small Diameter Tube. IIR Conference on Thermophysical Properties and Transfer Processes of New Refrigerants, October 3 – 5, Paderborn, Germany.

Kutateladze, S. S., 1948. On the transition to film boiling under natural convection. *Kotloturbostroenie,* Vol 3 No 10.

Kutateladze, S. S., 1961. Boiling Heat Transfer. *Int J. Heat Mass Transfer,* Vol 4, pp. 31-45.

Levitan, L.L., and Lantsman, F.P., 1975. Investigating burnout with flow of a steam-water mixture in a round tube. *Thermal Engineering* (USSR), English trnslation, Vol 22, No 1, pp. 102-107.

Liu, Z., and Winterton, R. H. S., 1988. Wet Wall Flow Boiling Correlation with Explicit Nucleate Boiling Term, in *Multiphase Transport and Particulate Phenomena,* Hemisphere, Vol 1, pp. 419-432.

Lombardi, C., and Carsana, C. G., 1992. A dimensionless pressure drop correlation for two-phase mixtures flowing upflow in vertical ducts covering wide parameter range, *Int. J. Heat and Technology*, Vol 10, No 1-2, pp. 125-141.

Lorentzen, G., Pettersen J., and Bang, R.R. 1993. Method and device for high side pressure regulation in transcritical vapor compression cycle. United States Patent 5,245,836, September 21

Lorentzen, G., and Pettersen J. 1992. New Possibilities for Non-CFC Refrigeration. Proceedings from International Symposium on Refrigeration, Energy and Environment, Trondheim, pp. 147-163, June

Milashenko, V, I., Nigmatulin, B. I., Pethukov, V. V., and Trubkin, 1989. Burnout and distribution of liquid in evaporative channels of various lengths. *Int J. Multiphase Flow,* Vol 15, pp. 393-402.

Moffat, R. J. 1988. Describing the Uncertainties in Experimental Results. *Experimental Thermal and Fluid Science,* Vol 1, pp. 3-17.

Monde, M. 1988. Characteristic of Heat Transfer Enhancement Due to Bubble Passing Through a Narrow Vertical Channel. Trans ASME, Journal of Heat Transfer, Vol 110, November, pp. 1017-1019.

Mostinski, I. L., 1963. Calculation of Heat Transfer and Internal Heat Fluxes in Boiling Liquid based on Law of Corresponding States, *Teploenergetika*, Vol 4, p. 66. English abstract in *Brit. Chem. Engrg.* Vol 8, No 8, p. 580, 1963

Munkejord, S. T. 1997. Varmeovergang og trykktap i ekstruderte multiportrør (Heat transfer and pressure drop in extruded multiport tubes), Hovedoppgave H9714 (Master dissertation), Department of Refrigeration and Air Conditioning, Norwegian University of Science and Technology.

Nishikawa, K., Yoshida, S., Mori, H., and Takamatsu, H., 1986. Post-dryout heat transfer to Freon in a vertical tube at high subcritical pressure. *Int J. Heat Mass Transfer,* Vol 29, No 8, pp. 1245-1251.

Ohadi, M., Molki, M., and Zhao, Y. 2000. CO_2 Heat Transfer and Fluid Flow. Presentation at Workshop on Vapor Compression with the Critical Point in Mind, University of Maryland, February.

Olson, D. A. 2000. Heat transfer of supercritical carbon dioxide flowing in a cooled horizontal tube. Preliminary Proceedings of the IIR Gustav Lorentzen Conference on Natural Working Fluids, Purdue University, W. Lafayette, IN, USA, July. pp. 251-258.

Peng, X. F., Wang, B. X., Peterson, G. P. and Ma, H. B. 1995. Experimental Investigation of Heat Transfer in Flat Plates with Rectangular Microchannels, *Int. J. Heat Mass Transfer*, Vol 38(1), pp. 127-137

Perry's Chemical Engineers Handbook, 1963. McGraw-Hill, 4th Edition.

Pettersen, J., Hafner, A., Skaugen, G., and Rekstad, H. 1998. Development of Compact Heat Exchangers for CO_2 Air-Conditioning Systems. *International Journal of Refrigeration*, Vol 21, No 3, pp. 180-193.

Pettersen, J., Rieberer, R., Munkejord, S.T. 2000. Heat Transfer and Pressure Drop for flow of Supercritical and Subcritical CO_2 in Microchannel Tubes. Final Technical Report. US Army, European Research Office, Contract N-68171-99-M-5674. Report issued by SINTEF Energy Research and Norwegian University of Science and Technology, February.

Pettersen, J., 2001. Unpublished laboratory test data on heat transfer in flow vaporization of CO_2 in a 2.4 mm ID stainless steel tube heated by water.

Pethukov, B. S. 1970. Advances in Heat Transfer, Vol 6, Academic Press, pp. 503-564.

Pitzer, K.S. and Schreiber, D.R. 1988. Improving Equations-of-state Accuracy in the Critical Region; Equations for Carbon Dioxide and Neopentane as Examples. *Fluid Phase Equilibria*, vol. 41, pp. 1–17.

Rieberer, R., 1998. CO_2 as Working Fluid for heat Pumps. Revised copy of doctoral thesis submitted to the Faculty of Mechanical Engineering, Graz University of Technology, December.

Rouhani, Z., and Axelsson, E., 1970. Calculation of Volume Void Fraction in the Subcooled and Quality Region, *Int. J. Heat Mass Transfer*, Vol 13, pp. 383-393

Sato, T., and Matsumura, H. 1964. *Bull. Japan. Soc. Mech. Eng.* Vol 7, p. 392.

Schrock, V. E., and Grossmann, L. M., 1962, Forced convection boiling in tubes, *Nuclear Science and Enginering*, Vol 12, pp. 474-481.

Selander, W. N., 1978. Explicit formulas for the computation of friction factors in turbulent pipe flow, AECL 6354, November.

Shah, M. M., 1976. A New Correlation for Heat Transfer During Boiling Flow Through Pipes, *ASHRAE Transactions,* Vol 82, Part II, pp. 66-86.

Shah, M. M., 1982. Chart Correlation for Saturated Boiling Heat Transfer: Equations and Further Study. ASHRAE Transactions, Vol 88, Part 1.

Shah, M. M., 1987. Improved general correlation for critical heat flux during upflow in uniformly heated vertical tubes, *Heat and Fluid Flow,* Vol 8, No 4, December, pp. 326-335.

Shah, M.M., and Siddiqui, M.A., 2000. A General Correlation for Heat Transfer During Dispersed-Flow Film Boiling in Tubes, *Heat Transfer Engineering,* Vol 21 No 4, pp. 18-32.

Shah, R. K., 1990. Assessment of Modified Wilson Plot Techniques for Obtaining Heat Exchanger Design Data. Proc. 9th Int. Heat Transfer Conference, Jerusalem, Israel, Vol. 5 pp. 51-56. Paper 14-HX-9.

Shrock, V. E., and Grossmann, L. M., 1959. Forced Convection Vaporization Project – Final report. University of California, Institute of Engineering Research, Report no 73308-UCX-2182, TID-14632.

Steiner, D. 1993. Heat transfer to boiling saturated liquids. Chapter Hbb in VDI Heat Atlas, English translation of VDI –Wärmeatlas, 6. auflage. Edited by VDI Gesellschaft Verfahrenstechnik und Chemieingenieurwesen. VDI-Verlag.

Steiner, D., and Taborek, J. 1992. Flow Boiling Heat Transfer in Vertical Tubes Correlated by an Asymptotic Model. *Heat Transfer Engineering,* Vol 13, No 2, pp. 43-69.

Stephan, K., and Preusser, P., 1979. Wärmeübergang und maximale Wärmestromdichte beim Behältersieden binärer und ternärer Flüssigkeitsgemische. *Chem Ing- Techn.* MS649/79, Synopsis in *Chem Ing. Techn.* Vol 51, p. 37.

Sun, Z., and Groll, E. 2001. CO_2 Flow Boiling In Horizontal Tubes. Ray W. Herrick Laboratories, Purdue University, Internal Report #229. HL-2001-8, W. Lafayette, Indiana, USA, April.

Taitel, Y., and Dukler, A. E., 1976. A model for predicting flow regime transitions in horizontal and near-horizontal gas-liquid flow. *AIChE J.* Vol 22, pp. 47-55.

Tang, H. K. 1998. Differences in calculation method of the heat transfer coefficient k. Student report, July 28, SINTEF Energy Research, Trondheim.

Thome, J. R., 1995. Flow Boiling in Horizontal Tubes: A Critical Assessment of Current Methodologies. International Symposium of Two-Phase Flow Modelling and Experimentation, Vol 1, Rome, Edizioni ETS, pp. 41-52.

Thome, J.R., 1996, Heat Transfer and Pressure Drop in the Dryout Region of Intube Evaporation with Refrigerant/Lubricant Mixtures. ASHRAE Project 800-RP Final Report, Swiss Federal Institute of Technology, December 13.

Thome, J. R. 1998. Boiling and Evaporation of Fluorocarbon and Other Refrigerants: A State-of-the-art Review. Report prepared for ARI, Arlington Virginia, March 27.

Tong, L.S., and Tang, Y.S. 1997. Boiling Heat Transfer and Two-Phase Flow. Second Edition. Taylor and Francis.

Tran, T. N., Wambsganss, M. W., Chyu, M.-C. and France, D. M. 1997. A Correlation for Flow Boiling in Small Channels. Proc. International Conference on Compact Heat Exchangers for the Process Industries, Snowbird, Utah, USA, June 22-27, pp. 353-363

Tran, T. N., Wambsganss, M. W., and France, D. M., 1999**,** Two-phase Pressure Drop of Refrigerants During Flow Boiling in Small Channels: An Experimental Investigation and Correlation Development. Int. Conference On Compact Heat Exchangers and Enhancement Technology for the Process Industry, Banff, Canada, July 18-23, pp 293-302.

Triplett, K. A., Ghiaasiaan, S. M., Abdel-Khalik, S. I., and Sadowski, D L., 1999. Gas-liquid flow in microchannels Part 1. two-phase flow patterns. *Int J. Multiphase Flow,* Vol 25, pp. 377-394.

Vesovic, V., Wakeham, W.A., Olchowy, G.A., Sengers, J.V., Watson, J.T.R. and Millat, J. 1990. The Transport Properties of Carbon Dioxide. *J. Phys. Chem. Ref. Data*, vol. 19, no. 3, pp.763–808.

Umekawa, H., Ozawa, M., Mitsunaga, T., Mishima, K., Hibiki, T., and Saito, Y., 1999. Scaling Parameter of CHF under Oscillatory Flow Conditions, *Heat Transfer – Asian Research,* Vol 28 No 6, pp. 541-550.

Utsuno, H., and Kaminaga, F., 1998. Prediction of Liquid Film Dryout in Two-Phase Annular-Mist Flow in a Uniformly Heated Narrow Tube – Development of Analytical Method under BWR Conditions. *J. Nuclear Science and Tech.,* Vol 35, No 9, pp. 643-653.

Wallis, G. B., 1969. One-dimensional Two-Phase Flow. McGraw-Hill.

Wambsganss, M. W., Jendrzejczyk, J. A., France, D. M., and Obot, N. T. 1992. Frictional Pressure Gradients in Two-Phase Flow in a Small Horizontal Rectangular Channel, *Experimental Thermal and Fluid Science,* Vol 5, pp. 40-56.

Wambsganss, M. W., Shah, R. K., Celata, G. P., and Zummo, G. 1997. Vaporization in Compact Heat Exchangers. *Experimental Heat Transfer, Fluid Mechanics and Thermodynamics 1997.* pp. 2049-2062

Wattelet, J.P., Chato, J.C., Souza, A.L., and Christoffersen, B. R., 1994. Evaporative Characteristics of R-12, R-134a, and a Mixture at Low Mass Fluxes, ASHRAE Transactions, Vol 100, No 1, pp. 603-615.

Webb, R. L., and Gupte, N. S., 1992. A Critical Review of Correlations for Convective Vaporization in Tubes and Tube Banks, *Heat Transfer Engineering*, Vol 13, No 3, pp. 58-81.

Weisman, J., Duncan, D., Gibson, J., and Crawford, T., 1979. Effect of Fluid Properties and Pipe Diameter on Two-Phase Flow Pattern in Horizontal Lines, *Int J. Multiphase Flow*, Vol 5, 1979, pp. 437-462

Wilson, E. E. 1915. A Basis for Rational Design of Heat Transfer Apparatus. *Trans ASME,* Vol 37, pp 47-70.

Wojs, K., and Tietze, T. 1997. Effects of temperature interference on the results obtained using the Wilson plot technique. *Heat and Mass Transfer* Vol 33, pp. 241-245.

Wu, W.-T., Yang, Y.-M., Maa, J.-R., 1998. Nucleate Pool Boiling Enhancement by Means of Surfactant Additives. *Experimental Thermal and Fluid Science*, Vol 18, pp. 195-209.

Yu, J., Momoki, S., and Koyama, S. 1999. Experimental study of surface effect on flow boiling heat transfer in horizontal smooth tubes, *Int. J. Heat Mass Trans.*, Vol 42, pp. 1909-1918.

Yun, R., Hwang, J. H., Kim, Y. C., and Kim, M. S. 2001. Evaporation Heat Transfer Characteristics of Carbon Dioxide in a Horizontal Smooth Tube, IIR Conference on Thermophysical Properties and Transfer Processes of New Refrigerants, October 3 – 5, Paderborn, Germany.

Zakeri, G.R., Nekså, P., Rekstad, H., Lang-Ree, K. and Olsen, T., 2000. Results and experiences with the first commercial pilot plant CO_2 heat pump water heater, , *4th IIR-Gustav Lorentzen Conference on Natural Working Fluids*, Purdue, USA, July 25-28.

Zhao, Y., Molki, M., Ohadi, M. M., Dessiatoun, S. V., 2000. Flow Boiling of CO_2 in Microchannels. *ASHRAE Transactions*, Vol. 106, Part 1.

Zuber, N. 1959. Hydrodynamic aspects of nucleate boiling, PhD dissertation, Dept. of Engineering, Univ. of California, Los Angeles.